



HAL
open science

Imaging the assembly of the phagocyte NADPH oxidase in live cells -a quantitative FRET-FLIM approach

Cornelia Susanne Ziegler

► To cite this version:

Cornelia Susanne Ziegler. Imaging the assembly of the phagocyte NADPH oxidase in live cells -a quantitative FRET-FLIM approach. Biophysics. Université Paris Saclay, 2016. English. NNT : . tel-01623408

HAL Id: tel-01623408

<https://hal.science/tel-01623408v1>

Submitted on 30 Oct 2017

HAL is a multi-disciplinary open access archive for the deposit and dissemination of scientific research documents, whether they are published or not. The documents may come from teaching and research institutions in France or abroad, or from public or private research centers.

L'archive ouverte pluridisciplinaire **HAL**, est destinée au dépôt et à la diffusion de documents scientifiques de niveau recherche, publiés ou non, émanant des établissements d'enseignement et de recherche français ou étrangers, des laboratoires publics ou privés.

NNT : 2016SACLS048

THESE DE DOCTORAT
DE
L'UNIVERSITE PARIS-SACLAY
PREPAREE A
L'UNIVERSITE PARIS SUD

ECOLE DOCTORALE N°571

Sciences chimiques : molécules, matériaux, instrumentation et biosystèmes

Spécialité de doctorat : Chimie

Cornelia Susanne Ziegler

Imaging the assembly of the phagocyte NADPH oxidase in live cells
- a quantitative FRET-FLIM approach

Thèse présentée et soutenue à Orsay, le 14 mars 2016 :

Composition du Jury :

Mme Bonneau Stéphanie
Mme Palet Marie Hélène
Mr Ostuni Mariano
Mr Van Tilbeurgh Herman
Mme Erard Marie
Mr Nüße Oliver

Maitre de Conférences, UPMC
Maitre de Conférences, Université Joseph Fourier
Professeur, Université Paris Diderot
Professeur, UPSud
Maitre de Conférences, UPSud
Professeur, UPSud

Rapporteur
Rapporteur
Examineur
Président du jury
Directeur de thèse
Co-directeur de thèse

für Mama

Acknowledgement

Foremost, I would like to express my sincere gratitude to Mehran Mostavafi, the former head of the LCP, to give me the opportunity to make my PhD in his laboratory. In the same context, I would like to thank all members of the laboratory and the administration for their ongoing support during my stay.

I am deeply grateful to my thesis committee, especially the rapporteurs Stéphanie Bonneau and Marie-Hélène Paclet, as well as the examinateurs Mariano Ostuni, and Herman Van Tilbeurgh to accept my thesis.

I would also like to thank Marc Tramier (IGDR, Rennes) for his collaboration to give me access to his laboratory and research facilities. Likewise, I would like to thank Dominique Durand (Université Paris Sud) for kindly and straightforward providing me the structure files which were indispensable for the structural modelling.

My sincere thanks also go to Fabienne Mérola, who gave me the chance to join her group and furthermore for the stimulating discussions and scientific input to my work.

Special thanks goes to my director Marie Erard for her continuous support in both scientific and private life, for the immense scientific input to my project, the advice, and patient explanations. She contributed greatly to the successful and pleasant time of my PhD project.

Likewise I would like to thank my co-director Oliver Nüße most sincerely for his guidance and strong scientific contribution to this project, the helpful discussions and his patience.

I am as well thankful to Sophie Dupré for her gentle advice and ongoing help during my project, as well as to Hélène Pasquier for her support. Special thanks goes to Yasmina Bousmah, her never-ending help for my practical lab work and for maintenance of the lab.

I would also like to thank warmly my fellow PhD students, namely Leila Bouchab for introducing me to the practical flow cytometer work and for her friendship, Myriam Moussaoui for her cheerfulness, with which she delighted the weekends and nights we spent together in the lab during the writing of our thesis, Ana-Laura Luna-Barron for the very good time we spent together and for her motivation, Damien Clavel for the rare but great evenings without ever talking about our work, Dahdjim Betolngar for facilitating my start in France, and finally Zhimin Song for his cheerfulness.

It is my personal intention to thank my husband Sven Böckmann for his love and his immense support in every respect. There are too many things to say. Without him in my back, this project would not have been possible. Likewise, I would like to thank my son Julian Erasmus to light up my days with his smile and to master the hard time of my writing with the help of his daddy.

Last but not least I would like to thank Antony Campbell, University of Cardiff, Wales, advisor of my master thesis, to instil the self-confidence and motivation in me to do a PhD and for his ongoing support.

Contents

1	Introduction	5
1.1	Quantitative fluorescence imaging of protein-protein interactions in the NADPH oxidase complex	6
1.2	Aim of the thesis	8
1.3	Fluorescence and Förster Resonance Energy Transfer	9
1.3.1	Fluorescence – the physical background	9
1.3.2	Förster resonance energy transfer	11
1.4	NADPH Oxidase	15
1.4.1	The phagocyte NADPH oxidase	17
1.4.1.1	Resting state, activation, and deactivation	18
1.4.1.2	Structure of the NADPH Oxidase	20
2	Material and Methods	30
2.1	Buffers	30
2.2	Methods	30
2.2.1	Bacterial cell culture	30
2.2.2	Plasmid preparation	31
2.2.3	Plasmid cloning	32
2.2.4	Production and purification of recombinant proteins	32
2.2.5	Eukaryotic cell culture	34
2.2.6	Transient transfection of COS cells	34
2.2.7	Western Blot	35
2.2.8	Luminescence Assay	38
2.2.9	Flow Cytometry	40
2.2.10	Microscopy	46
2.2.10.1	Total Internal Reflection Fluorescence (TIRF) Microscopy	46
2.2.10.2	FRET-FLIM	47
2.2.11	Fluorescence cross correlation spectroscopy	51
2.2.11.1	FCCS setup	55
2.2.12	Data acquisition and analysis with SymPhoTime software	56
2.2.13	Molecular structure visualisation and alignment	56
2.2.14	Statistical analysis	56
3	Results – methodology development for FRET quantification	57
3.1	Flow Cytometry	57
3.1.1	Elucidating the transfection efficiency by flow cytometry	57
3.1.2	FRET by Flow Cytometry	59

3.1.2.1	Optimization of the cytometer for FRET demands.....	60
3.1.2.2	Developing a FRET analysis method	62
3.2	Quantification of protein-protein interactions in live cells.....	66
3.2.1	Introduction to the methodology	66
3.2.2	Extraction of FRET parameters from fluorescence lifetime imaging microscopy data	67
3.2.3	Fluorescence intensity wide field microscopy	69
3.2.3.1	Determination of the donor and acceptor intensity.....	69
3.2.3.2	Determination of the ratio of the amount of acceptor/donor	73
3.2.4	Extraction of the quantitative data and specificity of the interaction.....	75
3.2.5	Estimation of the dissociation constant K_d	79
4	Results – Interactions between NADPH oxidase subunits.....	81
4.1	Proving functionality of the cytosolic subunits	81
4.1.1	Verification of the size of the expressed protein by Western Blot.....	81
4.1.2	Verifying the activatability of the complex.....	89
4.1.2.1	Tracking the arrival of the complex on the membrane	89
4.1.2.2	Measuring the hydrogen peroxide production	95
4.2	Interactions of the cytosolic subunits	97
4.2.1	Hetero-dimeric interactions between the subunits	97
4.2.1.1	Interaction of p67 ^{phox} with p47 ^{phox}	97
4.2.1.2	p67 ^{phox} interacts with p40 ^{phox}	102
4.2.1.3	p47 ^{phox} interacts with p40 ^{phox}	105
4.2.1.4	Homo-dimerization of the subunits	107
4.2.1.5	Intramolecular interactions	110
4.2.2	Results obtained from CFP-YFP FCCS	116
5	Discussion	119
5.1	Discussion of the quantitative approach.....	120
5.1.1	Interpretation of the bound fraction	120
5.1.1.1	Factors influencing the apparent bound fractions of proteins.....	122
5.1.1.2	Methodology specific biasing factors on the bound fraction.....	127
5.1.1.3	Conclusion on the apparent bound fraction	131
5.1.2	Dissociation constant estimated with FRET-FLIM and wide-field microscopy approach	133
5.2	Discussion of the structural information obtained by FRET-FLIM	134
5.2.1	Intra-molecular interactions	135
5.2.2	Inter-molecular Interactions	142
6	Conclusion.....	149
7	Perspectives.....	151

8	Appendix	153
8.1	Protein production and purification	153
8.1.1	Fluorescent proteins	153
8.1.2	Cytosolic subunits \pm FP tag.....	154
8.2	Determination of the intensity working frame	156
8.3	Derivation of the K_d resolved with the bound fraction.....	157
8.4	Influence the bound fraction on the K_d	158
8.5	Correction of the spectral bleed-through in FCS with FLCS	159
9	List of abbreviations.....	161
10	List of figures	162
11	Literature	165

1 Introduction

Proteins take on a variety of tasks in living organisms like structural, enzymatic and regulatory functions. The majority is not acting as individual proteins but in complex with other proteins – for the human proteome a share of 80 % is estimated. These interactions are mainly dynamic and allow the cells to react to environmental changes and stimuli. Signalling cascades are a good example of highly regulated transient protein interactions, in which conformational changes of at least one partner leads to the next step of the cascade. To understand these fundamental processes of life, numerous techniques were developed to discover and study protein-protein interactions such as protein microarrays, X-ray crystal structure, affinity tagging and pull-down assays, immunoprecipitation, peptide arrays or yeast two-hybrid and fluorescence microscopy (Dwane and Kiely, 2011). Most of these techniques are performed *in vitro* on purified proteins or on a lysed cell population except the two last that are compatible with live cell. The native environment of the proteins is important, since it is influencing the spatiotemporal dynamics of any process: It can differ from *in vitro* studies (Ganesan and Zhang, 2012). In addition, most of the quantitative data on protein interactions such as molecular affinities are obtained with *in vitro* studies and may differ by several orders of magnitudes from those prevailing under intracellular conditions (Cardarelli et al., 2009, Foo et al., 2012). Therefore, there is a strong need of truly *in situ* quantitative and dynamic approaches of these protein interactions. Here, we will concentrate on fluorescence imaging approaches and more particularly on those that allows their quantitative investigation.

1.1 Quantitative fluorescence imaging of protein-protein interactions in the NADPH oxidase complex

Powerful bioanalytical imaging techniques based on fluorescence resonance energy transfer (FRET) and Green Fluorescent Proteins (GFPs) are increasingly used in pharmacological and clinical research (Aoki et al., 2012, Lang et al., 2006, Lu and Wang, 2010, Prinz et al., 2008) as well as in environmental sciences and biotechnologies (Larrainzar et al., 2005). Donor and acceptor fluorescent proteins (FP) are linked to the proteins of interest. When these fusion proteins interact, the fluorophores come into close proximity, which allows the energy transfer (distance between FPs < 10 nm). FRET imaging provides an optical readout of the interaction events within complex media such as living cells (Sun et al., 2011b).

There are several possibilities to measure FRET: With regard to the fluorescence properties of the donor and acceptor fluorophore, the effect of FRET is different: It implies a shortening of the fluorescence lifetime and intensity of the donor and an increase of the fluorescence intensity of the acceptor upon donor excitation. Consequently, FRET can either be measured with approaches based on intensity changes (acceptor photobleaching, ratiometric measurement, and “3-cubes” approach) or on the decrease of donor fluorescence lifetime (fluorescence lifetime imaging microscopy (FLIM)) (Padilla-Parra and Tramier, 2012).

FRET has been used in numerous biological systems addressing molecular interactions, probing the conditions and even the location of these interactions. Over 8000 articles report FRET experiments in biomedicine. With respect to “quantitative FRET measurements”, there are different levels, which can be reached depending on the methodology: As a basic step, it can mean differentiation between FRET positive vs. negative outcome (Banning et al., 2010), and further between specific vs. unspecific FRET (Kenworthy and Edidin, 1998, Abankwa and Vogel, 2007, Day, 2014); or more advanced, it provides information about the stoichiometry (Hoppe et al., 2002, Hoppe and Swanson, 2004, Beemiller et al., 2006, Beemiller et al., 2010) and the structure of the interacting partners (Preus and Wilhelmsson, 2012, Banerjee and Pal, 2007). Finally, it allows even a full characterization of a protein-protein binding by a determination of the fraction of donor-fused protein to the acceptor-fused partner (bound fraction, β) of the donor-fused protein to its (Meyer et al., 2006, Cardarelli et al., 2009) and of the dissociation constant (K_d) (Cardarelli et al., 2009). Within this project we aim to demonstrate, how far a FRET-FLIM based quantitative approach can go in live cells using the newly engineered cyan fluorescent protein (CFP) variants mTurquoise (Goedhart et al., 2010) and Aquamarine (Erard et al., 2013):

Indeed, although CFP is used in most of FRET studies (> 60 %) as donor in combination with a yellow fluorescent protein (YFP) as an acceptor, quantitative FRET-FLIM studies have remained limited until now by the suboptimal performance of the donor fluorophore (ECFP). ECFP is characterized by a low brightness and low photostability, a complex photophysics including multi-exponential fluorescence decays, and a strong environmental sensitivity (Villoing et al., 2008). In the past years, the structure-based photophysical engineering of CFPs led to the development of improved variants in several laboratories including our group ((Merola et al., 2013) for a review). mTurquoise (ECFP T65S, S72A, H148D, S175G, A206K) and Aquamarine (ECFP T65S, H148G) used during my PhD have a fluorescence quantum yield close to 90% leading to an improved brightnessⁱ, a single-exponential fluorescence decay, an improved photostability, and an insensitivity to their environment (Goedhart et al., 2010, Erard et al., 2013). These donors with a single-exponential emission decay (in contrast to FPs with multi-exponential decay) combined with FLIM detection methods allow in principle accurate quantifications of interacting vs. non-interacting populations and the analysis of subunit stoichiometry within multi-protein complexes (Miyawaki, 2011, Berezin and Achilefu, 2010, Kumar et al., 2011). We wanted to explore the feasibility of an intracellular quantitative approach based on the new CFP variants mTurquoise and Aquamarine, previously demonstrated using the less widely used green GFP donor (Cardarelli et al., 2009). FRET studies were already used to clarify interactions in dynamic processes with respect to time and localization during phagocytosis like G-protein activation relative to actin movement (Hoppe and Swanson, 2004) or the G-protein dependent cyclic regulation of phosphatidylinositol-3-kinase activity (Beemiller et al., 2010). For testing our approach, we chose the NADPH oxidase complex.

The NADPH oxidase complex (NOX) is responsible of the oxidative burst of phagocytic cells like neutrophils that is a major element in antimicrobial defence: The superoxide anion produced by the NADPH oxidase is the precursor of most other ROS that are later produced in the phagosome (Segal, 2005). However, an overactivation of the NADPH oxidase may lead to oxidative stress responsible of tissue damages, as in chronic inflammatory diseases such as rheumatoid arthritis (El-Benna et al., 2009). To keep this potentially harmful enzyme under tight control, it is composed of several subunits that are maintained apart, or pre-assembled as inactive complexes, in the resting cell. The gp91^{phox} and p22^{phox} subunits are integral membrane proteins that form the flavocytochrome b558. In response to cell stimulation, the other regulatory cytosolic components, p67^{phox}, p47^{phox}, p40^{phox} and the small Gase Rac translocate

ⁱ The brightness of a fluorophore is given by the product of its molar extinction coefficient and its quantum yield.

to the flavocytochrome and induce superoxide production (Nauseef, 2004). Due to the difficulty to cultivate and transfect primary neutrophils, most of our knowledge about the assembly and activation of the NADPH oxidase comes from biochemical studies (Nauseef, 2004, Nordenfelt and Tapper, 2011, Nüsse, 2011). Furthermore the mechanisms responsible for the ending of the ROS production and for the NADPH oxidase deactivation are still unknown (DeCoursey and Ligeti, 2005). Recently video microscopy experiments combined with subunits tagged with fluorescent proteins gave new insights on the dynamic behaviour of the subunits in the complex ((Tlili et al., 2012, Li et al., 2009, Tian et al., 2008, Faure et al., 2013). For example, it has been shown that p67^{phox} needs p47^{phox} to translocate at the phagosomal membrane and that the interaction between p47^{phox} and p67^{phox} was disrupted just after the phagosome closure whereas the ROS production was prolonged for several minutes (Ueyama et al., 2007, Li et al., 2009, Faure et al., 2013, Tlili et al., 2012). These first observations raised numerous questions on the spatio-temporal re-organization of the subunits for sustained ROS production that can only be solved with imaging approaches. Deciphering the sequence of the NADPH oxidase assembly and activation, as well as the conditions of its subsequent deactivation, would be the key of new diagnosis or therapeutic strategies for many inflammatory and degenerative diseases.

1.2 Aim of the thesis

The aim of the thesis was first to probe the feasibility of the CFP variants mTurquoise and Aquamarine for quantitative live cell studies of protein-protein interactions with FRET-FLIM. We want to test out the maximum reachable quantification level and to compare it to other quantitative imaging approaches such as FCCS.

Second, we intended to develop a new imaging approach for studying the interactions between the cytosolic subunits of the phagocyte NADPH oxidase in time and space. These interactions have been shown by biochemical techniques. Our approach aimed at demonstrating these interactions in live cells. Furthermore, we were seeking structural information on the complex formed by the oxidase subunits under live cell conditions.

1.3 Fluorescence and Förster Resonance Energy Transfer

FRET allows the monitoring of dynamic processes of transient protein-protein interactions with spatial resolution in live cells. Therefore, it is a very useful tool for biosciences. Among a variety of techniques suited for FRET measurements we chose the lifetime based FRET-FLIM, which features high accuracy, fluorophore concentration independency, and no necessity for cross talk correction (Padilla-Parra and Tramier, 2012). The current paragraph addresses the theoretical background of this method.

1.3.1 Fluorescence – the physical background

To facilitate the understanding of the FRET phenomenon and the FLIM approach, a short introduction in the physics of fluorescence will be given.

Fluorescence is, together with phosphorescence, a luminescence phenomenon. The excitation is initiated by the absorption of a photon. The relaxation from the excited state happens via radiative and non-radiative processes summarized in the Jablonsky-Perrin diagram (Figure 1) and is detailed below.

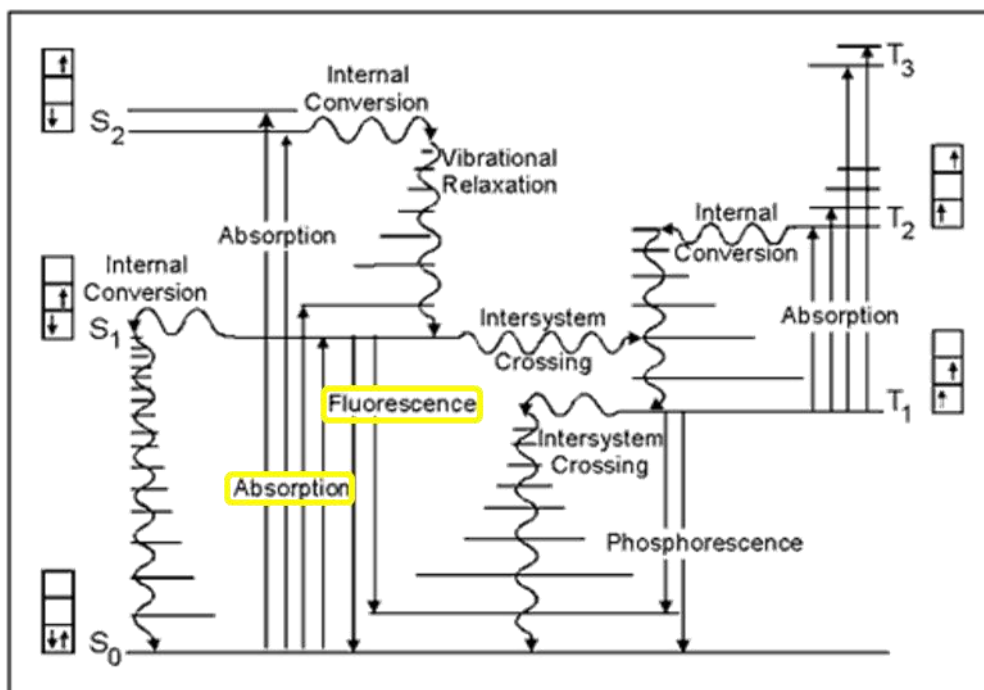


Figure 1 Jablonski diagram of the excitation and de-excitation pathways of a fluorophore

(Smith, 2009)

On the electron level, the excitation leads to a transition of an electron from an occupied or non-bonding orbital to an unoccupied one, whereby in principle the electron spin is conserved (= singlet state transition; $S_0 \rightarrow S_1$ or S_2). The probability of a transition is given by the absorbance $A(\lambda)$:

$$\text{Equation 1} \quad A(\lambda) = \log\left(\frac{I_{\lambda}^0}{I_{\lambda}}\right).$$

where I_{λ}^0 and I_{λ} are the intensities of the light before and after crossing the absorbing probe. Under certain circumstancesⁱⁱ, the absorbance is linearly proportional to the concentration, which is described by the Beer-Lambert Law:

$$\text{Equation 2} \quad A(\lambda) = \varepsilon(\lambda) \cdot l \cdot c$$

with $\varepsilon(\lambda)$, the molar extinction coefficient, l , the length of the absorption path, and c , the concentration of the absorbing probe.

The relaxation from the excited state happens via radiative and non-radiative processes. The radiative transition $S_1 \rightarrow S_0$ is called the fluorescence emission. The emitted photons have less energy than the excitation photons, which results in a shift of the excitation to the emission spectrum towards longer wavelengths. The difference in the maxima of the excitation and emission is called Stokes shift.

Other non-radiative de-excitation mechanisms can compete with the photon emitting fluorescence pathway (Figure 1): Internal conversion denotes a transition to a lower state with remaining spin orientation ($S_2 \rightarrow S_1$ or $S_1 \rightarrow S_0$), while the vibrational relaxation describes the de-excitation from a high vibrational level to the lowest one (high level $S_{1 \text{ or } 2} \rightarrow$ low level S_1 or S_0). The latter path is less energetically favoured and is in competition with the fluorescence pathway and intersystem crossing to the triplet state ($S_1 \rightarrow T_1$), which is as well a non-radiative relaxation process. The triplet state mainly de-excites through non-radiative mechanisms at room temperature.ⁱⁱⁱ

Fluorescence is only one of numerous de-excitation paths and the fraction of excited molecules, which de-excite through this way is the fluorescence quantum yield Φ , defined by the function of the rate constants of the radiative k_r and non-radiative processes k_{nr} :

$$\text{Equation 3} \quad \Phi = \frac{k_r}{k_r + k_{nr}}$$

With regard to the time, the photon absorption and electron transition to the excited state is a very fast process. In contrast, the electron can stay in the excited state from a few tens of ps to a few hundreds of ns before a relaxation (via photon emission, internal conversion, or

ⁱⁱ validate for homogeneous, low concentrated solutions with negligible scattering/variance of the $\varepsilon(\lambda)$ /self-emission, which are excited by monochromatic light

ⁱⁱⁱ At low temperatures, the radiative path (phosphorescence) is preferred ($T_1 \rightarrow S_0$). In contrast, with increasing temperature a reverse intersystem crossing ($T_1 \rightarrow S_1$) followed by a radiative relaxation to the ground state can occur, which is called delayed fluorescence. At high illumination power, a photon absorption of a molecule in T_1 leads to an electron transition to a higher level of triplet state T_2 (triplet-triplet transition).

intersystem crossing) takes place. This time is the fluorescence lifetime τ , which is characteristic for a specific molecule and is as well defined by the rate constants:

$$\text{Equation 4} \quad \tau = \frac{1}{k_r + k_{nr}}$$

Experimentally, the value of the fluorescence lifetime is calculated upon analysis of fluorescence emission decay after a very short excitation pulse. The fluorescence intensity $I(t)$ of a fluorophore follows an exponential decay law:

$$\text{Equation 5} \quad I(t) = k_r [FP^*]_0 \cdot e^{-\frac{t}{\tau}} = I_0 \cdot e^{-\frac{t}{\tau}}$$

where $[FP^*]_0$ is the fluorophore concentration in the excited state and I_0 is the fluorescence intensity at time point 0 (Valeur, 2006).

1.3.2 Förster resonance energy transfer

Förster resonance energy transfer (FRET) is an additional de-excitation pathway. It denotes the energy transfer via long-range dipole-dipole transition between a so-called donor and an acceptor fluorophore. It can only take place when the donor emission spectrum overlaps with the acceptor excitation spectrum, allowing energetically coupled (resonant) transitions. The rate constant of energy transfer k_T is given by:

$$\text{Equation 6} \quad k_T(r) = k_D \left[\frac{R_0}{r} \right]^6 = \frac{1}{\tau_D^0} \left[\frac{R_0}{r} \right]^6$$

with the emission rate constant of the donor k_D , the lifetime of the donor without energy transfer τ_D^0 , the distance between donor and acceptor r and the Förster radius R_0^{iv} . The latter one is defined by:

$$\text{Equation 7} \quad R_0^6 = \frac{9000(\ln 10)\kappa^2\Phi_D^0}{128\pi^5 N_A n^4} \int_0^\infty I_D(\lambda) \varepsilon_A(\lambda) \lambda^4 d\lambda$$

with the spatial orientation factor κ^2 , the fluorescence quantum yield of the donor (without energy transfer) Φ_D^0 , the refractive index of the medium n^v , and the Avogadro constant N_A . The integral depends on the spectral overlap and the intensity of the acceptor absorption: $I_D(\lambda)$ is

^{iv} For $r = R_0$, the probability of a spontaneous relaxation and an energy transfer are equally probable ($k_D = k_T$), which corresponds to an energy transfer of 50 %

^v refractive index of the cytosol: 1.36 – 1.39 CURL, C. L., BELLAIR, C. J., HARRIS, T., ALLMAN, B. E., HARRIS, P. J., STEWART, A. G., ROBERTS, A., NUGENT, K. A. & DELBRIDGE, L. M. D. (2005) Refractive index measurement in viable cells using quantitative phase-amplitude microscopy and confocal microscopy. *Cytometry Part A*, 65A, 88-92, VAN MANEN, H.-J., VERKUIJLEN, P., WITTENDORP, P., SUBRAMANIAM, V., VAN DEN BERG, T. K., ROOS, D. & OTTO, C. (2008) Refractive Index Sensing of Green Fluorescent Proteins in Living Cells Using Fluorescence Lifetime Imaging Microscopy. *Biophysical Journal*, 94, L67-L69, CHOI, W., FANG-YEN, C., BADIZADEGAN, K., OH, S., LUE, N., DASARI, R. R. & FELD, M. S. (2007) Tomographic phase microscopy. *Nat Meth*, 4, 717-719.

the normalized emission spectrum of the donor, i.e. $\int_0^\infty I_D(\lambda) d\lambda = 1$ and $\varepsilon_A(\lambda)$ is the molar extinction coefficient of the acceptor.

The spatial orientation factor κ^2 is given by the angle between donor (green) and acceptor (orange) transition moments θ_{DA} and the angles between these transition moments and the axis donor-acceptor θ_D and θ_A (Figure 2):

$$\text{Equation 8} \quad \kappa^2 = (\cos \theta_{DA} - 3 \cos \theta_D \cdot \cos \theta_A)^2$$

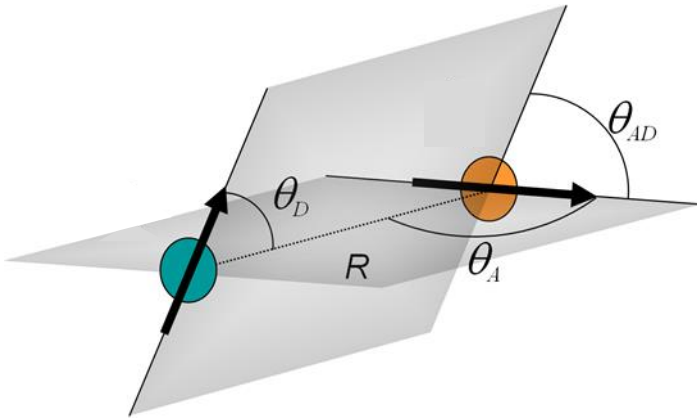


Figure 2 Angles involved in the definition of the orientation factor κ^2

The dipole moment of the donor (green) and acceptor (orange) is displayed with flashes. The axis between donor and acceptor is the separation vector. The angles between this vector and the dipole orientation of donor and acceptor θ_D and θ_A gives the dipole orientation while θ_{AD} gives the angle between the two dipole moments.

κ^2 can have values between 0 and 4 depending on the relative orientation of the transient dipole moments of the donor and the acceptor (perpendicular oriented dipoles \Rightarrow no FRET possible, coaxial aligned dipoles \Rightarrow perfect condition for FRET). Figure 3 A displays the influence of the spatial orientation on the Förster distance on the example of Aquamarine/Citrine couple: For very small κ^2 values, the influence on the Förster distance is high, but for values ≥ 0.5 the changes are moderate. It is possible to make some approximations about the κ^2 value under certain conditions. If both chromophores can be considered to move freely during their excited state, an isotropical orientation can be assumed and the value of κ^2 is $2/3$. For free GFP variants, the rotational diffusion is too slow (15-20 ns) to adopt this commonly used value of $2/3$, though (Heikal et al., 2000). In our case it may be more appropriate to take $\kappa^2 = 0.476$, a value calculated for molecules with frozen rotatory motion (Demchenko, 2008, Grailhe et al., 2006, Steinberg, 1968).

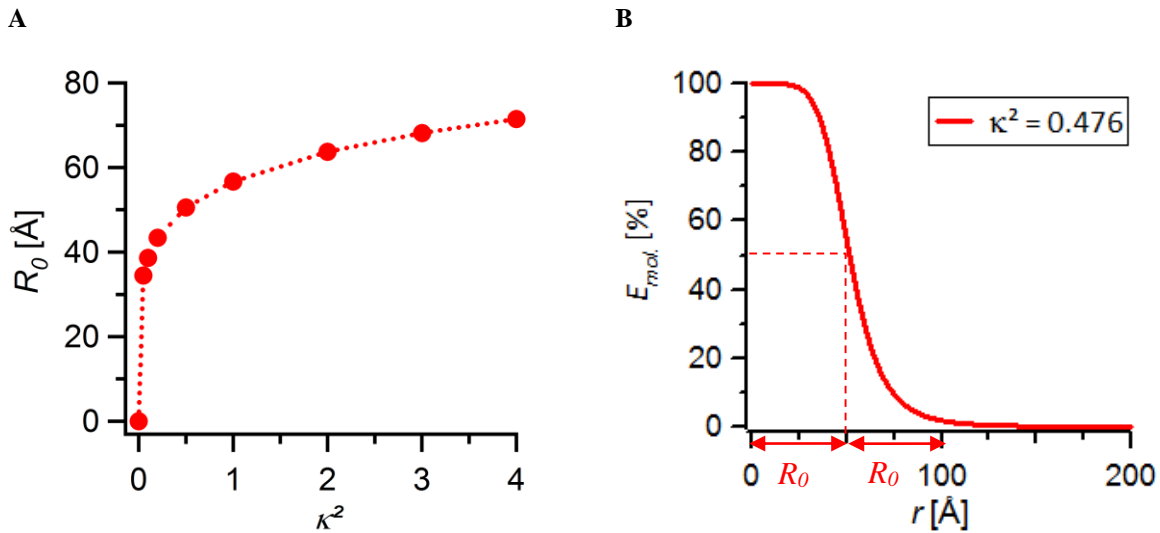


Figure 3 Förster distance and molecular FRET efficiency depend on the spatial orientation factor κ^2

A: The Förster distance R_0 is calculated for different values of κ^2 ($n = 1.4$, $\Phi = 0.76$).

B: Mathematical simulation of the variation of $E_{mol.}$ with the distance for $\kappa^2 = 0.476$

In conclusion, several conditions must be fulfilled to make the energy transfer possible: (i) The donor emission spectrum has to overlap with the acceptor excitation spectrum; (ii) the distance between the fluorophores has to be small (< 10 nm) (iii) the spatial orientation of the fluorophores towards each other must be favourable.

The molecular FRET efficiency, $E_{mol.}$, can be described either as a function of the rate constants, or by the donor –acceptor distance and the Förster radius:

$$\text{Equation 9} \quad E_{mol.} = \frac{k_T}{k_r + k_{nr} + k_T} = \frac{1}{1 + \left(\frac{r}{R_0}\right)^6}$$

As the equation shows, $E_{mol.}$ depends on R_0 , which – in turn – depend on κ^2 (Equation 7), hence the spatial orientation of the fluorophores influences the molecular FRET efficiency, as illustrated in Figure 3 B: Based on a $R_0 = 49 \text{ \AA}$ (calculated with $\kappa^2 = 0.476$, $n = 1.4$, $\Phi = 0.76$), we simulated the variation of $E_{mol.}$ by assuming distance values between 0 – 200 \AA . Due to the uncertainty on κ^2 , a measured $E_{mol.}$ does not allow a precise prediction of the distance between the fluorophores but on the other hand if a non-favourable orientation can be excluded, the absence of FRET allows to estimate the distance above $2 \cdot R_0$.

The fluorescence lifetime of the donor alone (τ_D) is expressed as in Equation 4 and the one of the donor in presence of the acceptor (τ_{DA}) can be expressed as follow:

$$\text{Equation 10} \quad \frac{1}{\tau_D} = k_r + k_{nr} \quad \text{and} \quad \frac{1}{\tau_{DA}} = k_r + k_{nr} + k_T$$

Introducing the expression of τ_D and τ_{DA} in Equation 9 gives the following expression of $E_{mol.}$:

$$\text{Equation 11 } E_{mol.} = 1 - \frac{\tau_{DA}}{\tau_D}$$

(Valeur, 2006, Lakowicz, 2006)

This expression highlights the fact that FRET measurements always necessitate the comparison of two situations without FRET (donor alone) and with FRET (donor with acceptor).

For my project, I used two newly engineered variants of the CFP Aquamarine and mTurquoise, Citrine as an improved variant of the YFP, and mCherry as a red FP (RFP) variant. They can be composed to three different FRET pairs, Aquamarine or mTurquoise + Citrine, and Citrine + mCherry. The photophysical properties, which are important for FRET are listed in Table 1 for the mentioned FPs.

Fluorescent proteins	$\lambda_{ex.}^+$	$\lambda_{em.}^+$	$\epsilon(\lambda)^\dagger$	Φ^\ddagger	$\langle\tau\rangle^*$	FRET donor for	R_0^Δ
CFP variants: Aquamarine	414	480	33,000	0.89	4.12 [◊]	Citrine	51.51
mTurquoise	414	480	26,000	0.84	4.06 [◊]	Citrine	51.02
YFP variant: Citrine	516	529	77,000	0.76	2.974 [#]	mCherry	55.37
RFP variant: mCherry	587	610	72,000	0.22			

Table 1 Fluorescent proteins used in this project and their main properties

⁺ excitation and emission maximum [nm], respectively

[†] extinction coefficient [$M^{-1}cm^{-1}$]

[‡] quantum yield

^{*} fluorescence lifetime [ns]

^Δ Förster radius [Å], calculated with a κ^2 of 0.476 (Steinberg, 1968)

[◊] in solution, 20 °C and pH 7.4 (Erard et al., 2013)

[#] in live cells, 37 °C (Walther et al., 2011)

1.4 NADPH Oxidase

The NADPH oxidases are an enzyme family designated to catalyse the reduction of oxygen to superoxide anions, a precursor for other reactive oxygen species (ROS) such as hydrogen peroxide and hypochlorous acid. Their members have the transmembrane subunit NOX (subfamily NOX 1 – 5^{vi} and DUOX 1 and 2) in common, which is the catalytic core of the enzyme (Figure 4): NADPH binds to its C-terminus where it is oxidised. The electron is transported via FAD and the two haem groups (coordinated between the transmembrane helices TM 3 and TM 5^{vii}) to the other side of the membrane, where it reduces molecular oxygen to superoxide anions (Sumimoto, 2008, Bedard and Krause, 2007).

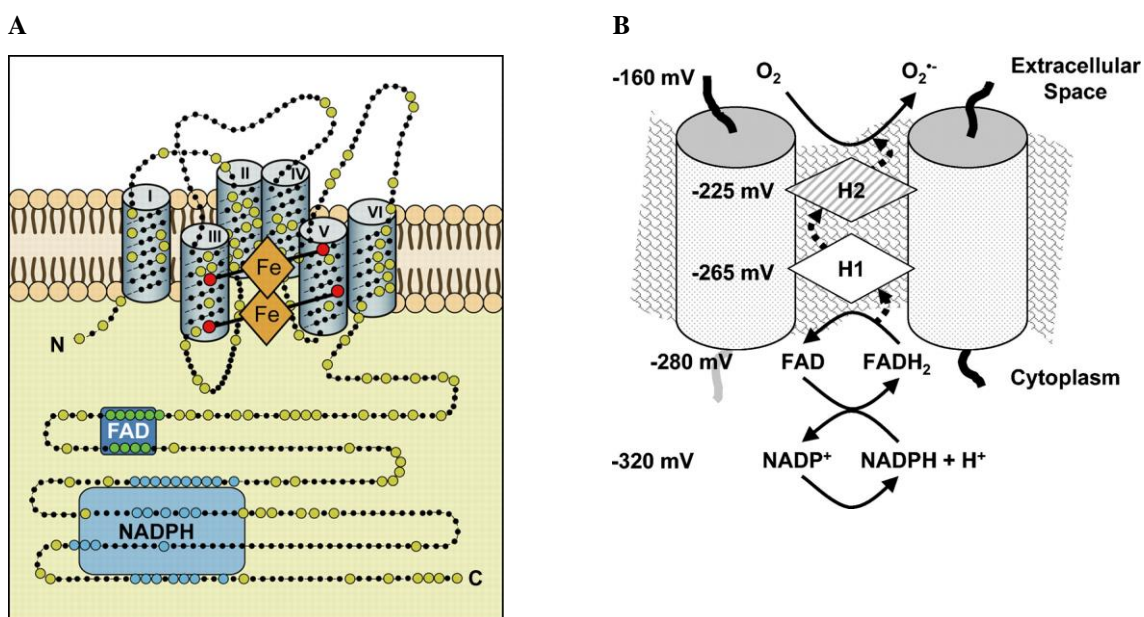


Figure 4 General structure and function of the NOX

The structure and function of the NOX subunit is highly conserved in all known NADPH oxidase family members. A: The NOX consists of the N-terminal membranous part consisting six transmembrane helices and two haem groups, which are coordinated between TM 3 and 5, and the C-terminal cytosolic “dehydrogenase domain” with its NADPH and FAD binding sites. (Bedard and Krause, 2007)

B: Electron transfer from the oxidation of NADPH to NADP⁺ to FAD, which is reduced in turn to FADH₂. The latter one delivers its electron via the two haem groups (H1 and H2) to the other side of the membrane, where it finally reduces O₂ to superoxide anions (O₂^{•-}) (Quinn and Gauss, 2004)

The different members of the NOX family are found in various tissues and cells, as it is summarized in Table 2 (Bedard and Krause, 2007). Based on tissue expression studies, diverse physiological (Table 2) and pathological roles (Figure 5) of the subfamilies were suggested.

^{vi} NOX4 produces hydrogen peroxide, though

^{vii} DUOX 1/2 contain an additional N-terminal TM, hence the haem groups are coordinated between TM 4 and TM 6)

However – beside the host defence function of the phagocyte NADPH oxidase and the involvement in biosynthetic processes like the thyroid hormone synthesis of DUOX2 and the otoconia formation of NOX3 – their exact function is not elucidated yet (Krause, 2004, Altenhöfer et al., 2014, Katsuyama et al., 2012).

Subfamily	High level expression	Intermediate to low level expression	Suggested (main) functions
NOX1	Colon	Smooth muscle, endothelium, uterus, placenta, prostate, osteoclasts, retinal pericytes	host defence (colon), stimulation of cell proliferation
NOX2	Phagocytes	B lymphocytes, neurons, cardiomyocytes, skeletal muscle, hepatocytes, endothelium, hematopoietic stem cells, smooth muscle	host defence
NOX3	Inner ear	Fetal kidney, fetal spleen, skull bone, brain	otoconia formation and as a consequence the vestibular sensing of the equilibrium
NOX4	Kidney, blood vessels	Osteoblasts, endothelium, smooth muscle, hematopoietic stem cells, fibroblasts, keratinocytes, melanoma cells, neurons	oxygen sensing in the kidney cortex, regulation of cell proliferation
NOX5	Lymphoid tissue, testis	Endothelium, smooth muscle, pancreas, placenta, ovary, uterus, stomach, various fetal tissues	ROS-dependent signalling and regulation of transcription factors (testis); lymphocyte differentiation
DUOX1	Thyroid	Airway epithelia, tongue epithelium, cerebellum, testis	pulmonary host defence
DUOX2	Thyroid	Salivary and rectal glands, gastrointestinal epithelia, airway epithelia, uterus, gall bladder, pancreatic islets	thyroid hormone synthesis

Table 2 Overview of the tissue/cell specificity of the NOX family members and their suggested functions
(Krause, 2004, Bedard and Krause, 2007, Katsuyama et al., 2012)

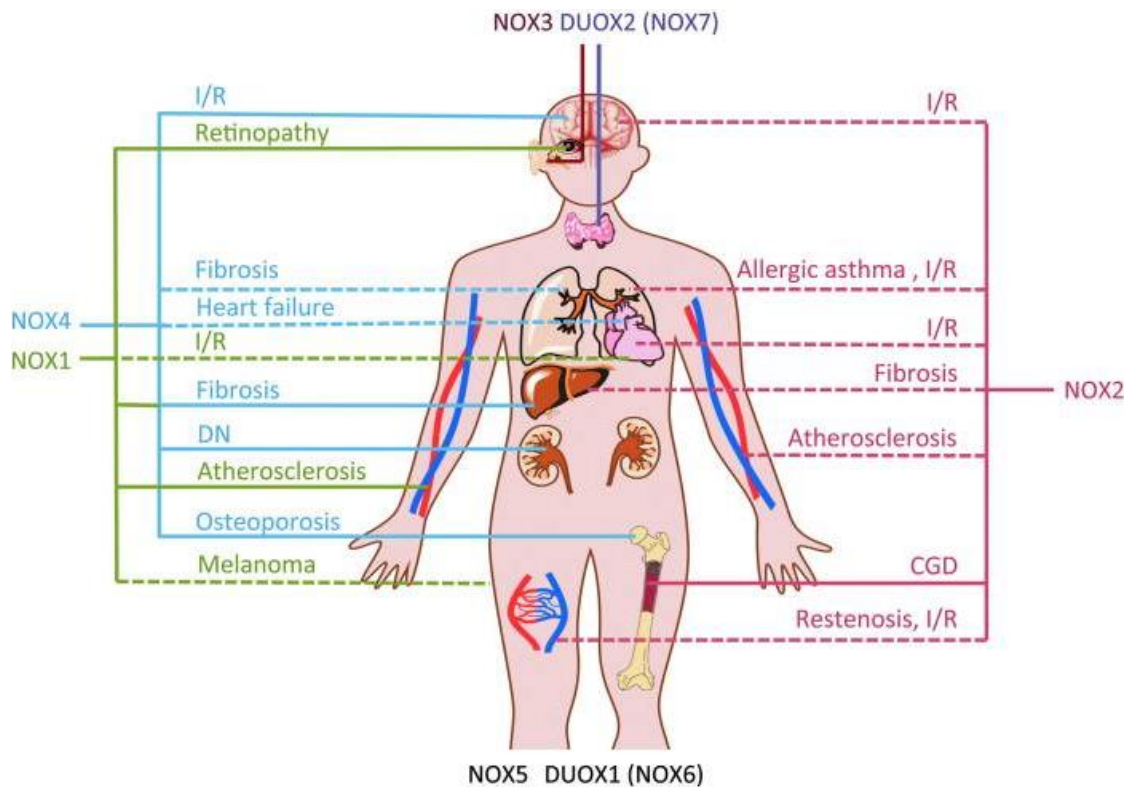


Figure 5 NADPH oxidases are associated with a variety of diseases

NOX1 (green) is associated with vascular diseases such as atherosclerosis, ischemic retinopathy, ischemia reperfusion of the heart, liver fibrosis, and perhaps with tumour (melanoma) angiogenesis. Involvement in inflammatory bowel disease and carcinogenesis was suggested.

Hyperactivity of NOX2 (pink) seems to be involved in a plethora of inflammatory (e.g. allergic asthma) and vascular diseases including arteriosclerosis and ischemic and reperfusion disorders such as stroke and heart attack, while its hypo- or in-activity is associated with the Chronic Granulomatous Disease (CGD), a severe immune deficiency syndrome.

NOX3 (violet) is involved in the synthesis of the otoconia, which are indispensable for the vestibular sensing system of the equilibrium. It is as well associated with cisplatin induced hearing loss.

The role of DUOX1 remains unclear, it may be involved in bladder or pulmonary immune defence.

DUOX2 is necessary for the synthesis of thyroid hormones. (Altenhöfer et al., 2014, Brown and Griendling, 2009)

1.4.1 The phagocyte NADPH oxidase

The phagocyte NADPH oxidase (in the following called NOX2 complex) is a major part of the host response to bacterial and fungal infections as well as to inflammations. Additionally, ROS are involved in signalling cascades of the host response, cell death of the phagocyte, and affects extracellularly the surrounding tissues and induce stress responses in microbes.

The importance of the respiratory burst – as the immense production of superoxide anions by the active oxidase is called – becomes apparent in case of activity-restricting genetic mutations of the oxidase leading to the Chronic Granulomatous Disease (CGD), which is characterized by a severe immune deficiency syndrome (chronic infections, impaired wound healing) (Nunes et al., 2013, Dupré-Crochet et al., 2013, Brown and Griendling, 2009). However, a hyperactivity

of the oxidase leads to excessive ROS production, which is associated with tissue damaging and oxidative stress. This imbalance is assumed to be involved in inflammatory, vascular, and ischemic diseases (Figure 5, pink). Furthermore, the oxidative stress induced by NOX2 complex might play a negative role in cerebrovascular dysfunctions^{viii} leading to hypertension, hypercholesterolemia, and advanced aging, as well as in neurodegenerative disorders including Alzheimer's disease (Brown and Griendling, 2009, Drummond et al., 2011, Altenhöfer et al., 2014). These facts point out the importance of a tight regulation of the activity of the oxidase.

1.4.1.1 Resting state, activation, and deactivation

The NADPH oxidase consists of five subunits, two membranous ones gp91^{phox} (also called NOX2) and p22^{phox}, which build a stable complex, the flavocytochrome b558, and three cytosolic subunits (p47^{phox}, p67^{phox}, and p40^{phox}). In the resting state of the neutrophil, the flavocytochrome b558 is mainly localized in the membranes of specific granules and to a minor part in the plasma membrane, while the three cytosolic subunits are assumed to be organized in a ternary complex (El-Benna et al., 2008).

The *in vivo* activation of the oxidase can be achieved by particle stimuli (opsonised bacteria or fungi), which are phagocytised, or by soluble activators such as pro-inflammatory agents. Both mechanisms lead to NADPH oxidase activation by protein kinases (e.g. PKC, MAPK^{ix}) induced phosphorylations of all subunits of the NADPH oxidase, which finally lead to the translocation of the cytosolic complex to the membranous subunits (Dupré-Crochet et al., 2013, Nauseef and Borregaard, 2014). Furthermore, phagocytosis induces a flavocytochrome b558 recruitment to the plasma membrane of which the phagosome will be built (El-Benna et al., 2008).

To establish the active NADPH oxidase, the small GTPase Rac has to assemble with the oxidase subunits. Its translocation is independent of the cytosolic subunits, though. In the resting state, Rac is in tight complex with the GDP dissociation inhibitor (RhoGDI), which renders Rac soluble and inhibits an interaction with phospholipids. A dissociation of RhoGDI is followed by translocation of Rac to the membrane, most probably due to electrostatic and hydrophobic interactions with the membrane (Pick, 2014).

The cytosolic subunits play different roles during activation. P47^{phox} is extensively phosphorylated mainly on the C-terminal part (amino acid 303 – 379^x) (El-Benna et al., 2009), whereby the phosphorylation of the serine residues S303/304/328/379 of p47^{phox} were shown to be critical for the enzyme activation (el Benna et al., 1994, Benna et al., 1996, Faust et al.,

^{viii} Angiotensin II dependent

^{ix} which kinase is activated is stimulus dependent

^x ≈ auto-inhibitory region (AIR) and proline rich region (PRR), which are described in paragraph 1.4.1.2.2

1996, Ago et al., 1999, Ago et al., 2003, Marcoux et al., 2010, Meijles et al., 2014), while the phosphorylation of S345 was shown to be an important priming mechanism for further phosphorylations (El-Benna et al., 2008)^{xi}. The phosphorylation induced conformational changes allow the binding to p22^{phox} and to the plasma membrane. The specificity for the plasma membrane is derived by two phospholipid binding sites^{xii}, one for phosphatidylinositol (3, 4) diphosphate (PI(3,4)P₂) and the other one phosphatidic acid or phosphatidylserine. On its way it recruits the cytosolic subunits to the membranous subunits (El-Benna et al., 2008, Nunes et al., 2013). The recruitment of p67^{phox} by p47^{phox} allows an interaction with gp91^{phox}, which induces conformational changes in the flavocytochrome (Paclet et al., 2000), enabling the electron transport from NADPH to FAD (Nisimoto et al., 1999). The role of p40^{phox} is not completely understood yet. This subunit is not necessary for the NADPH oxidase activation *in vitro*^{xiii}. In live cells, it was shown to have phospholipid binding properties with a preference for PI(3)P rich phagosomal membrane and enhances the ROS production (Tian et al., 2008, Nunes et al., 2013, Suh et al., 2006). The importance of the interaction of p40^{phox} to PI(3)P for the stability of the NADPH oxidase complex on the phagosomal membrane became apparent by a point mutation in the p40^{phox} binding domain to PI(3)P of a CGD patient (Matute et al., 2009). Regarding the role of p40^{phox} during translocation of the cytosolic subunits, it was shown that during FcγR induced activation, p40^{phox} needs the binding to p67^{phox} to be recruited to the membranous subunits (Tian et al., 2008), however for phagocytosis induced oxidase assembly it is speculated that p40^{phox} assists p47^{phox} in its carrier function during phagocytosis induced oxidase assembly (Ueyama et al., 2011). Rac is supposed to act as a carrier for p67^{phox} like p47^{phox}, and additionally to induce conformational changes in p67^{phox}, which trigger the binding to gp91^{phox} (Pick, 2014).

The maintenance of the complex in the active state was often assumed to be a continuous turnover (association and dissociation) of the cytosolic subunits on the membranous complex (DeCoursey and Ligeti, 2005). However, recent studies of our group give evidence that p47^{phox} and Rac dissociate from the membranous complex after activation of the NADPH oxidase (Tlili et al., 2012) maybe due to an disruption of the tail-to-tail binding of p47^{phox} and p67^{phox} (Li et al., 2009), while p67^{phox} is staying in the membrane complex (Tlili et al., 2012) most probably with the help of p40^{phox} (Song and Dupré-Crochet, unpublished data).

^{xi} In fact, all subunits are phosphorylated during activation which increases the affinity of the flavocytochrome b558 towards the cytosolic subunits; the exact role of the phosphorylations of p40^{phox} and p67^{phox} remains unclear, though.

^{xii} localized on the PX domain, see below

^{xiii} In live cells an activation of the NADPH oxidase without p40^{phox} is as well possible, but leads to strong reduction of the superoxide production.

The inactivation process is a crucial step in the NADPH oxidase regulation to prevent tissue damaging due to exaggerated superoxide anion production^{xiv}. Still, little is known about the mechanism of NADPH oxidase inactivation. Suggested conformational changes of Rac and dephosphorylation of p47^{phox} leading to a dissociation of these subunits from the complex and hence to its destabilization and inactivation (DeCoursey and Ligeti, 2005), are in contrast to the observed ongoing activity after the dissociation of p47^{phox} and Rac (Tlili et al., 2012, Faure et al., 2013). Both hypothesis (continuous turnover versus stable complex) might be tested by the difference in required Ca²⁺ signalling: While the turnover may demand sustained Ca²⁺ supply during the active phase, a stable complex may stay active without Ca²⁺ (Dupré-Crochet et al., 2013).

It is also possible that other modifications (e.g. phosphorylation/dephosphorylation) of subunits of the NADPH oxidase induce conformational changes, which result in a dissociation of the cytosolic subunits.

1.4.1.2 Structure of the NADPH Oxidase

The structure of a protein is important for the understanding of its interactions with e.g. other proteins, small molecules, or lipids and hence its function. The most detailed information is provided by X-ray crystal structures. In the case of the NADPH oxidase, no complete crystal structure, neither for the entire complex nor for the single subunits – beside the one of p40^{phox} (Honbou et al., 2007) – is available. The structural knowledge about the oxidase is mainly derived from binding studies, low resolution techniques such as small angle X-ray scattering (SAXS), and crystal or NMR structures of single domains. Computational modelling approaches constructed *in silico* full length structures of p22^{phox}, p47^{phox} and p67^{phox}, which are – beside of the one of p22^{phox} – mainly based on the available resolved structures of different domains (Durand et al., 2006, Durand et al., 2010, Meijles et al., 2012, Meijles et al., 2014). In the following, each subunit will be described with respect to its domains in context to its functions and interactions.

^{xiv} ROS is associated with a plethora of diseases, such as atherosclerosis, ischemic stroke, Parkinson disease, and aging (DeCoursey 2005)

1.4.1.2.1 The membranous subunits of the NADPH oxidase

The membranous subunits gp91^{phox} and p22^{phox} build together a stable, constitutively expressed complex, the flavocytochrome b558. This complex is important for the stability of gp91^{phox} (Porter et al., 1994, Yu et al., 1997).

gp91^{phox}

The membranous glycoprotein gp91^{phox} (570 aa, 65.3 kDa) is the catalytic core of the NADPH oxidase: It allows the electron transport from the NADPH oxidase molecules to molecular oxygen via FAD and two haem groups.

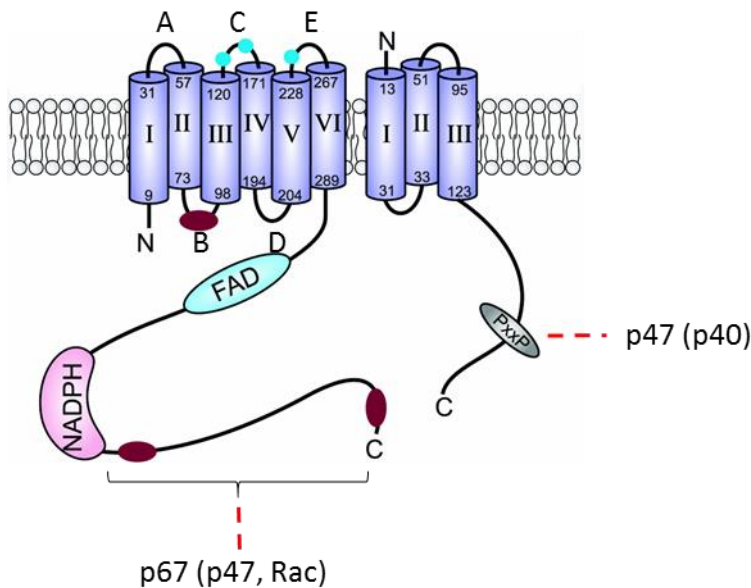


Figure 6 Structure of cytochrome b558

The cytochrome b558 consists of gp91^{phox} (left), with its N-terminal catalytic core built of six transmembrane α -helices, and with the C-terminally located binding sites for FAD and a NADPH, and of p22^{phox} (right), with its transmembrane domains, N-terminus and a cytosolic C-terminus holding a PRR domain, which includes a PxxP motive. Red, dashed lines: interactions after activation. Red ovals indicates predicted binding sites for p47^{phox}, cyan dots show glycosylation sites (modified from (Groemping and Rittinger, 2005)).

The protein can be distinguished in (Figure 6):

- N-terminal membranous part, consisting of:
 - six transmembrane (TM) α -helices I-VI, linked by loops A-E
 - two haem groups coordinated between TM helix 3 and 5
- C-terminal cytosolic part including:
 - FAD and NADPH binding sites
 - binding site for the regulatory cytosolic subunits

The N-terminus allows the electron transport through the membrane, which is accomplished by the two haem groups, which are coordinated between His101 and His115 of the TM helix 3 and His209 and His222 of TM helix 5 (Figure 4, right) (Biberstine-Kinkade et al., 2001, Finegold et al., 1996). At these haem groups the final reduction of molecular oxygen to superoxide anions takes place. Additionally, several binding sites for p67^{phox} (helix 2 (Picciocchi et al., 2011)), p47^{phox} (B loop (DeLeo et al., 1995, Biberstine-Kinkade et al., 1999)), and FAD (helix 2 (Picciocchi et al., 2011) and D-loop (Li et al., 2005)) were suggested. Another study is claiming that the main binding sites for p47^{phox}, p67^{phox}, and Rac are solely located on the C-terminal part of gp91^{phox}, though (von Löhneysen et al., 2010).

The C-terminal cytosolic part is homologous to ferredoxin-NADP⁺ reductase (FNR) and comprises the binding sites for FAD and NADPH oxidase (Segal et al., 1992, Rotrosen et al., 1992, Ravel and Lederer, 1993). In the resting state, the NADPH binding site is masked by the α -helical loop (Li et al., 2005). During activation it is set free and allows the interaction with p47^{phox} with aa 484-500^{xv} (Biberstine-Kinkade et al., 1999, Li et al., 2005) and aa 555-564 (Adams et al., 1997).

^{xv} However, a Δ 488-497 mutant did not affect the NADPH oxidase assembly, only the electron transfer from NADPH to FAD was impeded YU, L., CROSS, A. R., ZHEN, L. & DINAUER, M. C. (1999) *Functional Analysis of NADPH Oxidase in Granulocytic Cells Expressing a Δ 488-497 gp91 phox Deletion Mutant.*; one explanation might be that Asp500 was conserved which was shown to be indispensable for the p47^{phox} translocation LI, X. J., GRUNWALD, D., MATHIEU, J., MOREL, F. & STASIA, M.-J. (2005) Crucial Role of Two Potential Cytosolic Regions of Nox2, 191TSSTKTIRRS200 and 484DESQANHFVHHDEEKD500, on NADPH Oxidase Activation. *Journal of Biological Chemistry*, 280, 14962-14973.

p22^{phox}

P22^{phox} (195 aa, 21 kDa) is constitutively in complex with gp91^{phox} and serves as a maturation assistant and stabilizer of gp91^{phox} and as a membrane anchor for the complex of the three cytosolic subunits.

The detailed structure of p22^{phox} is still discussed controversially. It is assumed in consensus that it is built of N-terminal TM helices (2 – 4 were proposed (Dahan et al., 2002, Groemping and Rittinger, 2005, Campion et al., 2009, Meijles et al., 2012)) and a minor structured cytoplasmic C-terminus which comprises a proline-rich region (PRR) with its PxxP (proline – Xaa – Xaa – proline) motive, the binding site for the tandem SH3 domains of p47^{phox} ^{xvi}(Figure 6 and Figure 8) (Groemping and Rittinger, 2005). The localization of the N-terminus (extracellular or cytosolic) is as well not finally clarified (Dahan et al., 2002, Campion et al., 2009, Meijles et al., 2012).

^{xvi} Crystal structure resolved by Groemping et al. 2003

1.4.1.2.2 The cytosolic subunits of the NADPH oxidase

p47^{phox}

The cytosolic subunit *p47^{phox}* (390 aa, 44.7 kDA) is called the organizer of the NADPH oxidase since it is crucial both for activation induced translocation of the cytosolic complex and its anchoring to the membrane (Groemping and Rittinger, 2005, Sumimoto, 2008).

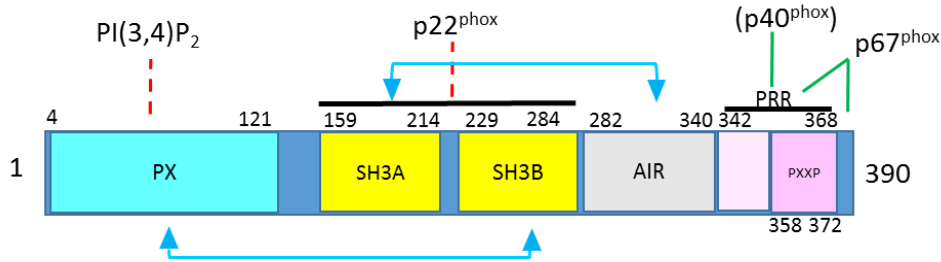


Figure 7 Domain structure of *p47^{phox}*

From the N- to the C-terminus: PX domain binds intra-molecularly to the SH3B domain in the inactive state preventing membrane anchoring, which is set free by phosphorylations in active state, SH3A and SH3B are blocked in the inactive state by internal interactions with the auto-inhibitory region (AIR) and allow the assembly with *p22^{phox}* after activation induced phosphorylations. The PRR domain is a binding site both for *p67^{phox}* and *p40^{phox}*, *in vitro* the affinity towards *p67^{phox}* is higher. Blue arrows: intramolecular interactions in the inactive state; green lines: constitutive intermolecular interactions; red, dashed lines: interactions after activation.

Regarding the function of the subunit, four main domains are described (from N-terminus to C-terminus, Figure 7):

- phagocyte oxidase (PX) domain, aa 4 – 121
- tandem Src homology (SH3) domains (SH3A, aa 159 – 214 and SH3B, aa 229 – 284)
- auto-inhibitory region (AIR), aa 282 – 340
- proline rich region (PRR), aa 342 – 368, including a PXXP motif between aa 358 – 372

The phagocyte oxidase (PX) domain is found both in *p47^{phox}* and *p40^{phox}*. It is crucial for the membrane binding properties (due to its phosphoinositide-binding capacity) of these subunits and thus important for the translocation of the cytosolic complex to the membrane. In the case of *p47^{phox}* it binds specifically phosphatidylinositol-3,4-bisphosphate [PI(3,4)P₂] (Sumimoto, 2008, Groemping and Rittinger, 2005, Stampoulis et al., 2012). In the inactive state, however, this domain is blocked by intra-molecular interactions with the SH3B domain. Due to phosphorylation of the serine residues S303/304/328 during activation, it is set free (Ago et al., 2003, Marcoux et al., 2010).

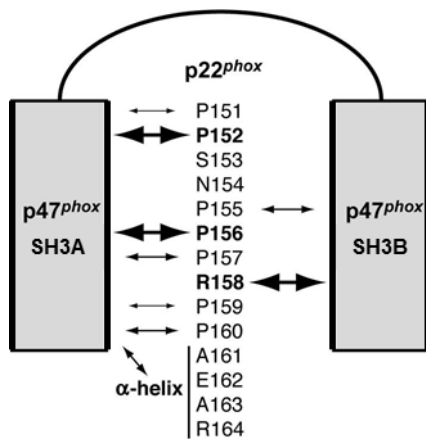


Figure 8 Interaction of p47^{phox} and p22^{phox}

The binding sites of p22^{phox} are marked with arrows. The crucial aa in the PRR motif are Pro152, Pro156 (interacting with SH3A of p47^{phox}) and Arg158 (interacting with SH3B of p47^{phox}). The C-terminal α -helix of p22^{phox} (aa 149-168) is important for the affinity of the two subunits (Nobuhisa et al., 2006), it enhances the affinity of the two subunits by a factor of 10 (Ogura et al., 2006).

The tandem SH3 domains of p47^{phox} are masked by intramolecular interactions with the AIR during resting state^{xvii} and interact with the C-terminus of p22^{phox} after activation by embedding the PRR of p22^{phox} between its two SH3 domains (Figure 8). This latter interaction is important for the assembly of the cytosolic complex with the membrane-bound subunits NOX2 and p22^{phox} (in the cell-free system p47^{phox} is dispensable for the activation in the presence of excess amounts of p67^{phox} and Rac, though) (Sumimoto, 2008).

The PRR mediates the interaction with the two other cytosolic subunits: The SH3B of p67^{phox} binds with high affinity to the PXXP motif of p47^{phox} and to its C-terminal α -helix (Sumimoto, 2008). The SH3 domain of p40^{phox} is another interaction partner of the PRR (Grizot et al., 2001b, Massenet et al., 2005, Fuchs et al., 1995, Wientjes et al., 1996, Ito et al., 1996) However, p47^{phox} has a higher affinity towards p67^{phox}, which is derived from the specific binding mode of Arg368 (part of PXXP motif of p47^{phox}) to p67^{phox}. Furthermore, the affinity of SH3 of p40^{phox} is decreased in the presence of the flanking PX and PB1 domains (Massenet et al., 2005). Live cell studies and immunoprecipitation could not confirm an interaction between p40^{phox} and p47^{phox} (Ueyama et al., 2007).

^{xvii} However, it is also described that the SH3 domains can only either block the PX domain or be blocked by AIR ITO, T., NAKAMURA, R., SUMIMOTO, H., TAKESHIGE, K. & SAKAKI, Y. (1996) An SH3 domain-mediated interaction between the phagocyte NADPH oxidase factors p40phox and p47phox. *FEBS Letters*, 385, 229-232, MARCOUX, J., MAN, P., CASTELLAN, M., VIVÈS, C., FOREST, E. & FIESCHI, F. (2009) Conformational changes in p47phox upon activation highlighted by mass spectrometry coupled to hydrogen/deuterium exchange and limited proteolysis. *Ibid.* 583, 835-840, MARCOUX, J., MAN, P., PETIT-HAERTLEIN, I., VIVES, C., FOREST, E. & FIESCHI, F. (2010) p47(phox) Molecular Activation for Assembly of the Neutrophil NADPH Oxidase Complex. *Journal of Biological Chemistry*, 285, 28980-28990.

The p47^{phox} C-terminus (PRR domain and downstream up to the very end) seems to be involved in rendering the subunit in the inactive state by interacting with the AIR. Phosphorylation of serine S379 interrupts this interaction and makes the phosphorylations of the AIR possible (Marcoux et al., 2010).

p67^{phox}

P67^{phox} (526 aa, 59.8 kDa) is the activator of the NADPH oxidase since it is directly interacting with the gp91^{phox}.

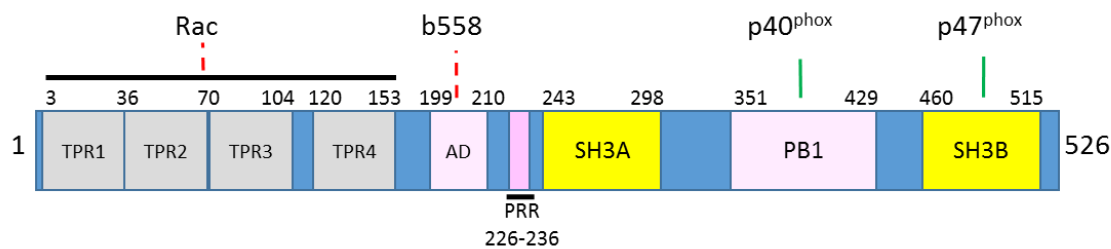


Figure 9 Domain structure of p67^{phox}

From the N- to the C-terminus: 4 TPRs, providing the Rac binding site; the activation domain (AD) is indispensable for the activation of the NADPH oxidase (an extension of the AD to aa 190-210 was suggested by (Maehara et al., 2010)); a PRR motif and a SH3A domain (in both cases, no interaction partners are identified at present); the PB1 domain provides the binding site for p40^{phox}; the SH3B domain is interacting with p47^{phox}. Green lines: intermolecular interactions in inactive state; red, dashed lines: interactions after activation.

It is structured as follows (N- to C-terminus, Figure 9) (Groemping and Rittinger, 2005, Sumimoto, 2008):

- four tetratricopeptide repeats (TPR) motifs, aa 3-36/36-70/70-104/120-153
- activation domain (AD), aa 201-210
- two SH3 domains, aa 243-298 and aa 460-515
- Phox and Bem1 (PB1) domain between the SH3 domains, aa 351-429

The TPR motif enables the interaction with Rac (Groemping and Rittinger, 2005). The binding of Rac is accomplished by the connection loops between TPR1 & TPR2, TPR2 & TPR3 as well as the hairpin intersection between the last two TPR motifs. (Sumimoto, 2008)

The activation domain is known to be crucial for the activation of oxidase complex, whereby Val204 is indispensable for the oxidase activation (Han et al., 1998, Sumimoto, 2008). A direct interaction with the flavocytochrome and perhaps an involvement in the electron transfer is assumed (Groemping and Rittinger, 2005). The region N-terminal of the AD is essential for the reconstitution of the NADPH oxidase complex (*in vivo* and *in vitro*), since it provides interaction sites for gp91^{phox} leading to an extended AD (aa 190-210) (Maehara et al., 2010).

Neither for the PRR nor for the SH3A was a binding partner identified (Groemping and Rittinger, 2005). However, in cells the SH3A domain is important for the superoxide production. Therefore, its role might be to promote the oxidase assembly (Maehara et al., 2009). The PB1 domain is strongly interacting with the PB1 domain of p40^{phox} (Groemping and Rittinger, 2005, Sumimoto, 2008).

The SH3B domain binds to the PRR domain of p47^{phox} as described in before. Thus this domain is indirectly responsible for the membrane translocation of p67^{phox}.

Oligomerization of p67^{phox} has not been shown, but N- (TPR motif) to C-terminal dimerization were suggested. However, Rac-p67^{phox} binding studies did not reveal any interference when C-terminal fragments of p67^{phox} were present (Groemping and Rittinger, 2005).

p40^{phox}

Despite the complete structural characterisation of p40^{phox} by crystal structure, the role of p40^{phox} (339 aa, 39 kDa) is not completely understood, but it is known to contribute to the membrane translocation of the ternary cytosolic complex due to its binding specificity of the phagosomal membrane (Sumimoto, 2008).

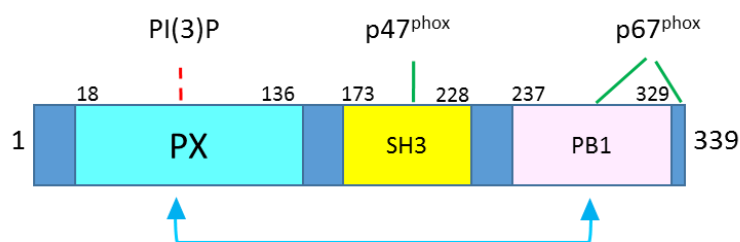


Figure 10 Structure of p40^{phox}

P40^{phox} comprises a PX domain, which allows the binding to the phagosomal membrane in the active state and which is masked by an intramolecular interaction with the PB1 domain in the resting state. The latter also provides the binding site for p67^{phox}, whereas the SH3 domain is interacting with the PRR of p47^{phox}

The following domains are described for p40^{phox} (Figure 10):

- PX domain, aa 18-136
- SH3 domain, aa 173-228
- PB1 domain, aa 237-329

The PX domain is capable to bind PI(3)P, a phosphoinositide, which is accumulated in the phagosomal membrane and hence enhancing the complex recruitment to the phagosome (Groemping and Rittinger, 2005). In the inactive state, the PX domain is masked by intramolecular interaction with the PB1 domain (Honbou et al., 2007, Ueyama et al., 2007).

The SH3 domain is the binding site for the PRR of p47^{phox}, as described before and to the PPR motif of p22^{phox}, but with lower affinity than for p47^{phox} (*in vitro*) (Tamura et al., 2007). A contribution of this domain to the activation of the NADPH oxidase was suggested from live cell experiments (Suh et al., 2006, Chessa et al., 2010).

The PB1 domain of p40^{phox} binds to the PB1 domain of p67^{phox} (crystallised by (Wilson et al., 2003)), while the C-terminal tail of p40^{phox} is as well indispensable for the interaction with p67^{phox} (Lys355) (Groemping and Rittinger, 2005)

1.4.1.2.3 The cytosolic complex in active and inactive state

The proposed models of the complex of the cytosolic subunits of the NADPH oxidase display schematically the known interaction sites of the different components (Figure 11), as they were described in the previous chapters. Briefly, p67^{phox} serves as an adaptor since it binds to the PRR domain of p47^{phox} via its SH3B domain and concomitantly to the PB1 domain of p40^{phox} by its own PB1 domain. Intramolecular interactions in p47^{phox} and p40^{phox} hinder the membrane binding capacities of the respective PX domains and a p22^{phox} binding of the tandem SH3 domains of p47^{phox}. During activation, these intramolecular interactions are broken by multiple phosphorylation steps in case of p47^{phox} and probably by hydrogen peroxide in case of p40^{phox}, hence allowing the translocation and anchoring of the cytosolic complex to the membrane and via p22^{phox} to the flavocytochrome b558. Rac translocates independently to the membranous complex. Its binding is assumed to contribute to the correct localization and fixation of the complex, which finally makes the electron transfer from the NADPH oxidation to the other side of the membrane possible, where molecular oxygen is reduced to superoxide anions. During the activation process, the intramolecular interactions of the ternary complex are preserved, but during ongoing activity p47^{phox} and Rac may leave the complex, while p67^{phox} and p40^{phox} are staying until its inactivation.

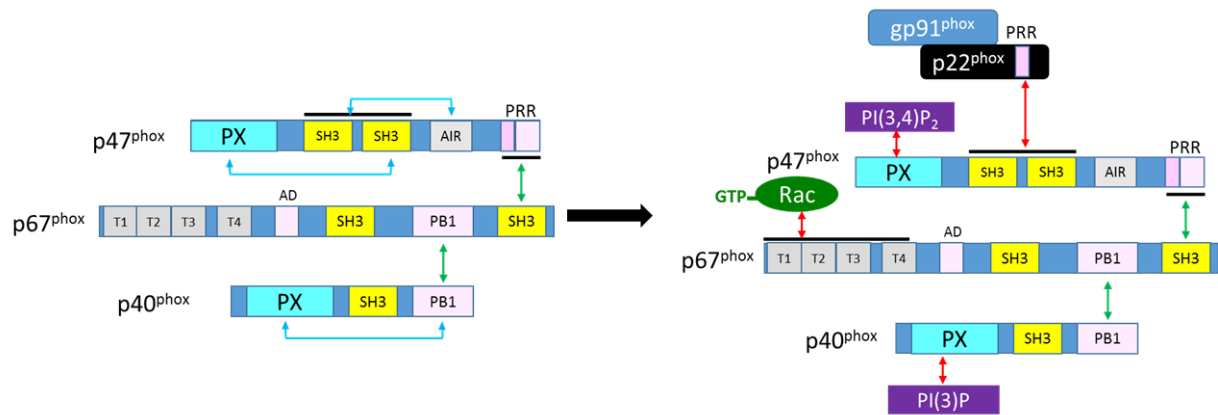


Figure 11 Model of the cytosolic complex in resting and active state

The inactive state (left) shows the C-terminal intermolecular interaction sites of the different subunits with green flashes and the intramolecular interactions of p47^{phox} and p40^{phox} with blue flashes. During activation, the latter open up to allow the interactions with the membranous subunits and the phospholipids (right, red flashes). During activation, Rac dissociates from its inhibitor RhoGDI entailing an exchange of GDP with GTP, which makes an interaction to p67^{phox} possible (modified from Sumimoto 2008). (Not all interactions are shown in this figure to improve the readability. A more complete picture is can be find in Nunes 2013)

However, due to the lack of a complete crystal structure of the complex, the information about the spatial organisation of the complex remains rudimentary.

Within this project we built a new model of the inactive cytosolic complex by aligning the spatial information of the FRET-FLIM studies derived from live cell experiments with the available structural data such as crystal structures, SAXS studies, and computational modelling. This model will contribute to a better understanding of the structure of the ternary cytosolic complex of the NADPH oxidase.

2 Material and Methods

2.1 Buffers

HEPES buffer (pH 7.4) [mM]	PBS (pH 7.4) [mM]	TBS-T (pH 7.4) [mM]
NaCl 140	KCl 2.7	NaCl 150
KCl 5	KH ₂ PO ₄ 1.5	Tris HCl 7.7
MgCl ₂ 1	Na ₂ HPO ₄ 8.1	Tween20 0.10%
CaCl ₂ 2	NaCl 137	
HEPES 10		
glucose 0.10%		
serum (decomplemented) 1%		

Buffers for plasmid preparation, standard protocol

Buffer P1 [mM]	Buffer P2	Buffer P3
Tris HCl (pH 8.0) 25	NaOH 0.2 M	K ₂ CH ₃ CO ₂ 5 M
EDTA 10	SDS 1 %	CH ₃ CO ₂ H 1.7 M
RNAse 20 μg/ml		

2.2 Methods

2.2.1 Bacterial cell culture

Bacterial cell lines (Table 3) were purchased from invitrogen (Thermo Fisher Scientific, Waltham, MA).

Strain	Genotype
<i>Escherichia coli</i> DH5α	F- Φ80lacZΔM15 Δ(lacZYA-argF) U169 recA1 endA1 hsdR17 (rK-, mK+) phoA supE44 λ- thi-1 gyrA96 relA1
Top10	F- mcrA Δ(mrr-hsdRMS-mcrBC) Φ80lacZΔM15 ΔlacX74 recA1 araD139 Δ(ara leu) 7697 galU galK rpsL (StrR) endA1 nupG

Table 3 Bacterial cell lines

Bacteria were grown from a single CFU over night (o.n.) in LB-broth containing the corresponding selection antibiotics with shaking (150 rpm) at 37 °C.

2.2.2 Plasmid preparation

Plasmids were prepared either with a non-commercial protocol (in the following called standard protocol) or with a commercial endotoxin free preparation kit (EndoFree Plasmid Maxi Kit, QIAGEN, Venlo, Netherlands). After preparation, the plasmid solutions were aliquoted and stored at -20 °C.

Standard protocol (mini-preparation):

Bacteria were grown o.n. in 5 ml LB broth. The suspension was centrifuged (8 min at 3000 g) and the supernatant discarded. The remaining pellet was resuspended with 200 µl buffer P1 by vortexing. For lysing the bacteria 200 µl of buffer P2 were added and mixed by gentle inversion of the tube, then incubated for 5 min at room temperature (RT). The reaction was stopped by the addition of 200 µl of buffer P3, which results in a fluffy white precipitation. After another centrifugation step (15 min, 13,000 rpm), the supernatant was transferred to a fresh tube. The containing DNA was precipitated by the addition of 420 µl of pure isopropanol and gentle shaking. This step is followed two more centrifugation steps (5 min, 13,000 g) and an intermediate washing step with 420 µl of 70 % ethanol. The received DNA palled was dried (approximately 5 – 10 min, 65 °C) and resuspended with 40 µl water. The protocol gave a typical yield of 40 µg DNA.

Endotoxin-free protocol (maxi-preparation)

The supplier's protocol was followed: A bacteria pre-culture was started from a single CFU and 5 ml LB broth containing the appropriate selective antibiotic (shaking incubation at 300 rpm for 8 h at 37 °C). 200 µl of the pre-culture was used to inoculate 100 ml of fresh LB medium containing the selective antibiotic, which was incubated o.n. at 37 °C and shaking at 300 rpm. The next day, the bacteria suspension was centrifuged at 3,000 g for 30 min at 4 °C. The received pellet was resuspended with 10 ml of the kit buffer P1 by vortexing, then 10 ml of the kit lysis buffer P2 was added and mixed by inversion. After an incubation of 5 min at RT, 10 ml of pre-cooled (4 °C) kit buffer P3 was added and gently mixed by inversing. The suspension was poured into the barrel of the QIAfilter Cartridge and incubated for 10 min. Afterwards, the suspension was filtered through the cartridge. 2.5 ml of the kit buffer ER was added to the filtrate, mixed by inversion, and then incubated on ice for 30 min. This solution was filtered through a buffer QBT equilibrated QIAGEN-tip by gravity flow. The flow-through was discarded. The tip was washed two times with 30 ml of buffer QC. Importantly, the following steps were performed using endotoxin-free plastic ware. The DNA was eluted from the tip with 15 ml buffer QN and precipitated by adding 10.5 ml isopropanol. After a centrifugation step (3,000 g, 1 h, 4 °C), the received pellet was washed with 40 ml of 70 % ethanol and centrifuged

again (3,000 g, 20 min). The final DNA pellet was air-dried for 5 – 10 min and redissolved in 500 μ l of endotoxin-free buffer TE. The protocol gave a typical yield of 400 μ g DNA.

2.2.3 Plasmid cloning

A library of the cytosolic subunits of the NADPH oxidase tagged with different FPs (overview of the linkers is given in Table 4), both on N- and C-terminus was built by molecular cloning (Table 5). Therefore, the bacterial vector and insert were digested with the selected restriction enzymes. DNA vectors and fragments were purified on 1 % agarose gels (DNA gel extraction performed with E.Z.N.A.[®] Gel Extraction Kit (Omega Bio-Tek, Norcross, GA)) and ligated using a T4 DNA ligase (all enzymes were purchased from New England Biolabs, Ipswich, MA). If necessary, DNA fragments were amplified or plasmids were mutated by T100[™] thermal cycler (Bio-Rad Laboratories Inc., Hercules, CA). The variants of the plasmids EGFP-N1 was mutated by removing the start codon (ATG). Primers were purchased from Eurogentec (part of Kaneka corp., Osaka, Japan), PfuTurbo DNA polymerase from Agilent Technologies (Santa Clara, CA).

tagged subunit	Linker	Length [aa]
p67 ^{phox} -Citrine/mTurquoise, C-ter. linker of the tandem	PRARDPPVAT	10
mTurquoise-p67 ^{phox}	SGLRSRAQAS	10
p47 ^{phox} -Citrine/Aquamarine, C-ter. linker of the tandem	LPVAT	5
Citrine-/mCherry-p40 ^{phox} and N-ter. linker of the tandem	SGLRSRA	7
Citrine-p67 ^{phox} -mTurquoise, N-ter. linker (C-ter. see above)	SGLELKLATM	10
Citrine-p47 ^{phox} -Aquamarine, N-ter. linker (C-ter. see above)	SGLRSRAQAY	10
mCherry-p40 ^{phox} -Citrine, C-ter. linker (N-ter. see above)	PRARDPPVAT	10

Table 4 Overview of the linkers between the subunit and the FP

2.2.4 Production and purification of recombinant proteins

The determination of the ratio of the amount of acceptor/donor demands a calibration of the fluorescence intensity to the concentration of the FP of interest, as it is described in paragraph 3.2.3.2. The purification of these proteins were not performed by myself but by Y. Bousmah, however a brief description of the protocol can be found in appendix 8.1.1.

Likewise, I gave a short summary of the procedure in appendix for the preliminary in vitro activation assay of the tagged vs. wild type subunits (performed by T. Bizouarn, paragraph 5.1.1.1) for which the subunits p67^{phox} \pm FP, p47^{phox} \pm FP, and Rac were purified by P. Machillot (appendix 8.1.2).

plasmid	vector	supplier
pECFP N1		Clontech, TAKARA Biotechnology (Dalian) Co., Ltd.
pECFP C1		as above
pEYFP-N1		as above
cherry c1		as above
Aquamarine N1	pECFP-N1	kindly provided by M. Erard*
Aquamarine C1	pECitrine-C1	
mTurquoise C1	pECitrine-C1	
mTurquoise N1	pECFP-C1	kindly provided by Y. Bousmah*
Citrine N1	pEYFP-N1	kindly provided by S. Dupré-Crochet*
Citrine C2		kindly provided by S. Dupré-Crochet*
Aquamarine-Citrine	pECFP-N1	kindly provided by D.B. Betolngar*
p67	pEGFP-N1	
p67-Turquoise	mTurquoise-N1	
mTurquoise-p67	mTurquoise C1	
p67-Citrine	pECitrine-N1	kindly provided by S. Dupré-Crochet*
p67-Citrine	pECitrine-C1	
Citrine-p67	pECitrine-N1	
mCherry-p67	mCherry-C1	kindly provided by S. Dupré-Crochet*
Citrine-p67-mTurquoise	pECitrine-C1	
p47	pEGFP-N1	
p47-Aquamarine	Aquamarine-N1	
p47 Δ C-Aq	Aquamarine-N1	
Aquamarine-p47	Aquamarine-C1	
p47-Citrine	pECitrine-N1	
p47 Δ C-Citrine	pECitrine-N1	
Citrine-p47	pECitrine-C1	
Citrine-p47-Aquamarine	pECitrine-C1	
p67-Citrine-IRES-p47-Aquamarine	pECitrine-C1	
p40	CMD8	
p40-Citrine	pECitrine-N1	
Citrine-p40	pECitrine-C1	
mCherry-p40	mCherry-C1	
mCherry-p40-Citrine	pECitrine-N1	

Table 5 Overview of the plasmids

*CNRS/ Université Paris Sud, Orsay, France

2.2.5 Eukaryotic cell culture

Eukaryotic cell line COS7 was obtained from American Type Culture Collection, Manassas, VA, COS^{gp91, p22} were kindly provided from M. Dinauer, Washington University, St. Louis, MO (Table 6). Unless specified otherwise, all cell culture products were supplied by Gibco, Thermo Fisher Scientific, Waltham, MA.

Name	Typification	Resistances
COS7	fibroblast-like kidney cells of the African Green Monkey	n/a
COS ^{gp91, p22}	COS7 cells, stably transfected with gp91 and p22	Geneticin Puromycin

Table 6 Eukaryotic cell lines

COS^{gp91, p22} cell line was kindly provided by M. Dinauer, Washington University, St. Louis, MO

COS7 and COS^{gp91phox, p22} cells were cultured at 37 °C and 5 % CO₂ in DMEM containing 10 % FBS, in case of COS^{gp91phox, p22phox} with the selecting antibiotics G418 (1.8 mg/ml final concentration) and Puromycin (1 µg/ml final concentration, Sigma Aldrich, St. Louis, MO), using 75 cm² cell culture flasks. For passaging, COS7 cells were washed three times with DPBS and incubated with 2 ml trypsin for 5 min at 37 °C. Reaction was stopped by adding 8 ml of growth medium. COS^{gp91, p22phox} cells were detached with enzyme free cell dissociation buffer. Briefly, cells were washed two times with DPBS and incubated for 5 min at 37 °C with 5 ml of the buffer (75 cm² flask). Afterwards, the supernatant was discarded and the cells detached by tapping the flask. Cells were taken after the addition of culture medium and diluted. For regular cell passaging, cells were diluted 1/5 to 1/7, the maximum passage number was P20. For 6-well plates cells were counted with the aid of a Malassez counting chamber and diluted to 4.5*10⁵ cells/well, for 24-well plates cells were diluted to 1.0*10⁵ cells/well.

2.2.6 Transient transfection of COS cells

The transfection efficiency had to be optimized especially for transfections with more than two plasmids at once (i.e. triple transfections). The transfection efficiency was monitored with Flow Cytometry (chapter 3.1.1).

We tested different transfection reagents and finally decided to change from Lipofectamine[®] 2000 (Thermo Fisher Scientific, Waltham, MA), which was routinely used in our group, to X-tremeGene HP DNA transfection reagent (Roche Diagnostics GmbH, Germany) since the latter provides a strongly increased cell viability after transfection, the efficiency of the transfection was similar, though. Afterwards, the optimal ratio of DNA to transfection reagent

was determined and found to be 1 : 3 (DNA [ng] : XtremeGene HP [μ l]). Beside this transfection optimization step, the cell culture was optimized in terms of regular passaging, maximal passaging numbers, and cell dilutions (the optimized protocol is described in chapter 2.2.5).

In the following, the general procedure of the transfection will be explained: Cells were seeded in 6-well-plates (for microscopy on glass cover slips, diameter 25 mm, thickness 0.13 - 0.16 mm, Gerhard Menzel GmbH, Germany) the day prior transfection and transfected following the suppliers' instructions.

Briefly, for Lipofectamine-based transfection, DNA was diluted in 50 μ l Opti-MEM[®], the Lipofectamine was mixed separately with other 50 μ l Opti-MEM[®]. After an incubation time of 5 min, the two solutions were united and gently mixed by pipetting and finally added to the cells containing 500 μ l fresh medium. Cells were used 20 – 30 h after transfection.

For the X-tremeGene HP based transfection, DNA was diluted with 200 μ l OptiMEM[®] (Gibco, life technologies) to a final total concentration of 0.1 – 3 ng/well^{xviii} together with three times more transfection reagent (i.e. 1 ng DNA needs 3 μ l transfection reagent). After an incubation of 30 min at 37 °C, the dilution was added to the cells containing 2 ml of regular growth medium. Cells were used 24 to 48 h after transfection.

2.2.7 Western Blot

Cell lysis

The lysis was performed using a commercial kit (complete Lysis M, Roche Diagnostics GmbH, Mannheim, Germany). The supplier's instructions were followed: Cells were transfected in 6-well plates 24 h (compare chapter 2.2.6) prior cell lysis. All following steps were performed at RT. The cell culture medium was discarded, the cells were washed with one time with PBS, the kit lysis buffer was added, and incubated for 5 min with gentle shaking. The lysate was collected and centrifuged at 14,000 g for 10 min. The supernatant was aliquoted and stored at -80 °C. The protein concentration was determined with a BCA assay. Typical yield was 600 μ g of total proteins per well.

Electrophoresis

Cell lysates or solutions of purified proteins were thawed on ice. Samples were prepared by adding Laemli buffer (1 : 1) to a final loading mass of 20 – 30 μ g (lysate) or 50 ng (purified protein). The solutions were denatured at 95 °C for 5 min and loaded to a Novex[®] NuPAGE

^{xviii} for 6-well plates

Bis-Tris SDS-PAGE gel of 10 % acrylamide (Thermo Fisher Scientific Inc., Waltham, MA). Electrophoresis was performed at 175 V for 30 – 45 min (buffer: NuPAGE® MES SDS Running Buffer, Thermo Fisher Scientific).

Transfer

For the blotting, a nitrocellulose membrane with a pore size of 0.2 µm and NuPAGE transfer buffer (both Thermo Fisher Scientific Inc., Waltham, MA) was used. The blotting conditions were the following: 100 V for 30 -45 min, on ice, with agitation.

Staining

The membrane was blocked with 5 % BSA in 0.1 % TBS-T. The first antibody (AB) was incubated o.n. at 4 °C with agitation, the second AB for 45 – 60 min at RT with agitation (please find the antibody concentrations in Table 7). Several washing steps were performed in between using 0.1 % TBS-T buffer.

The membrane was developed with enhanced chemiluminescence (ECL) using ECL RevelBlot intense® (OZYME, Montigny-Le-Bretonneux, France). Pictures were taken with PXi 4 synoptics (SynGene (division of Synoptics Ltd.), Cambridge, UK).

primary antibody	dilution	secondary antibody	dilution
anti-DSred * (monoclonal AB)	1:500	anti-mouse ECL # (goat)	1:10,000
anti-GFP + (mix of two monoclonal AB)	1:400	anti-mouse ECL # (goat)	1:10,000
anti-p40 ^{phox} # (monoclonal AB, epitope: N-terminus)	1:100	anti-mouse ECL # (goat)	1:10,000
anti-p47 ^{phox} † (polyclonal AB)	1:5,000	anti-rabbit ECL ‡ (donkey)	1:10,000
anti-p67 ^{phox} (polyclonal AB) ^Δ	1:1,000	anti-rabbit ECL ‡ (donkey)	1:10,000

Table 7 List of primary and secondary antibodies used for Western Blot

* anti-DsRed was used for mCherry; Clontech, TAKARA Biotechnology (Dalian) Co., Ltd.

+ anti-GFP was used for Citrine, mTurquoise, and Aquamarine; Roche Diagnostics GmbH, Mannheim, Germany

“N-20”, Santa Cruz Biotechnology, Inc., Dallas, TX

† kindly provided by F. Lederer, CNRS, Orsay, France

‡ GE healthcare, Little Chalfont, UK

^Δ EMD Millipore Corp., Temecula, CA

Stripping

WB were stripped with Restore™ Plus Western Blot Stripping Buffer (Thermo Fisher Scientific, Waltham, MA) following the supplier’s instructions. The complete removal of the primary AB was tested by incubating the stripped and BSA blocked membrane with the

secondary AB. After an incubation with the chemiluminescent substrate, a luminescence picture was taken with a 5 min exposure time. The absence of any band indicated a successful stripping. If necessary, the procedure was repeated.

Data analysis

The molecular mass of the band was assigned from the protein ladder, either Precision Plus Protein™ Dual Color Standards, 10 to 250 kDa, 10 bands (Bio-Rad Laboratories Inc., Hercules, CA) or EZ-Run prestained recombinant protein ladder, 10 to 170 kDa, 10 bands (ThermoFisher Scientific Inc., Waltham, MA) using GeneTools software (version 4.03.02.0, SynGene (division of Synoptics Ltd.), Cambridge, UK). This software gives as well the volume of the peak (integration parameters: baseline correction method: ROLLING DISK (radius 30), baseline correction offset, smoothing: SAVITSKY-GOLAY order 2 width 3), which was used to calculate the relative contribution of one bands to the sum of the band of one lane.

$$\text{Equation 12 } \textit{contribution of band}_x = \frac{V_{band_x}}{\sum_{n=1}^l V_{band_n}} \cdot 100 \%$$

protein	number of anti-FP staining	number of anti-SU staining
p67 ^{phox}	1 (negative)	3
p67 ^{phox} -mTurquoise	2	1
mTurquoise-p67 ^{phox}	1	1
p47 ^{phox}	-	3
p47 ^{phox} -Citrine	2	1*
p40 ^{phox}	-	4
mCherry-p40 ^{phox}	3	1

Table 8 Overview number of WBs

* optimization/repetition needed

2.2.8 Luminescence Assay

The luminescence assay was performed in order to investigate the activation of the NADPH oxidase: The active enzyme is producing superoxide anions, which can react quickly to hydrogen peroxide. Both species oxidise luminol in presence of the horseradish peroxidase to excited aminophthalate anion which emits lights when it falls back to the ground state (Freitas et al., 2009). This light can therefore be used as an indicator of the activity of the NADPH oxidase.

I tried different strategies aiming to find a robust method with good reproducibility (Table 9). Additionally, I optimized the transfection efficiency by optimizing the cell culture (compare 2.2.5) and testing different transfection reagents (2.2.6).

Method	comments
attached cells in 6-well plates	Pro: best reproducibility Contra: Control of cell number / layer very limited ⇒ inhomogeneity between different trials, no quantification possible No signal acceleration by white plates
Detached cells	Pro: 96-White plates for signal acceleration available Number of cells can be controlled ⇒ better comparability, perhaps quantification possible (if cells would have been sorted for triple transfection with a FACS ^{xix} or as an approximation by discriminating the transfection efficiency with flow cytometry and computing a similar amount of transfected cells/well/day) Contra: very bad reproducibility
With trypsin	Pro: classic method, efficient Contra: Cleavage of the membrane bound subunits gp91 ^{phox} and p22 ^{phox} possible ⇒ Might lead to deficient activation of the complex
With enzyme free buffer ^{xx}	Pro: no cleavage of the membrane bound subunits Contra: Method had to be optimized, less efficient in cell detachment

Table 9 Methods used finding a reproducible method for the LUMINESCENCE ASSAY assay

In spite of all efforts, the method is not yet reliable. Here, I will concentrate on my work on attached cells, since this method had the best reproducibility. The procedure was performed as follows:

^{xix} Fluorescence activated cell sorting

^{xx} Cell dissociation buffer, enzyme free, PBS (Gibco, Thermo Fisher Scientific Inc., Waltham, MA)

The luminometry experiment was performed with Wallac 1420 VICTOR³™ (PerkinElmer, Waltham, MA). COS^{gp91phox, p22phox} cells were triple transfected with all three cytosolic subunits (either with or without a FP-tag) the day before. For the experiment, the cell layer was washed three times with PBS and kept in HEPES buffer (2.1) at 37 °C. The background was measured for 5 min before adding 200 nM phorbol 12-myristate 13-acetat (PMA). Photons were collected for 7 seconds 60x/1 h.

2.2.9 Flow Cytometry

Flow cytometry allows the measurements of fluorescence intensities of microscopic particles (beads, yeast, eukaryotic cells...). In this method a liquid stream is transporting the particles through a flow cell, where they are hit by one or several laser beams. The velocity of the stream is adjusted in a way which allows only the passage of one cell at a time thus allowing a detection in a cell by cell manner. Within minutes, several 10,000 to 100,000 cells can be detected and counted, which gives statistically relevant results about the composition of a cell population. The flow cytometer is equipped with several lasers, pinholes, dichroic mirrors, selection filters, and detectors allowing the simultaneous detection of multi-coloured fluorescent labels in the same cell.

A cell passing through the laser beam scatters light, which is detected by forward (FSC) and side scattered light (SSC) detectors, respectively. The FSC (diffraction) is proportional to the volume of the cell, the SSC (refraction) depends on the composition of the cell, e.g. its granularity, size/composition of the nucleus, and its vesicles. A dot plot (one dot represents one cell, Table 10) of FSC against SSC allows the discrimination of live cells from debris or necrotic/apoptotic cells, and even a differentiation of distinct cell types (Shapiro, 2005). The flow cytometer used in this study is furnished with three lasers (405/488/561 nm) and detectors for CFP, YFP, mCherry and FRET. The light paths are detailed just below.

Technical equipment

Figure 12 shows a scheme of the cytometer (CyFlow[®] ML, Partec, today part of Sysmex Corp., Kobe, Japan), which is equipped with three lasers (405/488/561 nm), whereby the 405 nm and the 561 nm laser are co-aligned. The laser beams are directed to a flow cuvette, where the samples are passing by in a liquid stream. Importantly, the co-aligned laser beams do not hit the sample on the same spot as the 488 nm laser. The difference is translated to the detectors as a time delay of 100 μ s. The scattered light is collected by two lenses, only the forward scattered light is directly detected in a small angle to the illumination beam. The wide angle light is sorted by the different optical paths, whereby the cytometer is arranged to collect the light of the 488 nm excitation on the left hand side and the light of the co-aligned lasers on the right hand side. While fluorescence apertures (FA) allow the separation of the laser beams and the corresponding fluorescence by mechanic blocking of one of the beams, dichroic mirrors (DM) and band pass filters reflect/select the light according to its wavelength. The standard settings shown here allow the discrimination of several fluorophores, among others CFP (FL6), YFP (FL1), and mCherry (FL4), which are used in this project. For the mentioned FP variants, the

corresponding normalized excitation and emission spectra are overlaid with the DM and collection band pass filters in Figure 13.

To sum up, the specificity of the emission light is given both by the time delay component and the selection on the light path accomplished by a laser beam selection (FAs) and wavelength specific light filtering (DM, band pass filters).

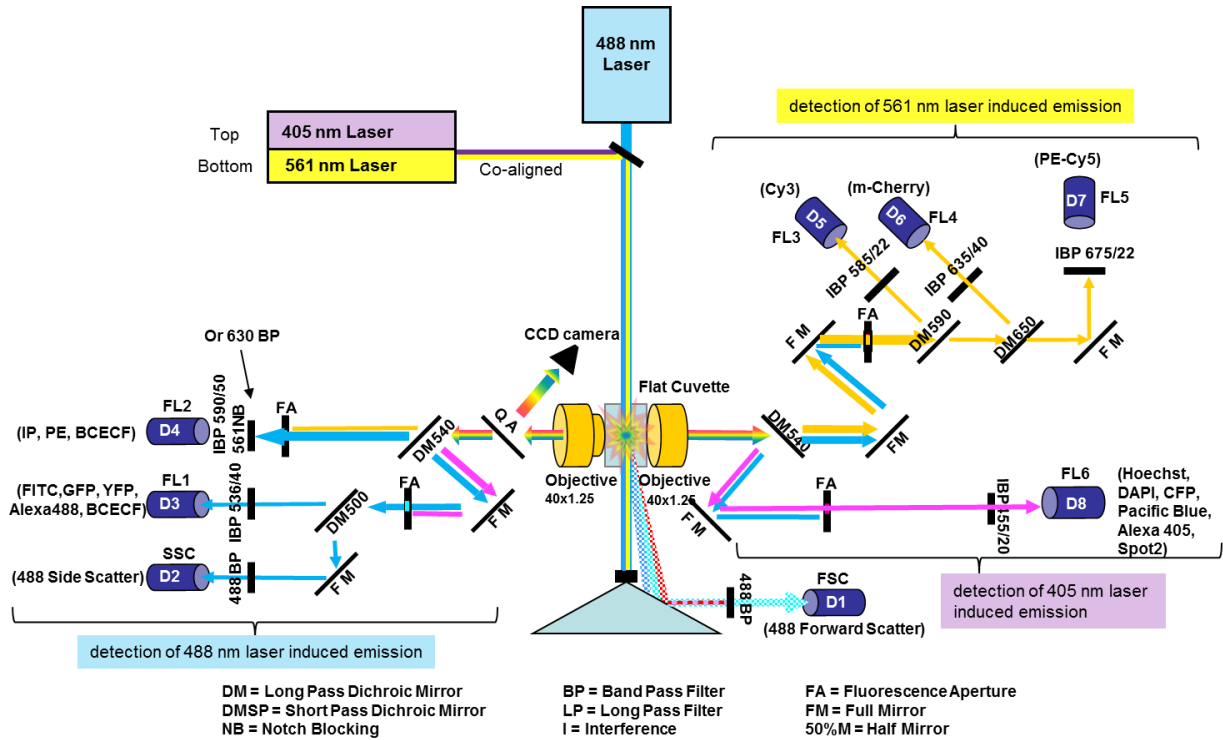


Figure 12 Partec Flow Cytometer – Scheme of the laser light sources, optical paths, and detectors

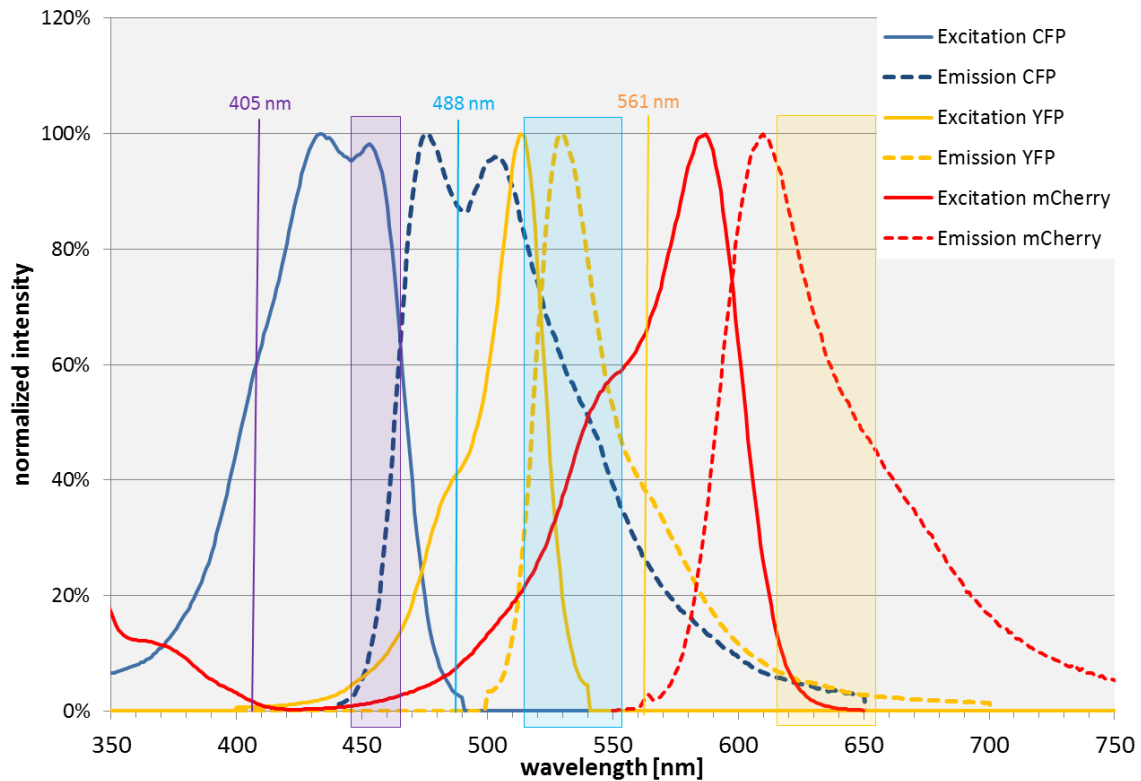


Figure 13 Laser excitation and emission detection of the Partec Flow Cytometer

The standard setup consists of a 405 nm laser here used for CFP excitation, which emission is collected by a 455/20 nm bandpassfilter; of a 488 nm laser for YFP excitation and its emission collection at 536/40 nm, and of a 561 nm laser used for mCherry excitation which emission is collected with a 635/40 nm bandpass filter.

Sample preparation

Cells were transfected 20 – 24 h prior Flow Cytometry experiments. The next day, cells were detached with trypsin, washed with PBS, and kept in PBS on ice. Aliquots of few ten thousands of cells were diluted in PBS and passed through the cytometer.

Data processing

For data analysis, the Summit software (Daco Colorado, Inc., Fort Collins, CO) was used.

Flow cytometry demands several controls in order to set gates to sort the signals from cells expressing one or two FPs (summarized in Table 10): First, we set a limit between auto-fluorescence and fluorescence using non-transfected cells (Table 10 B). The differentiation between mono- and multiple-coloured cells was done with mono-transfected cells for each colour. Finally, the positioning of the quadrant's cross was defined (Table 10 C). The cross defines populations that are above background for one or two fluorescence

parameters. In our case, a compensation of a spillover^{xxi} of CFP in the YFP channel is necessary (Table 10 D).

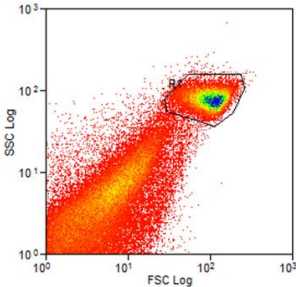
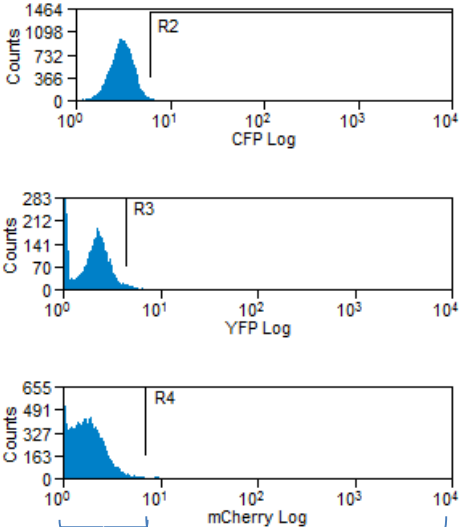
controls	aims	example
<p>non-transfected cells</p>	<p>discrimination of the cell population → selected by the gate R1 in the SSC-FSC plot → all further analysis are gated on R1</p> <p>excluding the auto-fluorescence from analysis → histograms of each channel</p>	<p>A</p>  <p>B</p>  <p>R2, R3, R4: only fluorescent cells will appear here</p>

Table 10, part 1: Flow Cytometry – list of controls both for transfection efficiency and FRET by Flow Cytometry

The controls are necessary to set the limits between fluorescent and auto-fluorescent cells

*RFP plots only necessary for transfection efficiency

^{xxi} spillover is coming from a spectral overlap of the emission of one fluorophore (here CFP) with the bandwidth of a detector designed for another fluorophore (here: YFP). The compensation corrects mathematically the spillover.

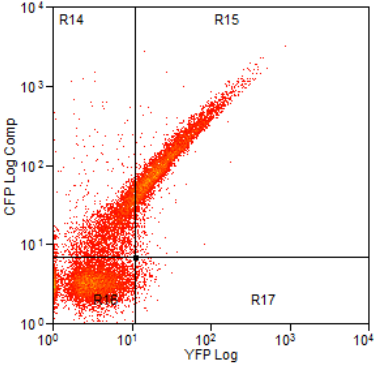
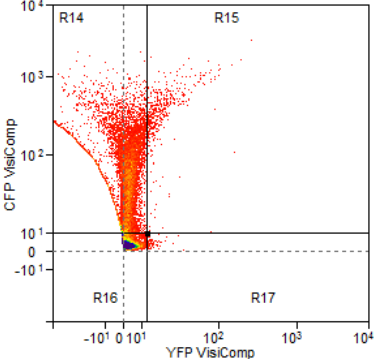
controls	aims	example
mono-transfected cells (CFP/YFP/RFP*)	compensation of spillover, in our conditions only necessary for CFP in YFP channel positioning of the quadrant's cross for all dot-plots CFP-YFP channel YFP-RFP* channel	<p>C CFP transfected cells before compensation</p>  <p>D after compensation (factor 20)</p>  <p>R14: CFP fluorescence R15: CFP & YFP (ideally empty for the control) R16: auto-fluorescence R17: YFP fluorescence</p>

Table 10, part 2: Flow Cytometry – list of controls both for transfection efficiency and FRET by Flow Cytometry

Compensation of the spillover of the cyan emission in the yellow detection channel

*YFP-RFP plots only necessary for transfection efficiency

The general procedure for multi-labelled samples is outlined in Table 11. For discriminating the transfection efficiency of a single label in a multi-labelled sample, the histogram of each colour can be used (Table 11 A). The second quadrant of a – e.g. CFP-YFP – dot-plot (R13, Table 11 B) reveals the percentage of double transfected cells. To discriminate the amount of triple transfected cells, a second dot-plot (here: YFP-RFP) was drawn and gated on R13. I.e., only cells which are double transfected (CFP and YFP), are selected for the plot. The amount of cells in the second quadrant (R10, Table 11 C) is equal to the number of triple transfected cells.

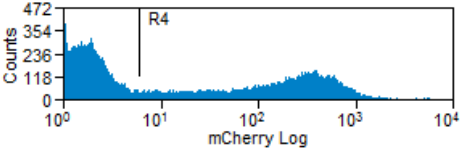
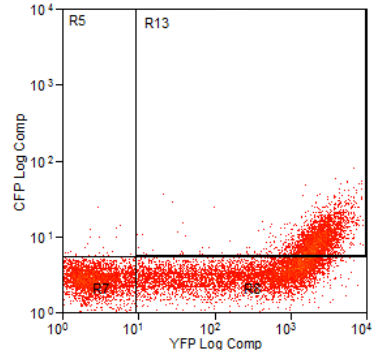
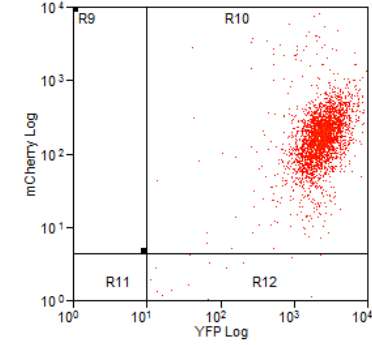
multi-labelled samples	aim	example									
CFP/YFP/RFP* tagged subunits	percentage of mono labelled positive cells → histograms (here: mCherry positive cells in R4)	<p>A mTurquoise-p67^{phox} + p47^{phox}-Citrine + mCherry-p40^{phox}</p>  <table border="1" data-bbox="948 636 1331 719"> <thead> <tr> <th>Region</th> <th>Count</th> <th>% Hist</th> </tr> </thead> <tbody> <tr> <td>R4</td> <td>10034</td> <td>43.4</td> </tr> </tbody> </table>	Region	Count	% Hist	R4	10034	43.4			
Region	Count	% Hist									
R4	10034	43.4									
	percentage of double tr. cells → dot plot (e.g. CFP-YFP), Total \triangleq cell population R1 R13 \triangleq double tr. cells	<p>B</p>  <table border="1" data-bbox="948 1135 1331 1256"> <thead> <tr> <th>Region</th> <th>Count</th> <th>% Hist</th> </tr> </thead> <tbody> <tr> <td>Total</td> <td>18769</td> <td>100</td> </tr> <tr> <td>R13</td> <td>3266</td> <td>17.4</td> </tr> </tbody> </table>	Region	Count	% Hist	Total	18769	100	R13	3266	17.4
Region	Count	% Hist									
Total	18769	100									
R13	3266	17.4									
	percentage of triple tr. cells, → RFP-YFP* dot plot, gated on R13 of CFP-YFP plot Total \triangleq R13 R10 \triangleq triple tr. cells	<p>C</p>  <table border="1" data-bbox="948 1673 1331 1787"> <thead> <tr> <th>Region</th> <th>Count</th> <th>% Hist</th> </tr> </thead> <tbody> <tr> <td>Total</td> <td>3266</td> <td>100</td> </tr> <tr> <td>R10</td> <td>3239</td> <td>99.2</td> </tr> </tbody> </table>	Region	Count	% Hist	Total	3266	100	R10	3239	99.2
Region	Count	% Hist									
Total	3266	100									
R10	3239	99.2									

Table 11 Flow Cytometry – multi-coloured samples both for transfection efficiency and FRET by Flow Cytometry

*RFP and YFP-RFP plots only necessary for transfection efficiency

2.2.10 Microscopy

2.2.10.1 Total Internal Reflection Fluorescence (TIRF) Microscopy

COS^{gp91phox, p22phox} cells were cultured on glass cover slips in 6 – well plates to 90 % confluency and triple transfected with Xtreme Gene HP (1.5 ng or 3.0 ng of total DNA/well, ratio of the plasmids: 1 : 1 : 1) as described in chapter 2.2.6. For the microscopy experiment, the cover slip was placed in a plastic holder. Cells were kept in 400 µl HEPES buffer (140 mM NaCl, 5 mM KCl, 1 mM MgCl₂, 2 mM CaCl₂, 140 mM HEPES, 0.1 % glucose; pH 7.4) at 37 °C. To activate the cells, 10 µl of prediluted PMA was added to reach a final concentration of 190 nM. Those experiments have been performed at the light microscopy facility Imagerie-Gif (Gif-sur-Yvette, France). The TIRF microscope was an inverted Nikon Eclipse Ti E with “perfect focus system”, equipped with 4 lasers (405/491/561/642 nm), dichroic mirror quad band 405/491/561 nm filters (Semrock, Rochester, NY). A special oil immersion objective was used for TIRF (60x APO TIRF, NA 1.49) The best compromised for the TIRF angle was taken to record 3 images, one for each fluorophore (mTurquoise, Citrine and mCherry). Time lapse sequences (1 picture for each color, every 30 s) were taken with an EMCCD camera (Evolve 512 Delta, Photometrics, Tucson, AZ). After two sets of picture, PMA was added. Data were collected for further 24 min.

Data analysis with ImageJ (National Institute of Health): An elliptic region of interest (ROI) was drawn to include as much as possible of the surface of the cell. The average intensity of this ROI was taken for each picture. After subtraction of the background taken outside the cell, data were normalized by dividing each intensity value by the maximum value of the time series. An average of normalized intensities from at least 5 cells was taken and plotted against the time (\pm SD) in Figure 36. For Figure 35, a line was drawn perpendicular to the edge of the cell. With the “plot profile” function, the intensity profile along this line was displayed and the values were copied to an excel sheet. This was done every 3rd picture.

2.2.10.2 FRET-FLIM

There are two major principles for FRET measurements. A first set of techniques are based on the fluorescence intensity changes of the donor (loss) and acceptor (gain) due to FRET (acceptor photobleaching, ratiometric FRET or 3-cube FRET). These techniques require cross-talk corrections and their outcome depends on FP concentrations that cannot be controlled in live cell. These difficulties can be circumvented with lifetime based approaches (FLIM) (Padilla-Parra and Tramier, 2012). We used the latter method, which will be described in more details below.

FLIM can be differentiated in the two main approaches, time domain (TD) and frequency domain (FD) FLIM. TD-FLIM is based on short laser-pulsed excitations and the collection of the emitted photons on a discrete timescale. The lifetime of the excited state corresponds to the time delay between excitation and emission. FD-FLIM is operating with a modulated light source and a modulated detector. The excitation light is modulated in intensity at a certain frequency. The induced fluorescence emission mirrors this modulation pattern and show, due to the fluorescence decay, a delay in time. The lifetime can be calculated from this delay (Sun et al., 2011a). Here, we will concentrate on the TD-FLIM. Our setup is based on time-correlated single photon counting (TCSPC), where single events are detected upon excitation with a pulsed laser. For each event, the arrival time (difference between start-stop times) is measured and the experiment is repeated until several hundred thousands to a few millions of photons are collected (Figure 14).

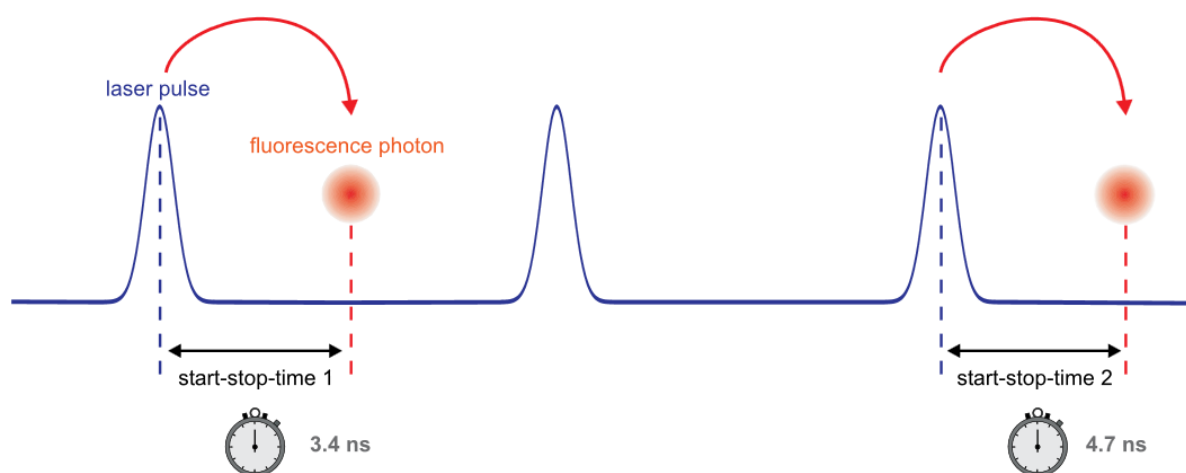


Figure 14 Principle of TCSPC

Repetitive laser pulses excite a fluorophore and measure the time between the pulse and the photon arrival whereby only very few pulses will lead to a photon emission to ensure the single photon registration.

The received histogram of the arrival time of all photons reflects the fluorescence decay (Figure 15), from which the lifetime can be calculated (compare chapter 3.2.2). This concept is true if the probability of registering more than one photon/cycle is low, as a consequence, the majority of laser pulses are not followed by a photon emission (Wahl, 2009).

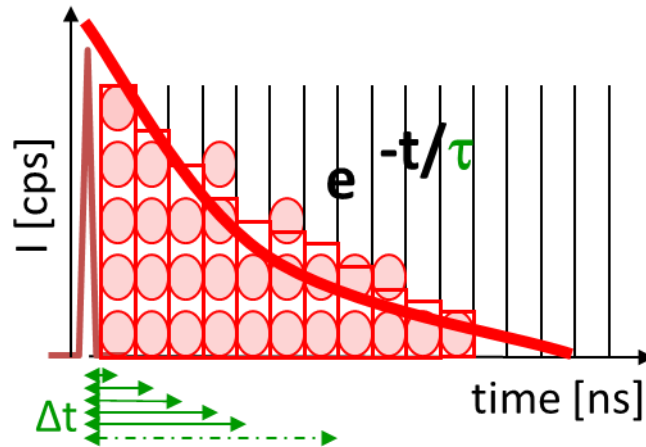


Figure 15 Fluorescence decay histogram

The arrival times of several hundred thousands to a few million photons are collected and plotted as a histogram (intensity vs. time) which reflects the fluorescence decay.

Microscopy and FLIM setup

Fluorescence intensity wide-field and time-resolved laser scanning TCSPC microscopy was performed on a custom-made setup, which was developed in the laboratory during the PhD of L. Alvarez (Alvarez, 2010). It is based on a TE2000 microscope equipped with a 60x, 1.2NA water immersion objective (Nikon Corp., Tokyo, Japan).

The excitation source in the epifluorescence detection path is an Hg lamp, which is coupled to a fast SmartShutter[®] (Sutter instrument). The power of the lamp was attenuated with neutral density (ND) filters, which are placed in the Lambda 10-3 filter wheel (Sutter instrument) and in a slider in front of the Hg lamp.

The attenuated light passes through a filter cube, which is equipped with wavelength specific excitation and fluorescence emission filters, and a dichroic mirror (Table 12 gives an overview of the filter cubes). The fluorescence emission is collected by a CCD camera (6.45*6.45 μm ; ORCA-AG, Hamamatsu Photonics K.K., Shizuoka, Japan). The system is controlled by $\mu\text{Mangager}$ (Vale Lab, University of California, San Francisco) and ImageJ (NIH).

cube	excitation filter	DM	emission filter
CFP (CFP 2432C) *	FF02-438/24-25	FF458-Di02	FF01-483/32-35
YFP (YFP 2427B) *	FF01-500/24-25	FF520-Di02	FF01-542/27-25
RFP (C156423 custom) ⁺	ET580/25x	ZT594rdc	ET625/30m

Table 12 Filter cubes of the epifluorescence light path

CFP cube was used for mTurquoise and Aquamarine, the YFP cube for Citrine, and the RFP cube for mCherry

* Semrock, (Rochester, NY)

⁺ Chroma Technology Corp. (Bellows Falls, VT)

The TCSPC FLIM setup is working with pulsed laser diodes at 440 nm for samples with a cyan donor and at 466 nm for samples with a yellow donor (PicoQuant GmbH, Berlin, Germany) driven by a PDL 800 driver (~100 ps FWHM, 20 MHz of repetition rate, PicoQuant GmbH, Berlin, Germany). The excitation sources are coupled to a C1 scanning head (Nikon) with a optical fiber. The scanning head was controlled by the EZ-C1 software (Nikon). The excitation beam crossed an empty position of the epi-fluorescence filter turret and was focused on the sample through the microscope's objective lens. The scanning head probed a 100 x 100 μm maximum field of view with a laser pixel dwell time of 61.44 μs . The TCSPC detection was inserted in the collimated section just below the microscope objective. The pathway was composed of a cube containing a dichroic mirror positioned at 45° from the optical path (SWP-500, Lambda Research Optics, Inc. Costa Mesa, CA), a focusing lens ($f = 20\text{cm}$, Thorlabs,

Newton, NJ), a set of filters to select the FP fluorescence and remove the excitation light and a detector (MCP-PMT, Hamamatsu). For CFPs, the dichroic mirror is a SWP-500 filter (Lambda Research Optics, Inc. Costa Mesa, CA) and the set of filters is composed of one 480AF30 filter (Omega Optical Inc., Brattleboro, VT) and two 458 nm Razor Edge Longpass filters (Semrock, Rochester, NY). For Citrine, the dichroic mirror is a T490spxr filter (Chroma Technology Corp) and the set of filters is composed of a 520/28-25 nm bandpass filter and a 488 nm longpass filter (both Semrock).

The signal was then amplified by a fast pulse preamplifier (Phillips Scientific, Mahwah, NJ) before reaching the PicoHarp300 TCSPC module (PicoQuant). The counting rate of the recording was routinely between 50,000 and 100,000 cts·s⁻¹. Lifetime measurements were analysed by the SymPhoTime software (v5.3.2, PicoQuant), which calculates the intensity image and the fluorescence lifetime image of the observed field of view. The TCSPC fluorescence decay of a chosen ROI was calculated by SymPhoTime and exported for further analysis in IGOR Pro (Wavemetrics, Lake Oswego, OR). Each field of view was scanned enough times to accumulate $1 - 6 \cdot 10^6$ cts per decay.

Experimental Part

Cells were transfected one day before on cover slips (chapter 2.2.6). These cover slips were placed in a holder and covered with approximately 2 ml DPBS (Gibco, Thermo Fisher Scientific, Waltham, MA) and maintained at 20 ± 0.3 °C by a cooling device. One cover slip was used for maximal 2 h.

A detailed description of the data collection can be found in chapter 3.2. Briefly, intensity pictures of the corresponding^{xxii} cubes were taken. Afterwards, the FLIM picture was recorded.

^{xxii} depending on the used FPs

2.2.11 Fluorescence cross correlation spectroscopy

Before the description of the experimental setup itself, the principle of the FCCS experiment will be presented to introduce the necessary concepts to understand the result (paragraph 4.2.2).

In fluorescence correlation spectroscopy (FCS) a focused laser beam illuminates a small volume, which is crossed randomly by fluorophores. The observation volume ($V_{obs} = 0.1 - 0.3$ fl) is usually obtained using a confocal microscopy setup Figure 16. During the crossing period, the fluorophore goes through several excitation/emission cycles thus producing a number of photons responsible of the fluctuation of fluorescence intensity in the small observed volume. The auto-correlation function of these fluctuations that compare the changes in intensity between two time points (t and $t + \tau$) is then calculated (Equation 13). The probability of a change of fluorescence is higher for fast moving molecules in comparison to slow moving one.

Equation 13 $G(\tau) = \frac{\langle F(t)F(t+\tau) \rangle}{\langle F(t) \rangle^2}$ with $F(t)$, the fluorescence intensity at time t and τ is the time delay.

The fit of $G(\tau)$ gives back the time needed by the fluorophore to cross the observation volume, τ_D . The latter is directly related to the diffusion coefficient. The amplitude of the auto-correlation curve, $G(0)$, is the inverse of the number of molecules in the observation volume, N (Lakowicz, 2006).

Equation 14 $G(0) = \frac{1}{N}$

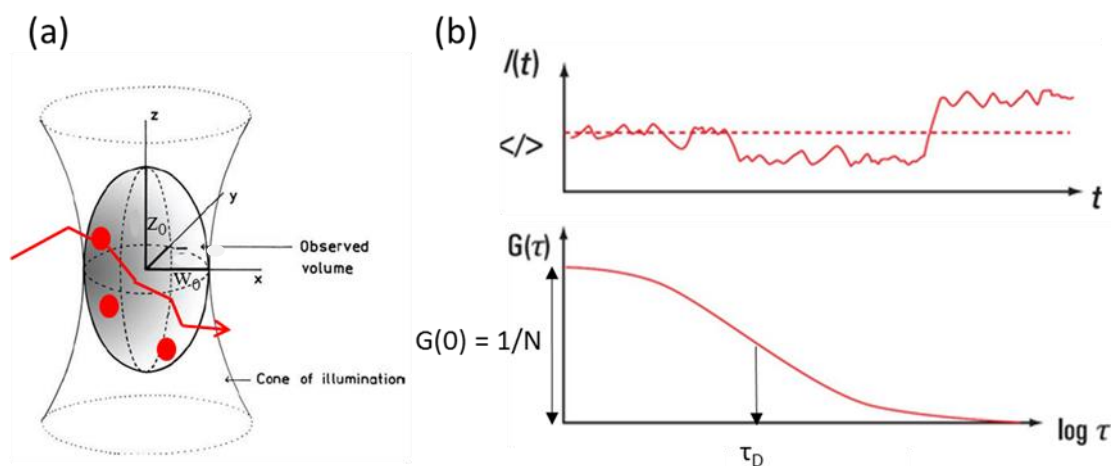


Figure 16 FCS principles and definition of the observed volume.

(a) Diffusion in the observed volume induces fluctuations of the number of molecules. The observed volume is defined as a vertical elongated ellipsoid, which can be described by its equatorial radius ω_0 and its vertical dimension z_0 (Lakowicz, 2006) (b) The fluorescence intensity in the observed volume fluctuates around its average value $\langle I \rangle$. The auto-correlation function of these fluctuations, $G(\tau)$, is presented below. (Figure adapted from Leica website)

The observation volume is shown in Figure 16 (a). With the knowledge about the dimension of the observation volume (axial z_0 and lateral ω_0), the concentration of fluorescent molecules, C , and their diffusion coefficient, D , can be calculated as follows:

$$\text{Equation 15} \quad C = \frac{N}{N_A \cdot V_{obs}} = \frac{N}{N_A \cdot \pi^2 \cdot z_0 \cdot \omega_0^2}$$

$$\text{Equation 16} \quad D = \frac{\omega_0^2}{4\tau_D}$$

Fluorescence cross correlation spectroscopy (FCCS) is the dual colour variant of the FCS: If two differently coloured probes are interacting, they diffuse together and thus cross the focal volume simultaneously. As Figure 17 indicates, the detectors collect the emission of both colours separately, the time dependency makes it possible to detect the co-diffusion.

Therefore the readout allows to calculate the auto-correlation function for each colour ($G(\tau)$ from Equation 13) and the cross-correlation function that characterises of the co-diffusion ($G_{cross}(\tau)$ from Equation 17).

$$\text{Equation 17} \quad G_{cross}(\tau) = \frac{\langle F_i(t)F_j(t+\tau) \rangle}{\langle F_i(t) \rangle \langle F_j(t) \rangle}$$

with $F_{ij}(t)$, the fluorescence intensity at time t in detection channel i or j and τ is the time delay.

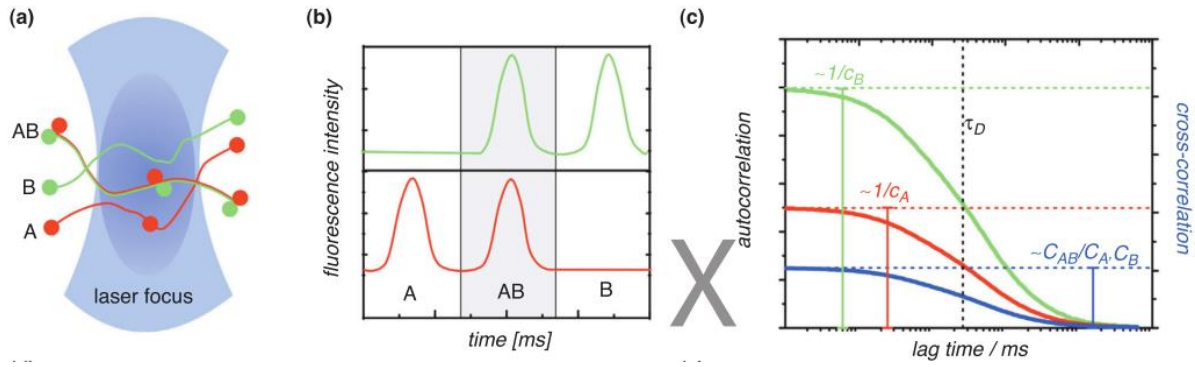


Figure 17 FCCS principles

(a) Two species A and B of different colours diffuse either singularly or together through the observation volume (b) The time scale allows the determination of intensity fluctuation of single fluorophore (A or B) and of simultaneous diffusing molecules (AB). (c) The auto-correlation functions, $G(\tau)$, for A and B, respectively in red and green, contain information about the number of diffusing molecules (inverse proportional to the amplitude, y-axis shifts) and thus their concentration, C_A and C_B and the diffusion time (x-axis shifts). The cross-correlation function, $G_{cross}(\tau)$, is in blue. Its amplitude is inverse proportional to $1/\frac{C_{AB}}{C_A C_B}$ and it increases with increasing degree of binding (y-axis shift). (graphic from (Piehler, 2014))

The concentration of A, B, and their complex AB can be expressed as follow:

$$\text{Equation 18} \quad C_A = \frac{1}{G_A(0)} \frac{1}{N_A} \frac{1}{V_A} \quad C_B = \frac{1}{G_B(0)} \frac{1}{N_A} \frac{1}{V_B} \quad C_{AB} = \frac{G_{cross}(0)}{G_A(0) \cdot G_B(0)} \frac{1}{N_A} \frac{1}{V_{cross}}$$

where N_A is the Avogadro number.

V_{obs} is different for each colour (V_A and V_B in Equation 18) due to the wavelength dependency of the diffraction. For an accurate quantification of the interaction with FCCS, the overlap of the detection volume for the two colours has to be carefully optimized. The effective cross-correlation volume, V_{cross} , is given by the geometrical average of V_A and V_B . If the overlap is accurate, its value is comprised between V_A and V_B . If not, it increases above V_A and V_B . The accuracy of the overlap can be monitored with a tandem where the two fluorophores are linked and thus diffuse together. In that case, the values of τ_D (time needed by the fluorophore to cross the observation volume or diffusion time) for the auto-correlation function in channel A ($\tau_{D,A}$), and B ($\tau_{D,B}$) and the cross-correlation function ($\tau_{D,cross}$) correlates with the volume sizes (suppl. data (Foo et al., 2012)f).

The ratio of the amplitudes of the cross-correlation and auto-correlation function correlates with the fraction of bound molecules, β_i (Equation 19). If the alignment of the volumes is optimized these ratios are expected to be close to one for a tandem ((Foo et al., 2012)).

$$\text{Equation 19} \quad \beta_A = \frac{G_{cross}(0)}{G_B(0)} \cdot 100 \% \quad \cdot \beta_B = \frac{G_{cross}(0)}{G_A(0)} \cdot 100 \%$$

The ratio of the amplitudes of the correlation will be calculated for several constructs in order to estimate the fraction of bound molecules in paragraph 4.2.2.

In conclusion; FCCS allows the quantification of protein-protein interactions and the determination of:

- the concentrations of the single and bound partners;
- the bound fraction;
- the dissociation constant (even for complex stoichiometries).

The method works only with bright fluorescent labels at low concentrations and for high affinity binding and does not provide spatial resolution (when performed standardly as single spot FCCS as we did). As all spectroscopic techniques the measurements can be affected by several issues as the presence of dark states or photobleaching and lack of volume overlap. Those points will be discussed in paragraph 5.1.1.1 ff.. The spectral cross talk between fluorophores can also limit interpretation of FCCS results.

We had to employ the same fusion proteins and thus the same fluorophores in FCCS than the ones we used for the FRET-FLIM measurements (mTurquoise and Citrine), since we wanted to compare both results. Their fluorescence spectra are very broad and upon excitation of mTurquoise, its fluorescence can be detected in the Citrine detection channel. In conventional FCCS, where both fluorophores are excited and detected at the same time, this bleed-through emission of mTurquoise in the Citrine detection channel affects the auto-correlation function (Citrine) and the cross correlation function hence ending in false positive results or changing the proportion of the measured bound fraction. There are several ways to circumvent this spectral cross talk. A simple possibility is to subtract the bleed-through determined in an independent experiment with non-interacting species from the cross-correlation function. For this method, the laser powers have to be kept constant for the whole series of experiments, though (Sahoo and Schwille, 2011, Padilla-Parra et al., 2011b). Another option is to use an alternating excitation (pulsed interleaved excitation), which switches faster than the diffusion time (Müller et al., 2005, Thews et al., 2005). We use a third option based on fluorescence lifetime correlation spectroscopy (FLCS). In the latter, the photons are “attributed” *a posteriori* during the data processing to their fluorophore on the basis of their fluorescence decay signature. In the setup we used, mTurquoise is excited with a pulsed laser and Citrine with a continuous wave laser. The correction induced by FLCS filters is independent of the fluorescence intensity and the laser power can be adapted during the experiment in order to

limit the photobleaching (Macháň et al., 2014). A more detailed description of the FLCS fluorescence lifetime filters can be found in appendix 8.5.

2.2.11.1 FCCS setup

The FCCS experiments were performed at the Microscopy Rennes Imaging Centre in collaboration with Marc Tramier (IGDR, Rennes, France) on a commercial setup equipped to excite mTurquoise and Citrine. Due to the low brightness of ECFP, the ancestor of mTurquoise very few setups are equipped with an excitation at 440nm.

The confocal microscope Leica TCS SP8 SMD (Leica Microsystems GmbH, Mannheim, Germany) is equipped with a DMI 6000 CS stand and a 63x/1.2 HC PL APO water immersion objective. The excitation lasers are a continuous argon laser (514 nm for Citrine) and a diode pulsed laser (440 nm for mTurquoise) (PicoQuant GmbH, Berlin, Germany). The fluorescence detection is performed through a double fibre coupler constituted of a 505 nm dichroic mirror and two band pass filters (478/22 nm and 540/30 nm) and connected on one side to the external port of the confocal microscope and on the other side to two APD detectors, one MPD and one TAU SPAD (Picoquant). At the detection, the SMD module is constituted of a PicoHarp 300 system for TTTR (Time Tagged Time Resolved) mode of single photon counting (Picoquant). The filters/dichroic mirrors of the epifluorescence path are listed in Table 13. Additionally, the microscope is equipped with an air-conditioned chamber (37 °C, 5 % CO₂). Data were acquired and analysed with the SymPhoTime software (PicoQuant).

FP	excitation filter	emission filter	dichroic mirror
mTurquoise	BP 450 – 490 nm	LP 515 nm	510 nm
Citrine	BP 515 – 560 nm	LP 590 nm	580 nm

Table 13 Fluorescence filters and dichroic mirrors of the FCS setup

2.2.12 Data acquisition and analysis with SymPhoTime software

Both for FRET-FLIM and FCCS, data acquisition was done with the SymPhoTime software (PicoQuant GmbH, Berlin, Germany). This software provides the possibility to record fluorescence decay as a TCSPC histogram and allows a fitting with a mono- to several exponential functions. It directly provides the average lifetime and the quality of the fit (as χ^2 value), the raw data can be exported as well and treated elsewhere (here, we used IgorPro, Wavemetrics, Lake Oswego, OR). Furthermore, it gives a multichannel scaler (MCS) trace, which shows the evolution of the fluorescence intensity in time. The precise monitoring of the average fluorescence intensity during the experiment allows a very good control of photobleaching.

With respect to FCCS experiments, the software can collect the FCS traces and fit it with the auto-/cross-correlation function. Data can be directly corrected with the FLCS fluorescence lifetime filters.

2.2.13 Molecular structure visualisation and alignment

Structure visualisation and alignment have been performed with VMD software (University of Illinois at Urbana–Champaign, IL; <http://www.ks.uiuc.edu/Research/vmd/>; (Humphrey et al., 1996)).

2.2.14 Statistical analysis

All statistical tests were performed with GraphPad Prism (version 5, GraphPad software inc., La Jolla, CA). A t-test was performed to compare the means of two groups which differ in only one parameter. To compare three or more groups, ANOVA tests were performed: One way ANOVA shows whether the means of the groups are statistically different. Time series were tested with 2-way ANOVA, since these data sets differ in two variables. A $P \leq 0.05$ indicated in any test a statistical significant difference between the two populations. All data are represented as mean \pm standard deviation (SD) unless indicated otherwise.

3 Results – methodology development for FRET quantification

3.1 Flow Cytometry

3.1.1 Elucidating the transfection efficiency by flow cytometry

The transfection efficiency is a very important parameter for transiently transfected cells since all experiments will be affected by it. During my work I often struggled with the luminescence assay most probably due to insufficient transfection efficiencies. As well it is necessary to test, how and how far the transfection ratios of transfection between the different plasmids can be influenced by DNA preparation qualities, cell culture and transfection conditions, subunits, and FP-tag position. In the case of multiple transfections, the transfection efficiency can be different for the single plasmids, which is necessary to know for the trouble shooting.

Therefore it is desirable to have the possibility to monitor the transfection efficiency especially during its optimization.

One step of the optimization of the transfection efficiency was to switch from standardly prepared plasmid (with home-made protocol) to an endotoxin-free preparation kit^{xxiii}, which is shown as an example of the flow cytometry based surveillance of transfection efficiency (Figure 18): Cells were transfected with three plasmids at once (mTurquoise-p67^{phox}, p47^{phox}-Citrine, mCherry-p40^{phox}), differing only in the preparation of DNA. The transfection was performed with 1.5/3/6 µg of DNA. Beside a general gain in transfection efficiency accomplished by the endotoxin free plasmid preparation, the difference between mCherry-p40^{phox} (\cong RFP) and p47^{phox}-Citrine (\cong YFP) expression is significantly reduced due to increased mCherry-p40^{phox} expression (endotoxin free vs. standard plasmid: RFP/YFP = 87 ± 4 [%] vs. 55 ± 5 [%]^{xxiv}; t-test: $p = 0.001$).

^{xxiii} for details about the DNA preparation got to chapter 2.2.2, and for the optimization of the transfection go to chapter 2.2.6

^{xxiv} averaged ratio of three different trials (variation of amount of the endotoxin free DNA) shown in Figure 18 (mean \pm SD)

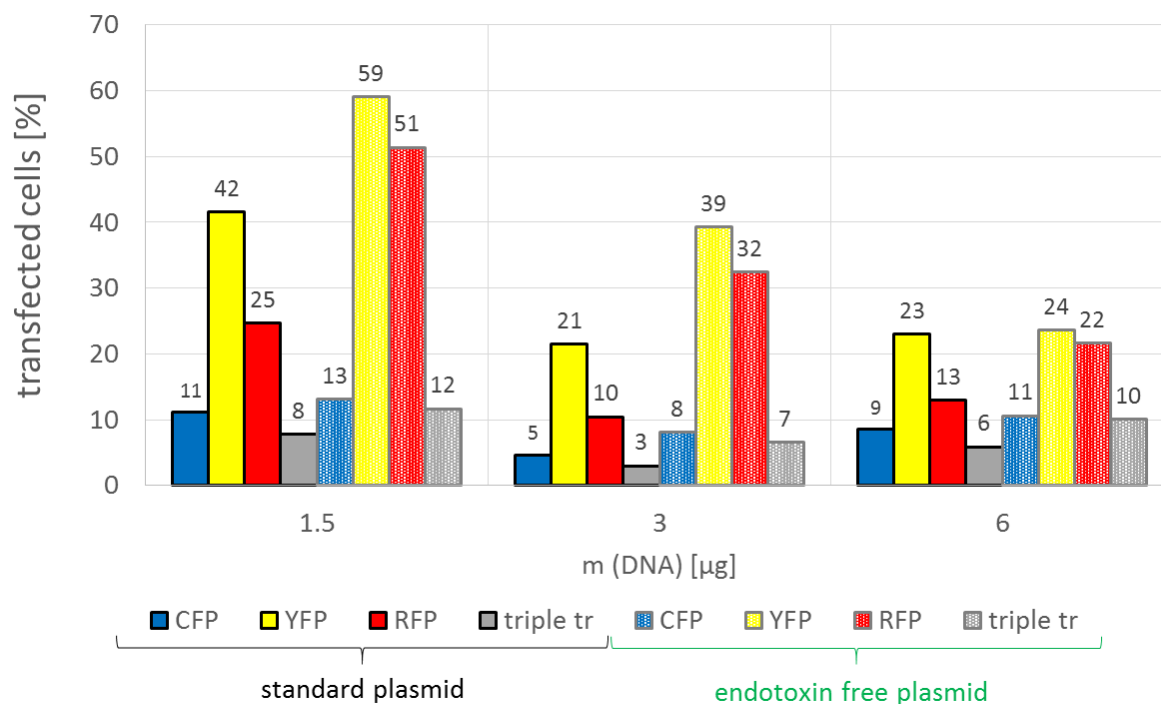


Figure 18 Distribution single and triple transfection efficiency

Cells were transfected triple (mTurquoise-p67^{phox}, p47^{phox}-Citrine, mCherry-p40^{phox}, in the figure called CFP, YFP, and RFP, respectively). Two parameters were varied: (i) amounts of total DNA (1.5/3/6 µg) and (ii) the DNA preparation method (standard vs. endotoxin free). The percentage of cells positive for each single FP label is plotted as well as the share of triple transfection cells.

However, the transfection seems to work a lot better for the p47^{phox}-Citrine and mCherry-p40^{phox} in comparison to the mTurquoise-p67^{phox} (\cong CFP) and seems to be independent of the plasmid preparation (endotoxin-free vs. standard plasmid: CFP/YFP= 29 ± 11 [%] vs. 28 ± 7 [%]). Several explanations may explain this phenomenon: The intensity of CFP will decrease when FRET occurs. However, with regard to the low FRET levels observed between mTurquoise-p67^{phox} and p47^{phox}-Citrine (Figure 40), its influence can be assumed to be of minor relevance. Another possibility may be the cytotoxicity of p67^{phox} (Dupré-Crochet, unpublished observation) which in general impedes its expression, but that does not fit with the impression I got from the microscope (more or less every cell which is successfully transfected expresses all three plasmids).

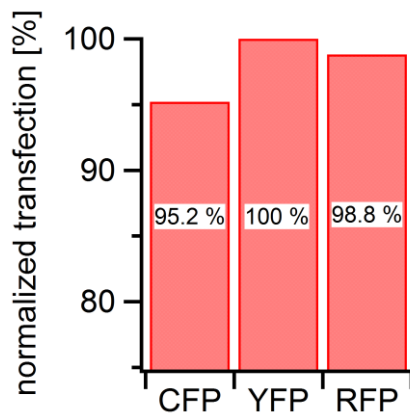


Figure 19 Fluorescence intensity microscopy reveals triple transfected cells

Triple transfected cells (CFP = mTurquoise-p67^{phox}, YFP = p47^{phox}-Citrine, RFP = mCherry-p40^{phox}) were counted manually. All transfected cells were transfected with YFP (number of cells is normalized towards the number of cells with YFP). 95.2 % of all cells expressing YFP were at least double transfected with CFP, and 98.8 % were at least double transfected with RFP. (n ≥ 239 cells)

To verify whether the flow cytometer trials gave misleading results concerning the CFP transfection efficiency, a simple microscope counting experiment was performed: Photos of triple transfected cells (same conditions as for the flow cytometry experiment) were taken for each fluorescent channel and the transfected cells were counted manually for each channel. All transfected cells were at least expressing p47^{phox}-Citrine (\cong YFP), therefore the counts of mTurquoise-p67^{phox} (\cong CFP) and mCherry-p40^{phox} (\cong RFP) are given as a percentage of YFP transfected cells. As Figure 19 shows, 95 % of the cells were transfected with YFP and CFP and 99 % of the cells with YFP and RFP, which means that more or less all cells were triple transfected. This is far away from what was found by flow cytometry, which gives CFP/YFP ratio of only 29 ± 11 [%], however the ratio of RFP/YFP (87 ± 4 [%]) is comparable to the one of the manual counting. This results leads to the conclusion that the cytometer is missing some CFP fluorescent cells, which is in line with the observation that the CFP transfected cells never give higher percentages of transfection efficiencies than the triple transfection or the other way around the transfection efficiency depends only on the expression of CFP.

We believe that the conditions of our flow cytometer setup are not optimal for CFP excitation and detection and causes the CFP underestimation (Figure 13). This might have been reinforced by unfavourable laser alignment during certain time periods of the project.

3.1.2 FRET by Flow Cytometry

To have an on hand method which allows a quick detection of protein-protein interactions with a statistically relevant sample size would increase the speed of interaction discovery compared to manual microscopy experiments. FRET by Flow Cytometry fulfils these criteria: It allows a

screening of several 10,000s of cells within minutes and methods were described for FRET detection by flow cytometry (Trón et al., 1984, Banning et al., 2010). We adopted the method described by Banning and co-workers (3.1.2.2), but the first step was to adapt the cytometer to the demands of FRET measurements and to develop the data processing.

3.1.2.1 Optimization of the cytometer for FRET demands

A FRET detection pathway had to be inserted in the standard settings (described in chapter 0). Therefore, the light path dedicated to the detection of the emission induced by the 561 nm laser was modified. Figure 20 shows the changes entered to achieve the FRET configuration: To optimize the yield of light arriving at the detector, the dichroic mirror (DM) 540 nm was exchanged by a DM 500 nm and the interference bandpass filter (IBP 585/22 nm) in front of the FRET detector was exchanged by a 536/40 nm filter. The direct YFP excitation light path (488 nm laser) remains unchanged in the FRET settings.

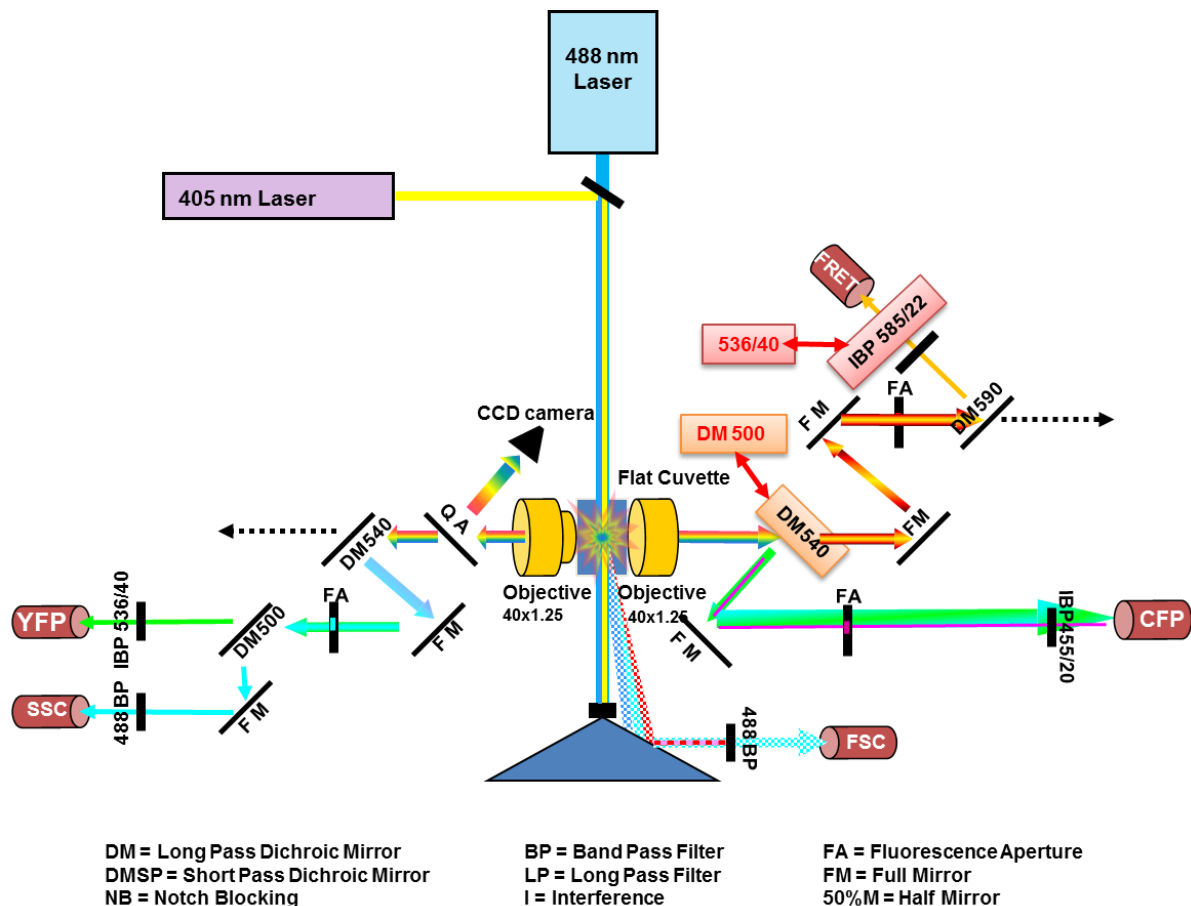


Figure 20 Scheme of the flow cytometer adopted for FRET measurements

The right hand side of the scheme is collecting the light coming from 405 nm laser (CFP excitation). The DM 540 nm was exchanged by a 500 nm one, as well as the IBP 585/22 nm in front of the FRET detector was exchanged by a 536/40 nm one to allow the detection of the sensitized emission (\triangleq YFP emission)

Figure 21 shows the improvement on the spectral selection achieved with the new DM and band pass filter: The new DM (500 nm) let the maximum YFP emission (530 nm) pass through, which is cut off by the standard DM (540 nm). The bandwidth of the collected light with the FRET settings includes the maximum YFP emission (IBP 536/40 nm), and allow the fluorescence collection at wavelengths where the ratio of intensities YFP/CFP is the most favourable.

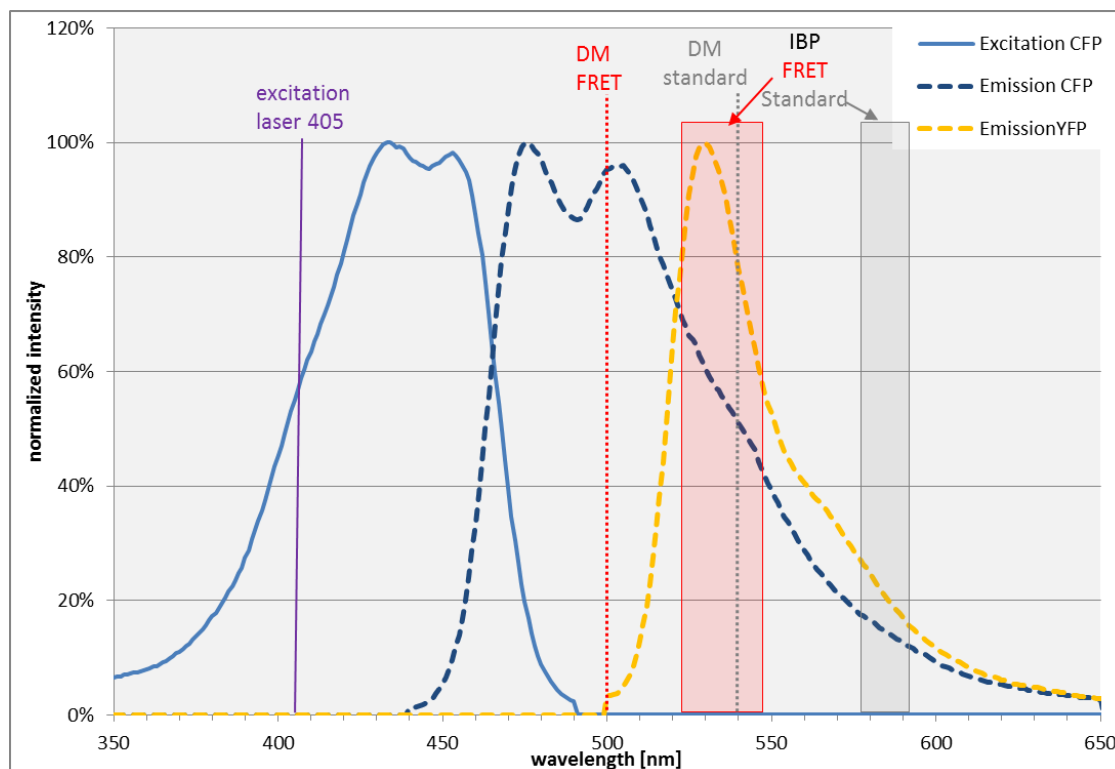


Figure 21 Flow Cytometer – spectral selection optimized for FRET detection

Normalized spectra of fluorescence excitation of CFP and emission of CFP and YFP (\cong sensitized emission). Standard settings (grey): DM excludes the maximum YFP emission, band pass filter (IBP) collects light on the tail of the emission spectrum of YFP with an unfavourable ratio of YFP/CFP emission.

FRET settings (red): DM allows the maximum emission of YFP to pass, the bandpass filter collects the maximum emission peak, whereby the ratio YFP/CFP emission is improved.

In praxis, the improvements of the changes were proven by an increased contribution of the FRET detector signal when measuring CFP transfected cells displayed in a FRET-CFP dot-plot (Figure 22). Unfortunately, I did not measure a CFP-YFP tandem under both conditions. Such a sample should have led to an even more prominent upshift of the cell population, due to the more favourable ratio of YFP/CFP (compare Figure 21).

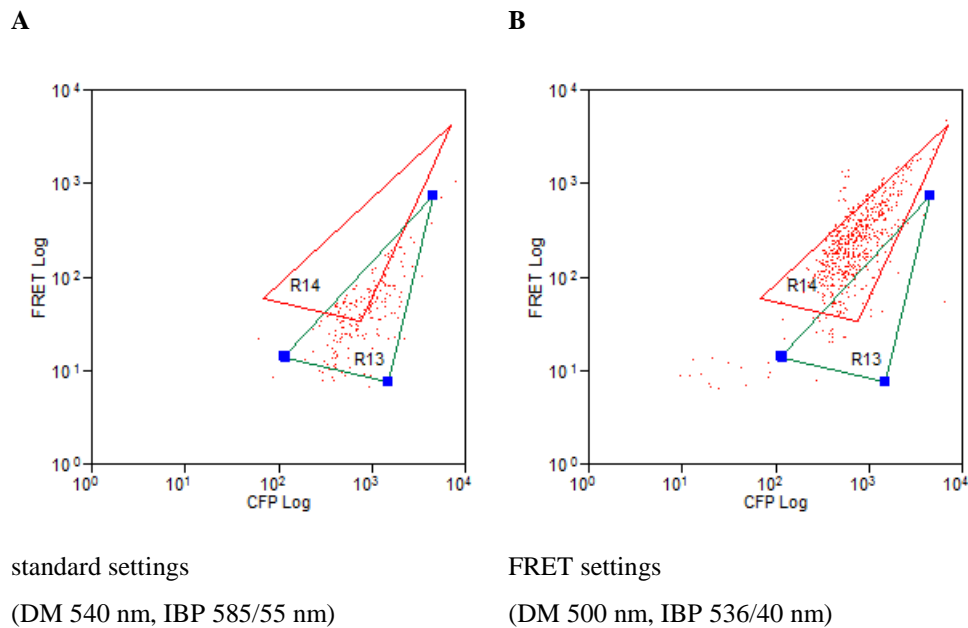


Figure 22 Flow Cytometry: Effect of the FRET settings on CFP transfected cells in FRET-CFP plot

In comparison to the CFP intensities derived with the standard settings of the cytometer (R13, A), the one derived with the FRET settings (R14, B) is up-shifted (signal recognised with the FRET detector is increased).

3.1.2.2 Developing a FRET analysis method

The method used here is adapted from the one described by Banning and co-workers which is supposed to be sensitive enough to detect non-membrane bound protein-protein interactions (Banning et al., 2010).

It is based on a gating strategy aiming to select for FRET positive cells hence giving a percentage of FRET positive cells within the cell population. This strategy starts with the standard procedure described in Table 10 and Table 11 (paragraph 2.2.9, p. 43 ff). The next steps – which are specific for FRET analysis – are summarized in Table 14. First, a contamination of the FRET channel by the direct excitation of YFP by the 405 nm laser has to be excluded. Thus, another control of YFP positive cells was done and plotted in a FRET-YFP dot-plot: Very bright YFP cells appear on the right end of the YFP axis and are excluded by the gate. The gate defined with the FRET-YFP plot is set on the FRET-CFP plot (sensitized YFP emission against CFP emission). Within the latter one, a triangle gate (R11) discriminates between sensitized YFP emission (FRET, inside the gate) and direct CFP emission (excluded). This gate is set manually with a control of CFP & YFP positive cells.

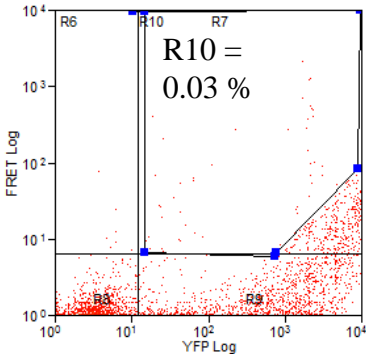
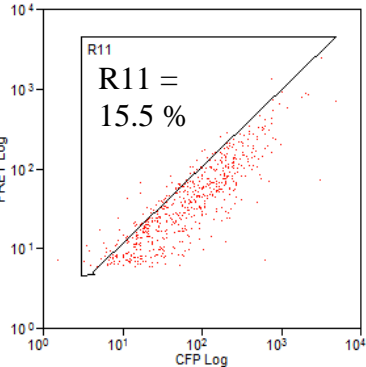
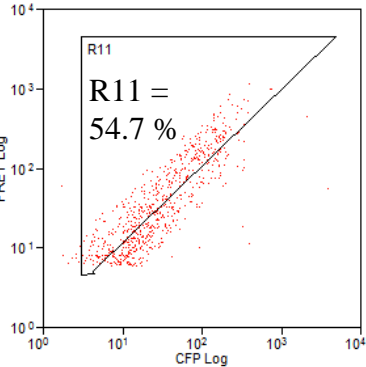
dot plot	aim	example
FRET-YFP	Excluding direct excitation of YFP by 405 laser which appears in the FRET channel → control YFP transfected cells, setting a gate (R10)	control: YFP tr.cells 
FRET-CFP	Discriminating between direct CFP excitation and FRET: Defining a gate (R11) which excludes direct CFP excitation → control with CFP + YFP transfected cells (no FRET), (gated on R10) revealing FRET positive cells → cells inside the gate R11 are FRET positive	control: CFP + YFP tr. cells  sample: Aqua.-Citrine tandem 

Table 14 Discriminating FRET by Flow Cytometry – a gating strategy

The FRET by Flow Cytometry method described here feature quick sample screening of large numbers of cells, a simple application and easy analysis (standard flow cytometry software is sufficient). Even if the gating is subjective since the gates are chosen by eye, the outcome – a qualitative answer to FRET positive vs. FRET negative cells – is still given (compare Table 15). To enhance the sensitivity, an optimization of the CFP detection could be achieved by a better alignment of the lasers (done by the manufacturer) and optimization of the detection light path.

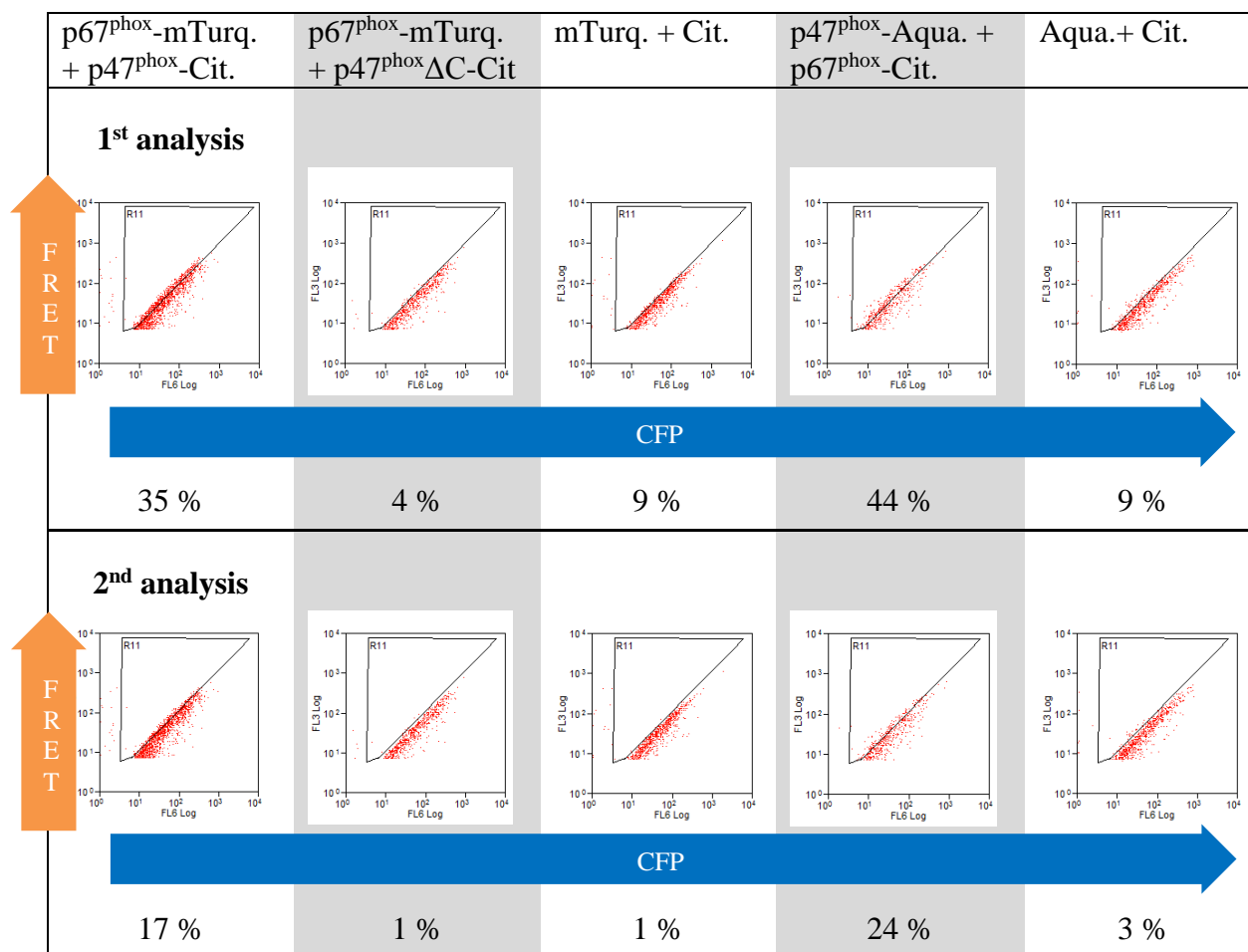


Table 15 Influence of the gating on the FRET by Flow Cytometry result

Depending on the position and angle of the triangle, the percentage of FRET positive cells changes, as shown here as two different analysis of the same data set.

In conclusion, the method introduced here, fulfils the demands of a quick qualitative search of protein-protein interactions. We applied this method successfully to intermolecular and intramolecular interaction studies of the subunits of the NADPH oxidase, as it is shown in paragraph 4.2.1.1 and 4.2.1.5.1, respectively.

The group of Damjanovich and Szöllösi has developed a method allowing the discrimination of FRET efficiency on individual cells by Flow Cytometry, which they call flow cytometric

resonance energy transfer (first publication (Trón et al., 1984)). They developed an algorithm for quantifying FRET by flow cytometry data and built a free software (Szentesi et al., 2004). A crucial point of the calculation of the FRET efficiency is the scaling factor α which normalizes the readout of the donor and acceptor detector with respect to the different equipment sensitivities $\frac{\eta_A}{\eta_D}$ and quantum efficiencies $\frac{\Phi_A}{\Phi_D}$ towards donor and acceptor ($\alpha = \frac{\eta_A}{\eta_D} \cdot \frac{\Phi_A}{\Phi_D}$). This factor can be relatively easily determined for labelled samples for which a linear dependency of dye concentration and fluorescence intensity can be assumed (Szentesi et al., 2004, Trón et al., 1984), however for more complex samples and FP fusion proteins an approximation of α based on stochastic estimations (Nagy et al., 2005) or on intensity correlation (Bene et al., 2013) has to be used.

First trials with the software revealed the need of large sample sizes (number of cells) and relative long time for analysis in comparison to the method described above: The quantification of FRET demands a sophisticated strategy, which is accompanied by more complex and therefore more time consuming analysis compared to the qualitative approach described above. Still, it would be worth to test this method in future, especially due to the large number of cells that can be analysed in a short time of Flow Cytometry in comparison to FRET-FLIM.

3.2 Quantification of protein-protein interactions in live cells

3.2.1 Introduction to the methodology

The quantification of protein-protein interactions is important to get a complete description of the amount of protein in complex, the affinity of the interaction (K_d), its stoichiometry, as well as the identification of the interaction sites. These tasks remain challenging in live cells and FRET-FLIM approaches may be fully appropriate as they have the great advantage to provide information about the bound fraction and provide – due to the distance dependence of FRET – insights in the structure of the observed proteins (Becker, 2012, Padilla-Parra et al., 2011a).

We present here a mutual quantitative approach of FRET-FLIM and fluorescence wide-field microscopy to propose a complete overview of the interactions of the cytosolic subunits of the NADPH oxidase in live cell. We aim to elucidate the quantitative and structural properties of the complex such as the extent of proteins bound in complex and the affinity of the different interactions, as well as the molecular localization of the interaction.

While the bound fraction of donor interacting with acceptor could be directly extracted from the FRET-FLIM data, the determination of the affinity is more complicate. Indeed, in a test tube, this question is tackled by titrations: One partner is kept constant while the second partner is added successively. Thereby it is possible to follow the assembly of the protein with an appropriate method. Such an experiment gives a saturation curve: When the first partner is saturated with the second one, a plateau is reached. In live cell, the assembly can be followed via the apparent FRET efficiency measured by FLIM, which is proportional to the fraction of interacting proteins (paragraph 3.2.4). However, in cells neither a direct titration as in a test tube nor a change of the protein expression on demand is possible. Nevertheless, due to the variety of expression levels for both partners, it is possible to explore systematically FRET efficiencies for different ratios of the two proteins ($\frac{n_A}{n_D}$) and thus to obtain a saturation curve where each point will be the measurement for one single cell. A difficulty of this method is to find enough cells with different expression ratios – most of the cells gave only a small range of ratios and the possibilities of influencing the expression level are limited. Several options have been tested for the optimization of the transfection (go to paragraph 2.2.6 for details about this optimisation). Furthermore we were able to tune the expression ratio by varying the amount of DNA used for transfection.

An overview of the mutual FRET-FLIM wide field microscopy approach is given in Table 16 below. In the next paragraphs, it will be presented how each parameter was measured.

Method	measurement parameter	outcome
FRET-FLIM	<ul style="list-style-type: none"> apparent FRET efficiency molecular FRET efficiency 	<ul style="list-style-type: none"> fraction of donor bound to an acceptor structural information about the interacting partners
wide-field	<ul style="list-style-type: none"> donor and acceptor intensities 	<ul style="list-style-type: none"> relative amount of acceptor vs donor : molar ratio n_A/n_D(calibration based)
mutual approach		<ul style="list-style-type: none"> specificity of FRET molecular dissociation constant K_d

Table 16 Overview of the mutual FRET-FLIM-wide-field microscopy approach

3.2.2 Extraction of FRET parameters from fluorescence lifetime imaging microscopy data

A FLIM image was recorded with the TCSPC setup for cells expressing a subunit fused to the donor or two subunits each one fused to the donor or the acceptor (Figure 23 A). The fluorescence decay corresponding to the photons collected in the whole cytosol was constructed by the acquisition software (green, Figure 23 B).

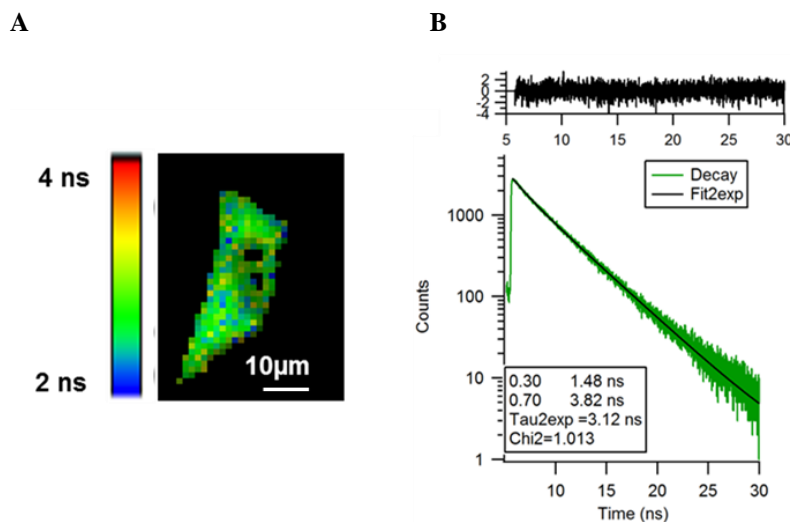


Figure 23 Data derived from FLIM

A) Lifetime image of a COS7 cell transfected with p47^{phox}-Citrine and p67^{phox}-mTurquoise.

B) top: residual distribution of the fit; bottom: Cumulative photon counts (green) over time after the excitation pulse fitted with a bi-exponential function (black).

The measured fluorescence decay was either fit with a mono-exponential fit function for cells expressing donor alone or cells which have a negligible FRET level (Equation 20) or with a

bi-exponential fit function for cells expressing both donor and acceptor, revealing FRET (Equation 21):

$$\text{Equation 20} \quad I(t) = \alpha_D \cdot e^{-(t-t_0)/\tau_D} + B$$

$$\text{Equation 21} \quad I(t) = \alpha_D \cdot e^{-(t-t_0)/\tau_D} + \alpha_{DA} \cdot e^{-(t-t_0)/\tau_{DA}} + B$$

t_0 is the time origine and B a constant that take in account the background level of photons. τ_D is the lifetime of the donor alone and τ_{DA} the one of the donor in presence of acceptor. α_D and α_{DA} represent the contribution of each exponential in the fluorescence decay. The goodness of the fit is evaluated by the residual distribution as shown in Figure 23 B (black curve on the top) and the Pearson's χ^2 test (perfect fit: $\chi^2 = 1$).

It is then possible to calculate the average lifetime of donor in presence of acceptor $\langle\tau_{DA}\rangle$, the apparent FRET efficiency, $E_{app.}$, and the fraction of donors bound to an acceptor, β :

$$\text{Equation 22} \quad \langle\tau_{DA}\rangle = \frac{\alpha_D\tau_D + \alpha_{DA}\tau_{DA}}{\alpha_D + \alpha_{DA}}$$

$$\text{Equation 23} \quad E_{app.} = 1 - \frac{\langle\tau_{DA}\rangle}{\tau_D}$$

$$\text{Equation 24} \quad \beta = \frac{\alpha_{DA}}{\alpha_{DA} + \alpha_D}$$

In addition, β is the proportional constant between the molecular FRET efficiency E_{mol} ($E_{mol} = 1 - \tau_{DA}/\tau_D$, Equation 11) and the apparent FRET efficiency $E_{app.}$

$$\text{Equation 25} \quad E_{app.} = \beta \cdot E_{mol.}$$

These parameters were calculated for each cell from the fluorescence decay with a good accuracy that can be deduced from the low dispersion of the experimental data.

3.2.3 Fluorescence intensity wide field microscopy

3.2.3.1 Determination of the donor and acceptor intensity

The CCD camera of our microscope setup allows the acquisition of wide-field intensity images of the same cells as studied with FLIM. The fluorescence intensity (I_{FP}) collected in each pixel of the images is the product of several parameters that can be gathered from Equation 26.

$$\text{Equation 26} \quad I_{FP} = P_{lamp}(\lambda_{ex}) \cdot K_{ex} \cdot K_{em} \cdot c_{FP} \cdot V_{obs} \cdot N_A \cdot \varepsilon(\lambda_{ex}) \cdot \Phi(\lambda_{em}) \cdot f(\lambda_{em})$$

The instrumental parameters are independent of the sample itself: The power of the lamp at the excitation wavelength, $P_{lamp}(\lambda_{ex})$, the device constants of the excitation K_{ex} (objective parameters – arising from the magnification, the numerical aperture and the transmission efficiency – and the wavelength selection filters), and the one of the emission K_{em} (comprising filters and the quantum efficacy of the CCD camera). K_{ex} and K_{em} do not a lot. Their major variation might be due to the aging of the excitation filters, which is checked regularly. In the contrary, we have observed that $P_{lamp}(\lambda_{ex})$ depends on the age of the mercury lamp and its alignment. The latter influences the homogeneity of the illumination in the field of view and is controlled and optimized several times a year. The power of the lamp is carefully monitored at the beginning of each experiment and the value is used in the data normalization (see below). In addition, in this conventional wide field microscopy setup there is no volume selection along the Z axis. It has been shown previously by the group that the fluorescence from the whole cell thickness is collected (Figure 25 A) (Alvarez, 2010).

As Equation 26 shows, I_{FP} depends also on the fluorescence properties of the FP: Their brightness, which is the product of molar extinction coefficient $\varepsilon(\lambda_{ex})$ and quantum yield $\Phi(\lambda_{em})$, and their emission spectrum $f(\lambda_{em})$.

Finally, I_{FP} contains the most interesting information for quantification: The number of FPs, N_{FP} (Equation 26), which is the product of its concentration c_{FP} , the Avogadro constant N_A , and the observation volume, V_{obs} .

In the following, the detailed procedure of the intensity measurement and normalization will be described.

First, pictures of the cell were taken for each channel (donor and acceptor). The volume of the cell from which photons are collected is V_{obs} . It depends on the size of the chosen region of interest (surface) and on the thickness of the cell (height).

We determined the height of 13 cells with their membrane tagged with MyrPalm-Aquamarine with a spinning disk microscope that allows a good resolution along the Z axis. For a complete

estimation of the cell volume, this experiment needs to be repeated. However, the measured thickness of the cell was rather homogeneous around the nucleus and decreased to the cellular edges (Figure 24). Even if it is not possible to measure accurately the whole cell volume, the observation volume has to be kept constant during the analysis. That is why we decided to calculate the fluorescence intensities in regions of interest around the nucleus and not in the whole cellular cytoplasm.

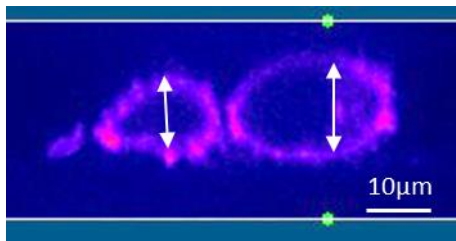


Figure 24 Estimation of the height of the cell

Picture of COS7 cells expressing membrane tagged Aquamarine, made with spinning disk microscope and reconstituted with *ImageJ* 3D volume viewer.

Consequently, in the first step of image analysis, five identical regions of interest (12*12 [pixel²]) were chosen inside the cell in the vicinity of the nucleus (as well as one for the background (25*25 [pixel²]) outside of the cells. The mean raw intensities of these regions of interest were calculated (*ImageJ*).

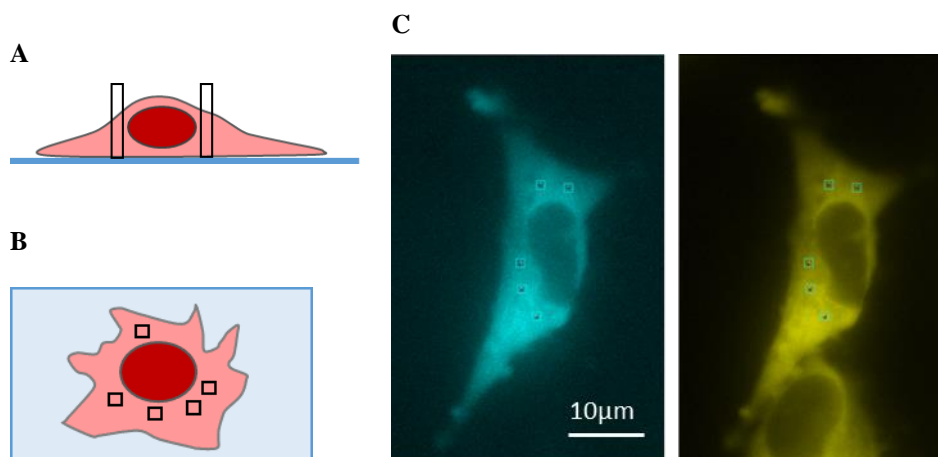


Figure 25 Fluorescence intensity is measured in regions of interest in the cell

Fluorescence intensity was measured in 5 regions of interest around the nucleus, where the volume is assumed to be approximately the same. Scheme of a cell with the five regions of interest as cross section (A) and from the top (B). (C): example of a cell, in CFP and YFP channel.

To make data from different cells and days comparable, it is necessary to normalize the measured fluorescence intensity with respect to:

- exposure time of each snap shot, $t_{exposure}$
- neutral density used to attenuate the excitation intensity in order to prevent photobleaching, $f(ND)$
- power of the lamp, $P_{lamp}(\lambda_{ex})$

The normalized intensity of the FP, $I(FP)$, is calculated from the measured intensity, I_{raw} , after subtracting the background, I_{BG} , as follows:

$$\text{Equation 27} \quad I(FP) = (I_{raw} - I_{BG}) \cdot \frac{1}{t_{exposure}[100 \text{ ms}]} \cdot \frac{1}{P_{lamp}(\lambda_{ex})} \cdot f(ND)$$

The excitation power arriving at the sample, $P_{lamp}(\lambda_{ex})$, depends on the lamp itself but also on optical devices (dichroic mirrors, band pass filters, ND filters) in the light pathway before the sample for each fluorescence channel. We used several ND filters to attenuate the power of the lamp in order to avoid photobleaching (Tramier et al., 2006) and pixel saturation of the CCD camera. These ND are positioned in a slider or in a wheel in front of the lamp. To abrogate the difference in excitation light power and to normalize ND filters to ND 0 (i.e. as if any ND filter would have been placed), the ND correction factors are used. In praxis, the power of the lamp was measured for each channel with all possible ND filter combinations, the ND correction factor $f(ND)$ is defined as the ratio of the power of the lamp with the attenuation of one filter, P_{ND_i} , divided by the power of the lamp without any attenuation (ND 0), P_{ND_0} , for each fluorescence channel (CFP, YFP and RFP):

$$\text{Equation 28} \quad f(ND)_{channel(x)} = \frac{P_{ND_i}}{P_{ND_0}}$$

Examples for the values of $f(ND)$ can be found in Table 17.

	YFP	CFP	RFP
ND 2.6	652	955	609
ND 1.9	82	91	88
ND 1.6	44	48	47
ND 1.1	13	14	14
ND 0.6	4	4	4.2

Table 17 Examples for the ND correction factor for different attenuations (ND filters) and different fluorescent channels

Finally, the values for the five regions of interest are averaged. The average value of $I(FP)$ for the acceptor can be plotted directly as $I(A)$. The average value of $I(FP)$ for the donor, $I(D)$, must be corrected from FRET if it occurs, since the intensity of the donor is decreased due to the energy transfer to the acceptor. The corrected donor intensity $I^*(D)$ is defined as

$$\text{Equation 29} \quad I^*(D) = \frac{I(D)}{1 - \frac{E_{app.}}{100}}$$

This careful normalisation of fluorescence intensities allow the comparison of data sets acquired at different days but also to set limits for $I(A)$ and $I^*(D)$. Indeed, if $I^*(D)$ is too low, the contribution of cellular auto-fluorescence may be unneglectable (Ishikawa-Ankerhold et al., 2012, Becker, 2012). The main consequence of this contamination is a decrease of the donor lifetime as auto-fluorescence is usually characterised by short lifetimes. If $I(A)$ is too high, there is some proximity FRET derived from the proximity of acceptors in large excess. This adds to the FRET due to the specific interactions (Grailhe et al., 2006, Fábíán et al., 2010, Zacharias et al., 2002). To exclude these misleading influences, an intensity-based thresholds were settled with controls. For more details, go to appendix 8.2.

3.2.3.2 Determination of the ratio of the amount of acceptor/donor

With wide field fluorescence microscopy it is not possible to calculate the concentration of the FPs expressed in the cell directly from the fluorescence intensities as the cellular volume is not known. Nevertheless, the relative expression level of the subunits, which is equivalent to the ratio of the amount of acceptor over donor, is proportional to the ratio of their fluorescence intensities $\left(\frac{n_A}{n_D} \propto \frac{I(A)}{I^*(D)}\right)$. An external calibration using solutions of purified fluorescent proteins allows the calculation of the coefficient of proportionality between $\frac{I(A)}{I^*(D)}$ and $\frac{n_A}{n_D}$. Indeed, in this ratiometric approach, the observation volume is the same for acceptor and donor, either in the cell or in the 50 μ L droplet of purified FP solutions used for calibration. The coefficient of proportionality – or calibration factor as it will be called in the following – includes the instrumental factor $K_{ex} \cdot K_{em}$ and the FP dependant factor $\varepsilon(\lambda_{ex}) \cdot \Phi(\lambda_{em}) \cdot f(\lambda_{em})$ from Equation 26. The detailed procedure will be described here.

Serial dilutions of all FPs with known concentration (verified by spectrophotometry) were prepared. A droplet (50 μ l) of such a solution was placed on a glass cover slip (Figure 26) in a chamber. It was covered by a second cover slip to avoid evaporation, which would lead to an increased protein concentration. Intensity pictures were taken for each neutral density filters (ND 0/0.5/1.0/1.3/2.0) for each protein concentration.



Figure 26 Droplet of purified protein

Serial dilutions of known concentrations of FPs were prepared and the fluorescence intensities were measured. The illuminated volume (yellow) is in the centre of the drop.

From these pictures, the mean intensity of the whole field of view was taken in account and normalized by dividing by the power of the lamp (measured on a daily basis for each fluorescence channel) and the exposure time. The normalized intensity is expressed in [counts/mW/s] and is plotted against the protein concentration. A linear fit function (with an intercept set to 0) was calculated for each neutral density series (Figure 27).

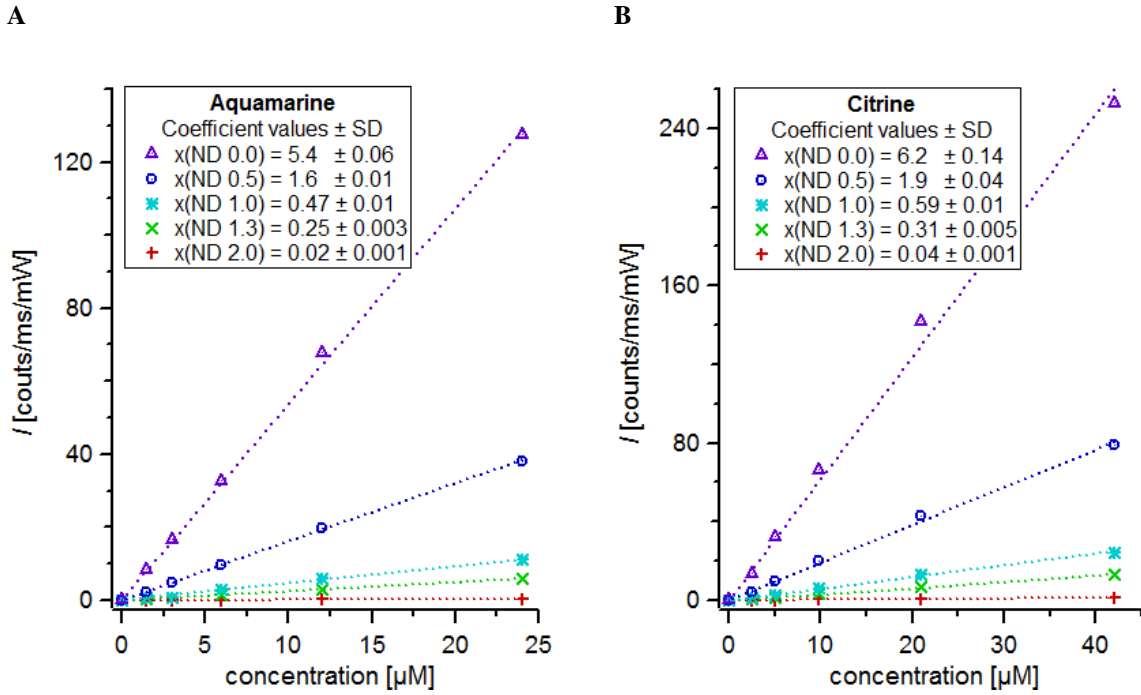


Figure 27 Calibration curves of purified FPs for the discrimination of the calibration factor $f\left(\frac{A}{D}\right)$, shown on the example of Aquamarine and Citrine

Serial dilutions of known concentrations of Aquamarine (A) and Citrine (B) were prepared and their fluorescence intensity was measured with the FRET-FLIM microscope set up with different attenuations (ND filters). The normalized fluorescence intensity is plotted against concentration, the single series were fitted with a linear fit function.

The slopes of the acceptor curves were divided by the slopes of the corresponding donor curve for each ND. The obtained ratios were averaged and gave the calibration factor $f\left(\frac{A}{D}\right)$, Equation 30. In some cases, the slopes for extreme ND (0 or 2.0) had to be excluded.

$$\text{Equation 30} \quad f\left(\frac{A}{D}\right) = \left\langle \frac{\text{slope}(A)_{ND_i}}{\text{slope}(D)_{ND_i}} \right\rangle$$

The ratio of the amount of acceptor/donor $\frac{n_A}{n_D}$ in cells can be calculated from the ratio of acceptor intensity ($I(A)$) to corrected donor intensity ($I^*(D)$) by dividing by the calibration factor:

$$\text{Equation 31} \quad \frac{n_A}{n_D} = \frac{I(A)}{I^*(D)} \cdot \frac{1}{f\left(\frac{A}{D}\right)}$$

The ratio $\frac{n_A}{n_D}$ reflects the stoichiometric ratio of the cellular expression level of the co-expressed subunits.

3.2.4 Extraction of the quantitative data and specificity of the interaction

To give an example, we will focus in this paragraph on the interaction between C-terminal tagged p47^{phox} and p67^{phox} using the Aquamarine / Citrine FRET couple. The apparent FRET efficiency is first plotted against the intensity of the acceptor for each cell in a range devoid of proximity FRET (Figure 28 A). A significant FRET ($E_{app.} = 12\%$) reveals a specific protein-protein interaction clearly above the negative control, which is more scattered and varies between $E_{app.} = 0 - 5\%$. The intensity plot can also point out changes in the interaction or confirmation due to modifications in the protein (cleavage, mutations etc.) or chemical treatment. In the sample shown here the cleavage of the potential interaction site of p47^{phox} (p47^{phox}ΔC) results in a complete loss of any specific FRET.

The apparent FRET efficiency and the bound fraction was plot against this ratio $\frac{n_A}{n_D}$ (Figure 28 B) and fitted with a saturation curve (Equation 32). This fitting curve is our approximation to a test tube titration curve as described in paragraph 3.2.1.

$$\text{Equation 32} \quad E_{app} \left(\frac{n_A}{n_D} \right) = \frac{E_{app,max} \cdot \frac{n_A}{n_D}}{C + \frac{n_A}{n_D}} \quad \text{or} \quad \beta \left(\frac{n_A}{n_D} \right) = \frac{\beta_{max} \cdot \frac{n_A}{n_D}}{C + \frac{n_A}{n_D}}$$

with the maximum apparent FRET efficiency $E_{app,max}$, and the value C of $\frac{n_A}{n_D}$ corresponding to $\frac{E_{app,max}}{2}$.

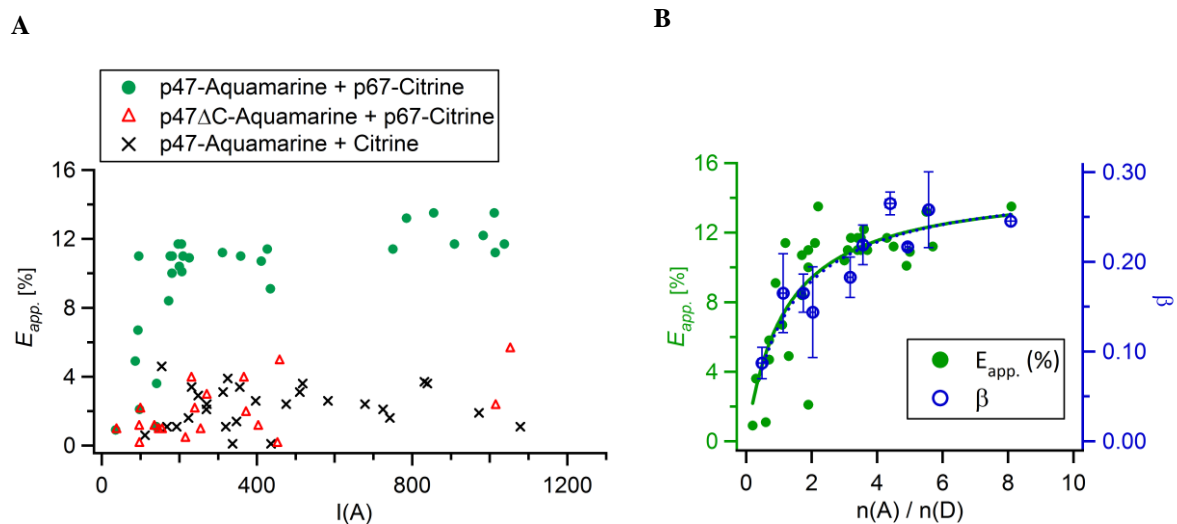


Figure 28 FRET by FLIM confirms specific CC-terminal interaction between p47^{phox} and p67^{phox}

A: The intensity plot shows a FRET level of around 12 % of p47^{phox} co-expressed with p67^{phox} in contrast to the low FRET levels of the negative control (p47^{phox} co-expressed with FP). Truncated p47^{phox} (p47^{phox} Δ C) co-expressed with p67^{phox} shows the same FRET efficiency as the negative control.

B: The ratio plot of p47^{phox} and p67^{phox} reveals a dependency of the apparent FRET efficiency and the ratio of the amount of protein, which describes a saturation curve (green). The bound fraction β is perfectly in line, and reaches a plateau around 25 %.

The successful fit confirms the specificity of the interaction: With rising amount of acceptor (p67^{phox}) to donor (p47^{phox}), the E_{app} increases until a plateau is reached, i.e. even with higher ratios, the donor fusion protein (p47^{phox}) will not bind more acceptor fusion protein (p67^{phox}). For each cell the fraction of donor bound to an acceptor has been calculated (Equation 24). The values for cells with similar $\frac{n_A}{n_D}$ ratio have been averaged and the corresponding SDs were added. Surprisingly, only around 25 % of the donor is bound when saturation is reached (Figure 28 B). This means that the majority of the subunits labelled with a donor are free instead of being bound in complex. The fitting curve of the bound fraction is perfectly aligned with the one of the E_{app} . (as expected from the theoretical background, compare Equation 25).

The exchange of the position of the donor and acceptor on the subunit (p47^{phox}-Aquamarine + p67^{phox}-Citrine versus p67^{phox}-mTurquoise + p47^{phox}-Citrine) gave similar results (Figure 29).

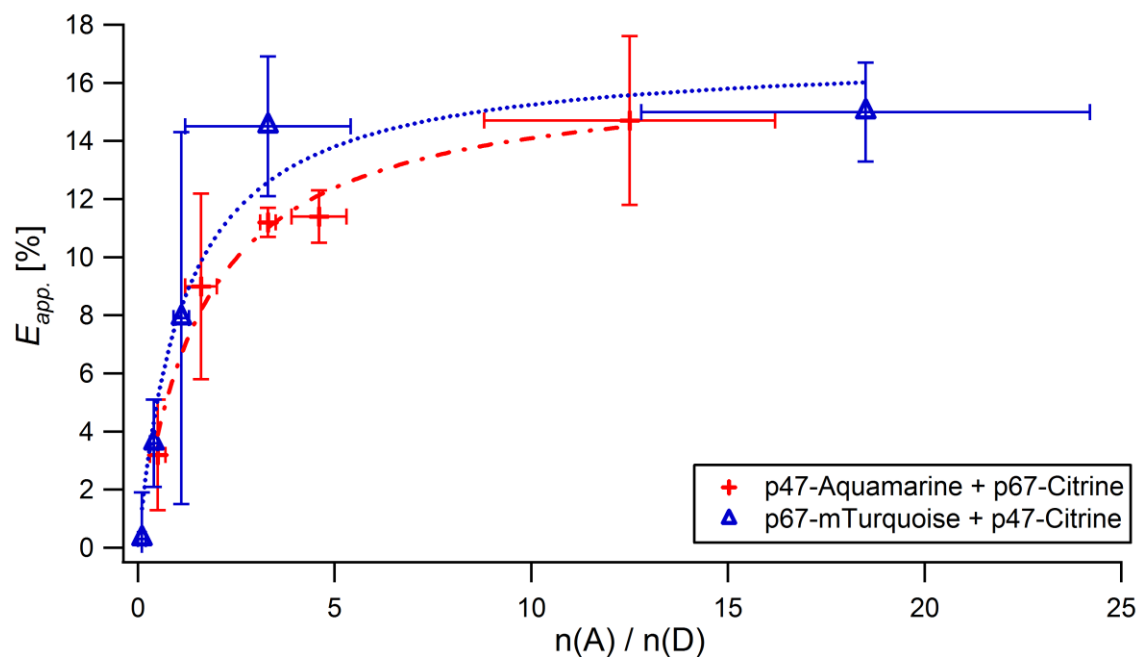


Figure 29 FRET by FLIM: Influence of the label on the results of p47^{phox} – p67^{phox} interaction

The position of donor and acceptor was exchanged on p47^{phox} and p67^{phox}. Each point represent several cells ($n \geq 4$) with similar expression levels. Data presented mean \pm SD ($n_{\text{total}}(\text{P47}^{\text{phox}}\text{-Aquamarine} + \text{p67}^{\text{phox}}\text{-Citrine}) = 35$; $n_{\text{total}}(\text{p67}^{\text{phox}}\text{-mTurquoise} + \text{p47}^{\text{phox}}\text{-Citrine}) = 47$).

In Figure 30, the lifetimes of the donor (τ_D and τ_{DA}) extracted from the bi-exponential fit (Equation 21) of cells co-expressing donor and acceptor each bound to a cytosolic subunit (p47^{phox}-Aquamarine + p67^{phox}-Citrine or p67^{phox}-mTurquoise + p47^{phox}-Citrine in Figure 29) are plotted. As references, the lifetime of mTurquoise and Aquamarine, each mono-expressed in cells and fitted with the mono-exponential fit function (Equation 20), were added.

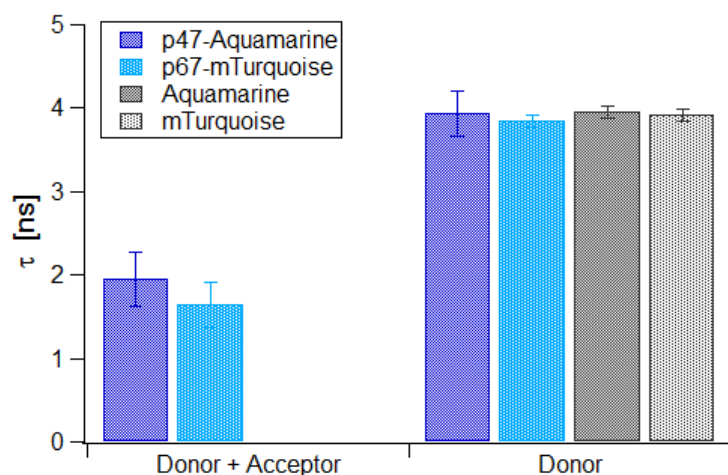


Figure 30 Two lifetimes of the donor derived from the bi-exponential fit of cells co-expressing donor and acceptor:

Short lifetime of the donor (p47^{phox}-Aquamarine, dark blue; p67^{phox}-mTurquoise, light blue) bound to the acceptor (p67^{phox}-Citrine, p47^{phox}-Citrite respectively), and the long lifetime of corresponding the free donors are plotted. As a control the lifetime of Aquamarine (dark grey), mTurquoise (light grey), are derived from a mono-exponential fit. (mean ± SD; n ≥ 7, days ≥ 2) p47^{phox} Aquamarine: 1.94 ± 0.33 [ns] and 3.94 ± 0.27 [ns] (student t-test p = 0.0004) ref. Aquamarine: 3.95 ± 0.07[ns] p67^{phox}-mTurquoise: 1.65 ± 0.27 [ns] and 3.85 ± 0.08 [ns] (student t-test p = 0.0003) reference mTurquoise: 3.91 ± 0.08 [ns].

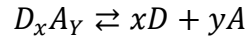
The long lifetime, τ_D , of p47^{phox}-Aquamarine and p67^{phox}-mTurquoise are not significantly different from their reference value while the short lifetimes (τ_{DA}) are significant decreased. In addition those lifetimes allow the computation of the molecular FRET efficiencies. For C-C terminal tagged p47^{phox} and p67^{phox}, an $E_{mol.}$ between 52 – 58 % was found^{xxv}.

Both, the perfect alinement of the two saturation curves ($E_{app.}$ or β as a function of $\frac{n_A}{n_D}$) and the equivalence of the lifetime of the free donor, support the consistency of the quantitative approach.

^{xxv} p47^{phox}-Aquamarine + p67^{phox}-Citrite 52 ± 8 [%]; p67^{phox}-mTurquoise + p47^{phox}-Citrite 58 ± 7 [%]

3.2.5 Estimation of the dissociation constant K_d

The dissociation constant gives information about the affinity of two binding partners at the equilibrium:



With the concentration of D, A and $D_x A_y$ at the equilibrium, the dissociation constant K_d can be defined as follows:

$$\text{Equation 33} \quad K_d = \frac{[D]^x \cdot [A]^y}{[D_x A_y]}$$

Here, a stoichiometry of 1 : 1 ($x, y = 1$) is assumed, as *in vitro* studies (Groemping and Rittinger, 2005) and our negative homo-dimerization (4.2.1.4) results indicate.

In transiently transfected cells expressing various levels of FP tagged subunits, the concentration measurement is tricky as it was explained in the previous paragraphs. Therefore, we rewrite the formula as an expression of the fraction of donor bound to an acceptor β derived from the bi-exponential fit of the fluorescence decay, $\frac{n_D}{n_A}$ derived from the wide-field images, and the total acceptor concentration $[A]_{tot}$. For the detailed derivation of Equation 34 go to annex 8.3.

$$\text{Equation 34} \quad K_D = \frac{(1-\beta)}{\beta} \cdot \left(1 - \beta \frac{n_{D,tot}}{n_{A,tot}}\right) \cdot [A]_{tot}$$

For each cell, $\frac{(1-\beta)}{\beta} \cdot \left(1 - \beta \frac{n_{D,tot}}{n_{A,tot}}\right)$ has been calculated and an averaged value was calculated. $I(A)$ is proportional to $[A]_{tot}$ and from Figure 28 we know that there is roughly a factor of 10 from the palest to the brightest cells (from 100 cps to 1000 cps approximatively). The total acceptor concentration needs to be approximated. It can be estimated from concentrations derived by FCCS, since its data contain information about the fluorophore concentration (compare paragraph 2.2.11). FCCS demands a very low fluorophore concentration^{xxvi}, in comparison the concentrations needed for FRET-FLIM are higher, since a minimum amount of counts is needed to overcome a significant contribution of auto-fluorescence. The concentrations found in FCCS experiments were between 0.1 – 0.6 μM . As an approximation we assumed a value for $[A]_{tot}$ between 1 – 10 μM for the FLIM measurements. This value is also in agreement with the concentration usually assumed in cells expressing FPs in fusion with proteins (Grailhe et al., 2006). For the interaction between p47^{phox} and p67^{phox}, both C-terminal tagged, K_d values around 4 – 40 μM were found (Table 20).

^{xxvi} since the relative fluctuation becomes bigger with decreasing number of fluorophores (compare Equation 14)

The workflow presented in this paragraph 3.2 has been followed for all the interactions probed by FRET-FLIM. Results are presented in paragraph 4.2. Therein, the results for the interaction between C-terminal tagged subunits p47^{phox} and p67^{phox} already presented in this paragraph, will be summarized to have a complete overview of the interactions in the same chapter.

4 Results – Interactions between NADPH oxidase subunits

This chapter is organized as follows: It starts with proving of the functionality of the proteins expressed by the COS7 cells: In a first step, the size of the proteins is verified; in a second step the preserved ability of the tagged subunits to translocate to the plasma membrane and to successfully reconstitute the active NADPH oxidase complex upon stimulation is shown. The successfully proven maintained functionality of the subunits give the green light for the main study – the qualitative and quantitative analysis of the hetero- and homo-dimeric interactions of the subunits in live cells investigated by FRET-FLIM and FCCS.

4.1 Proving functionality of the cytosolic subunits

4.1.1 Verification of the size of the expressed protein by Western Blot

It is important to ensure that the proteins expressed by the cells have their full length and the right size, as well as to know whether free FPs are expressed, which would, in the case of the donor, influence the FRET by FLIM and FCCS results. Therefore, western blots (WB) of the major proteins used in this project were made with anti-FP staining. We used anti-GFP in case of tagged p67^{phox} and p47^{phox} tagged with either Citrine or mTurquoise and anti-DsRed in case of mCherry-p40^{phox} and a specific antibody against the subunits anti-p67^{phox} /-p47^{phox}/ -p40^{phox}.^{xxvii} Examples of the WB are shown in Figure 31 – Figure 34. To facilitate the understanding, Table 18 gives an overview published sizes of the FPs and the subunits ± FP tag. As described in chapter 2.2.7, the size of the protein was assigned from a protein standard, as well as the relative contribution of one peak to the sum of the peaks of one row (compare Equation 12), which allows an estimation of the amount of protein with a specific size.

The anti-GFP staining was performed in order to determine the size of p67^{phox}-mTurquoise, mTurquoise-p67^{phox}, and p47^{phox}-Citrine as well as to estimate the amount of free FP, if present.

p67^{phox} anti-GFP staining

The C-terminal tagged p67^{phox} (p67^{phox}-mTurquoise) revealed two bands with a major one (70 %) with 90 kDa and a minor one with 56 kDa (30 %) (Figure 31 A). The major band is in good agreement with the literature, where a band around 100 kDa was found (p67^{phox}-Citrine^{xxviii}, same linker) (Tlili et al., 2012). The second band is most probably a degradation product of p67^{phox}-mTurquoise. There is a light smear around 25 kDa (where free

^{xxvii} Table 8 (chapter 2.2.7) gives an overview about the number of WB done in each conditions

^{xxviii} no difference in terms of size and mass of mTurquoise and Citrine

FPs are expected), for which it is hard to determine the size and the quantity, so the amount of free FPs was judged to be negligible.

The WB of the N-terminal tagged p67^{phox} (mTurquoise-p67^{phox}) reveals a major band (97 %) with 88 kDa and a very pale one (3 %) at 39 kDa (Figure 31 B). The first band is in line with the major band of the positive control (100 kDa, purified mTurquoise-p67^{phox}, obviously slightly degraded)^{xxix}. There is no band occurring at the same size of mTurquoise, as a comparison with the positive control (purified mTurquoise) confirms. The main band matches perfectly with the results obtained for p67^{phox}-mTurquoise, which is in line with the expectation that C- and N-terminal tagged p67^{phox} have the same size.

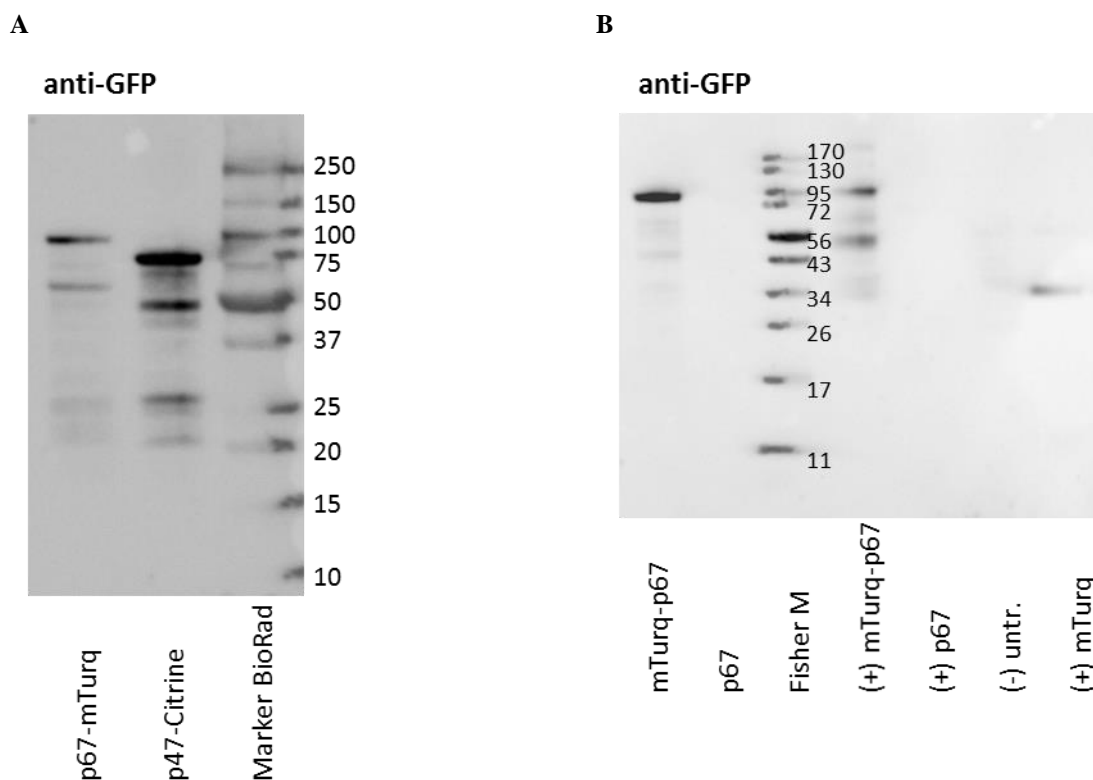


Figure 31 WB anti-GFP

A: p67^{phox}-mTurquoise and p47^{phox}-Citricine reveal several bands, the major band is at 90 kDa for the first one and 72 kDa for the latter one.

B: Samples (cell lysates from transfected COS7 cells) are blotted on the left hand side of the marker, controls right hand side (positive controls: purified proteins, negative control untransfected COS7 cells); mTurquoise-p67^{phox} reveals a main band at 88 kDa which is in line with the positive control (purified mTurquoise-p67^{phox}, 100 kDa), and no band at the size of mTurquoise alone (control positive, purified protein, 26 kDa). P67^{phox} does not appear in the anti-GFP blot.

^{xxix} The difference between control and sample is most likely coming from the assignment of the software, visually, the two bands are running at the same position.

p67^{phox} – anti-p67^{phox} staining

For the C-terminal tagged p67 (p67^{phox}-mTurquoise) and p67^{phox}, a separate blot with anti-p67^{phox} staining was prepared (Figure 32 A): Three bands were found for p67^{phox}-mTurquoise, the major one reveals at 98 kDa (81 %) and the minor ones exhibit at 70/63 kDa (14/5 %). The light band at 70 kDa may be p67^{phox} missing the FP tag (running approximately at the same level as the main band of p67^{phox} (71 kDa, 77 %) and the major band of the (already degraded) positive control, i.e. purified p67^{phox}, 76 kDa). The lane of the untagged p67^{phox} exhibits two bands, a major one (77 %) at 71 kDa (as mentioned above) and a minor one at 36 kDa (23 %). The prominent band is running at the same level as the positive control (76 kDa), the small one is most probably a degradation product due to sample preparation, since it is not found on the 2nd anti-p67^{phox} blot (Figure 32 B).

The WB of the N-terminal tagged p67^{phox} (mTurquoise-p67^{phox}, Figure 31 B) was stripped^{xxx} and re-stained with anti-p67^{phox} AB (Figure 32 B). The band for mTurquoise-p67^{phox} reappeared (84 kDa, 100 %), which is again in line with the positive control (purified mTurquoise-p67^{phox}, 92 kDa, 100 %). For p67^{phox} a single band occurred with 68 kDa (100 %) as well as for its positive control (purified p67^{phox}, five bands identified, most prominently a double band at 70/67 kDa, 48/45 %, respectively). These findings are in good agreement with values from literature around 65 – 68 kDa (DeLeo and Quinn, 1996) and 75 kDa (Tlili et al., 2012).

To sum up the results of the p67^{phox} constructs, for the most part the right size of the protein was found.

^{xxx} The successfulness of the stripping was tested (compare chapter 2.2.7). Directly visibly, the band of purified mTurquoise vanished.

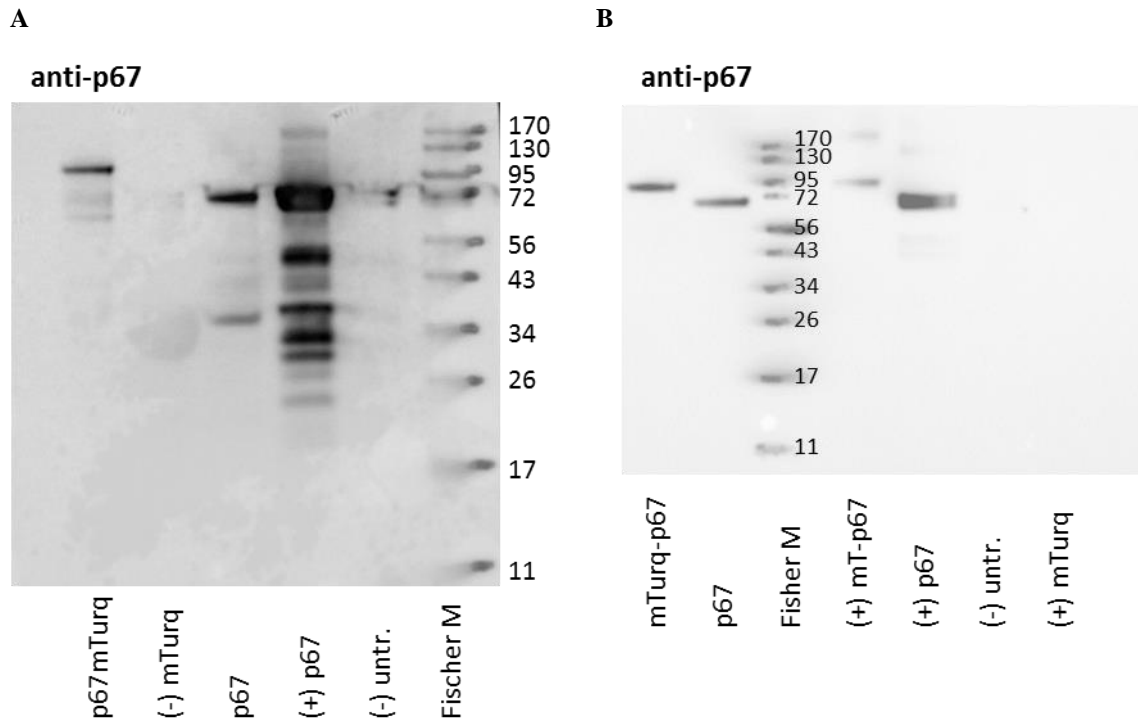


Figure 32 WB anti-p67^{phox}

A: p67^{phox}-mTurquoise from transfected COS7 cells exhibits three bands (98/70/63 kDa), p67^{phox} two (71/36 kDa), and the positive control ((+) p67^{phox} = purified human p67^{phox}) several with a main one around 76 kDa

B: mTurquoise-p67^{phox} gives a single band at 84 kDa, p67^{phox} one at 68 kDa, and the positive controls (purified proteins) one at 92 kDa (mTurquoise-p67^{phox}) and two at 70/67 kDa (p67^{phox}). Redeveloped WB after stripping (compare Figure 31 B)

p47^{phox} – anti-GFP staining

P47^{phox}-Citrine reveals five bands of which the most prominent is occurring at 72 kDa (60 %), which is in line with findings from the literature (around 75 kDa, same linker) (Faure et al., 2013). The other four bands appear at 63 kDa (9 %), 48 kDa (15 %), 26 kDa (13 %), and 20 kDa (2 %), whereby it is likely that the band at 26 kDa is free Citrine, the other bands are most probably degradation products of p47^{phox}-Citrine.

p47^{phox} – anti-p47^{phox} staining

P47^{phox} and p47^{phox}-Citrine WBs were stained with an anti-p47^{phox} AB, whereas the results for p47^{phox}-Citrine are preliminary (Figure 33 A). This plot was performed only once to this time point and is not optimized with respect to the amount of loaded protein, ending in an uneven brightness of the different samples. For this reason, p47^{phox} had to be covered to allow the development of p47^{phox}-Citrine both as sample (cell lysate) and positive control (purified p47^{phox}-Citrine). However, the WB reveals four bands for the sample, two equal ones at 74 kDa (33 %) and 55 kDa (38 %) and two minor ones at 35/30 kDa (14/16 %). The positive control

give similar results for band 1, 2, and 4 (83/52/33 kDa, 15/49/11 %) and an extra band at 46 kDa (25 %). A conclusion may be, that the first band refers to the full length p47^{phox}-Citrine and that the band around 52 – 55 kDa is the major degradation product: Since both sample and control show this band and the anti-GFP staining reveal a band with similar size (48 kDa), it is less likely to be p47^{phox} expressed without FP tag.

The blot of p47^{phox} stained with anti-p47 shows three bands, a prominent at 51 kDa (88 %) and two light bands at 23/21 kDa (10/2 %). The major bands of p47^{phox} and p47^{phox}-Citrine are in line with the values around 45 kDa and 75 kDa, respectively derived from literature (same staining, same linker in case of p47^{phox}-Citrine) (Faure et al., 2013).

Summarizing the results of the p47^{phox} constructs, we found the majority of the cases the respect proteins at the expected size.

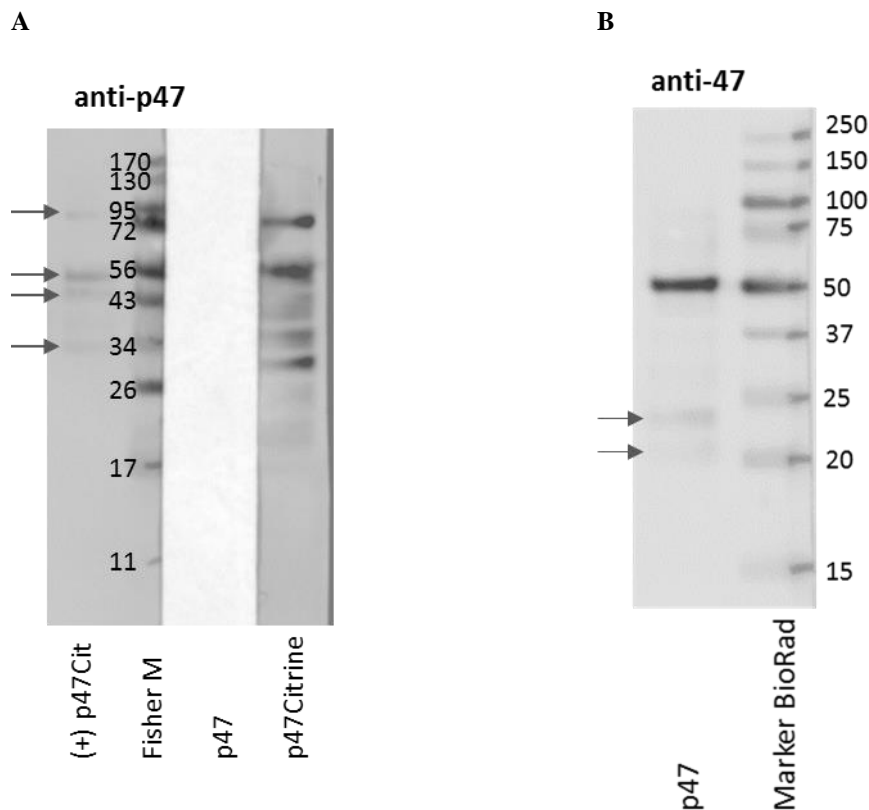


Figure 33 WB anti-p47^{phox}

A: First results exhibit a light bands for the positive control at 83/52/46/33 kDa and several bands for p47^{phox}-Citrine (74/55/35/30 kDa); annotation: p47^{phox} was covered since it was too bright to allow an analysis of the other two samples

B: Anti-p47^{phox} staining gives a major band for p47^{phox} at 51 kDa

p40^{phox} – anti-DsRed staining

P40^{phox} and mCherry-p40^{phox} were also stained against its FP (anti-DsRed) and anti-p40^{phox} (Figure 34). MCherry-p40^{phox} anti-DsRed-staining show a very strong band at 69 kDa (approx. 100 %). The very light smear/bands below were judged to be negligible. Another blot with mCherry-p40^{phox} stained against p40^{phox}, however, reveals four bands, two large ones around 75/65 kDa (57/27 %) and two inferior ones (57/41 kDa, 3/13 %). It is well-known that mCherry easily fragments during the heat denaturation step of the sample preparation (37 kDa → 15 kDa + 22 kDa)^{xxxix} (Gross et al., 2000, Shaner et al., 2004). Assuming this fragmentation, three bands at 77/62/55 kDa are expected for the labelled p40^{phox}, which fits with the three first bands we found. The band at 41 kDa may refer to p40^{phox} without FP tag, it runs at the same level as the p40^{phox} lysat, which in turn is in line with values found in the literature (around 40 kDa (Ueyama et al., 2011)).

p40^{phox} – anti-p40^{phox} staining

P40^{phox} gives only a single band at 42 kDa^{xxxix}. The band of mCherry (37 kDa, comparable with values from the literature (Schiller et al., 2013, Gross et al., 2000)) is false positive, perhaps due to an extreme protein-overload, which was not completely blocked and allows the unspecific binding of the AB.

The p40^{phox} constructs reveal – like the other subunits – the majority of the proteins at the right size.

^{xxxix} hydrolysis of an acylimine group, a double which is present in DsRed and its derivatives (like mCherry) but not in GFP and its derivatives

^{xxxix} To develop p40^{phox} better, the very bright bands of the first row were covered, which circumvent the relative scaling of the picture brightness by the camera. Still, only one band was found

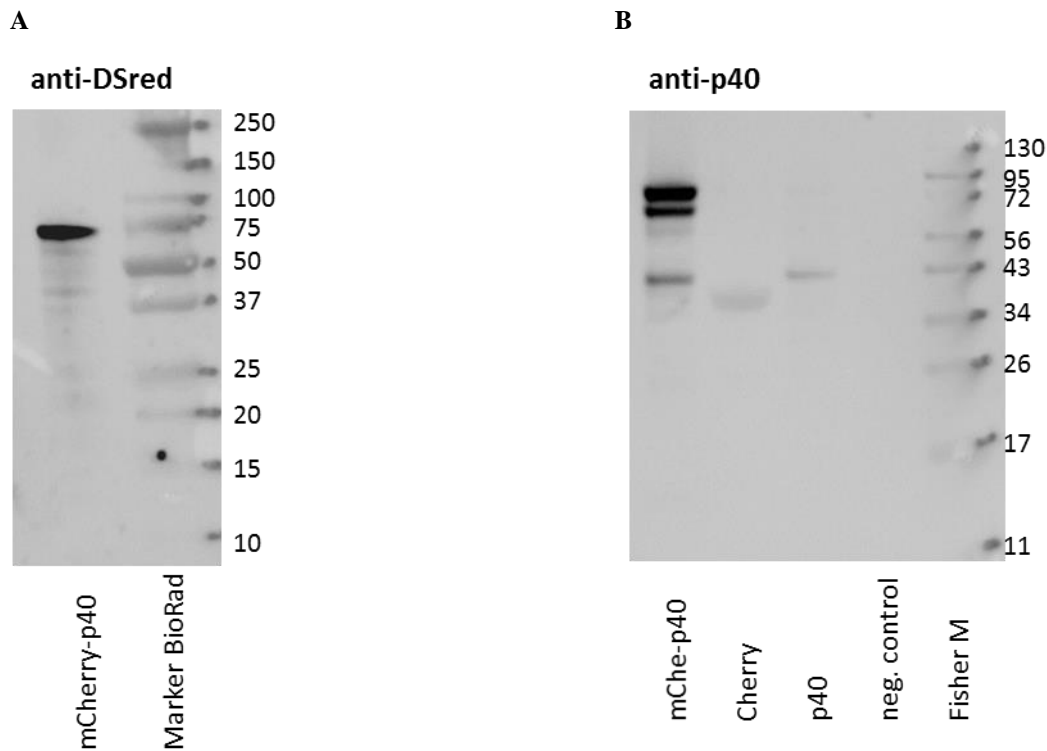


Figure 34 WB of p40^{phox} ± mCherry 0

A: Anti-DsRed staining of mCherry-p40^{phox} exhibits a very prominent band with 69 kDa.

B: Anti-p40^{phox} staining reveals three bands (75/65/41 kDa) for mCherry-p40^{phox} and one band (42 kDa) for p40^{phox}

An overview of the WB results is given in Table 19. To summarize the outcomes, in the majority of the cases the protein was found with the right size in a reasonable percentage sometimes in company of a minor amount of degradation products. In three cases (p47^{phox}-Citrine, p67^{phox}-mTurquoise, and mCherry-p40^{phox}), the expression of free FPs (in the first case) or without FPs (in the two latter cases) cannot be excluded, though. Concerning p67^{phox}-mTurquoise, it is likely that the too small band is caused by degradation during sample preparation, since no free FP was found in the anti-GFP blots. In case of p47^{phox}-Citrine and mCherry-p40^{phox} it is still possible, that the shorter bands may come from degradation during sample preparation: The lack of both promotor and the Kosak-consensus-sequence^{xxxiii} in its direct vicinity makes the expression of the C-terminal part of the fusion proteins less probable. Thus we assume that all constructs are expressed with the right size.

^{xxxiii} important for the initiation of the translation process

protein	- FP [kDa]	+ FP [kDa]
Aquamarine, mTurquoise, Citrine	-	27 [*]
mCherry	-	37 ⁺
p67 ^{phox}	75 [†]	100 [†]
p47 ^{phox}	45 [‡]	75 [‡]
p40 ^{phox}	40 [◇]	n/a

Table 18 Overview of the apparent sizes of the FPs and the subunits ± FP tag

^{*} anti-GFP antibody suppliers instructions, Roche Diagnostics; ⁺ (Gross et al., 2000, Schiller et al., 2013); [†] (Tlili et al., 2012); [‡] (Faure et al., 2013); [◇] (Ueyama et al., 2011)

protein	anti-FP		anti-subunit [%]	
	size [kDa]	proportion [%]	size [kDa]	proportion [%]
p67 ^{phox} -mTurquoise	90	70	98 (70, without FP?)	81 (14)
mTurquoise-p67 ^{phox}	88	97	84	100
p67 ^{phox}	-	-	68	100
p47 ^{phox} -Citrine	72 (26, free FP?)	60 (13)	74	33 (preliminary)
p47 ^{phox}	-	-	51	88
mCherry-p40 ^{phox}	69	100	75/65/57* (41, without FP?)	87 (together) (14)
p40 ^{phox}	-	-	42	100

Table 19 Overview Western Blots

Correctly sized band [kDa] and its contribution as the proportion [%] of all bands in the same lane (compare Equation 12). The occurrence of free FPs or subunits without FPs are mentioned in brackets.

*mCherry degraded partly during sample preparation, leading to three bands of mCherry-p40^{phox}

4.1.2 Verifying the activatability of the complex

The FP may have an influence on the protein with which it is fused: Due to its size of around 27 kDa, steric hindrance may affect folding, function or targeting of the fusion protein (Snapp, 2005, Sahoo and Schwille, 2011). Therefore, it is necessary to verify that the tagged cytosolic proteins are still capable to assemble correctly and form an active enzyme. Those experiments have been performed in COS^{gp91^{phox}, p22^{phox}} cells stably transfected with the membranous subunits and constitutively expressing the GTPase, Rac (Price et al., 2002). We first probed the membranous localisation of the tagged subunits in triple transfected cells upon activation by a soluble stimuli (PMA). The presence of each subunit on the cell membrane was studied with TIRF microscopy. The advantage of this method is the small illumination depth around 0.1 – 0.2 μm allowing the collection of the fluorescence emission mainly originated from the direct vicinity of the cell membrane and not from the cytosol (4.1.2.1). The activity itself was probed by a luminometry assay, which allows the measurement of the production of superoxide anions upon activation. This experiment aims to prove that protein-protein interactions between the three tagged cytosolic subunits and the membranous ones are sufficiently strong to maintain a sustained ROS production (4.1.2.2).

4.1.2.1 Tracking the arrival of the complex on the membrane

The TIRF experiment was performed with different tag positions on p67^{phox} and p47^{phox} and N-terminal tagged p40^{phox}:

- p67^{phox}-mTurquoise + p47^{phox}-Citrine + mCherry-p40^{phox} (CCN-tagged sample)
- p67^{phox}-mTurquoise + Citrine-p47^{phox} + mCherry-p40^{phox} (CNN-tagged sample)
- mTurquoise-p67^{phox} + Citrine-p47^{phox} + mCherry-p40^{phox} (NNN-tagged sample)

The results for the three samples are similar. As an example, the intensity pictures of one CNN transfected cell are shown in Figure 35 for timepoint 0.5 min (top), 15 min (2nd line), and 21.5 min (3rd line) after activation with 190 nM PMA. The mTurquoise fluorescence seems to be derived from a slightly deeper observation volume and hence including more cytosolic emission than it is the case for Citrine and mCherry. Indeed, the penetration depth of the illumination light of the TIRF microscope depends on incident illumination angle, the refractive index^{xxxiv}, and the wavelength. As a consequence the angle has to be adapted for each wavelength to reach the same penetration depth. However, it was not possible to change it during the recording of the time series, since one photo for each channel was taken at every

^{xxxiv} The refractive index itself is as well wavelength dependent.

time point. Therefore, the chosen incident illumination angle is a compromise for the three wavelengths, leading to slightly different penetration depths.

15 min after activation, minor changes in the shape of the cell (less lamellipodia) were observed. For the blue tagged p67^{phox} a remarkable gain in intensity – most prominently on the membrane – and the shadow of the nucleus become visible after 15 min. In contrast, the pictures of p47^{phox} and p40^{phox} show only slight rises in intensity. Around 20 min, the pictures for the three colours are similar: An inhomogeneous distribution of intensity is shown, whilst the edges of the membrane are especially bright (this effect is stronger for p47^{phox} and p40^{phox} than for p67^{phox}, though).

The intensity profiles of the cross section of one edge of this cell (Figure 35, bottom line) makes these changes more clear, since it shows the concerted gain of intensity around 15 min after activation with similar pattern (biased gain of intensity on the edge of the cell 19.5 min after activation) for p47^{phox} and p40^{phox}. However, p67^{phox} shows from the beginning a rise in intensity, as well as a stronger gain on the edge of the cell and finally a loss of intensity.

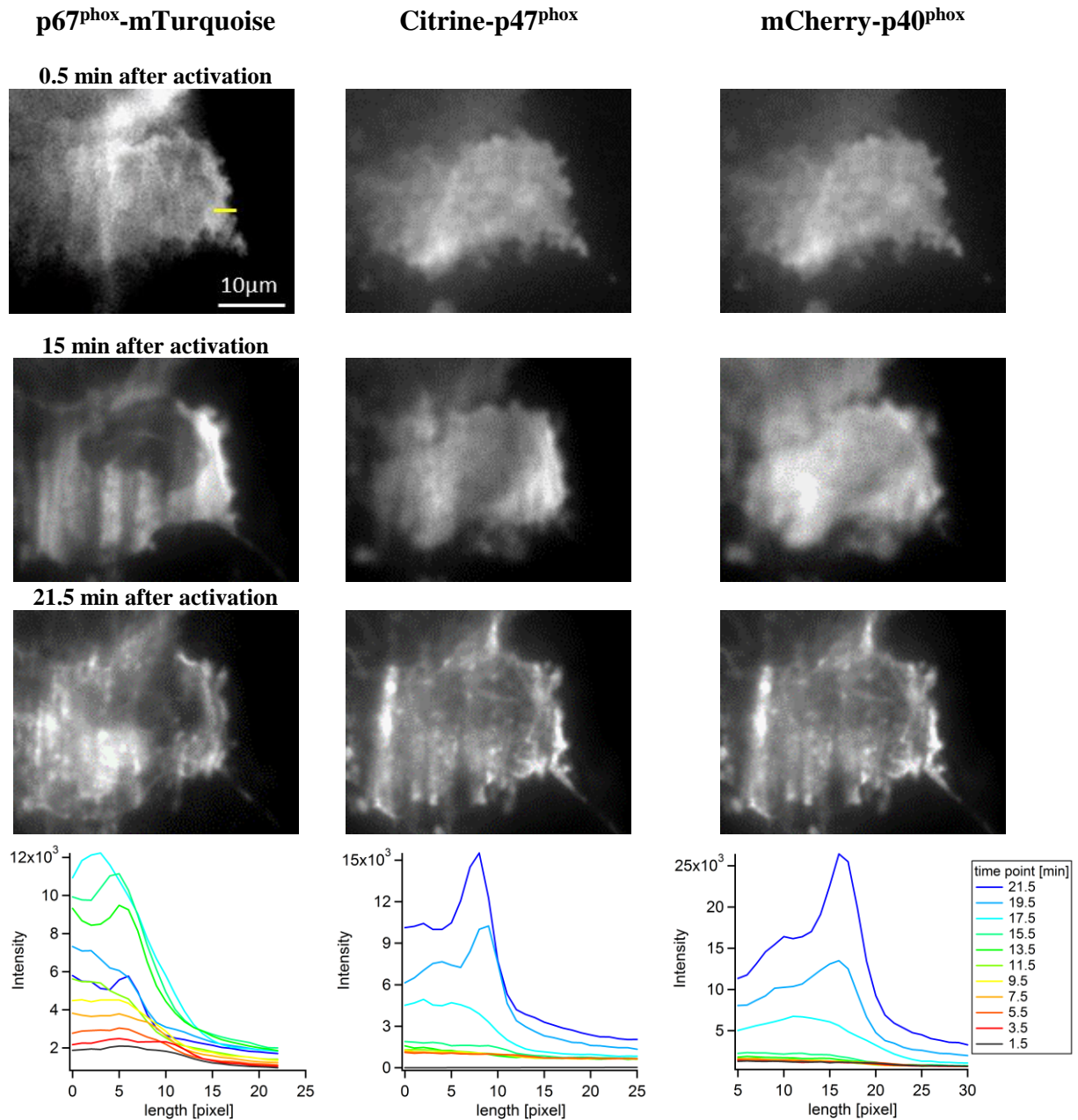


Figure 35 TIRF: Time series of the subunits' arrival on the membrane and intensity profile plot

Line 1 – 3: Snapshots of one cell 0.5 – 15 – 21.5 min after activation: The first row displays the slightly different focal plane of the cyan channel and the yellow/red channels. The second one shows an increase in yellow/red intensity and the arrival of p67^{phox} on the membrane. The 3rd row elucidates bright patches on the membrane, especially on the edge of the cell (yellow and red).

Line 4: Intensity profile plots of a cross section (yellow bar, shown only for the first picture) of the cell: p47^{phox} and p40^{phox} show the same intensity profile: 13.5 min after activation, a fast rise in intensity occurs, i.e. the arrival of those subunits. The rise in intensity is especially prominent on the very edge of the cell. In comparison, the intensity of p67^{phox} increases directly after initiation. The profile is less clearly biased to the edge of the cell.

Figure 36A-C shows the arrival of the different subunits on the membrane after activation as a time series plot for the three samples (CCN, CNN, and NNN): The pattern is in all cases very similar, thus the position of the fluorescent tag on p67^{phox} and p47^{phox} does not seem to influence its translocation behaviour.

Prominently, the cyan signal is clearly different from the yellow and red ones and it is a lot more scattered: It starts to rise around 5 min after activation and reaches a plateau after 16 – 19 min. However, the yellow and red signal initiate to increase around minute 12 – 15, but the rise is steeper, so the maximum is reached at minute 21 – 23 (the maximum of the NNN-tagged sample is not reached during the recording time, though). A 2-way ANOVA reveals a significant difference in the time evolution between p67^{phox} and p47^{phox}/p40^{phox} between minute 9 – 20 ($p < 0.05$). The curves corresponding to the yellow and red signals are developing equivalently, which gives rise to the assumption that p47^{phox} and p40^{phox} arrive at the membrane within the same time window, which is consistent with the literature (Ueyama et al., 2011). One of the reasons for the apparent early arrival of p67 at the membrane might be technical and related to the colour of its tag, as explained before.

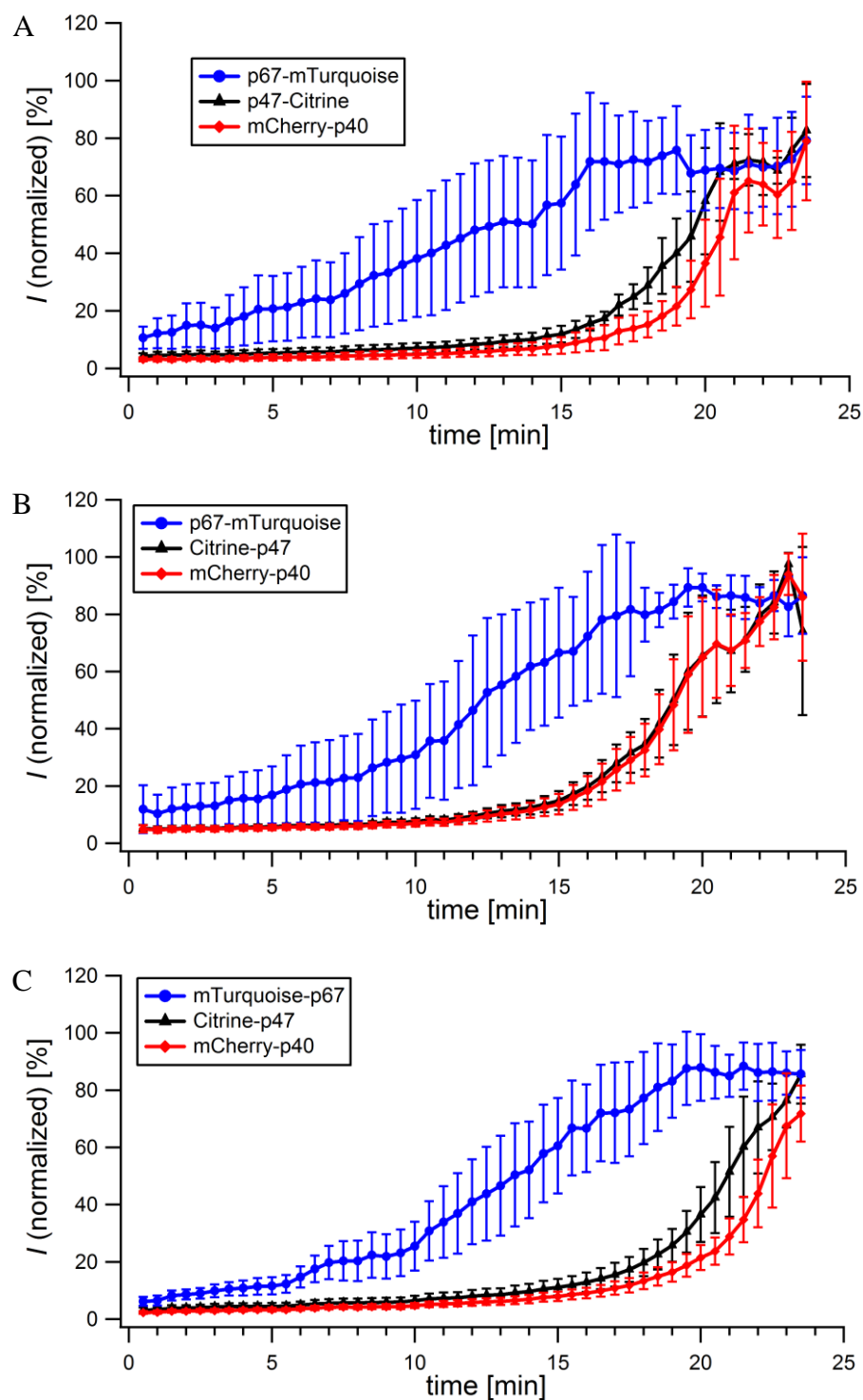


Figure 36 TIRF: Intensity-time series plot of the subunits' arrival on the cell membrane

Triple transfected COS^{gp91^{phox}, p22^{phox}} cells (A: p67^{phox}-mTurquoise + P47^{phox}-Citrine + mCherry-p40^{phox} = CCN; B: p67^{phox}-mTurquoise + Citrine-p47^{phox} + mCherry-p40^{phox} = CNN; C: mTurquoise-p67^{phox} + Citrine-p47^{phox} + mCherry-p40^{phox} = NNN-terminal interaction) were activated with 190 nM PMA (time point 0 min) and the arrival of the cytosolic subunits was followed with TIRF microscopy. The time evolution of p67^{phox} is significantly different from p47^{phox} and p40^{phox} between minutes 9 - 20 (2-way ANOVA: $p < 0.05$; mean \pm SD, $n \geq 5$).

Data were normalized to the maximum fluorescence intensity of each channel.

We conclude from this experiment, that all three combinations of differently tagged subunits are able to translocate to the membrane after activation in a similar fashion and that – at least – p47^{phox} and p40^{phox} most probably translocate together. To compare accurately the arrival time of the subunits at the membrane, it will be necessary to exchange the FPs tags on the subunits: If the pattern of the activation is again the same, i.e. the blue tagged subunit arrives earlier than the yellow and red one, the difference will most probably have a technical – rather than a biological – reason.

4.1.2.2 Measuring the hydrogen peroxide production

The function of the active NOX2 complex is the production of superoxide anions, which dismutate to hydrogen peroxide (Dupré-Crochet et al., 2013). These reactive oxygen species can be detected with the luminescence assay, both intra- and extracellularly (Freitas et al., 2009). The reconstitution of the fully functional NOX2 complex in presence of FP tagged subunits indicates, that the FP tags do not impede the function of its fusion proteins (TSU: tagged subunits, i.e. p67^{phox}-mTurquoise, p47^{phox}-Citrine, and mCherry-p40^{phox}). As a control, the experiment was also performed with cells expressing the untagged subunits (SU, i.e. p67^{phox}, p47^{phox}, and p40^{phox}) and non-transfected cells (NonTr).

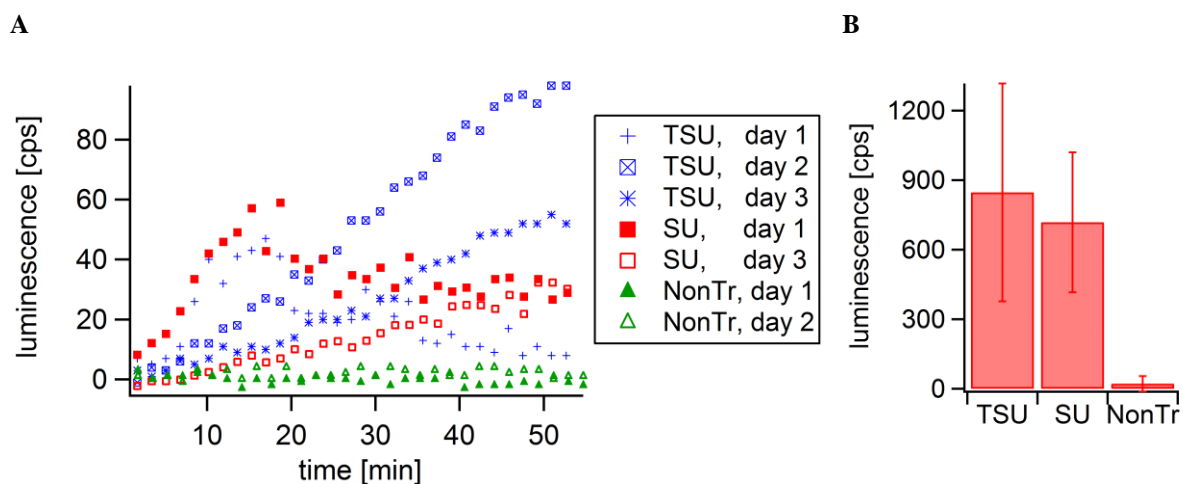


Figure 37 Luminometry confirms the activatability of the complex

Both cells co-expressing three tagged subunits (TSU, i.e. p67^{phox}-mTurquoise, p47^{phox}-Citrine, and mCherry-p40^{phox}) as well as cells expressing the native subunits (SU, i.e. p67^{phox}, p47^{phox}, and p40^{phox}) are able to reconstitute the active complex after activation with 200 nM PMA (negative control: non-transfected cells (NonTr)).

A: Time series of the activation of different experiments (day 1/2/3) of TSU, SU, and NonTr exhibit different kinetics depending on the day not on the TSU vs. SU.

B: Averaged integrated luminescence show no significant difference (1-way ANOVA: $p = 0.24$; results: mean \pm SD, $n \geq 2$)

As shown in Figure 37 A, both cells expressing either the TSU or SU are able to produce ROS and thus assemble to the active NOX2 complex upon activation with 200 nM PMA. However, the activation pattern differs with the different trials: For example, on day 1 the activation is fast and reaches a maximum after around 18 min and decreases slowly afterwards. In contrast, on day 2 the response after activation is less fast but relatively constant for the whole measurement. For both trials, the pattern is similar for the TSU and SU. Therefore, I suppose that this effect depends on a variation in transfection efficiency, the amount of cells in focus

(both factors were hardly controlled in this experiment, compare 2.2.8) and perhaps as well on the PMA, which may show different activation kinetics depending on its diffusion speed to the cells in case of mono- or multi-layers of cells. Figure 37 B shows the column plot of the averaged area under curve for TSU, SU and NonTr, which represent to total amount of ROS produced. Due to the inhomogeneity of the trials, the SD are very large. The outcomes are not significantly different (1-way ANOVA: $p = 0.24$). These findings are in line with an *in vitro* activation of $p47^{\text{phox}} \pm \text{Citrine}$ and $p67^{\text{phox}} \pm \text{mTurquoise}$ performed with purified proteins of our constructs, which demonstrate an identical superoxide production for $P47^{\text{phox}}$ -Citrine and a slightly impeded production in the presence of $p67^{\text{phox}}$ -mTurquoise (Bizouarn, unpublished data).

To sum up 4.1.2, we can conclude that the tagged subunit translocate at the membrane and that the active NOX2 complex can be reconstituted with FP-tagged subunits.

4.2 Interactions of the cytosolic subunits

After proofing the maintained functionality of the FP-tagged subunits, the qualitative and quantitative approach described in chapter 3 was applied to all possible hetero- and homo-dimeric combinations.

4.2.1 Hetero-dimeric interactions between the subunits

The intermolecular interactions of p67^{phox} & p47^{phox}, p67^{phox} & p40^{phox}, and p47^{phox} & p40^{phox} were investigated for a broad variety of C- and N-terminal tag positions.

4.2.1.1 Interaction of p67^{phox} with p47^{phox}

CC-terminal interaction

P67^{phox} and p47^{phox} are supposed to interact on their C-termini, as described in the introduction. To elucidate this interaction in live cells, C-terminal tagged constructs of these two subunits were built (p47^{phox}-Aquamarine and p67^{phox}-Citrine, and with exchanged donor/acceptor position p67^{phox}-mTurquoise and p47^{phox}-Citrine), as well as a truncated version of p47^{phox} (aa 1 – 342; p47^{phox}ΔC-Aquamarine and p47^{phox}ΔC-Citrine), which is missing the PRR domain – the binding side for p67^{phox} (Marcoux et al., 2010, Marcoux et al., 2009). This construct served as a negative control in co-expression with p67^{phox}-Citrine.

A flow cytometry screening revealed FRET between the two subunits, which is independent of the position of donor/acceptor. The truncated version of p47^{phox} lost its binding capacity for p67^{phox}, as the loss of FRET indicates (Figure 38).

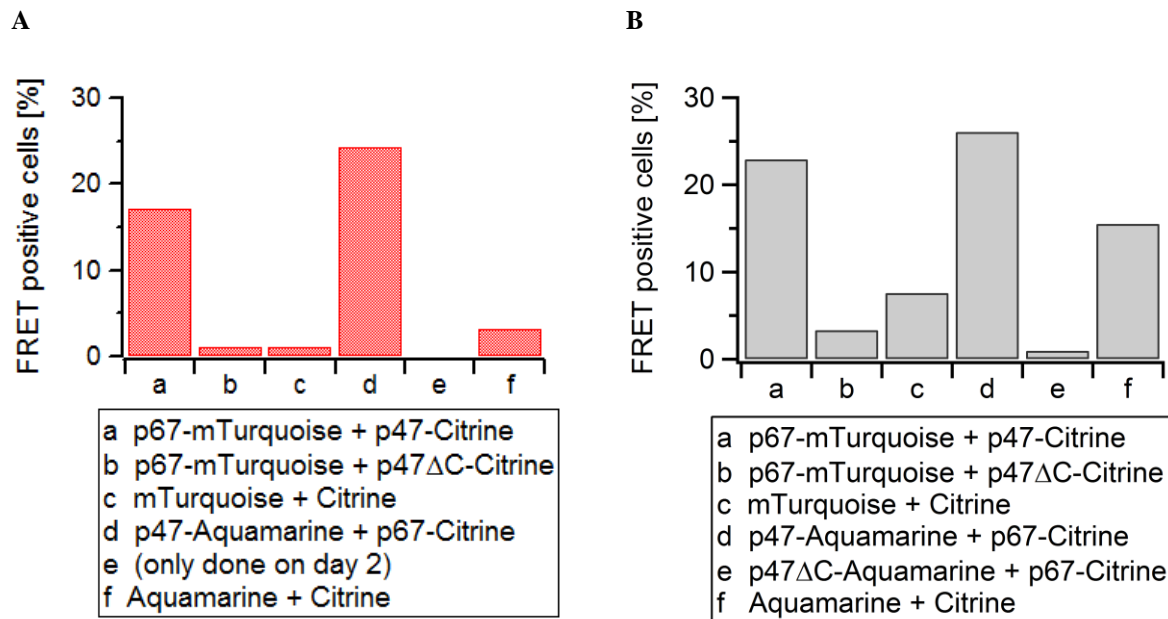


Figure 38 FCET reveals interaction between p67^{phox} and p47^{phox}

FRET by flow cytometry exhibits an interaction between p67^{phox} co-expressed with p47^{phox} (both C terminal tagged) which is mediated by the C-terminus of p47^{phox} as percentage of FRET positive cells: a co-expression of full length p67^{phox} with truncated p47^{phox} (p47^{phox} Δ C) does not show any FRET anymore (b left; b and e right). The interaction is independent of the position of the donor (a: donor on p67^{phox} vs. d: donor on p47^{phox}).

Results of two independent days: A: day 1, b: day 2)

After the identification of two FRET positive couples with FRET by Flow Cytometry, FRET-FLIM experiments (Figure 39) were performed to gain quantifiable information about these interactions. First, the interaction of p47^{phox}-Aquamarine with p67^{phox}-Citrine was investigated, as shown in Figure 29 (paragraph 3.2.4, page 75): The intensity plot (Figure 29 A) confirms the results from the FRET by Flow cytometry experiments: The apparent FRET efficiency of full length p47^{phox} co-expressed with p67^{phox} is clearly above the two negative controls (p47^{phox}-Aquamarine + FP and p47^{phox} Δ C-Aquamarine + p67^{phox}-Citrine, respectively). FRET-FLIM and FRET by Flow Cytometry confirms that the unique binding site of p47^{phox} for p67^{phox} in live cells is the C-terminal PRR domain as presumed from *in vitro* studies (Kami et al., 2002, Leusen et al., 1995, Finan et al., 1994).

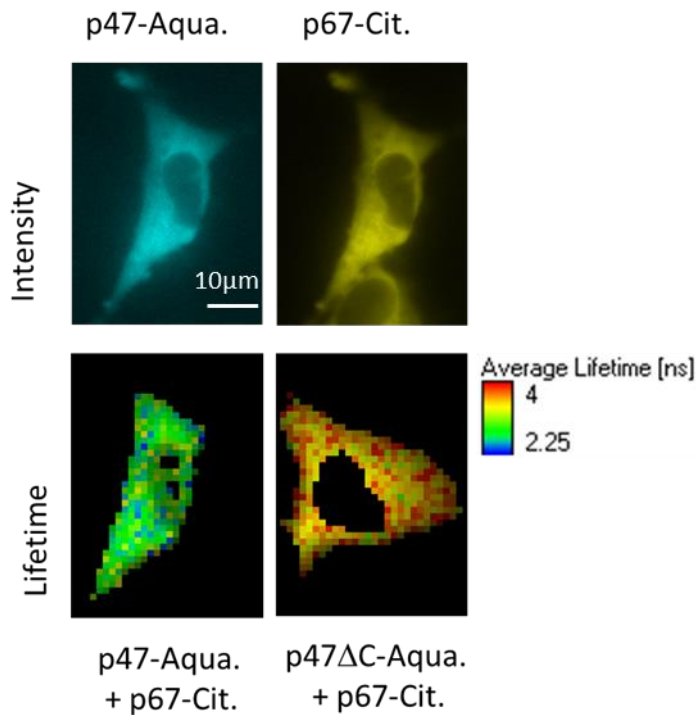


Figure 39 Interaction of p47^{phox} and p67^{phox} is mediated by the C-terminus of p47^{phox}

Top: Intensity pictures of p47^{phox}-Aquamarine (CFP channel) and p67^{phox}-Citrine (YFP channel)

Bottom: Lifetime images of full length (left) and truncated (right) p47^{phox} reveal a short lifetime around 3 ns for the first and a long lifetime (4 ns, equivalent to the lifetime of the donor alone) for the latter one.

The results of the quantitative approach applied to the CC-terminal interaction was already shown in paragraph 3.2.4. To summarize the outcome, the specificity of this interaction found in flow cytometry could be confirmed. A molecular FRET efficiency of 52 ± 8 [%] was found and a maximal bound fraction of 20 ± 6 [%], of which a K_d of 4.0 ± 1.1 [μ M] was estimated.

NC-terminal interaction

Next step was to investigate the interaction between N- (p67^{phox}) and C-terminus (p47^{phox}). As the intensity plot (Figure 40 A) shows, dots are cloudy and do not show any trend, but a lot of dots are above the few control points (p67^{phox} + p47^{phox}ΔC).

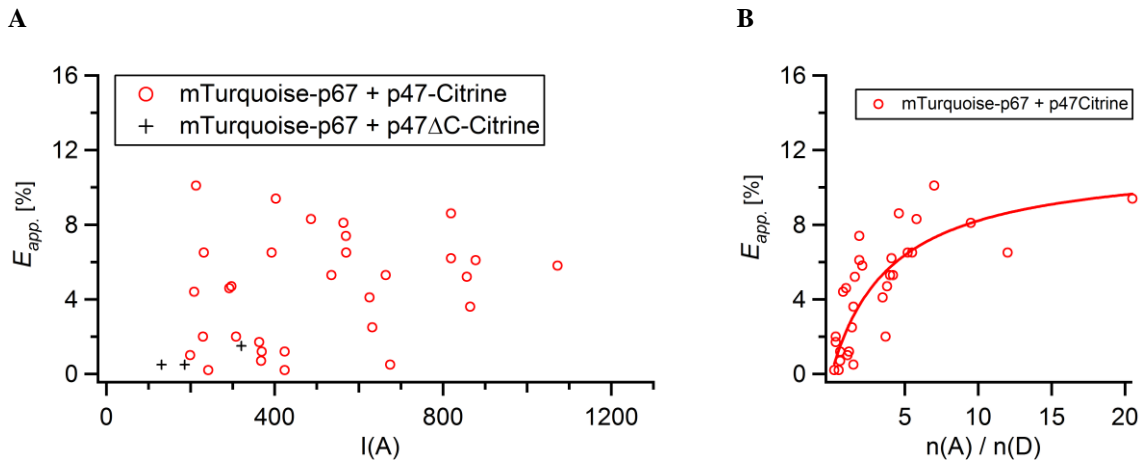


Figure 40 NC-terminal interaction of p67^{phox} and p47^{phox} show a low FRET efficiency

Results for a co-expression of mTurquoise-p67^{phox} + p47^{phox}-Citrine:

A: The intensity plot is very cloudy and does not reveal a trend. However, the majority of the values for p67^{phox} co-expressed with p47^{phox} (red circles) are above the control (full length p67^{phox} and C-terminal truncated p47^{phox}; black crosses)

B: The ratio plot reveals a specific interaction with a maximal FRET efficiency of around 8 %

However, when the ratio $\frac{n_A}{n_D}$ is plotted against the $E_{app.}$ (Figure 40 B), a saturation curve reveals with a maximum apparent FRET efficiency around 8 %. Since this is a clear indication for a specific interaction, we extracted the maximum bound fraction and the molecular FRET efficiency for the data point on the plateau of the saturation curve, which gave values of $\beta_{max} = 18 \pm 4 [\%]$ and $E_{mol.} = 71 \pm 6 [\%]$. The K_d estimated with the bound fraction was around 4.6 μM .

NN-terminal interaction

Finally, a NN terminal tagged p67^{phox} and p47^{phox} were tested. The co-expression of mTurquoise-p67^{phox} + Citrine-p47^{phox} does not show any significant FRET, neither when the intensity of the acceptor (Figure 41 A), nor when the ratio $\frac{n_A}{n_D}$ (Figure 41 B) is plotted against the apparent FRET efficiency. Even if a negative control is missing, the found FRET efficiency is with around 4 % in the range where usually the controls appear (compare Figure 29 A).

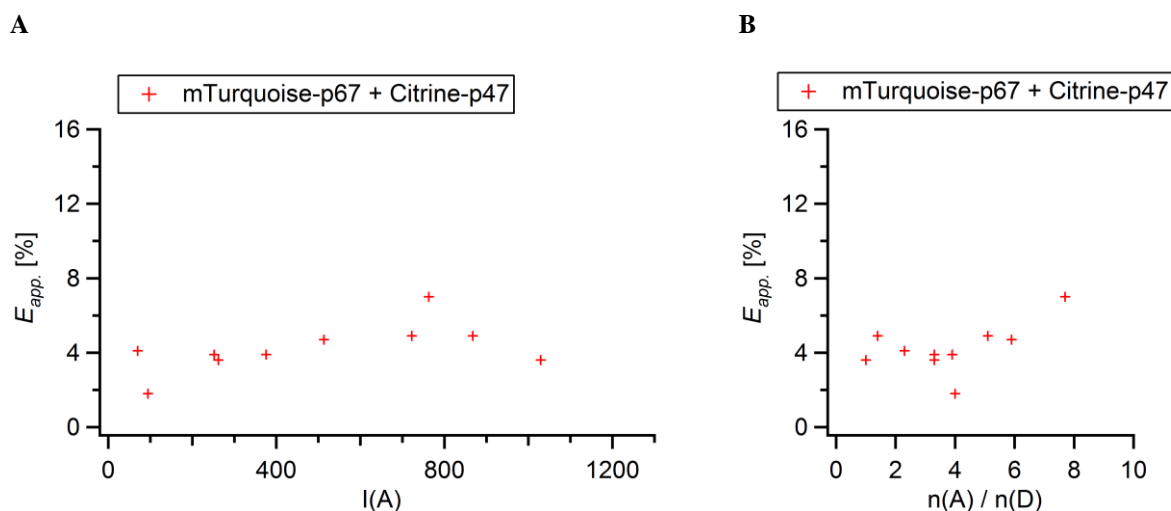


Figure 41: NN-terminal tagged p67^{phox} and p47^{phox} do not show any FRET

Results for a co-expression of mTurquoise-p67^{phox} and Citrine-p47^{phox}

A: The intensity blot displays a FRET efficiency around 4 % for the whole intensity range of the acceptor.

B: The ratio plot does not show any increase of the FRET efficiency with rising amount of acceptor/donor.

To summarize the outcomes of the interaction between p67^{phox} and p47^{phox}, our results could confirm the CC-terminal localization of the interactions. Furthermore, the absence of any specific FRET in case of a co-expression of NN-terminal tagged subunits strongly indicates, that the distance between these termini is too large to allow any FRET ($> 2 \cdot R_0 \approx 100 \text{ \AA}^{\text{xxxv}}$). This will be discussed in detail in the next chapter.

^{xxxv} Estimation based on a R_0 of 51.02 Å calculated with a κ^2 of 0.476 (for further explanations go back to paragraph 1.3.2)

4.2.1.2 p67^{phox} interacts with p40^{phox}

The interaction of p67^{phox} and p40^{phox} were mainly performed with yellow-red FRET couples and one cyan-yellow FRET couple, depending on the availability of the subunits.

To distinguish between specific and unspecific FRET, each donor-tagged subunit was co-expressed with the free acceptor hence given a negative control. The FRET revealed by this negative control refers to unspecific FRET. Results are shown in Figure 42: On the left hand side, the intensity plots are found and on the right hand side the ratio plots. For all four cases (p67^{phox} + p40^{phox}: NN-, CN-, NC-, and CC-terminal interaction) the intensity plot shows specific FRET above the control with a maximum apparent FRET efficiency of around 8 – 12 % (controls around 0 – 4 %). However, the variation of the expressing ratio between the two partners was difficult in case of the CN-terminal interaction (p67^{phox}-mTurquoise + Citrine-p40^{phox}, Figure 42 B) and the NC-terminal interaction (mCherry-p67^{phox} + p40^{phox}-Citrine, Figure 42 D).

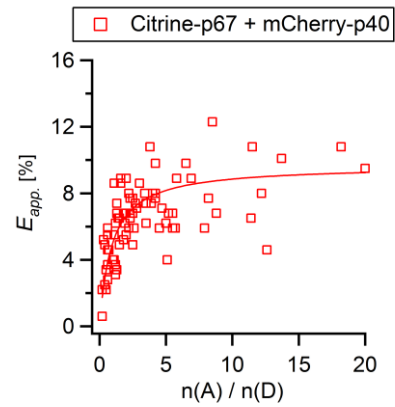
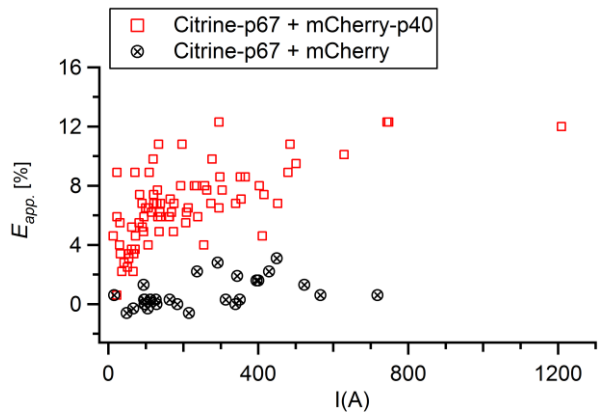
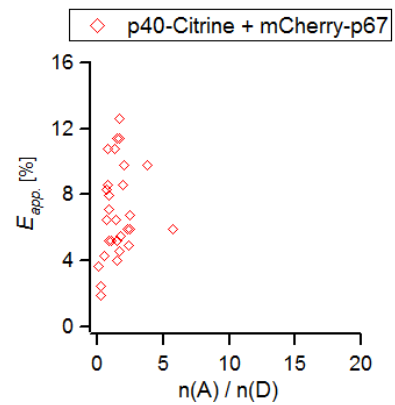
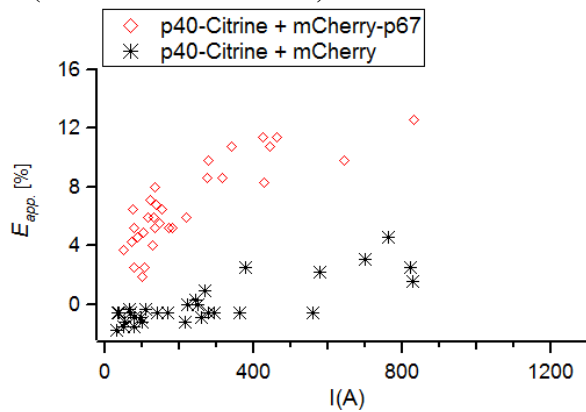
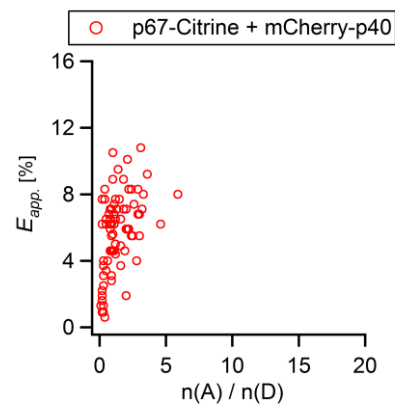
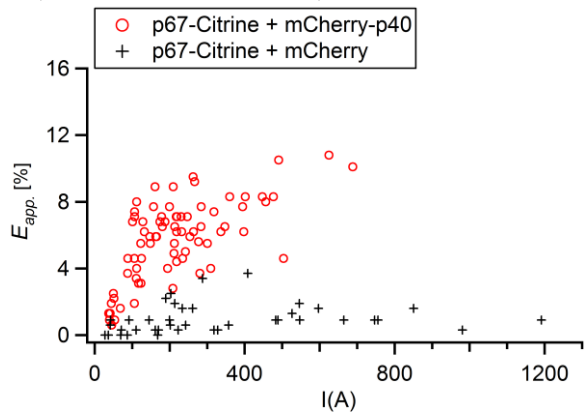
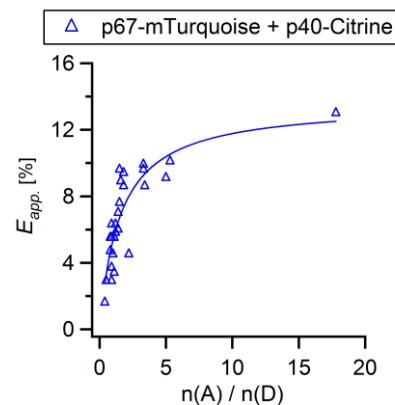
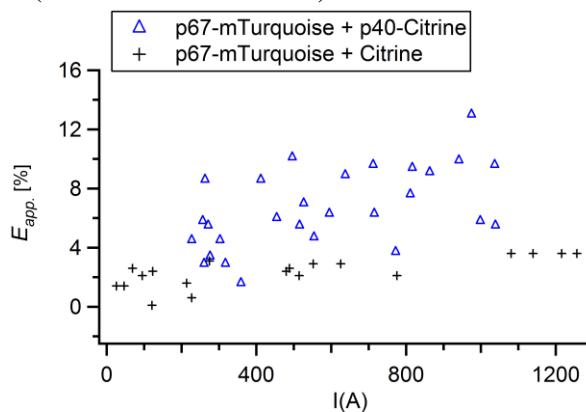
A (NN-terminal interaction)**B (CN-terminal interaction)****C (CN-terminal interaction)****D (CC-terminal interaction)****Figure 42: Interactions of p67^{phox} with p40^{phox} with different tag positions**

Figure 43 shows the plot of the lifetime distribution of the lifetime of the donor in presence of the acceptor (left) and the lifetime of the free donor (right)^{xxxvi} in comparison to the lifetime of the donor alone (positive control)^{xxxvii}. In more detail (mean \pm SD):

- Citrine-p67^{phox}: 1.20 \pm 0.33 [ns] and 3.18 \pm 0.04 [ns]
- Citrine: 3.26 \pm 0.03 [ns]
- p67^{phox}-mTurquoise: 1.72 \pm 0.33 [ns] and 3.82 \pm 0.08 [ns]
- mTurquoise: 3.90 \pm 0.09 [ns]

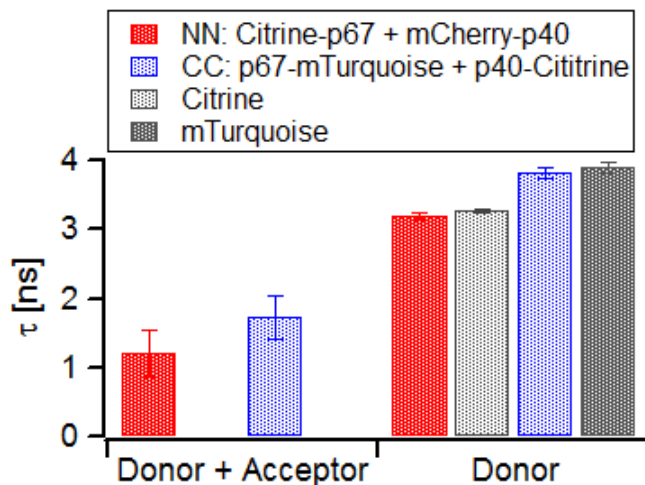


Figure 43 Lifetime distribution of NN- and CC-terminal tagged p67^{phox} and p40^{phox}

Short lifetime of the donor (Citrine-p67^{phox}, red; or p67^{phox}-mTurquoise, blue, respectively) bound to the acceptor (mCherry-p40^{phox} or p40^{phox}-Citrine, respectively), and the long lifetime of the free donor. These data are derived from a bi-exponential fit. As a control the lifetime of Citrine and mTurquoise are plotted (grey and dark grey, respectively; derived from a mono-exponential fit).

The maximum bound fraction – derived from data points on the plateau of the ratio plot – was determined for the NN- and CC-terminal tagged subunits, respectively and used to estimate the K_d : The bound fraction was found were calculated: $\beta_{max}(NN) = 16.3 \pm 2.2$ [%] (n = 9) and at $\beta_{max}(CC) = 16.8 \pm 4.4$ [%] (n = 6). Again, the concentration of the acceptor was assumed to be 1 μ M, which results in K_d values between 5.8 ± 1.8 [μ M] for the CC terminal interaction, and 5.2 ± 0.8 μ M interaction. For CN- or NC-terminal tagged subunits, the plateau is missing, so they were not analysed any further.

^{xxxvi} Derived from bi-exponential fit function of cells co-expressing donor and acceptor

^{xxxvii} Derived from mono-exponential fit function of cells expressing only the donor

4.2.1.3 p47^{phox} interacts with p40^{phox}

Whether interaction between p47^{phox} and p40^{phox} is physiological or an artificial phenomenon is not completely clarified yet. However, the possible interaction sites were identified to be the SH3 domain of p40^{phox} and the PRR domain of p47^{phox}. To show in live cells that the p47^{phox} C-terminus is responsible for this binding, we co-expressed p47^{phox} or p47^{phox}ΔC with p40^{phox}. As shown in the intensity plot, the results for the CN-terminal interaction show rising FRET levels with higher acceptor intensity for the full length p47^{phox} (Figure 44 A). However, the truncated version of p47^{phox} did not reveal any FRET above the negative control (p47^{phox} C-terminal tagged + FP). This proves that the C-terminus is essential for the interaction with p40^{phox}. The ratio plot (Figure 44 B) gives a maximum apparent FRET efficiency around 12 %. From the plateau values, the maximum bound fraction was calculated ($\beta_{max}(CN) = 16 \pm 1$ [%]; $n = 5$) as well as the molecular FRET efficiency ($E_{mol.} = 60 \pm 4$ [%]). The bound fraction leads to a K_d of 5.0 ± 0.4 [μ M].

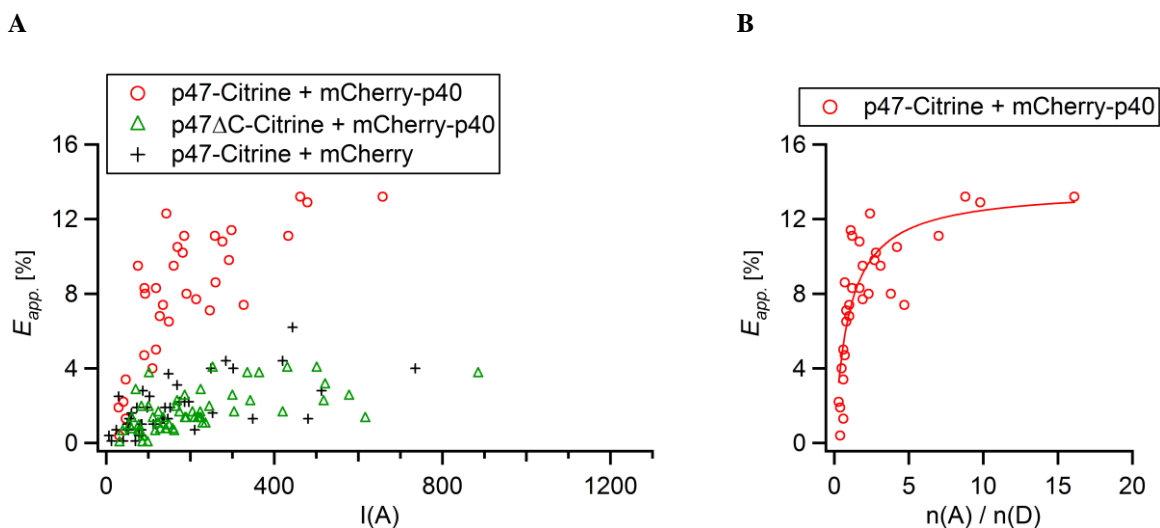


Figure 44 CN-terminal tagged p47^{phox} and p40^{phox} show a specific interaction mediated via the C-terminus of p47^{phox}

A: P47^{phox} and p40^{phox} reveal a CN-terminal interaction (red circles), which is mediated by the C-terminus of p47^{phox}, since with its deletion mutant the specific FRET could not be found (green triangles) – its FRET efficiency is in the same range as the negative control (p47^{phox} + FP, black crosses).

B: The ratio plot gives a maximum apparent FRET efficiency around 12 %.

Even if the result for the CC-terminal interaction are more scattered and less clearly separated from the negative control (Figure 45 A), the ratio plot clearly reveals a specific interaction between these two subunits (Figure 45 B).

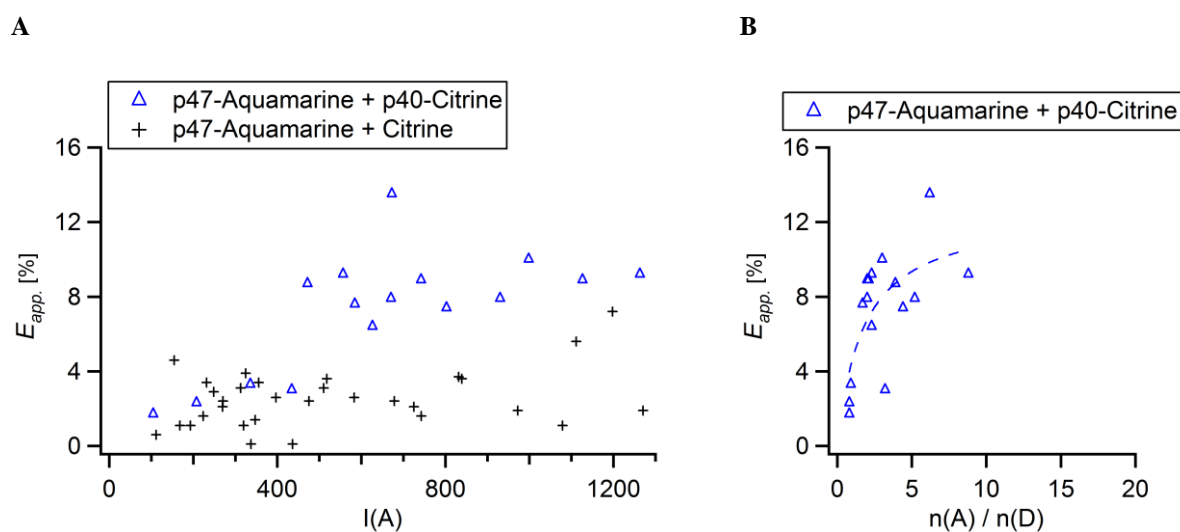


Figure 45 p47^{phox} interacts with p40^{phox} via its PRR domain

P47^{phox} and p40^{phox} reveal a C-N terminal interaction (red circles), which is mediated with the PRR domain of p47^{phox}, since with its depletion the specific FRET could not be found (green triangles) – its FRET efficiency is in the same range as the negative control (p47^{phox} + FP, black crosses).

4.2.1.4 Homo-dimerization of the subunits

The cytosolic subunits are assumed to be organized in a complex with a 1 : 1 : 1 stoichiometry (Stasia and Li, 2008, Nauseef, 2004, Bedard and Krause, 2007). However, in neutrophils, p47^{phox} was found to have 2 – 3x the concentration of p67^{phox} (DeLeo and Quinn, 1996). This raises the question, whether some of the subunits are organized in homodimers.

For p67^{phox} intermolecular dimerization was suggested (Grizot et al., 2001b), but their existence was doubted mainly due to the N-terminal binding side of RacGTP binding at this position (Han et al., 1998, Lapouge et al., 2000). To clarify, whether p67^{phox} homo-dimerises or not p67^{phox} was tagged with either donor or acceptor both on the C-terminus or on N- and C-terminus and co-expressed in the same cell (Figure 46). In none of the cases we examined FRET (left). The ratio plot (right) only shows very small ratios for the NC-terminal interaction, thus a homo-dimerization cannot be completely excluded for the moment (a range of ratio from 1 to 5 would be necessary for drawing a conclusion). The ratio span for the CC-terminal interaction is sufficient, though, but did not show any hint of dimerization. We conclude from our results, that a homo-dimerization of p67^{phox} is very improbable, which is consistent with the *in vitro* findings (Lapouge et al., 2002).

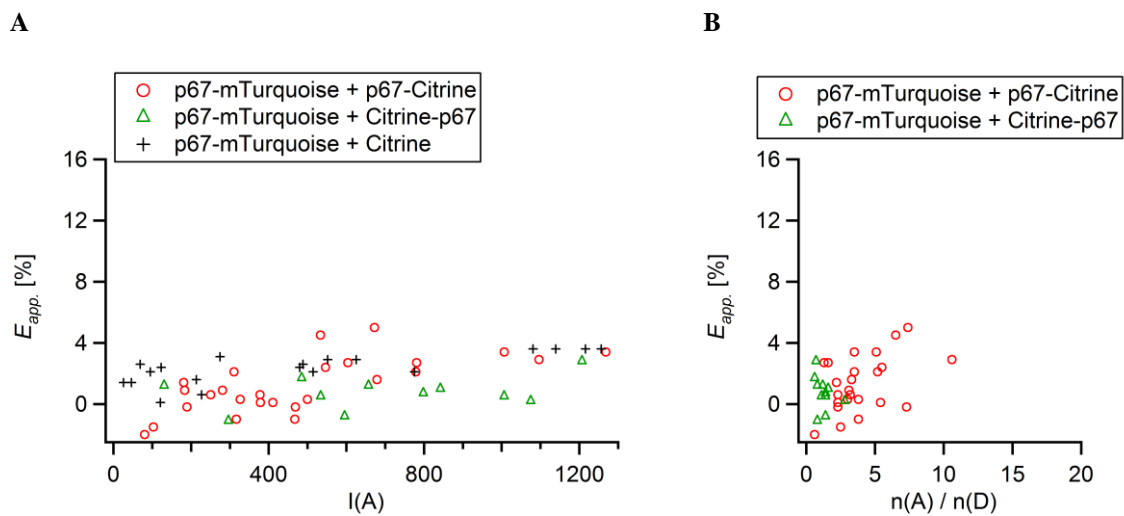


Figure 46 p67^{phox} does not show any homo-dimerization

A: p67^{phox} CC- (red circles) and NN- (green triangles) terminal tagged dimers show similar FRET levels as the negative control (p67^{phox} C-terminal tagged + FP), i.e. no interaction could be revealed from the intensity plot. This result is confirmed for the CC-terminal tagged p67^{phox} by the ratio plot (B). The range of the CN terminal tagged dimers is too small to give any further information.

P47^{phox} homo-dimerization was investigated as well. Our results did not reveal any dimerization of p47^{phox} using CC-terminal tagged p47 (intensity plot (Figure 47 A): FRET level of the sample (red diamonds) is in the same range as the one of the control (black crosses); the ratio plot (Figure 47 B) only exhibits randomly scattered dots with low FRET levels). This finding is in agreement with *in vitro* findings (Grizot et al., 2001b, Yuzawa et al., 2004).

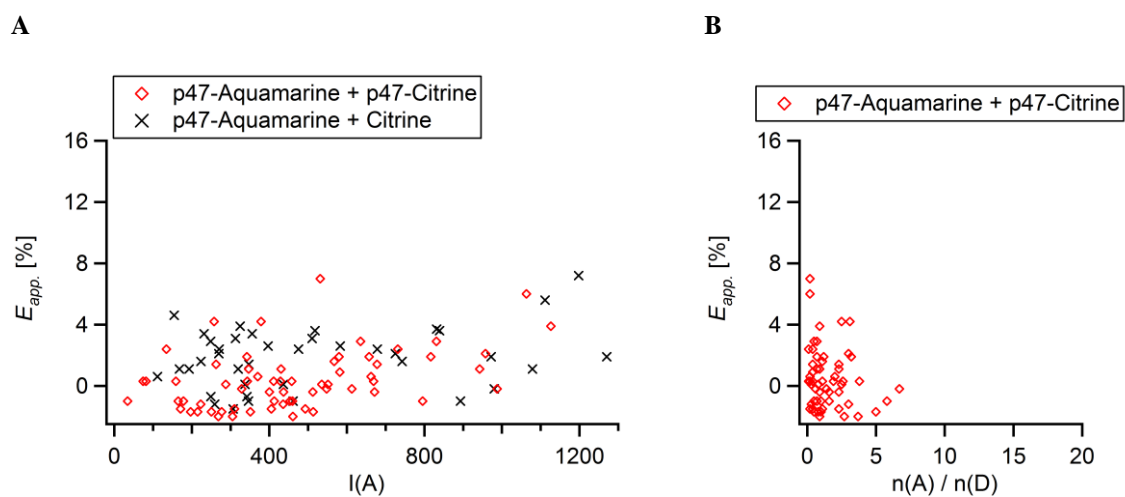


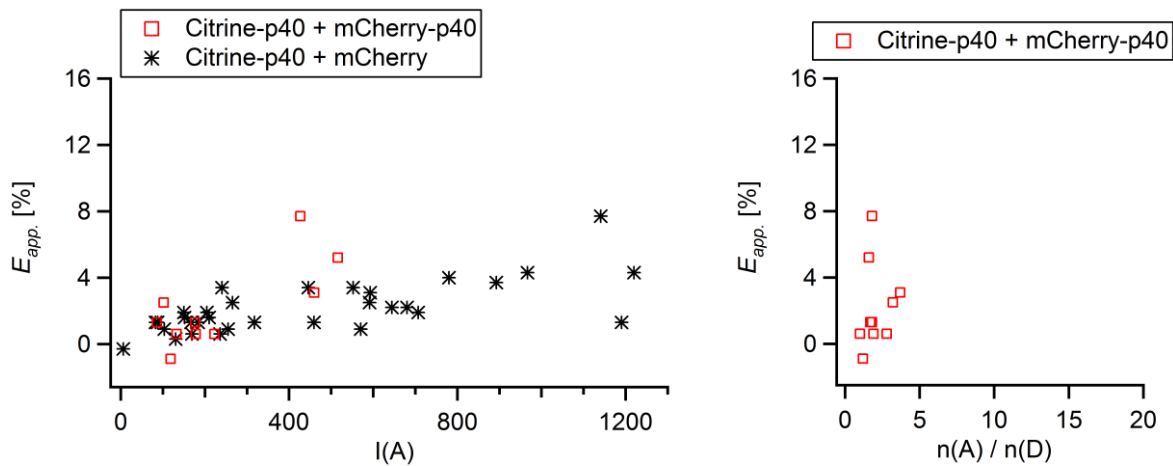
Figure 47 p47^{phox} does not reveal any dimerization

A: p47^{phox} CC-terminal tagged (red diamonds) does not give any hint of dimerization, the FRET values are equal to the negative control neither (p47^{phox} C-terminal tagged + FP, black crosses).

B: The ratio plot strengthens this finding – no hint of any correlation between $E_{app.}$ and $\frac{n_A}{n_D}$

We also performed first experiments addressing the question of homo-dimerization of p40^{phox} with both NN- (Figure 48 A) or CN-tagged p40^{phox} (Figure 48 B). The intensity plots (left) does not give rise for any dimerization since the FRET levels are in the same range of the control, (tagged p40^{phox} co-expressed with mCherry). However, only very small ratios were achieved for the ratio plot (right), which does not allow any conclusion for so far. Following literature, p40^{phox} homodimers are improbable (Grizot et al., 2001b).

A (p40^{phox}, NN-terminal tagged)



B (p40^{phox}, CN-terminal tagged)

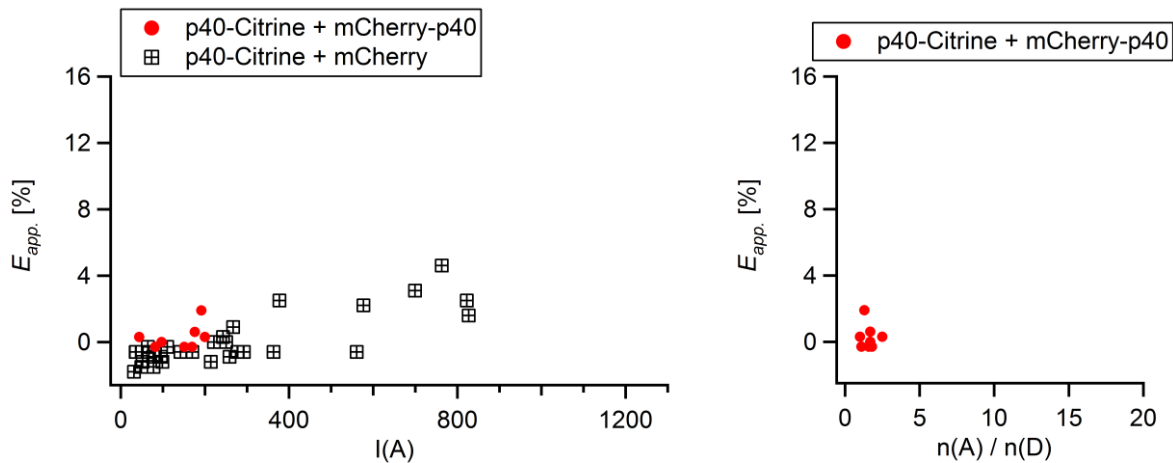


Figure 48 Overview homo-dimerization of the cytosolic subunits

A: First results for p40^{phox} CN- (red dots) and NN- (red squares) terminal tagged p40^{phox} does not indicate any specific interaction.

B: For the ratio plot, a broader span of ratios is necessary to allow any conclusions.

To sum up our findings, for none of the subunits we found any hint of dimerization.

4.2.1.5 Intramolecular interactions

P47^{phox} and p40^{phox} are folded in their auto-inhibitory confirmation in the resting state, while p67^{phox} is assumed to be elongated, as described in detail in the introduction (paragraph 1.4.1.2.2). To get structural information from live cells, we tagged all cytosolic subunits on both ends with donor and acceptor FPs and measured FRET. In the following, those constructs will be called “tandems”.

4.2.1.5.1 p47^{phox}-tandem

As a first test, a FRET by Flow Cytometry experiment was performed for the p47^{phox}-tandem (n = 2) and p67^{phox}-tandem (n = 1)^{xxxviii}. The results for p47^{phox}-tandem (Figure 49) show low percentages of FRET positive cells, which are just above the control (3.4 ± 0.5 [%] = mean \pm SD, after subtraction of the negative reference). P67^{phox}-tandem revealed as well a very low percentage of FRET positive cells (6.5 % = mean, after subtraction of the negative reference). In comparison, the amount of FRET positive cells after transfection with an Aquamarine-Citrine-tandem (only connected with a 27 aa linker) is around (46 ± 6.8 [%] = mean \pm SD, after subtraction of the negative reference).

^{xxxviii} p40^{phox}-tandem was not tested, since our flow cytometer was not equipped to measure yellow-red FRET at those days.

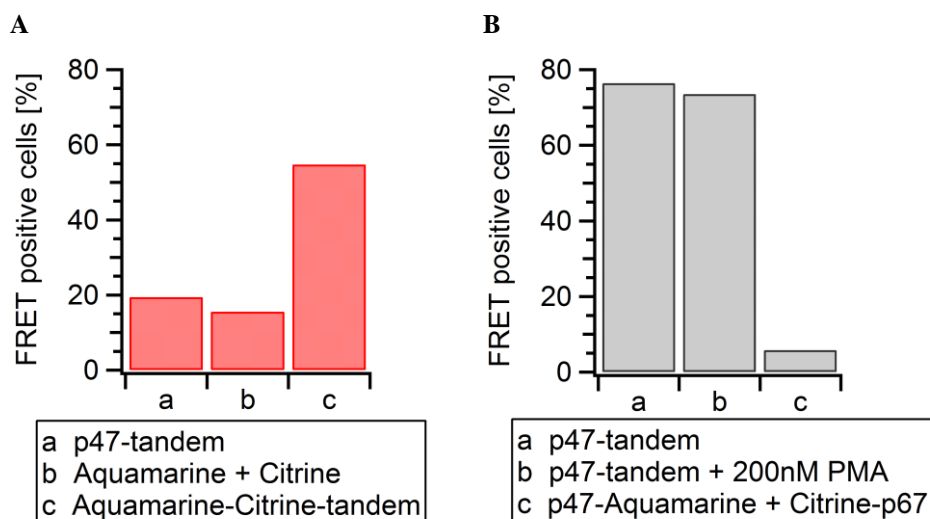


Figure 49 FRET by Flow Cytometry shows very small amount of FRET positive cells for the p47^{phox} tandem

The figure shows the percentage of FRET positive cells of the p47tande two days of experiment

A: The tandem (a) is only slightly above the negative control (i.e. free FPs, b). The positive control (simple donor-acceptor tandem (c) show a high percentage of FRET positive cells.

B: The tandem shows a very high amount of FRET positive cells (a) in comparison to C-terminal tagged p47^{phox} co-expressed with N-terminal tagged p67^{phox} (b). An activation of the tandem with 200 nM PMA shows a minimal decrease of FRET positive cells after an incubation time of 2.5 h.

Even if the flow cytometry data were not encouraging, we performed a FRET-FLIM study. P47^{phox} shows a stable FRET level in the save intensity range, as it is expected for a tandem. Its value is around 9.5 ± 1.3 % (Figure 50). The lifetime distribution derived from the bi-exponential fit (Equation 21) reveals a short lifetime of 1.6 ± 0.31 [ns] and a long one of 3.89 ± 0.05 [ns]. While the short lifetime corresponds to a high FRET efficiency ($E_{mol.} = 60 \pm 8$ %, compare as well with Table 20), the long lifetime is – surprisingly – in the same range as the lifetime of the donor (Aquamarine) alone (3.95 ± 0.07 [ns]), i.e. no FRET occurs. These results have been compared with those of a tandem composed of Aquamarine and Citrine, connected with a 27 amino acid linker (Aquamarine-Citrine tandem). The lifetime data of these tandems were also fitted with a bi-exponential fit. It gives as well two lifetimes (1.07 ± 0.08 [ns], 35 % and 3.5 ± 0.05 [ns], 65 %), however none of them is equivalent to the lifetime of the donor alone. Both lifetimes are associated with significant FRET efficiencies (short lifetime: $E_{mol.} = 73 \pm 2$ [%] and long lifetime: $E_{mol.} = 11 \pm 1$ [%]), respectively). Nevertheless, the higher molecular FRET efficiency only concerns a minority of the tandem population (35 ± 2 [%]). The lifetime distributions are for all tandems are shown in Figure 51

That means in turn, that only a minority of conformations/ spatial orientations of the tandem allow a maximum FRET. Nonetheless, the (major) long lifetime fraction still reveals FRET.

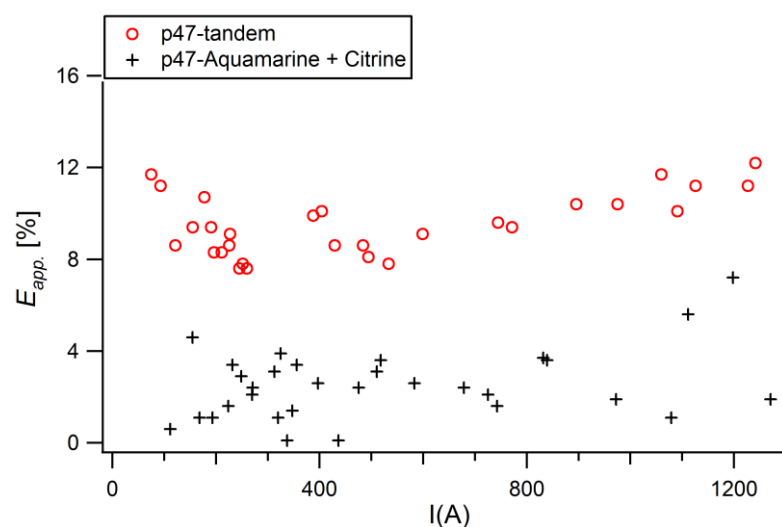


Figure 50 p47^{phox} tandem reveals a moderate FRET level

The FRET level of the p47^{phox} tandem is 9.5 ± 1.3 % in comparison to the control (tagged p47^{phox} co-expressed with FP) which gives 1.8 ± 1.9 %

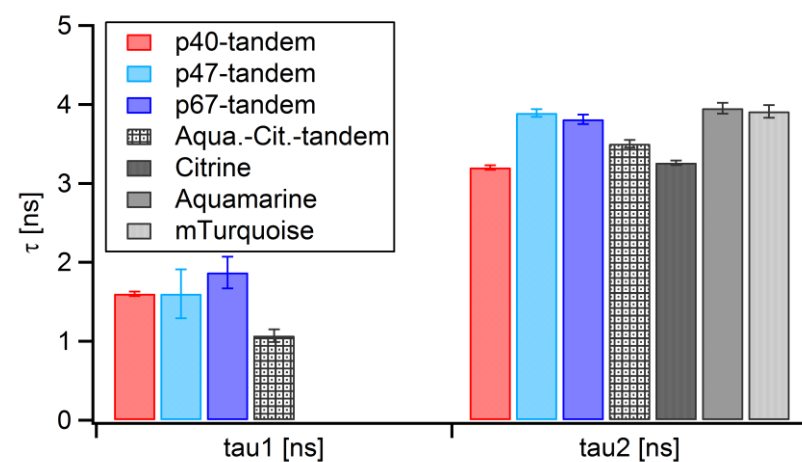


Figure 51 Lifetime distribution of the CN-terminal tagged subunits (tandems)

A bi-exponential fit reveals two lifetimes for all tandems, a short one (tau1) and a longer one (tau2). In case of the subunit-tandems, the long lifetime is identical with the lifetime of the donor alone (Citrine, mTurquoise, or Aquamarine, derived from mono-exponential fits) while tau1 is significantly shorter (t-test in all three cases $p < 0.0001$). The Aquamarine-Citrine tandem, however, shows a significant shorter tau2 than the lifetime of Aquamarine (t-test $p < 0.0001$)

4.2.1.5.1 p67^{phox}-tandem

Low levels of FRET were measured for the p67^{phox}-tandem (7.5 ± 2.2 %, compare Figure 52), which are, nevertheless, remarkably higher than the control level. Derived from the bi-exponential fit, a short (1.9 ± 0.2 [ns]) and a long lifetime (3.81 ± 0.06 [ns]) was extracted (Figure 51), whereby the contribution of the short lifetime is 20 ± 4 %. Again, the short lifetime corresponds to a high FRET efficiency ($E_{mol.} = 52 \pm 6$ %) and long lifetime is in the same range of the lifetime of the donor alone (mTurquoise, 3.91 ± 0.08 [ns]).

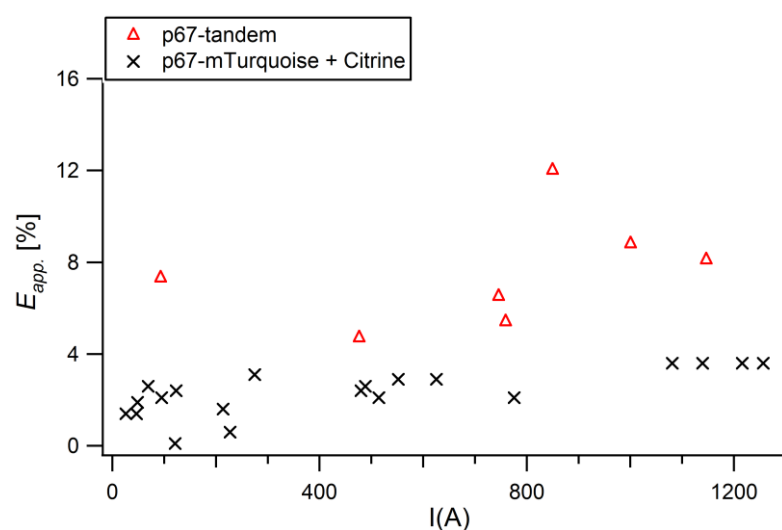


Figure 52 p67^{phox} tandem shows low FRET levels

The FRET level of the p67^{phox} tandem is 7.5 ± 2.2 %, the one of the control (p67^{phox} C-terminal tagged + FP) is around 2.4 ± 0.99 %.

4.2.1.5.1 p40^{phox}-tandem

First results (Figure 53) exhibit a FRET level around $13.3 \pm 2.4 \%$, which is slightly above the level achieved by the p47^{phox} tandem. The bi-exponential fit (Figure 51) reveals a short lifetime of 1.6 ± 0.03 [ns] (with a share of $26 \pm 4 \%$) and a long lifetime of 3.2 ± 0.03 [ns]. The latter is in the same range as the lifetime of the donor alone (Citrine, 3.26 ± 0.03 [ns]), as observed for the other tandems. Computed from the short lifetime, a molecular FRET efficiency of $51 \pm 0.8 \%$ was found, which is – surprisingly – in the same range as for the p67^{phox}-tandem ($E_{mol.} = 52 \pm 6 \%$) despite the fact that the size of p67^{phox} is expected to be larger.

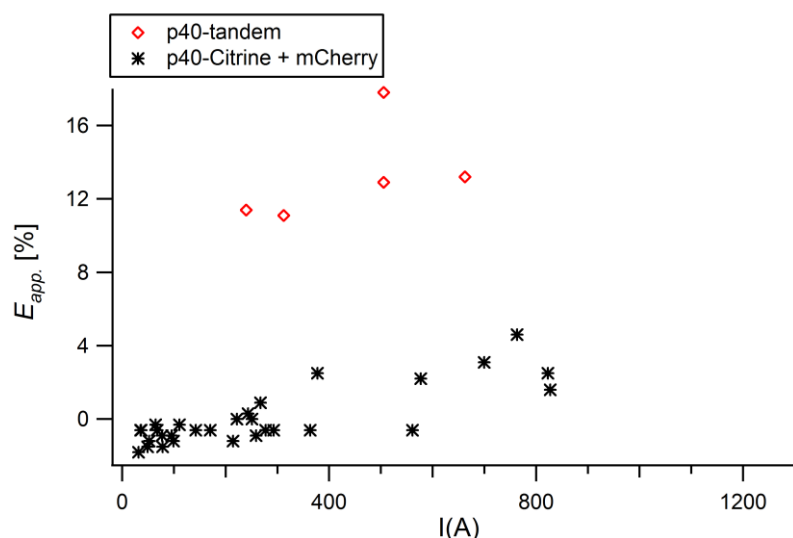


Figure 53 Preliminary results for p40^{phox} tandem reveal FRET

The p40^{phox} tandem shows FRET levels between $13.3 \pm 2.4 \%$, whilst the control (p40^{phox} C-terminal tagged + FP) reveals $0.03 \pm 1.5 \%$

In conclusion, the study of the intramolecular interactions could reveal for all cases FRET, which means that their N- and C-termini are closer than $2 \cdot R_0$, i.e. $< 100 \text{ \AA}$ (for further explanations, go back to paragraph 1.3.2). The fact, that only a small fraction of short lifetime was found, may have different reasons: (i) The acceptor is not visible due to incomplete expression of the protein, which remains to be verified by western blot; (ii) incorrect folding and maturation of the acceptor; (iii) there is only a minority of conformations which leads to a favourable spatial orientation allowing FRET, or (iv) the distance between N- and C-terminus is too large in the majority of the conformations, since p47^{phox} and p40^{phox} can go into an open state, p67^{phox} is due to its flexibility in the majority of the cases in an elongated conformation (no FRET possible), but in a minority bent (FRET possible). For detailed discussion, please go to paragraph 5.2.1.

p67^{phox}	p47^{phox}	p40^{phox}	β_{max} [%] \pm SD	K_d^* [μM] \pm SD	$E_{mol.}$ [%]
C [#]	C ⁺	-	20 \pm 6	4.0 \pm 1.1	52 \pm 8
N [†]	C [#]	-	18 \pm 4	4.6 \pm 1.0	71 \pm 6
N [†]	N [#]	-	no FRET	no FRET	no FRET
C [†]	-	C [#]	17 \pm 4	5.0 \pm 1.8	56 \pm 8
N [†]	-	N [#]	16 \pm 2	5.2 \pm 0.8	63 \pm 10
-	C [#]	N [‡]	16 \pm 1	5.0 \pm 0.4	60 \pm 4
p40 N [‡] +C [#] tagged			26 \pm 4		51 \pm 0.8
p47 N [#] +C ⁺ tagged			18 \pm 2		60 \pm 8
p67 N [#] +C [†] tagged			20 \pm 4		52 \pm 6

Table 20: Overview of the maximum found bound fraction β_{max} , the dissociation constant K_d , and the molecular FRET efficiency $E_{mol.}$.

* The K_d is declared with an assumed acceptor concentration of 1 μ M. The acceptor concentration may also be 10 μ M, thus the K_d may have values which are ten times higher as shown in the table.

Citrine, + Aquamarine, † mTurquoise, ‡ mCherry

4.2.2 Results obtained from CFP-YFP FCCS

The results presented in the previous paragraph showed that the bound fractions of donor in heterodimeric interaction are comprised between 16 and 26 %. FRET is highly dependent on the geometry of the interaction, i.e. distance and spatial orientation between the fluorophores. This may be an issue. In comparison, the fluorescence cross correlation between co-diffusing fluorophores is independent of this issue, thus the interaction between the subunits can be observed without any structural prerequisite.

This paragraph presents the results of a single experiment, during which only a few constructs were studied. We decided to probe the interaction between p67^{phox} and p47^{phox} (CC- and NC-terminal tagged). P67^{phox}-mTurquoise co-expressed with Citrine serves as a negative control (no co-diffusion) and the p67^{phox}-tandem as a positive control (both FPs are linked via p67^{phox} and hence must co-diffuse).

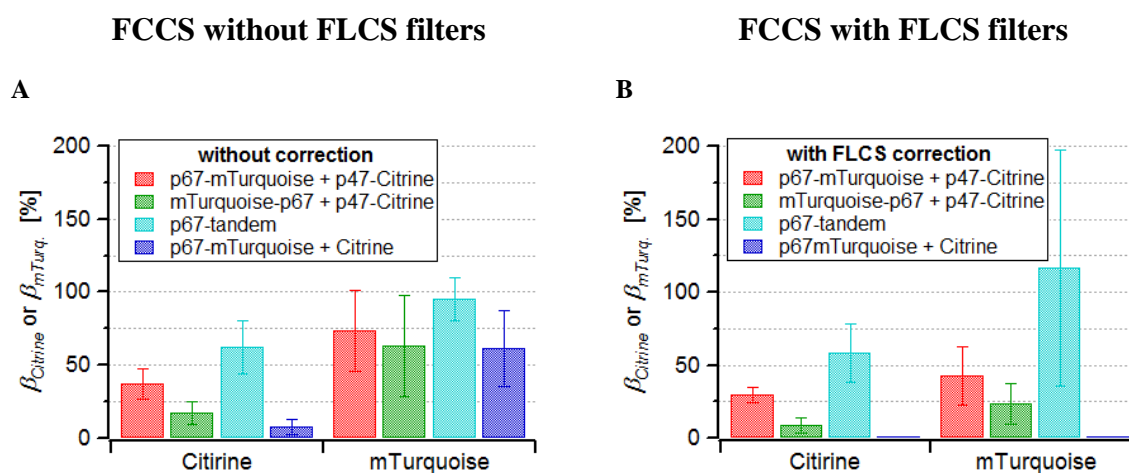


Figure 54 Comparison of the results of the bound fraction obtained with FCCS with and without FLCS filters

A (without FLCS): The bound fraction measured in the cyan channel is higher than the one observed in the yellow channel. The negative control (p67^{phox}-mTurquoise + Citrine, dark blue) shows a bound fraction caused by the spectral bleed through.

B: The FLCS correction completely erases the bleed through, as the negative control at 0 % shows. Both the bound fraction of Citrine and mTurquoise are decreased, whereby the effect on the latter is stronger. ($n_{\text{cell}} = 4 - 6$, same day). Only the Citrine bound fractions of CC- (red) vs. CN-terminal (green) tagged p67^{phox} and p47^{phox} are significantly different (t-test, $p = 0.0006$)

In Figure 54 the fraction of protein in complex refers to the ratio of the amplitudes of the cross-correlation and auto-correlation function, which is defined in paragraph 2.2.11, Equation 19.

To facilitate the understanding, the equation is specified for both mTurquoise and Citrine as follows:

$$\text{Equation 35} \quad \beta_{mTurq} = \frac{G_{cross}(0)}{G_{Citrine}(0)} \cdot 100 \% \text{ with } G_{Citrine}(0) = 1/N_{Citrine}$$

$$\text{Equation 36} \quad \beta_{Citrine} = \frac{G_{cross}(0)}{G_{mTurq}(0)} \cdot 100 \% \text{ with } G_{mTurquoise}(0) = 1/N_{mTurquoise}$$

A main difficulty of FCCS is to correct the data from the bleed trough of the mTurquoise fluorescence photons in the Citrine detection channel. Its major consequence is the detection of more photons than the ones emitted by Citrine ($\Rightarrow N_{Citrine}$ falsely high). Consequently, (i) the amplitude of the auto-correlation function of Citrine is underestimated and (ii) the cross-correlation is overestimated (all “blead-through photons” are cross correlated, since they originate from the same emission source, i.e. mTurquoise). Therefore, it is crucial to correct the data from the bleed-trough, which we have achieved with FLCS filters (appendix 8.5).

FLCS filters correct the autocorrelation of Citrine from the “blead-through photons”. As a consequence, the number of observed yellow molecules is reduced ($N_{Citrine} \downarrow$), which leads to an increased auto-correlation amplitude ($G_{Citrine}(0) \uparrow$) due to their reciprocal relation $G(0) = \frac{1}{N}$. The removed photons cannot falsifying the cross-correlation anymore, i.e. the cross-correlation amplitude decreases ($G_{cross}(0) \downarrow$). As a consequence, the FLCS correction on the bound fraction of mTurquoise is stronger affected than on the one of Citrine (Equation 35 and Equation 36) as Figure 54 shows. To verify the efficiency of the FLCS filters we use as a negative control p67^{phox}-mTurquoise and Citrine. Without correction, this sample shows a bound fraction for each fluorophore (β_{mTurq} and $\beta_{Citrine}$) due to the misleading cross-correlation ($G_{cross}(0) \neq 0$). The percentage of the cyan bound fraction is significantly higher than the yellow one (t-test, $p = 0.013$). After correction, the cross-correlation disappeared proving that the FLCS filters efficiently remove the bleed trough.

The bound fraction will only be discussed for the FLCS corrected results. First comparing the CC-, NC tagged samples of p67^{phox} and p47^{phox} (green and red Figure 54 B), a statistically higher bound fraction of the CC was found for the yellow (t-test, $p = 0.0006$) but not for the cyan bound fraction (t-test, $p = 0.1199$). The bound fractions of the intermolecular interactions are always smaller than the one of the tandem. This indicates that not all subunits may be bound in a complex. Second, comparing the bound fraction of Citrine and mTurquoise, the one for Citrine is always smaller than for mTurquoise, which means that the total number of observed mTurquoise is smaller than the one for Citrine ($\beta_{Citrine} < \beta_{mTurquoise} \Leftrightarrow N_{mTurquoise} < N_{Citrine}$). This is expected: Cells with a Citrine overexpression were chosen to saturate the mTurquoise-tagged

subunit with the Citrine to have comparable results to the FRET-FLIM studies. The Citrine and mTurquoise bound fraction of the tandem should be the same after the bleed through correction (blue bars Figure 54 B), however a trend to a lower Citrine fraction cannot be ignored. A detailed discussion about the influence factors on the FCCS bound fraction is given in paragraph 5.1.1.

5 Discussion

One aim of this project was to prove the feasibility of the improved CFP variants mTurquoise and Aquamarine for quantitative studies in live cells in FRET-FLIM. We choose to investigate the protein-protein interactions of the cytosolic subunits of the NOX2 complex. The main knowledge about the structural organization of this enzyme is derived from *in vitro* data, which may not necessarily reflect the situation in live cells: Due to the complex cellular environment, interactions with other cellular components or spatial separation in different compartments may occur. One open question is, whether the subunits are all organized in a complex or not. In neutrophils, for example, it was shown that p47^{phox} is in excess to p67^{phox} by a factor of 2 – 3 (DeLeo and Quinn, 1996). Quantitative FRET-FLIM is prone to answer this question, since it gives directly the bound fraction of the subunit bound to the donor to its acceptor tagged binding partner. This bound fraction is related to the dissociation constant K_d . The mutual approach of FRET-FLIM with fluorescence wide-field microscopy allows an estimation of the K_d within live cells.

A first study using FRET-FLIM based quantification was the characterization of nuclear import mechanisms in live cells. The authors showed the successful determination of both bound fraction and K_d in live cells (Cardarelli et al., 2009) using EGFP and mCherry as donor/acceptor couple. Day published a quantitative FRET-FLIM/wide-field microscopy method based on mTurquoise and mVenus. His approach is similar to ours, since he uses plots of the apparent FRET efficiency against the ratio of fluorescence intensities acceptor/donor to reveal specific interactions (Day, 2014). With our method, we went further, not only with respect to the more accurate data treatment, but also by extracting the bound fraction, which was further used for an estimation of the K_d . In paragraph 5.1 the quantitative approach developed during this project will be discussed.

Furthermore, FRET contains structural information due to its small working distance. Even if it is not possible to measure the distance between the FRET couple, the extraction of the molecular FRET efficiency from the FLIM data still gives insights in the geometrical organization of the protein(s) to which the fluorophores are linked. We compared our findings with available structural data of the NOX2, which turn out to be in good agreement. Hence we built the first complete 3D model of the NOX2 complex, which we could enrich with estimations about its flexibility. This model is prone to give new ideas about the functionality of this enzyme. Paragraph 5.2 will discuss these points in greater detail.

5.1 Discussion of the quantitative approach

FRET-FLIM data contains an information about the donor-fusion protein in complex with its acceptor linked partner, which is an interesting biological parameter and can further be used to estimate the dissociation constant. Therefore, the bound fraction is as well the bottleneck of our quantitative approach and must be questioned carefully for a valid interpretation of the biological meanings. Different experimental biases can lead to a misestimation of this value. To have an independent method giving the bound fraction, we performed a FCCS experiment. In the following, we will first (i) compare the two techniques and their outcomes, then discuss (ii) the parameters that could influence the fraction of bound molecules and (iii) their consequences on FRET-FLIM and FCCS data.

5.1.1 Interpretation of the bound fraction

With FRET-FLIM, we found a bound fraction of 16 – 20 % for the heterodimeric interactions, and of 20 – 26 % for the intramolecular interactions (tandems). An overview for each studied interaction is given in Table 20. Such a low bound fraction for the heterodimeric interactions is in contradiction to the common belief, that the cytosolic subunits are all bound in complex. Since at least p47^{phox} and p67^{phox} are not expressed in the same ratio in neutrophils (2 – 3 times more p47^{phox} (DeLeo and Quinn, 1996)), it is just not possible, that all subunits are organized in the complex of the cytosolic subunits assuming that the 1 : 1 : 1 stoichiometry (Stasia and Li, 2008) is true. Still, it is surprising, that all bound fractions are so similar values, especially in comparison of intra- and intermolecular interactions. Regarding the importance of this outcome for the biological input of this study and for the determination of the K_d , we did a first FCCS experiment to verify the FRET-FLIM derived bound fractions (the two techniques are summarized in Table 21).

	FRET-FLIM	FCCS
general aspects		
distance	$d < 10$ nm for FRET	independent
structure	gives structural insights on the folding and the flexibility of the proteins and on the localization of the interaction	no structural insights
investigation	imaging mode ⇒ cellular localization of the interaction	single spot ⇒ no cellular localization
protein concentration	μ M range artefacts may arise from artificial overexpression	single molecules up to nM range physiological conditions achievable
data processing	bi-exponential fit (or phasor plot)	auto/cross-correlation function, focal volume calibration and alignment, correction of spectral cross talk
quantification		
discovery of protein-protein interactions	with an E_{app} higher than a negative control	with cross-correlation function
bound fraction	derived from bi-exponential fit (or phasor plot)	calculated from the ratio of the cross- to auto-correlation function
number of molecules	not measured can be achieved by a combined FLIM – wide-field fluorescence microscopy approach (calibration gives ratio of n_A/n_D)	directly given, depending on the observation volume
Concentration	not measured approximation with a combined FLIM- fluorescence intensity microscopy possible	directly given by the number of molecules in the observation volume
K_d	calculation based on bound fraction and on an estimation of acceptor concentration	directly from the concentrations

Table 21 Comparison of FRET-FLIM and FCCS

(Sahoo and Schwille, 2011, Bacia et al., 2006, Piehler, 2014)

Table 22 compares the values found with the two methods. In general, the FRET-FLIM bound fraction is lower (20 % for the CC- and 18 % for the NC-terminal tagged p67^{phox}/p47^{phox}) and less scattered than the one found with FCCS (values for the mTurquoise bound fraction around 43 % for the CC- and 23 % for the NC-terminal tagged p67^{phox}/p47^{phox}), i.e. both techniques gives results in the same range. In order to know, whether these apparent bound fractions indeed reflects the biological situation, other factors, which might bias their interpretation, must be taken into consideration.

Tested interaction		β (FCCS) _{FLCS} (Average \pm SD)	β (FLIM) (Average \pm SD)
p67 ^{phox} -mTurquoise + p47 ^{phox} -Citrine	[%] of Citrine	29 \pm 5	
	[%] of mTurquoise	43 \pm 20	20 \pm 6
	n	4	12
mTurquoise-p67 ^{phox} + p47 ^{phox} -Citrine	[%] of Citrine	9 \pm 5	
	[%] of Cyan	23 \pm 14	18 \pm 4
	n	5	7
p67 ^{phox} -tandem (positive control)	[%] of Citrine	58 \pm 20	
	[%] of Cyan	116 \pm 81	20 \pm 4
	n	6	7

Table 22 Comparison of the bound fraction obtained by FCCS and FRET by FLIM

5.1.1.1 Factors influencing the apparent bound fractions of proteins

In order to get reliable results for both techniques, two points have to be considered: First, FP based studies demand specific preconditions concerning the FP itself and the fusion protein; second, each method has its specific limitations. The following paragraph (5.1.1.2) is dedicated to clarify these points regarding the FRET-FLIM and FCCS approach of this project and their outcomes.

Photobleaching of the FP and insufficient maturation are the most common phenomena rendering FPs to a non-fluorescent state, which will bias the outcomes. Thus, these problems must be minimized by choosing the appropriate experimental conditions. Furthermore, the FP tag can impede or even abrogate protein-protein interactions. Therefore, it is important to

perform functional studies of the used fusion proteins. In the following, these points will be discussed in greater detail.

Photobleaching

Fluorescent proteins, as any fluorophore, can undergo a large variety of photoreactions upon irradiation and some of them are irreversible and induce a slow loss of their fluorescence by the so-called photobleaching (Bourgeois et al., 2012). Photobleaching induces the formation of a complex mixture of photoproducts. It includes (i) dark species that do not contribute to the fluorescence signal and do not absorb anymore and (ii) irreversibly modified but still fluorescent FPs displaying changes in their fluorescence properties. The proportion of each photoproducts and the mechanisms involved in their formation depend on the excitation regime (Duan et al., 2013). The formation of dark species influences directly the amount of fluorophores and the modification of their fluorescence properties may change the interpretation of the experiments. Photobleaching should be monitored and carefully avoided.

For wide field microscopy, we use a short excitation time of usually 800 ms and a set of neutral densities to attenuate the light power leading to 0.17 W/cm² (CFP channel), 0.04 W/cm² (YFP channel), and 0.25 W/cm² (mCherry channel). No photobleaching is expected here.

FLIM and FCCS data have been acquired with the SymPhoTime software (v5.3.2, PicoQuant). It has a function (multichannel scaler or MCS) that shows the evolution of the fluorescence intensity during the recording time. In case of photobleaching, a decrease of the fluorescence intensity in the MCS is observed.

For the FLIM setup, the laser is pulsed and scans the field of view. A rough estimation of the maximal power was made to be at 340 W/cm². The monitoring of the donor fluorescence with the MCS trace did not reveal any photobleaching. In addition, the reference lifetimes for the donors are comparable to values from the literature for cyan donors (mTurquoise $\tau = 3.90 \pm 0.09$ [ns], reference 4.06 ns *in vitro* (Fredj et al., 2012)/ 3.48 ns in live cells at 37 °C (Walther et al., 2011), Aquamarine $\tau = 3.95 \pm 0.07$ [ns] (Erard et al., 2013), and for Citrine ($\tau = 3.00 \pm 0.07$ [ns] at 20°C against 2.97 [ns] at 37°C (Walther et al., 2011)). Citrine is also an acceptor. In that case, the excitation is performed by the energy transfer (FRET) and its power is a fraction of the direct excitation of the donor. If it does not bleach as a donor, it may not bleach as an acceptor. For mCherry as an acceptor, we do not have any monitoring of the bleaching, but from literature it can be assumed to have a good photostability (Shaner et al., 2004, Shaner et al., 2007). Therefore, we consider that in FLIM –FRET experiment we do not have photobleaching.

In FCCS, we monitor the MCS traces of both fluorophores (mTurquoise and Citrine). Photobleaching was not observed on the MCS trace of mTurquoise. The FCCS detection setup is not optimized for Citrine, thus we had to increase the power of the laser to collect a reasonable amount of photons. As a consequence, we observed some bleaching in the beginning of the MCS trace. We select the photons acquired after this fast bleaching to calculate the correlation function.

Dark states

Fluorescent proteins undergo upon illumination, even with a very low quantum yield, different types of reversible photoreactions to the so-called dark i.e. non-fluorescent states. They include triplet state conversion under intense illumination, excited state proton transfer (Merola et al., 2010), and light driven photo-switching (also known as blinking). The latter was observed for Citrine (Heikal et al., 2000, Sinnecker et al., 2005) and for mCherry (Hendrix et al.), but was barely detectable for Turquoise and Aquamarine (Erard et al., 2013). We cannot predict the relative occurrence of these phenomena in our conditions of illuminations and did our best to minimize them.

Fluorophores in dark states would bias both, FRET-FLIM and FCCS measurement: In the case of the FRET-FLIM, only acceptors in dark states are relevant, since a dark donor is simply not measured and hence does not appear in the measurement data of the bound fraction. In contrast, a dark acceptor increases the donor average lifetime ($\langle \tau_{DA} \rangle \uparrow$) leading to a decrease of the apparent bound fraction of donor ($\beta_{Donor} \downarrow$). In FCCS, a dark state of any FP would bias the results. Since a dark state is only probable for Citrine and not for mTurquoise, the auto-correlation amplitude of Citrine would be overestimated (apparent $G_{Citrine}(0) \uparrow$) resulting in a too small apparent cyan bound fraction of mTurquoise ($\beta_{mTura} \downarrow$). Hence, the effect of Citrine in dark states goes in the same direction as for FRET-FLIM^{xxxix}. However, since the dark states are light driven, i.e. the probability of their occurrence increases with the density of illumination, their probability might be higher for FCCS, which we think is operating at higher illumination regime.

^{xxxix} Citrine = acceptor

Maturation and misfolding issues

Insufficient maturation can affect the FP and/or the protein to which the FP is fused. A non-mature FP is non-fluorescent and thus bias any fluorescence measurement. The cyan variants mTurquoise and Aquamarine (Erard et al., 2013) as well as Citrine (Griesbeck et al., 2001) mature very well in eukaryotic cells at 37 °C, therefore we assume not to face maturation problems for these proteins. However, maturation problems of mCherry are well known (Heikal et al., 2000, Padilla-Parra et al., 2011b, Foo et al., 2012, Hillesheim et al., 2006). With regard to the used measurement techniques, only the FLIM measurement based on a Citrine-mCherry FRET couple may be concerned ($\langle \tau_{DA} \rangle \uparrow \Leftrightarrow \beta_{Donor} \downarrow$). However, no obvious hint for maturation problems were found, neither during the transfection efficiency optimization, which show 99 % of mCherry positive cells in comparison to Citrine (Figure 19).

It is as well possible, that the fusion protein is not completely expressed (without the FP or shortened subunit) or that free FPs occur. Western Blots of the subunits \pm FP, developed with anti-subunit and anti-FP antibodies, give some evidence of untagged NOX subunits for p67^{phox}-mTurquoise (14 %) and for mCherry-p40^{phox} (14 %) as well as for free Citrine (13 %, p47^{phox}-Citrine blot). It is likely, that these observations are related to sample preparations, as explained in further detail in paragraph 4.1.1. Even if the proteins are fully expressed, their functionality is not necessarily given. Therefore, we tested, whether our fusion construct maintained their functionality.

Proving the functionality

FPs can impede or prevent physiological interactions of its fusion protein to its partners both by direct interaction and by introduction of mechanical/energetic barriers such as sterical hindrance or electrostatic repulsion. Additionally, the NOX subunit can be incorrectly folded due to the presence of the FP tag, which may lead to the same result (Sun et al., 2011a).

Therefore, it is crucial to test the maintenance of the functionality of the FP fusion proteins. Within this study, we performed successfully a TIRF experiment for three different compositions of FP tagged NOX subunits: CCN-, CNN-, and NNN-tagged p67^{phox}/p47^{phox}/p40^{phox}^{x1}. After activation with PMA, all three tagged subunits translocated to the membrane. Since no difference between the three samples were observed (Figure 36), it can be assumed, that the position of the fluorophore (N- or C-terminal), has no or only a minor influence on the activation induced translocation of the subunits. However, this experiment does not finally prove, that full functionality of the NOX2 complex is conserved. To tackle this

^{x1} P67^{phox} was always tagged with mTurquoise, p47^{phox} with Citrine, and p40^{phox} with mCherry.

question, a luminescence assay was performed. The production of superoxide anions, which is monitored by this assay Figure 37, finally proved that the NOX2 complex could be reconstituted. These two assays clearly show, that the fusion proteins used in this study maintained their functionality.

To get a better idea about the quantitative impact on the protein assembly, a cell free *in vitro* activation assay was performed. This assay uses membranes of neutrophils containing gp91^{phox}/p22^{phox} complex and recombinant cytosolic proteins purified from *E.coli*. These experiment were performed by a colleague of the group, T. Bizouarn. She compared the activity of the cell free system in three situations: p67^{phox} ± N-terminal tag and p47^{phox} ± C-terminal tag and the wild type (Table 23). It shows clearly, that only the N-terminal tag on p67^{phox} decreases the activity (V_{max}) and increases the EC_{50} value of the activated NOX2 complex. It might be speculated, whether the N-terminal position of the FP influence the interaction of p67^{phox} with Rac and/or with the flavocytochrome b558, which is located in the vicinity of the p67^{phox} N-terminus Figure 64.

		p67^{phox}	mTurquoise-p67^{phox}
p47^{phox}	EC_{50}	12.5 ± 3.7	47.0 ± 14
	V_{max}	161 ± 8	109 ± 8
p47^{phox}-Citrine	EC_{50}	13.3 ± 1.5	not done
	V_{max}	169 ± 3	

Table 23 EC_{50} derived from *in vitro* activation assays

EC_{50} [nM], V_{max} [mole O₂^{•-}/s/mole Cyto_{b558}]

5.1.1.2 Methodology specific biasing factors on the bound fraction

FRET-FLIM

Beside other influence factors mentioned and summarized for FRET-FLIM in Table 24, we consider that conformational changes induced by the FP are likely to have the strongest impact on the FRET-FLIM based apparent bound fraction: They can either lead (i) to an inability of protein interactions, (ii) to an unfavourable spatial orientation or (iii) to too large distance between the fluorophores and hence allowing only a discrete number of energetically favourable conformations of which only some may allow FRET.

The last two points may lead to an open conformation in the case of p47^{phox} and p40^{phox} tagged on both ends (tandems). These subunits are supposed to bind to membranes in their open conformation. Indeed, the p40^{phox} tandem showed some bright patches on the membrane, but only in a minor extent which cannot explain the small bound fraction of around 20 %. Since these patches were mainly found in the Citrine channel and not in the mCherry channel, they may be due to incomplete expressed proteins. In contrast, the p47^{phox} tandem never exhibited in any experiment a trace of membrane binding. Hence, an open confirmation of p47^{phox} does not seem to be induced by the attached FPs.

In conclusion, we do not have a direct proof, that conformational heterogeneity abrogated the energy transfer and hence mislead the outcome of the bound fraction.

factors influencing β_{Donor}	consequence for FLIM results [°]	Probability
<ul style="list-style-type: none"> • Photobleached donor[*] 	<ul style="list-style-type: none"> - bi-exponential decay for Aquamarine/ mTurquoise $\Rightarrow \langle \tau_{DA} \rangle \downarrow, \beta_{Donor} \uparrow$ - no effect for Citrine 	not observed
<ul style="list-style-type: none"> • Non-absorbing acceptor⁺ <ul style="list-style-type: none"> ○ photobleaching ○ missing acceptor <ul style="list-style-type: none"> - insufficient maturation - incomplete expression ○ dark state[◇] 	<ul style="list-style-type: none"> \Rightarrow functional acceptor \downarrow $\Rightarrow \langle \tau_{DA} \rangle \uparrow, \beta_{Donor} \downarrow$ 	negligible
<ul style="list-style-type: none"> • FP induced conformational changes[#] 	<ul style="list-style-type: none"> impeded protein-protein interaction $\Rightarrow \langle \tau_{DA} \rangle \approx \tau_D \Rightarrow \beta_{Donor} \downarrow.$ 	possible (see discussion below)
<ul style="list-style-type: none"> • structural influence <ul style="list-style-type: none"> ○ distance $\geq 100 \text{ \AA}$ ○ unfavourable orientation 	<ul style="list-style-type: none"> $\langle \tau_{DA} \rangle \approx \tau_D \Rightarrow \beta_{Donor} \downarrow.$ $\kappa^2 = 0 \Rightarrow \langle \tau_{DA} \rangle \approx \tau_D$ $\Rightarrow \beta_{Donor} \downarrow$ 	<ul style="list-style-type: none"> interaction specific possible (compare 1.3.2)

Table 24 Non-biological factors influencing the bound fraction derived from FRET-FLIM

Each factor or a mix of them can influence the apparent bound fraction.

[°] The apparent bound fraction of the donor reflects a mix of affected and unaffected interactions

^{*}(Tramier et al., 2006, Hoffmann et al., 2008, Walther et al., 2011)

⁺(Bastiaens et al., 1996, Sun et al., 2011a)

[#](Snapp, 2005)

[◇](Heikal et al., 2000, Sinnecker et al., 2005, Hendrix et al., Erard et al., 2013)

FCCS

FCCS does not depend on distance and orientations, therefore it is a good method to clarify, whether there are conformational heterogeneities, which do not hinder the interaction itself, but prevent FRET. Here, we will describe the factors that specifically influence the methodology, namely the observation volume. A general overview of all factors described in the previous paragraph on FCCS can be found in Table 25.

The main bottleneck of FCCS measurements is the observation (or focal) volume. As we explained in part 2.2.11, the observation volumes for mTurquoise ($V_{mTurquoise}$) and Citrine ($V_{Citrine}$) should have the same centre. If this condition is fulfilled, the cross correlation volume (V_{cross}) is also aligned and has a value comprised between $V_{mTurquoise}$ and $V_{Citrine}$. Thus V_{cross} depends mainly on the emission volume of the different colours and can be displaced due to misalignment of the excitation sources and chromatic aberration of the optics^{xli}. Difference in the volumes of mTurquoise ($V_{mTurquoise}$), Citrine ($V_{Citrine}$), and cross correlation (V_{cross}), can be detected from the measured diffusion times τ_D of a tandem (here p67^{phox}-tandem). If the alignment of the volumes is appropriate, $\tau_{D(cross)}$ should be comprised between $\tau_{D(Citrine)}$ and $\tau_{D(mTurquoise)}$. The measured values give the following order: $\tau_{D(Citrine)} \approx \tau_{D(mTurquoise)} < \tau_{D(cross)}$. The slight differences between Citrine and mTurquoise can be explained by the wavelength dependents diffraction of the light, which leads to slightly different observation volumes of mTurquoise and Citrine. The longer diffusion time (about 1.4 times longer) for the cross correlation function is most probably a consequence of the larger V_{cross} , which can be explained by a displacement of $V_{mTurquoise}$ and $V_{Citrine}$ relative to each other. This misalignment ends in a lower cross-correlation amplitude compared to the auto-correlation ones and finally in a decrease of the observed bound fraction for both colour (Foo et al., 2012, Bacia et al., 2006).

Like a dark state, an underestimation of one colour can also be caused by the insufficient sensitivity of the setup for this colour (Bacia et al., 2006). In our case, the Citrine detection is not optimized, so we cannot exclude that some photons are lost in the noise leading therefore to an underestimation of the cyan bound fraction. Finally, the occurrence of FRET influences the observed bound fraction: The auto-correlation amplitudes increase, while the cross-correlation one decreases, which ends up in a loss of bound fraction (Hom and Verkman, 2002, Foo et al., 2012).

As mentioned in the results part, Citrine is overexpressed in our experiment, thus the expected yellow bound fraction should be smaller than the one of mTurquoise ($N_{mTurquoise} < N_{Citrine} \Leftrightarrow$

^{xli} The problem with the focal volume occurs as well when a single-wavelength FCCS is performed, which means in turn that an insufficient laser alignment is not the only explanation of this phenomenon.

$\beta_{\text{Citrine}} < \beta_{\text{mTurquoise}}$). For the cyan bound fraction, the amount of cyan molecules in complex and the amount of non-fluorescent yellow proteins in complex is crucial. According to the relatively low mTurquoise expression and the occurrence of non-fluorescent Citrine (photobleaching, dark states), the cyan bound fraction is relatively high. The bound fraction of Citrine depends on the number of yellow molecules in complex and on the number of non-fluorescent cyan in complex (Foo et al., 2012). This theoretic approach matches the values observed in our experiment.

factors influencing β	consequence for FCCS results	Probability
<ul style="list-style-type: none"> • Non-fluorescence FPs <ul style="list-style-type: none"> ○ Photobleaching <ul style="list-style-type: none"> - mTurquoise - Citrine ○ dark state ○ missing FP <ul style="list-style-type: none"> - insufficient maturation - incomplete expression • FP induced conformational changes 	<ul style="list-style-type: none"> - mTurquoise: $G_{\text{mTurq}}(0) \uparrow \Rightarrow \beta_{\text{Citrine}} \downarrow$ - Citrine: $G_{\text{Citrine}}(0) \uparrow \Rightarrow \beta_{\text{mTurq}} \downarrow$ - impeded protein-protein interaction $\Rightarrow G_{\text{cross}}(0) \downarrow \Rightarrow \beta_{\text{Citrine or mTurq}} \downarrow$ 	<ul style="list-style-type: none"> - <u>not</u> observed - observed - Aquamarine/mTurquoise: unlikely - Citrine: up to 30 % depending on the illumination regime - low for Aquamarine/mTurquoise/ Citrine - max. 13 % (WB results) - possible (see discussion above)
<ul style="list-style-type: none"> • vocal volume 	<ul style="list-style-type: none"> - $V_{\text{cross}} > V_{\text{Citrine or mTurq}}$ $\Rightarrow G_{\text{cross}}(0) < G_{\text{Citrine or mTurq}}(0)$ $\Rightarrow \beta_{\text{Citrine or mTurq}} \downarrow$ 	<ul style="list-style-type: none"> - observed (see discussion above)
<ul style="list-style-type: none"> • FRET 	<ul style="list-style-type: none"> - $G_{\text{Citrine or mTurq}}(0) \uparrow, G_{\text{cross}}(0) \downarrow$ $\Rightarrow \beta_{\text{Citrine or mTurq}} \downarrow$ 	<ul style="list-style-type: none"> - low (low FRET levels observed)

Table 25 Non-biological factors influencing the bound fraction derived from FCCS

Each factor or a mix of them can influence the apparent bound fraction.

(Foo et al., 2012, Hom and Verkman, 2002)

5.1.1.3 Conclusion on the apparent bound fraction

As the previous discussion exposes, the values of the bound fraction of proteins may be influenced by several parameter ($\Rightarrow \beta_{\text{apparent}} < \beta_{\text{true}}$) and their interpretation as a biological fact is not trivial.

In the ideal case, a tandem reveal 100 % of bound fraction in the FCCS, since both fluorophores are linked together and hence must co-diffuse. Accordingly, an observed bound fraction of an intermolecular protein-protein interaction below the tandem bound fraction, would have a biological reason. Our first FCCS results reveals a cyan bound fraction of the p67^{phox} tandem around 100 %, largely scattered, though. Provided that the scheduled repetition of this experiment will support the first results with better precision, we face the ideal case for this tandem, i.e. the discussed influencing factors would be negligible. Such a result would still leave two options for the interpretation of the intermolecular interaction of p67^{phox} and p47^{phox}: Either, it reflects the interference of the FP-tag with the interaction; or the low bound fraction observed with FCCS indeed reflects the biological interaction between these subunits. We assume that the interference of the FP tag rather improbable, as the in vitro experiments indicate. This leads us to the conclusion, that the low bound fraction observed with FCCS has most probably a biological reason.

How would such a FCCS result influence the interpretation of the bound fraction derived from FRET-FLIM? If $\beta_{\text{FRET-FLIM}} \approx \beta_{\text{FCCS}}$, it could be assumed that distance and orientation did not have a major impact on the apparent bound fraction obtained with FRET-FLIM and hence lead to the same conclusion as for FCCS. Regarding the outcomes of the heterodimeric interactions between p67^{phox} and p47^{phox}, we found with both methods the same results (table 21). In contrast, the results for the p67^{phox}-tandem are different^{xliii}. It might be possible, that this difference is related to distance and orientation problems, including a misfolding of the tandem, which would not affect the FCCS outcome.

Walther and co-workers propose that the apparent “bound fraction” of a tandem observed with FRET-FLIM could be equated to a 100 % true bound fraction (Walther et al., 2011). This would give rise to the contradictory interpretation that p47^{phox} and p67^{phox} are 100% bound since the apparent bound fraction of the tandem is similar to the heterodimeric ones (Table 22): The low bound fraction observed in FLIM would be a bias induced by the photophysical properties of the acceptor and not of biological relevance at least for the p47^{phox}/p67^{phox} interaction. We think it is questionable to assume that the apparent bound fraction of the tandem derived by FLIM refers to a 100 % binding and to extrapolate this assumption to intermolecular bindings: (i) The

^{xliii} assuming that the 100 % bound fraction (FCCS) will be confirmed by a repetition of the experiment

folding of a tandem tagged on both termini may be different from a protein tagged only on one terminus; (ii) the apparent FRET efficiencies of a tandem and intramolecular interactions can be different simply due to the orientation/distance between the FPs, which is likely to be the case.

Therefore, we give preference to the FCCS based interpretation of the bound fraction derived from FRET-FLIM. Thus, we believe that the observed low bound fraction of the heterodimeric interaction reflects a biological fact: only a fraction of p67^{phox} and p47^{phox} form a complex in live cells.

5.1.2 Dissociation constant estimated with FRET-FLIM and wide-field microscopy approach

It is challenging to estimate the concentration of FP labelled proteins in cells but mandatory for an estimation of the K_d . Here we partly circumvent this problem by describing the K_d with the bound fraction determined by FRET-FLIM and estimating the total acceptor concentration from FCS measurements. Alternatively to this concentration approximation, the acceptor concentration could be calculated with proportionality factor between N_{FP} and I_{FP} (3.2.3.1, Equation 26). An additional calibration step would be necessary to get this factor, which can, for example, be derived from micro-droplets of known fluorophore concentration.

The influence of the bound fraction on the K_d is critical (appendix 8.4) and a valid interpretation of the biological meaning of the K_d must be done very carefully, since the uncertainties of the bound fraction are not dispelled yet. Repetition of the FCCS experiments may give more precise information about the bound fraction, which will contribute to a better interpretation of β and subsequently of the K_d obtained by FRET-FLIM.

The K_d we found is an order of a magnitude higher than the low nM range, which was found by *in vitro* studies (Lapouge et al., 2002, Karimi et al., 2014). Such a difference between K_d obtained in live cell and *in vitro* has already been observed in several studies (Cardarelli et al., 2009, Foo et al., 2012) and may be explained by the complex cellular environment, which may allow interactions with other proteins (Ganesan and Zhang, 2012).

Additionally, FCCS offers the possibility for direct concentration determination and hence for K_d estimations. It would be interesting to compare these results obtained with the two different methods. Since for FCCS, a detailed correction strategy for reliable concentration and K_d measurements was already developed by Foo and co-workers^{xliii} (Foo et al., 2012, Müller et al., 2005), it can serve as a reference for the accuracy of the FRET-FLIM based approach presented here.

^{xliii} correction of the different volumes, estimation of the probability of non-fluorescent and label-free species, estimation of the individual FRET level by pulsed internal excitation FCCS

5.2 Discussion of the structural information obtained by FRET-FLIM

The spatial organisation of the ternary complex between the cytosolic subunits of the NADPH oxidase remains unclear. Although some domains of the subunits as well as the intra- and inter-molecular interaction sites are crystallized, the complete picture is missing. Additionally, the available information is derived from *in vitro* studies like small angle x-ray scattering (SAXS), neutron scattering, and x-ray crystallography. The first two are low resolution techniques ($\sim 100 - 300 \text{ \AA}$) working in aqueous solutions, containing information about the shape (radius of gyration R_g) and size of a protein (maximum distance D_{max}). The R_g measures average of square centre-of-mass distances in the molecule and therefore gives the equilibrium conformation of a set of conformations, while the D_{max} gives the maximum distance within the protein (Glatter and Kratky, 1982, Lobanov et al., 2008). The X-ray crystallography gives the best resolution ($\sim 1.5 \text{ \AA}$) but it can only be derived from crystallized samples. X-ray crystallography and its interpretation can be challenging (Wlodawer et al., 2008). However, *in vitro* structures do not necessarily reflect the situation in live cells.

Here, we compare published data from *in vitro* studies with the structural information derived from the molecular FRET efficiency values of the intra- and inter-molecular interactions of the cytosolic subunits. We aim to build a complete model for the ternary complex. Please note, that the molecular FRET efficiency contains only information from conformations where FRET is possible^{xliv}. This means that the main factors influencing the molecular FRET efficiency are the distance between the fluorophores and their spatial orientation, which are both influenced by the flexibility of the subunit and the length and flexibility of the linker between the FP and the subunit. As a general remark, the linkers are of random amino acid composition and have a length between 5 – 10 amino acids (2.2.3, Table 4). An improvement in linker design in terms of flexibility (glycine-rich linker) and length may result both in higher FRET efficiencies and increased short lifetime fraction (Shimozono and Miyawaki, 2008). Nevertheless, even an optimized CFP-YFP-tandem ($E_{mol.} = 98 \%$) with a two aa linker has only 71 % of short lifetime component i.e. 71 % of CFP able to transfer their energy to the nearby acceptor (Shimozono et al., 2006). This example demonstrate, how sensitive FRET is towards the spatial orientation of the chromophores. The linker will only be discussed for situations, for which a significant influence on the outcome can be assumed.

^{xliv} For a detailed discussion why FRET only occurs for a minority of the molecules (including the bound fraction and K_d) please go back to paragraph 2.2.3.

5.2.1 Intra-molecular interactions

p47^{phox} has a compact N-terminus and a semi-flexible, moving C-terminus

In vitro studies showed, that p47^{phox} is folded in an S-shape structure by an intramolecular interaction with the SH3B domain (Ago et al., 2003) to prevent the membrane interaction of the PX domain. The tandem SH3 domains are in complex with the auto-inhibitory region (AIR) to obstruct a binding to p22^{phox} (Sumimoto, 2008), while the C-terminus is a mostly unfolded chain (Durand et al., 2006). Until now, a complete crystal structure of p47^{phox} is missing. However, several domains have been crystalized: PX (PDB 1KQ6, (Wahl et al., 2003)), tandem-SH3/AIR (PDB 1NG2, (Groemping et al., 2003)), and PRR (PDB 1K4U (Kami et al., 2002)). They were modeled in silico to a full structure (Meijles et al., 2014). Unfortunately, no PDB file exists, so we labelled the termini for the PX and PRR domain from their crystal structures and re-identified them in the full length model Figure 55.

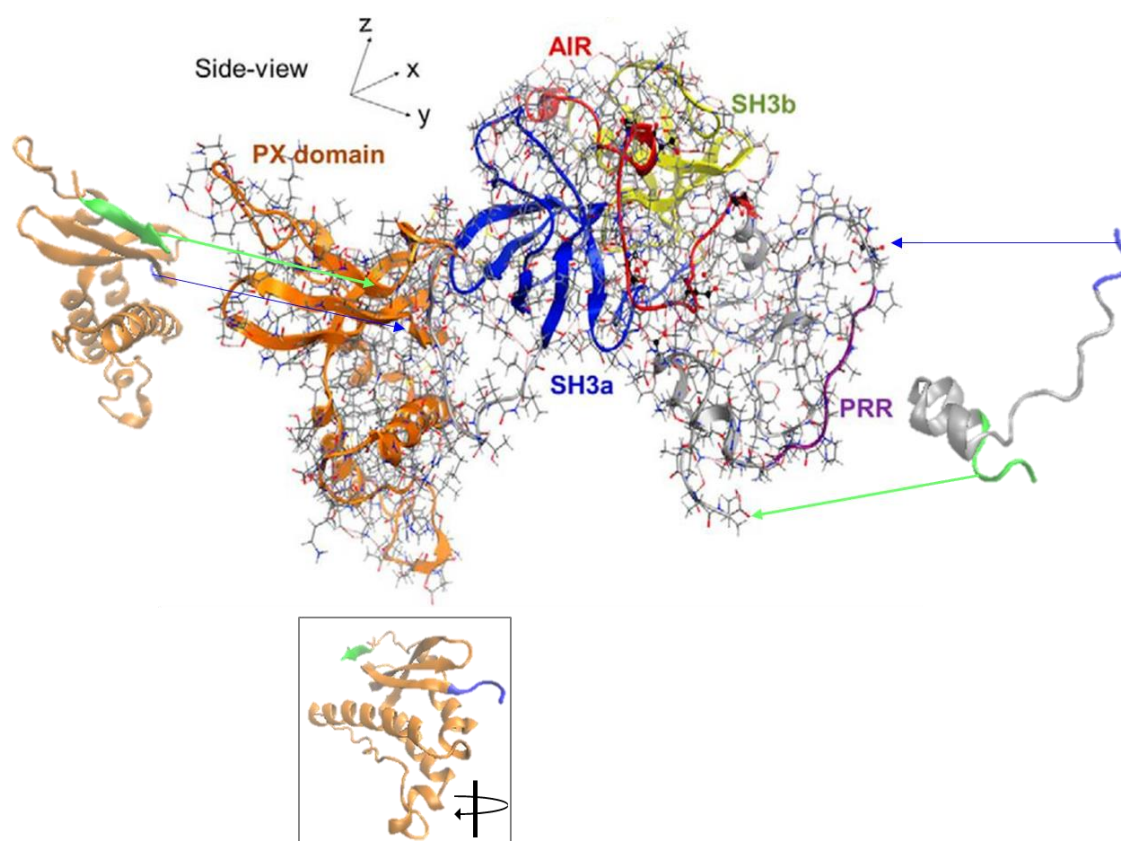


Figure 55 In silico construct of full length p47^{phox} in resting state

Meijles and co-workers published the in silico model shown in the centre (grey). Ribbon models of the structural elements (PX-domain, SH3a, SH3b, AIR and PRR) were superimposed. Since no PDB file of this structure is existing (Meijles et al., 2014), the termini (N-termini in blue, C-termini in green) were identified with the aid of the crystal structures of the PX (PDB 1KQ6) and PRR domain (PDB 1K4U). The arrows point to the position of N- and C-termini in the complete model. To facilitate the understanding of the directions in the PX domain, an axial rotate position of the PX domain is displayed in the insert. This model was developed with VMD based on published data and structures in the Protein Data Bank (PDB).

We built a p47^{phox} tandem to investigate the intra-molecular interactions between the N- and the C-terminus by tagging both ends with FPs (Citrine and Aquamarine, respectively). A molecular FRET efficiency of 60 ± 8 [%] and a short lifetime fraction (corresponding to the FRET positive fraction) of 18 ± 2 [%] was found for this construct. Regarding the compactly packed amino acids 1 – 358 of p47^{phox} ($R_g = 28$ Å (Grizot et al., 2001b)) and the *in silico* model proposed in Figure 55, the N-terminal FP can be assumed to be in a fixed position. The C-terminal part of p47^{phox} is expected to be elongated and less structured, leading to a $R_g = 31 - 36$ Å and a $D_{max} = 90 - 125$ Å for full length p47^{phox} (Durand et al., 2006, Grizot et al., 2001b, Yuzawa et al., 2009) Those values are higher than the one expected for a globular

protein of this size)^{xlv}. Therefore we anticipated that p47^{phox} is flexible downstream the auto-inhibitory region.

Considering all factors influencing FRET, we believe that conformational changes of the flexible C-terminus towards the fixed position of the N-terminal tag result in a mixed FRET efficiency of the various proximities and orientations as well as in orientations, which do not allow any FRET (Sun et al., 2013).

In conclusion, our data support the hypothesis that p47^{phox} consists of a compact N-terminus and a semi-flexible C-terminus, which is in motion in live cell conditions.

^{xlv} For globular proteins of this size, the R_g is around 22 – 24 Å, the D_{max} around 70 – 80 Å (Durand et al., 2006)

p40^{phox} is organised in a rigid complex

In the resting state, p40^{phox} is in an auto-inhibitory state to prevent a membrane binding of p40^{phox} to phosphatidylinositol 3-phosphate (PI(3)P) rich membranes. This state is accomplished by an interaction between the N-terminal PX domain and the C-terminal PB1 domain (Ueyama et al., 2007, Bravo et al., 2001). The complete crystal structure of p40^{phox} (Honbou et al., 2006, Honbou et al., 2007) reveals a compact molecule, which is in line with the R_g found by SAXS or neutron scattering (R_g between 27.7 – 29.5 Å (Grizot et al., 2001b, Yuzawa et al., 2009)). The maximal distance D_{max} was determined to be at 85 Å (Yuzawa et al., 2009), which shall be small enough to allow FRET ($< 2 * R_0 \approx 100$ Å (compare 1.3.2)).

We studied the intra-molecular interactions of p40^{phox} with FRET-FLIM by tagging its N-terminus with mCherry and the C-terminus with Citrine. Our data give a molecular FRET efficiency around 51 %. We explain these findings by structural properties of the construct: Figure 56 shows an *in silico* model of this tandem derived from the crystal structures of each sub-molecules.

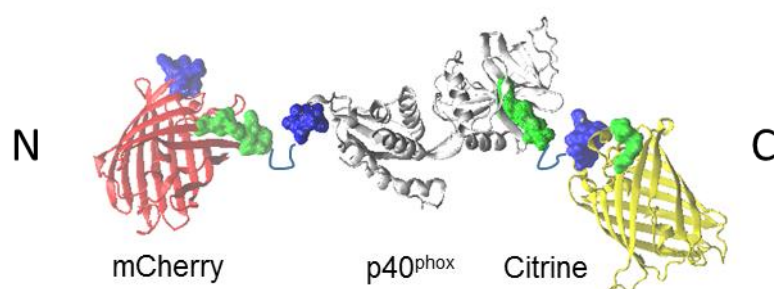


Figure 56 Structure of the p40^{phox} tandem

The structure shows the crystal structures of mCherry (PDB 2H5Q), p40^{phox} (PDB 2DYB), and Citrine (PDB 1HUY) which are schematically linked together (the linkers in the tandem have a length of 7 and 10 aa, respectively). Blue surface structures refers to the first N-terminal aa, the green one to the last five C-terminal aa of each protein component. The structure was built with VMD without any refinement of the orientation. It is prone to give an idea about the approximate localization of the FPs and about the proportion regarding the size of the different components.

It visualises the large volume of the FPs in comparison to p40^{phox}, which gives rise to the assumption that the FPs cannot move freely and are likely to arrange themselves in only a few possible conformations due to sterical hindrance. These conformations are induced constraint orientations of the chromophores, which influence the energy transfer.

Additionally, the crystal structure exhibits that the termini of p40^{phox} are relatively far away from each other (around 66 Å, measured with VMD and point out to opposite directions (Figure

56, p40^{phox} displayed in grey). Even if the distance between the termini is smaller than the D_{max} (which should still allow FRET), this distance will not be optimal for the energy transfer.

In conclusion, our findings for the intra-molecular interactions of the p40^{phox} tandem are consistent with a compact structure of reduced flexibility with N- and C-termini on opposite sides in good agreement with the available structural data.

p67^{phox} is elongated and semi-flexible

P67^{phox} is an elongated molecule, as the R_g around 45 – 55 [Å] and the D_{max} of 145 – 160 [Å] clearly indicate (Grizot et al., 2001a, Yuzawa et al., 2009, Durand et al., 2010). Only some parts of its structure were resolved: TPR (PDB 1WM5 (Inagaki and Suzuki, 2005) and 1HH8 (Grizot et al., 2001a), SH3A (PDB 2DMO (Tochio et al., 2006)), PB1 in complex with p40^{phox} (PDB 1OEY (Wilson et al., 2003)), and SH3B in complex with the C-terminus of p47^{phox} (PDB 1K4U (Kami et al., 2002)). Based on these partial structures Durand and co-workers built an *in silico* model of the complete structure of p67^{phox}. They determined the R_g both experimentally (SAXS) and from the structural simulations of random conformations, which led to diverging results (45 vs. 51 [Å]). This gives rise to the assumption that – even if p67^{phox} is a flexible molecule, only some tertiary structures can be occupied (Durand et al., 2010). In order to study the p67^{phox} structure in live cells, we built a N- and C-terminal tagged p67^{phox} (10 aa linkers), which is schematically displayed in Figure 57 (the model of Durand was linked to the crystal structures of Citrine and mTurquoise without any spatial optimization for the representation of FPs).

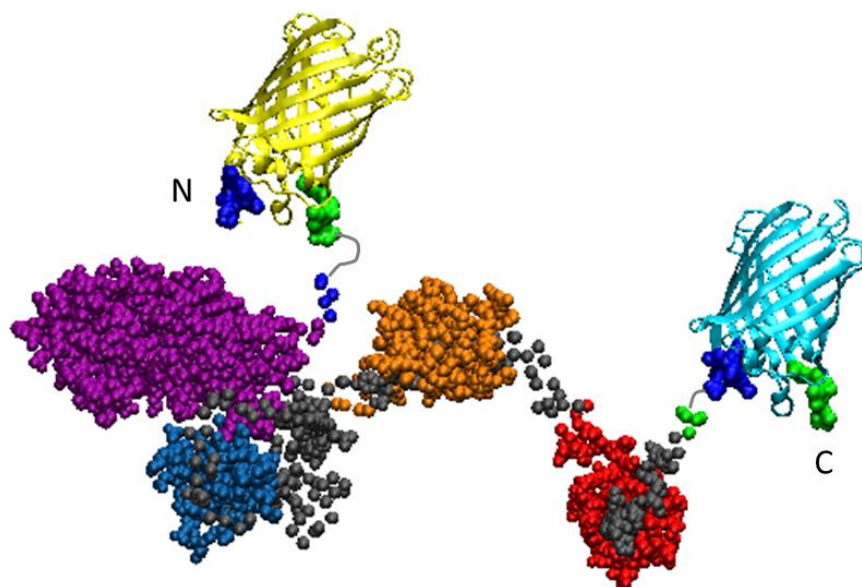


Figure 57 Structure of the p67^{phox} tandem

The *in silico* (BUNCH) model of full length p67^{phox} (Durand et al., 2010) is linked schematically to the crystal structures of Citrine (yellow, PDB 1HUY) and mTurquoise (cyan, PDB 4AR7) to display the constructed p67^{phox} tandem. N- and C-terminus of each protein are labelled in dark blue and green, respectively.

Colour code of the p67^{phox} domains: violet = TPR motif, blue = SH3A, orange = PB1, red = SH3B

Our findings reveal a molecular FRET efficiency of 52 ± 6 [%]. This finding is in line with the *in vitro* structure: The two ends of p67^{phox} are much closer than the maximal possible distance than the D_{max} of 145 – 160 [Å]. In fact, the N-terminus is facing inside while the compact TPR motif is facing outside, which brings the two termini to closer proximity. For the conformation as displayed here, a distance of 92 Å was measured with VMD from the PDB file of the structure, which was kindly provided by D. Durand. This is already below $2 \cdot R_0 \approx 100$ Å and thus allowing FRET. Additionally, the flexibility in the structure will allow several conformations (Durand et al., 2010) leading to various distances and spatial orientations of the fluorophores and as a consequence multiple FRET and non-FRET states.

To compare the outcomes of the three tandems with respect to their flexibility, we investigated a simple FP tandem, in which the fluorophores are connected with a 27 aa random linker (Aquamarine-Citrine tandem). This linker can be assumed to provide high flexibility to the FRET couple. It reveals two lifetimes both shorter than the lifetime of the donor alone with different proportions (35 %, 1.07 ns and 65 %, 3.51 ns), i.e. in all conformations, FRET is possible. This example clearly shows that even a short linker and/or the volume of the FPs can induce enough sterical hindrance to lead to two distinguishable energy transfers. Each of them

reflects a mix of finite orientations and distances, which cannot merge due to high energy barriers or a motion too slow to be registered by the method.

All subunit tandems show only one lifetime, which is reduced in comparison to the lifetime of the donor alone (Figure 51), i.e. only some of the conformations allow FRET. Conformational changes depend on the flexibility of the subunit, which is affected in turn by: (i) Strong intramolecular interactions, which can render a protein rigid like p40^{phox} and the N-terminus of p47^{phox}; (ii) by non-specific mechanical (sterical hindrance) or energetic reasons (hydrophobic/hydrophilic or electrostatic attraction/repulsion); and (iii) the time necessary to change between the conformations, which is influenced by the hydrodynamic radius of the structural subdomains of a molecule and time scale in which the movements can happen. Therefore, it is not surprising that even p67^{phox} – the most flexible subunit – shows only a minority of conformations allowing FRET due to impeded or slowed down motions.

To sum up, our method allows us to gain insight in the structure of all cytosolic subunits of the NADPH oxidase in live cells. Our findings are in line with the available *in vitro* data and point out that the C-terminus of p47^{phox} and the complete p67^{phox} molecule have a semi-flexible structure.

5.2.2 Inter-molecular Interactions

We investigated the interactions between the cytosolic subunits in two component models.

p67^{phox} and p47^{phox} interact via its C-termini in an anti-parallel orientation

In vitro studies showed the interaction of p67^{phox} and p47^{phox} via an interaction of the SH3B domain of p67^{phox} and the PRR motive and the downstream C-terminus of p47^{phox} (Fuchs et al., 1996, Kami et al., 2002, Massenet et al., 2005) The molecular structure of this binding was clarified by NMR as shown in Figure 58.

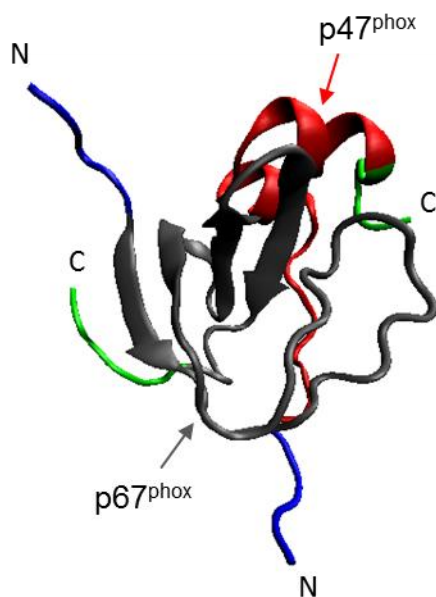


Figure 58 Structure of the interaction between p67^{phox} and p47^{phox}

NMR derived structure of the interaction side of p67^{phox} (SH3B domain, grey) and the one of p47^{phox} (PRR and downstream C-terminus, red). The N-termini are displayed in blue, the C-termini in green. The structure is derived from the PDB 1K4U file and developed in VMD.

The display clearly shows the antiparallel direction of the termini of p67^{phox} and p47^{phox}, which is in line with the findings of an increased D_{max} for the p67^{phox}/p47^{phox} heterodimer compared to the monomers: 180 Å for p67^{phox} + p47^{phox} vs. 145 Å for p67^{phox} alone and 90 Å for p47^{phox} alone (Yuzawa et al., 2009).

The FRET-FLIM approach reveals similar results in live cells: For the NN-terminal tagged p67^{phox} co-expressed with p47, no specific FRET could be measured, i.e. the distance between the fluorophores is too large to allow any energy transfer. This is expected regarding to the D_{max} , however – as shown before for the p67^{phox}-tandem – this parameter does not reflect the distance between the termini of the molecules. This proves that FRET gives structural information complementary to the SAXS measurement.

For the CC-terminal interaction, a molecular FRET efficiency of 52 ± 8 [%] was calculated, surprisingly, the NC-terminal tagged subunits^{xlvi} give a higher molecular FRET efficiency of 71 ± 6 [%]. An alignment with VMD of the solved NMR structure of the p47^{phox}/p67^{phox} binding domain (PDB 1K4U, (Kami et al., 2002)) and the *in silico* model of p67^{phox} (Durand et al., 2010)– shown in Figure 59 – reveals that the p67^{phox} N-terminus and the p47^{phox} C-terminus are in proximity (NC distance 76 Å Figure 59) but the two C-termini are nearer (CC distance 53 Å Figure 59). Despite the fact that p67^{phox} C-terminus can be assumed to be a flexible chain and that the FP is linked with a 10 aa linker, we could propose two reasons for the lower molecular FRET efficiency in the CC interaction. First, as we already showed with the p67^{phox} tandem, p67^{phox} is semi-flexible, which may bring the N- and C-termini even closer. In contrast, the energy transfer between the FPs linked to the C-termini of p67^{phox} and p47^{phox} may be impeded by the voluminous SH3B domain of p67^{phox} and the constrained mobility of the C-terminus of p47^{phox} due to its structure and the short 5 aa linker to the FP. Second, both C-termini point out in opposite direction, which might be less favourable for FRET.

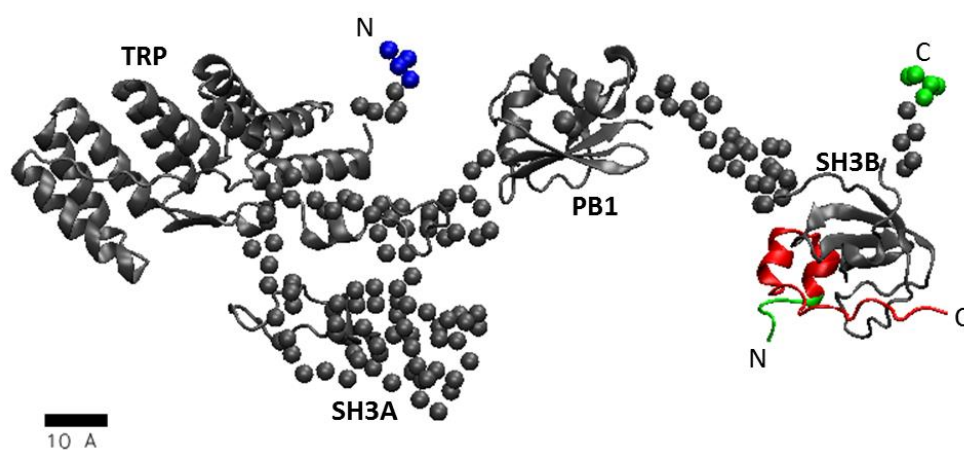


Figure 59 Localization of the p47^{phox} C-terminus in interaction with p67^{phox}

p67^{phox} (grey, *in silico* structure of (Durand et al., 2010)) interacts via its SH3B domain with the C-terminus of p47^{phox} (red). The model was built by an alignment of the resolved structure of the interaction site (PDB 1K4U), which was used as well for the structure simulation of p67^{phox} with VMD. The distance between the p67^{phox} N-terminus and p47^{phox} C-terminus is 76 Å and 55 Å between the two C-termini for the conformation as displayed here. N- and C-termini of the structure are labelled in blue and green, respectively.

^{xlvi} mTurquoise-p67^{phox} and p47^{phox}-Citrine

p40^{phox} interaction site is placed in the centre of p67^{phox} with similar distances to its termini

We investigated as well the interaction of p67^{phox} with p40^{phox}. The interaction is mediated by the PB1 domains of each subunit (Fuchs et al., 1995, Fuchs et al., 1996). Figure 60 shows the crystal structure of the two partners (Wilson et al., 2003).

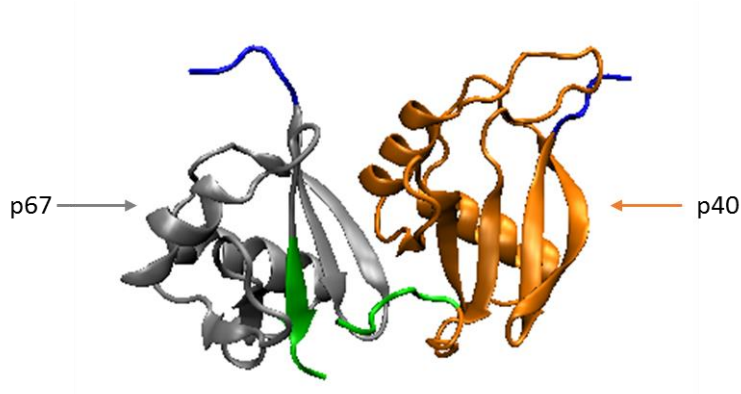


Figure 60 Crystal structure of the interacting PB1 domains of p67^{phox} and p40^{phox}

The PB1 domains of p67^{phox} and p40^{phox} are displayed in grey and orange, respectively. The N- and C-termini are labelled in blue and green, respectively. (PDB 1OEY, (Wilson et al., 2003))

The full length structure of p40^{phox} was overlaid with the full length construct of p67^{phox} with VMD (Figure 61). It suggests that p40^{phox} is arranged underneath p67^{phox} and that its SH3 of p40^{phox} points out above the paper plane, while the N-terminal PX-domain may be located below the PB1 domain of p40^{phox} thus below the paper plane.

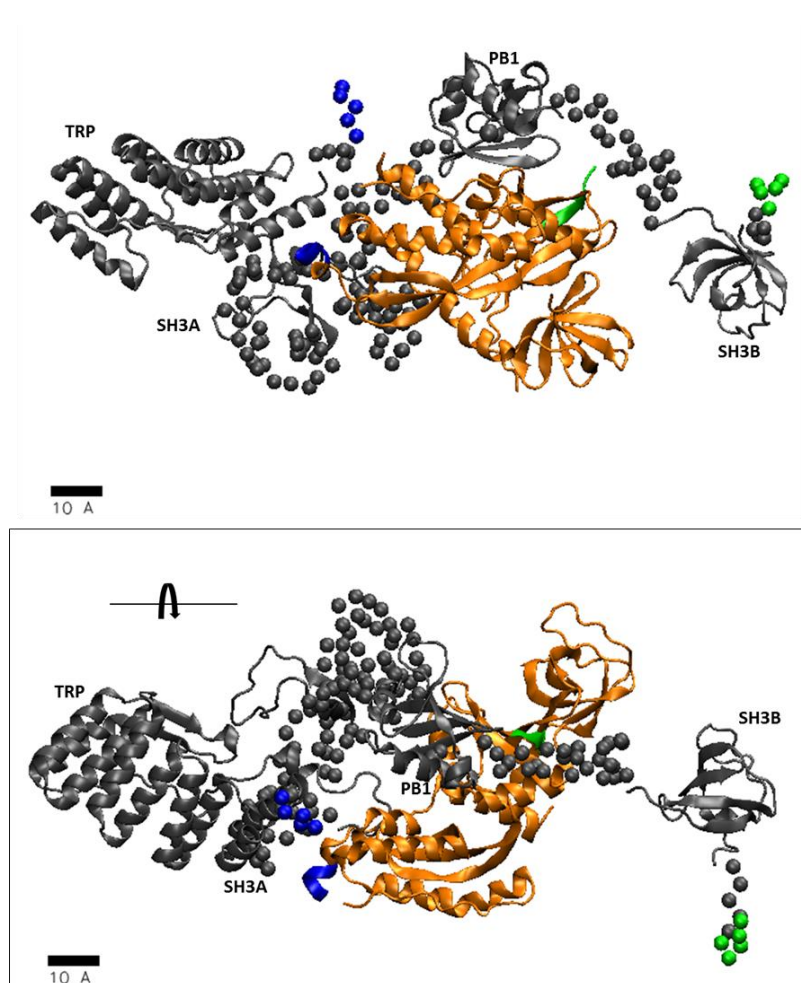


Figure 61 Interaction site of p67^{phox} and the PB1 domain of p40^{phox}

The *in silico* structure of p67^{phox} (Durand et al., 2010) was aligned with the crystal structure of full length p40^{phox} (PDB 2DYB). p67^{phox} is displayed in grey, p40^{phox} in orange, its N- and C-terminus in blue and green, respectively. The figure on the bottom shows a horizontally flipped version, which aims to contribute to the understanding of the 3D structure.

The molecular FRET efficiencies measured for CC- and NN-terminal tagged subunits are similar (CC: 56 ± 8 [%], NN: 63 ± 10 [%]). Since p40^{phox} is bound to the PB1 domain of p67^{phox}, FRET efficiencies can be expected in the same range, especially since the latter one may be able to move, whilst the first one has a stiff conformation, as discussed above. These findings fit perfectly to the values for the R_g for p67^{phox} alone and in complex with p40^{phox} (45 vs. 48 Å), which means that the addition of p40^{phox} has only a minor influence in the compactness of p67^{phox} (in contrast, R_g of p47^{phox}+p67^{phox} is 58 Å). The maximal distance is not changed with the addition of p40^{phox} (145 Å) (Yuzawa et al., 2009).

p47^{phox} interacts with p40^{phox} with similar affinity as to p67^{phox}

P40^{phox} interacts with the C-terminus of p47^{phox} via its SH3 domain (Grizot et al., 2001b, Massenet et al., 2005, Fuchs et al., 1995, Fuchs et al., 1996, Sathyamoorthy et al., 1997). The crystal structure of the interaction sites (PDB 1W70 (Massenet et al., 2005)) is shown in Figure 62.

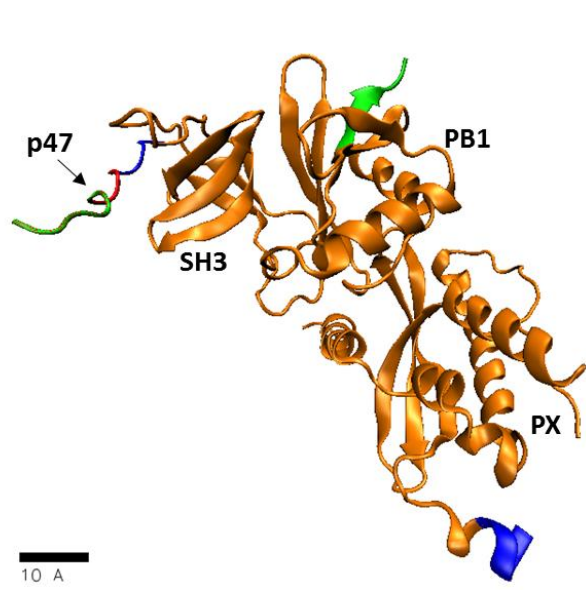


Figure 62 Alignment of the full-length crystal structure of p40^{phox} with the one of the interaction to p47^{phox}

C-terminus of p47^{phox} (red, chain C (12 aa) of PDB 1W70) in interaction with full length p40^{phox} (orange, PDB 2DYB). Alignment was done with VMD. N- and C-termini are labelled in blue and green, respectively.

For the moment it is only known, that the R_g of the p40^{phox}-p47^{phox} complex is larger than the single subunits (complex: 45 Å vs. p40^{phox}: 29.5 Å and p47^{phox}: 36 Å (Grizot et al., 2001b)), which indicates that the two molecules are organized in an elongated complex. Figure 63 shows a manual overlay of the crystal structure of p40^{phox} with the *in silico* structure of full length p47^{phox}, which was kindly provided by D. Durand (Durand et al., 2006). We have no structural information about the linker between the PRR and SH3A domains of p47^{phox}. The distance between these domains may be shorter than shown in the model (Figure 63) as shown in the *in silico* model of p47^{phox} discussed above (Meijles et al., 2014).

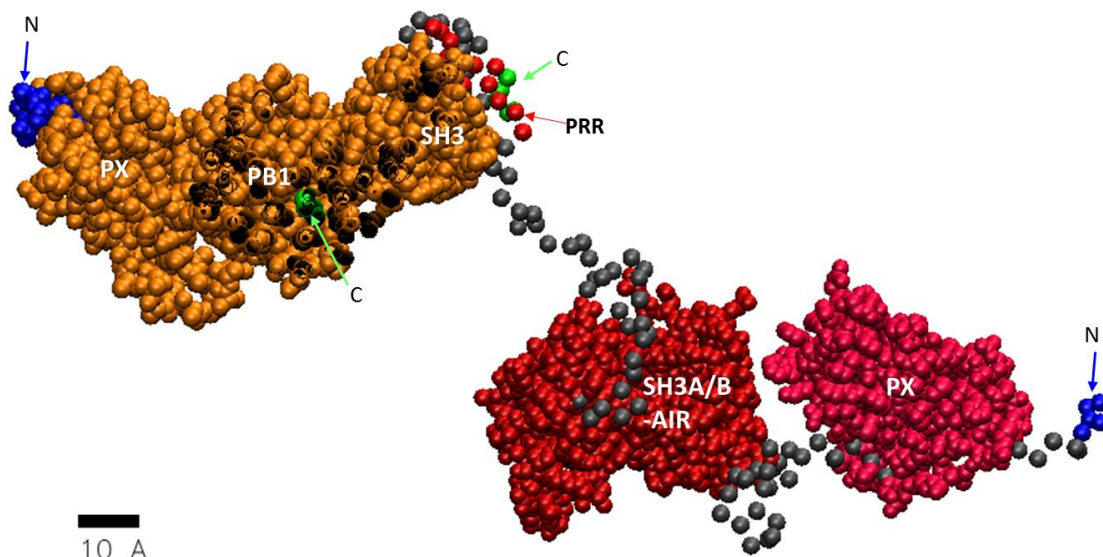


Figure 63 Full-length p40^{phox} in interaction with full length p47^{phox}

The model is a rough construction of p40^{phox} (PDB 2DYB) and p47^{phox} in interaction. We used the overlaid structure of p40^{phox} (orange) and linked it to the full length p47^{phox} model of Durand and co-workers (grey: chain of unknown structure; the position of the PRR is highlighted as red spheres; dark red: complex of the two SH3 domains and AIR, and magenta: PX domain (Durand et al., 2006)). This figure should give an idea of the possible distances between the termini of the two molecules.

However, the binding of p40^{phox} and p47^{phox} is assumed to be artificial, since the C-terminal binding side of p47^{phox} is the same as the one for the p67^{phox} binding. We built a model of the complete cytosolic complex (Figure 64) with the structures shown above. It reveals a close proximity between the p40^{phox} SH3 domain and the p67^{phox} SH3B/ p47^{phox} PRR complex of with. Please not, that the display of the model gives only one conformation. Due to the flexibility of low structured parts of p47^{phox} and p67^{phox}, the dimension of the complex will be variable.

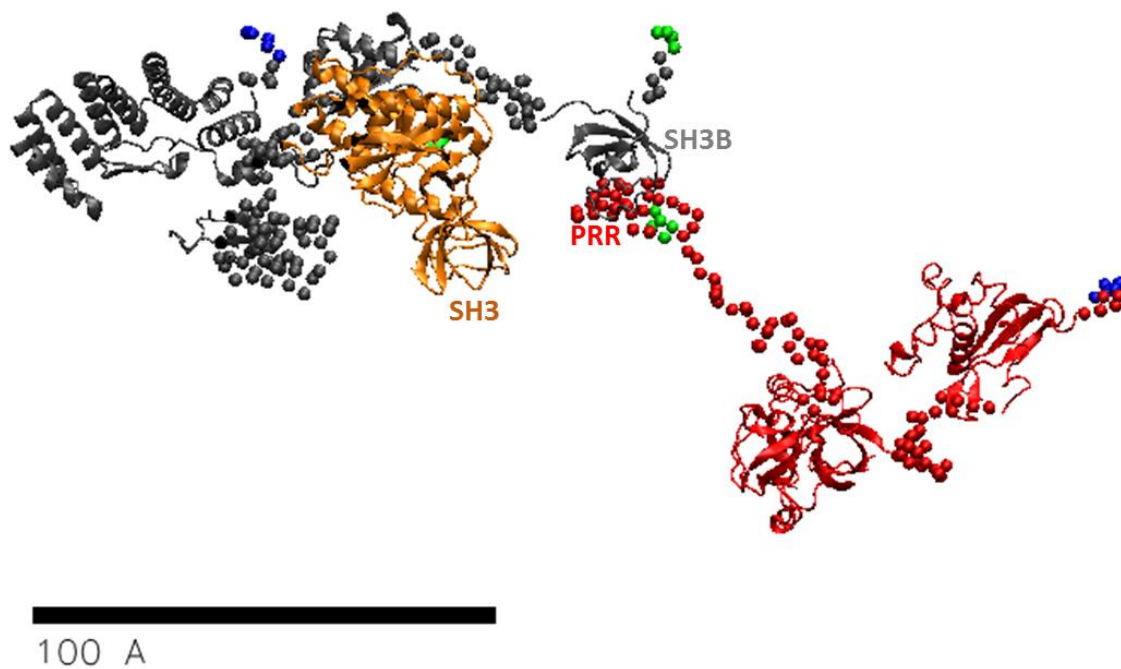


Figure 64 Model of the complete cytosolic complex

The *in silico* model of p67^{phox} (grey, (Durand et al., 2010)) was successfully aligned with the crystal structure of p40^{phox} (orange, PDB 2DYB) and overlaid with the *in silico* model of p47^{phox} (red, (Durand et al., 2006)). The model reveals the close proximity between the SH3 domain of p40^{phox} and the p67^{phox} SH3B-p47PRR complex. The flexibility of the less structured parts of p47^{phox} and p67^{phox} introduces a certain flexibility and hence allowing different expansions of the complex size.

6 Conclusion

Within this study, we showed that the new cyan variants, mTurquoise and Aquamarine, are suitable for quantitative analysis of protein-protein interactions in live cells. As FRET donors in the FRET-FLIM approach, they prove to allow highly sensitive detection of protein-protein interactions, since their long mono-exponential lifetimes allow a clear distinction between non-specific and low but specific FRET. For FCCS studies, ECFP, the ancestor of those new variants, was not commonly used due to its low brightness and low photostability, including a high photobleaching sensitivity and up to 30% of photoswitching, which both transform an uncontrolled fraction of the FP to a dark state (Fredj et al., 2012). With our FCCS experiment, we showed – to our knowledge – for the first time, that mTurquoise is fully appropriate for this technique. In addition, their photostability improves quantitative analysis of FCCS results, it is a clear progress in comparison to ECFP. Furthermore, our FRET-FLIM approach allowed us the detection of inter- and intramolecular interactions for the three cytosolic subunits in live cells. The quantification indicates that only around 20 % of the subunits of the NADPH oxidase are bound in complex, which was supported by a first FCCS experiment. However, as the detailed discussion of the factors influencing the fraction of bound proteins reveals, the interpretation of the biological outcome is not easy.

The structural information, which we extracted from the FRET-FLIM data is not concerned by these difficulties: It allowed us to get new insights in the complex organisation of the cytosolic subunits of the NADPH oxidase in live cells. We were able to compare our findings with the available structures and models derived from *in vitro* studies. The successful alignment of the different structures allows us to propose for the first time a 3D-model of the cytosolic complex of the NADPH oxidase covering the *in vitro* as well as the live cell situation (Figure 64). Figure 65 shows this model as a scheme of the three cytosolic subunits with their main subdomains. In comparison to the standard models composed of (i) bars representing the subunits and their subdomain arrangement and (ii) arrows representing the known interactions (Groemping and Rittinger, 2005, Sumimoto, 2008, Nunes et al., 2013), our 3D model may be a better approximation of the real live situation, and may render a better understanding of the complex structure and give new ideas about the functions of this cytosolic complex.

This model points out the strength of the FRET-FLIM approach towards the structural precision of its data and is therefore a good – perhaps the only available – tool to render this information from living cells. In combination with high resolution techniques such as X-ray crystal structure analysis detailed models can be obtained.

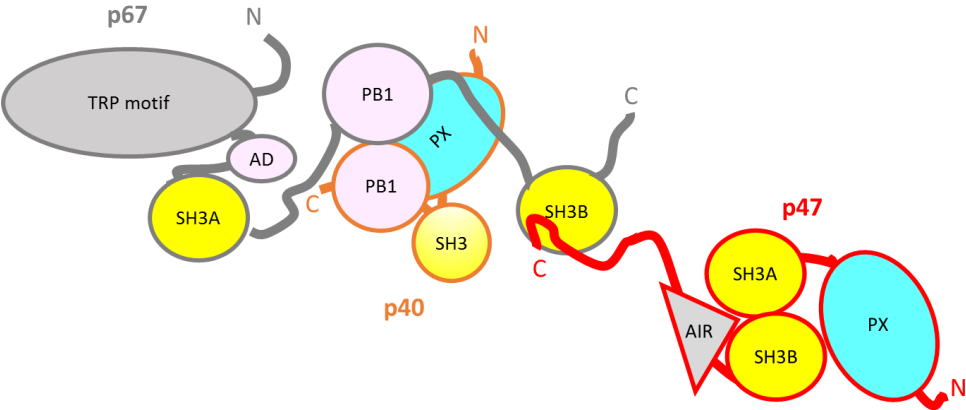


Figure 65 New model of the cytosolic complex

The structure shows the organisation of the cytosolic complex of p67^{phox} (grey), p40^{phox} (orange), and p47^{phox} (red). The subdomains are shown as ellipsoids, while the flexible chains are shown as lines.

7 Perspectives

In this project, we demonstrated that the new cyan FP variants are appropriate both for quantitative FRET-FLIM and FCCS. However, Citrine reveals several defaults in these applications urging the development of new yellow FPs with improved photostability including reduced photostability and photoswitching for better quantification with both FRET-FLIM and FCCS experiments. The development of new YFP variants is currently under investigation in our lab.

Furthermore, we investigated the resting state interactions of the cytosolic subunits by studying both intermolecular interactions as one-by-one combinations and the intramolecular ones of the single subunits.

With respect to the intermolecular interactions, the next step will be to investigate cells co-expressing all three cytosolic subunits. Such an experiment would contribute to a better understanding of the organization of the ternary complex: Even if the main interaction sites were identified, some open questions remain, for example whether p40^{phox} binds to p47^{phox} in live cells or whether it only binds to p67^{phox} due to a stronger affinity as it was observed in *in vitro* studies (Wientjes et al., 1996, Lapouge et al., 2002, Massenet et al., 2005, Grizot et al., 2001b). The K_d values obtained by our FRET-FLIM approach do not reveal any difference (p67^{phox} + p47^{phox} \approx 4 μ M, p47^{phox} + p40^{phox} \approx 5 μ M)^{xlvii}. A FRET-FLIM experiment with all three components could clarify this question: If the apparent FRET efficiency decreases for a CC-terminal tagged p47^{phox} and p67^{phox} in presence of p40^{phox}, it could be assumed, that p40^{phox} influences the binding of the other two subunits. Regarding the 3D model presented here, the competing SH3 domains of p67^{phox} and p40^{phox} are in close proximity. This might lead to the hypothesis, that this proximity has a function during dynamic processes like activation and deactivation, e.g. by exchanging the binding partners.

Our wide-field FRET approach would not be the best option to investigate such dynamic processes. A TIRF-FRET study might be more appropriate, because it allows the monitoring of the interaction during the activation induced assembly on the membrane. Any change in the interaction would be registered by its impact on the apparent FRET efficiency. Such an experiment could not only clarify the mentioned interaction between p67^{phox} and/or p47^{phox} to p40^{phox}, but could also reveal the dynamics of activation and inactivation.

^{xlvii} here, we only compare the relative K_d values due to the described uncertainties of its determination.

Concerning the intramolecular interactions and the folding of the subunits, a first step would be to do further investigations (more samples) of the p40^{phox} and p67^{phox} tandems in order to refine the outcomes. Additionally, we would like to investigate the structural changes in p40^{phox} under hydrogen peroxide treatment, which was described to introduce the translocation of p40^{phox} to the endosomal membrane (Ueyama et al., 2011). Since hydrogen peroxide is an oxidant, its effect on the fluorophore itself has to be tested first. With this respect, we already investigated the effect of hydrogen peroxide on mCherry, which reveals to be only affected by high concentrations. To our knowledge, the impact of hydrogen peroxide on the fluorescence properties of Citrine is not described yet. EYFP fluorescence was slightly affected (Tsourkas et al., 2005), which is in agreement with first tests done in our lab.

Similarly, we plan to study the effect of PMA induced phosphorylation (Price et al., 2002) on the structure of p47^{phox}, which is assumed to set the tandem SH3 domains and the PX domain free (Ago et al., 1999, Ago et al., 2003, Groemping et al., 2003, Autore et al., 2010, Meijles et al., 2014). This would result in strong conformational changes, which we would like to investigate with FRET. First trials did not show any differences in FRET. This may be due to an adaption of conformation(s) in the phosphorylated state or due to insufficient phosphorylation caused by an inaccurate control of PMA concentration. A phosphorylation mimicking mutant (Ago et al., 1999) mimicking the open state might be a useful positive control.

All these studies would contain spatial information, which are helpful for a better understanding of the structure of the ternary complex. Since these studies would include dynamics, it might be helpful to apply a more sophisticated modeling approach with simulation of possible dynamic changes in the structure – crystal structures do only describe one frozen conformation and are hence limited for the description of dynamic molecules. Therefore, modeling would contribute to a better understanding and interpretation of the data.

8 Appendix

8.1 Protein production and purification

8.1.1 Fluorescent proteins

Production and purification of His-tagged recombinant Aquamarine, mTurquoise, Citrine, and mCherry was performed using Top10 bacterial cells. Competent cells were transformed with the pHis-CFP vector (a generous gift from Dr. R. Grailhe, Institut Pasteur, Korea). A starter culture which was grown o.n. was used (25 ml) to inoculate the 1.5 l of Luria-Bertani medium containing 100 µg/ml selecting antibiotic ampicillin. At an $OD_{600} \sim 0.6$, protein production was induced by adding isopropyl- β -d-thio-galactopyranoside (IPTG, 1 mM) and cultured for 18 h at 30 °C. This suspension was centrifuged and frozen. The cells were resuspended in lysis buffer (30 ml; 50 mM Tris-HCl, 5 mM 2-mercaptoethanol, 1 mM phenylmethylsulphonyl fluoride and 0.02 mg/ml DNase), and sonicated. A centrifugation step (120,000 g, 1 h 30, 6 °C) was performed to remove debris. The received supernatant was filtered with a 0.22 µm filter and diluted by a factor 2 with phosphate buffer (30 mM NaH_2PO_4 , 700 mM NaCl and 30 mM imidazole, pH 7.5). A nickel-nitriloacetic acid agarose (Ni-NTA) column (15 ml; Sigma) was loaded with this dilution and incubated for 1 h. Afterwards, the protein was eluted (30 mM NaH_2PO_4 , 100 mM NaCl and 150 mM imidazole, pH 7.5) and further concentrated. The His-tag was cleaved with a tobacco etch virus protease (RT, 5 h; cleavage buffer: 50 mM Tris-HCl, 0.5 mM EDTA and 1 mM dithiothreitol, pH 8), which was controlled by SDS-PAGE (the protein band shifts from 29 to 27 kDa). To remove the His tag and the protease for this solution, a Ni-NTA agarose column without any affinity to the cleaved enzyme was used. After a final dialysis step (dialysis buffer: 30 mM phosphate, pH 7.5), the concentration of the purified protein solution was measured by absorption and stored at -20 °C.

8.1.2 Cytosolic subunits ± FP tag

The protocol of the protein purification of the cytosolic subunits ± FP tag is similar to the one of the FPs. A detailed description is given in (Baciou et al., 2009, Karimi, 2014). Table 26 highlights the key data of the production and purification.

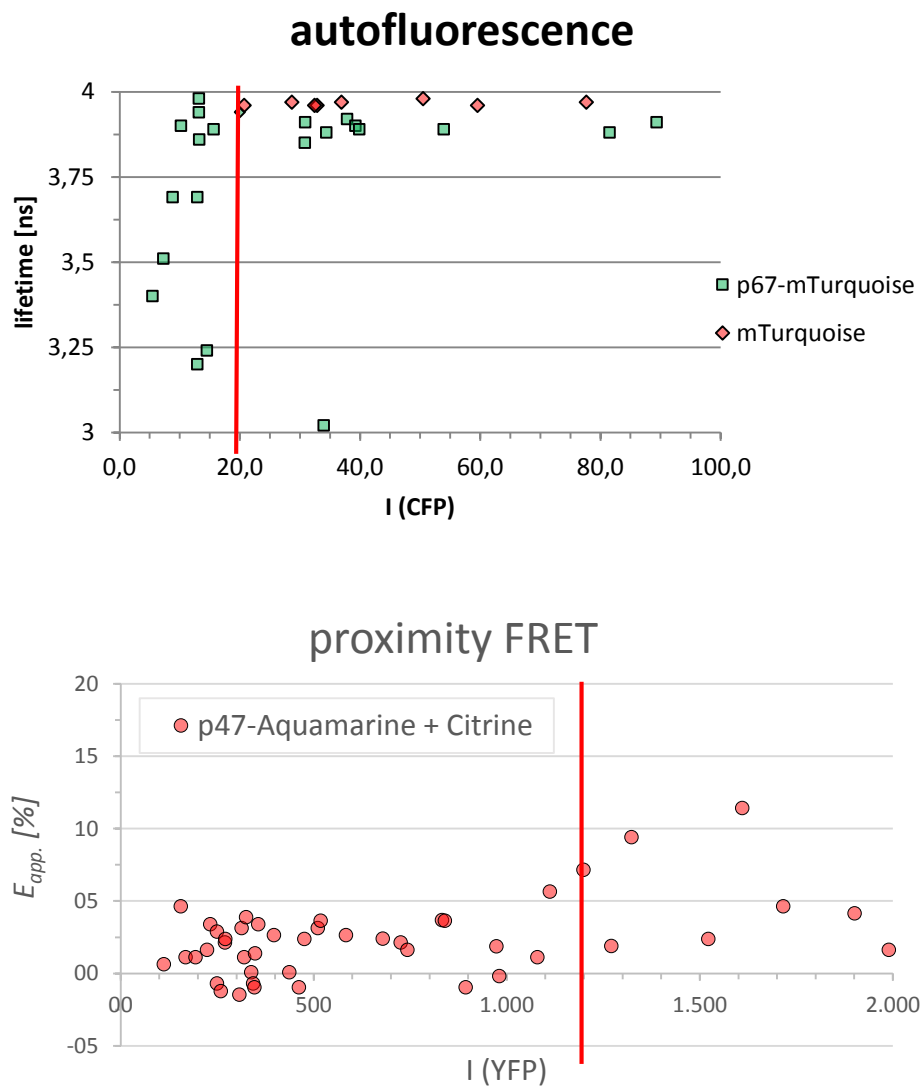
Protein	p67 ^{phox} WT, p47 ^{phox} WT, Rac1Q61L ^{xlvi}	p47 ^{phox} -Citrine, mTurquoise-p67 ^{phox}
vector	pET15b (p67 ^{phox} , p47 ^{phox}), pGEX2T (Rac)	pProEX
Tag:	6xHis (p67, p47), GST (Rac)	6xHis
Bacterial strain	<i>Escherichia coli</i> BL21(DE3)	<i>Escherichia coli</i> Top10
Conditions protein production	o.n., 30 °C	o.n., 28 °C
Affinity chromatography	<ul style="list-style-type: none"> • p47^{phox} : <ol style="list-style-type: none"> 1. SP-Sepharose chromatography 2. Nickel chromatography • p67^{phox}, Rac: <ol style="list-style-type: none"> 1. Q-Sepharose-FF chromatography 2. Glutathione-Sepharose-4B affinity column (Rac) Nickel chromatography (p67^{phox}) 	<ol style="list-style-type: none"> 1. Q-Sepharose chromatography 2. Nickel chromatography
Elution buffer	<ul style="list-style-type: none"> • p67^{phox} / p47^{phox} : <ol style="list-style-type: none"> 1. 20 mM HEPES, 500 mM NaCl, 1 mM PMSF, pH 7.5 2. 150 mM imidazole, 0.1 M NaCl, 30 mM NaH₂PO₄, pH 7.5 • Rac: <ol style="list-style-type: none"> 1. 20 mM HEPES, 500 mM NaCl, 1 mM PMSF, pH 7.5 2. 50 mM Tris, 10 mM reduced glutathione, pH 8.0 	<ol style="list-style-type: none"> 1. 20 mM HEPES, 500 mM NaCl, 1 mM PMSF, pH 7.5 2. 150 mM imidazole, 0.1 M NaCl, 30 mM NaH₂PO₄, pH 7.5
Tag cleavage	not performed	tobacco etch virus protease
Dialysis	o.n., phosphate buffer (30 mM sodium phosphate, 100 mM NaCl, pH 7.5,)	o.n., phosphate buffer (30 mM sodium phosphate, 100 mM NaCl, pH 7.5,)
Storage conditions	-80 °C	-80 °C

^{xlvi} The GTP like form of Rac1 obtained by the mutation Q61L

Table 26 Summary of the production and purification of the cytosolic subunits of the NADPH oxidase

8.2 Determination of the intensity working frame

To exclude both a bias induced by autofluorescence and by molecular crowding, intensity thresholds were settled based on controls (p67^{phox}-mTurquoise or p47^{phox}-Aquamarine co-expressed with Citrine, respectively). Intensity values below 20 cts/s/100mW in the cyan channel or above 1200 cts/s/100mW in the yellow one were not taken into account for data analysis.



8.3 Derivation of the K_d resolved with the bound fraction

The bound fraction correlates the equilibrium concentration $[D]_{eq}$, $[A]_{eq}$, and $[DA]_{eq}$ with the total concentration of donor $[D]_{tot}$ and acceptor $[A]_{tot}$:

$$[D]_{eq} = (1 - \beta)[D]_{tot}$$

$$[A]_{eq} = [A]_{tot} - \beta[D]_{tot}$$

$$[AD]_{eq} = \beta[D]_{tot}$$

The next step is to replace the equilibrium concentrations in the K_d equation with the formulas mentioned above:

$$K_D = \frac{[A]_{eq} \cdot [D]_{eq}}{[AD]_{eq}}$$

$$K_D = \frac{([A]_{tot} - \beta[D]_{tot}) \cdot (1 - \beta)[D]_{tot}}{\beta[D]_{tot}}$$

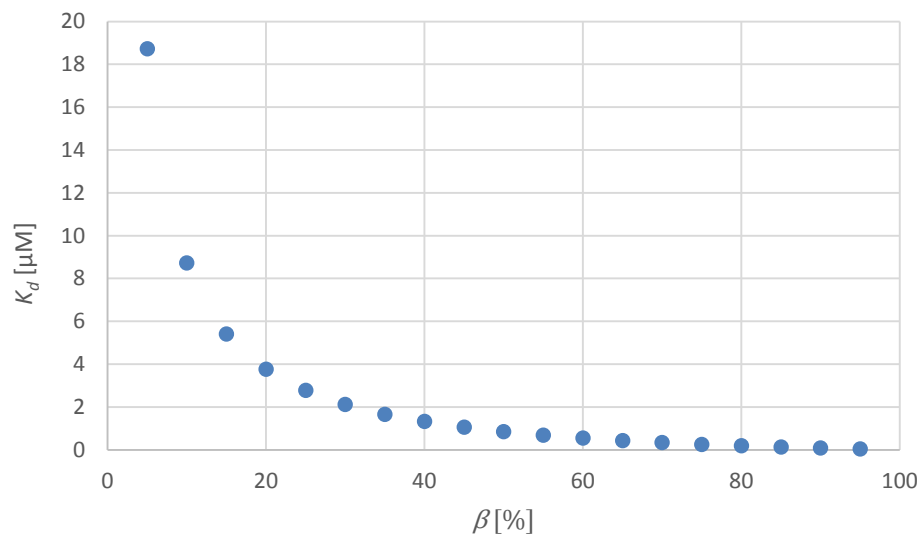
$$K_D = \frac{(1 - \beta)}{\beta} \cdot ([A]_{tot} - \beta[D]_{tot})$$

$$K_D = \frac{(1 - \beta)}{\beta} \cdot [A]_{tot} \cdot \left(1 - \beta \frac{[D]_{tot}}{[A]_{tot}}\right)$$

$$K_D = \frac{(1 - \beta)}{\beta} \cdot \left(1 - \beta \frac{n_{D,tot}}{n_{A,tot}}\right) \cdot [A]_{tot}$$

8.4 Influence the bound fraction on the K_d

The influence of the bound fraction β on the calculated K_d was simulated by assuming a $1 \mu\text{M}$ concentration and a ratio of $n(\text{A})/n(\text{D})$ of 3.5 of acceptor and varying β from 5 – 95 %. The K_d was calculated (8.3) and plotted against β .



8.5 Correction of the spectral bleed-through in FCS with FLCS

In its original version, FLCS uses the same pulsed excitation laser for both fluorophores, which need to have sufficiently different lifetime decays. The removal of the spectral bleed through is performed by data sorting. This is achieved by a statistical weighting of the photons according to their decay profile. The FLCS weighting gives a probability from which fluorophore the photon originates (Kapusta et al., 2007, Macháň et al., 2014, Macháň and Wohland, 2014).

In the experimental FCCS setup we used, the excitation laser of one fluorophore (here mTurquoise) is pulsed and allows the time correlated single photon counting (TCSPC) for the FLCS. The second laser (here Citrine excitation) is a continuous wave laser. The TCSPC records the delay between the excitation pulse and the emission signal (as used for FLIM, ps time scale) and the global arrival time (relative to the start of the experiment, ns time scale). The latter one is used as a normal FCS.

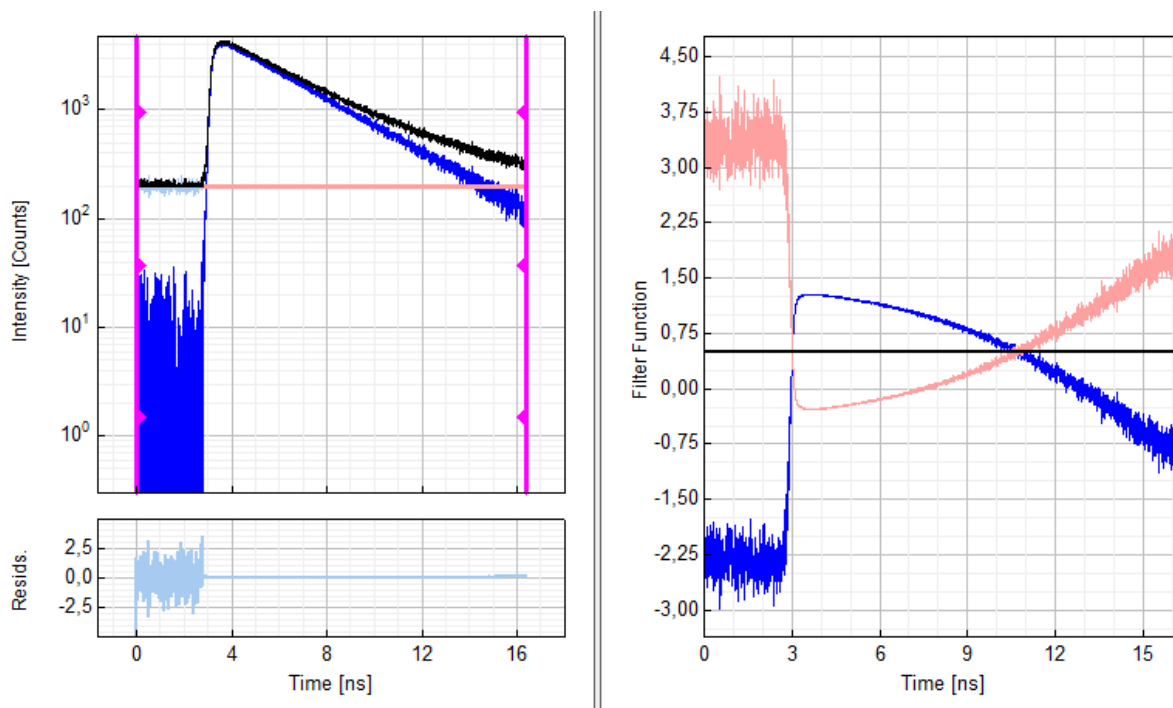


Figure 66 Fluorescence lifetime filters for spectral cross talk correction of FCCS

left: Fluorescence decay (blue) and background (pink) gives experimental fluorescence time-correlated histogram (linear combination, black).

right: corresponding FLCS filters of the fluorescence decay for the cyan channel correction (blue) and of the background for the yellow channel correction (pink).

The FLCS can be used to apply different statistical weightings on every single photon depending on its emitter's temporal fingerprint (either with fluorescence decay or background/steady state fluorescence, Figure 66), which are directly applied on the auto-

correlation and cross-correlation function (Padilla-Parra et al., 2011b, Macháň et al., 2014, Kapusta et al., 2007).

9 List of abbreviations

aa	amino acid
AB	antibody
AD	activation domain
AIR	autoinhibitory region of p47 ^{phox}
CGD	Chronic Granulomatous Disease
CFP	cyan fluorescent protein
DM	dichroic mirror
D _{max}	maximum distance
ECL	enhanced chemiluminescence
FCCS	fluorescence cross-correlation spectroscopy
FCS	fluorescence correlation spectroscopy
FP	fluorescent protein
IBP	interference bandpass filter
MCS	multichannel scaler
ND	neutral density
PB1	Phox and Bem1
PDB	protein data base
PI(3)P	phosphatidylinositol 3-phosphate
PI(3,4)P ₂	phosphatidylinositol-(3,4)-bisphosphate
PRR	proline-rich region
PS	phosphatidylserine
PX domain	phagocyte oxidase domain
Rac	<u>R</u> as-related- <u>C</u> 3 botulinum toxin substrate, a small GTPase
R _g	radius of gyration
RhoGDI	Rho GDP dissociation inhibitor
ROI	region of interest
ROS	reactive oxygen species
rpm	rounds per minute
RT	room temperature
SAXS	small angle X-ray scattering
SD	standard deviation
SH3 domain	SRC homology 3 domain
SU	subunit
TCSPC	time correlated single photon counting
ter.	terminal
TIRF	Total Internal Reflection Fluorescence microscopy
TM	transmembrane helices
TPR	tetratricopeptide repeat
TSU	tagged subunit
VMD	Visual Molecular Dynamics software
WB	Western Blot
YFP	yellow fluorescent protein

10 List of figures

Figure 1 Jablonski diagram of the excitation and de-excitation pathways of a fluorophore.....	9
Figure 2 Angles involved in the definition of the orientation factor κ^2	12
Figure 3 Förster distance and molecular FRET efficiency depend on the spatial orientation factor κ^2	13
Figure 4 General structure and function of the NOX.....	15
Figure 5 NADPH oxidases are associated with a variety of diseases	17
Figure 6 Structure of cytochrome b_{558}	21
Figure 7 Domain structure of $p47^{\text{phox}}$	24
Figure 8 Interaction of $p47^{\text{phox}}$ and $p22^{\text{phox}}$	25
Figure 9 Domain structure of $p67^{\text{phox}}$	26
Figure 10 Structure of $p40^{\text{phox}}$	27
Figure 11 Model of the cytosolic complex in resting and active state	29
Figure 12 Partec Flow Cytometer – Scheme of the laser light sources, optical paths, and detectors.....	41
Figure 13 Laser excitation and emission detection of the Partec Flow Cytometer.....	42
Figure 14 Principle of TCSPC	47
Figure 15 Fluorescence decay histogram	48
Figure 16 FCS principles and definition of the observed volume.....	52
Figure 17 FCCS principles.....	53
Figure 18 Distribution single and triple transfection efficiency	58
Figure 19 Fluorescence intensity microscopy reveals triple transfected cells	59
Figure 20 Scheme of the flow cytometer adopted for FRET measurements	60
Figure 21 Flow Cytometer – spectral selection optimized for FRET detection.....	61
Figure 22 Flow Cytometry: Effect of the FRET settings on CFP transfected cells in FRET-CFP plot.....	62
Figure 23 Data derived from FLIM.....	67
Figure 24 Estimation of the height of the cell	70
Figure 25 Fluorescence intensity is measured in regions of interest in the cell.....	70
Figure 26 Droplet of purified protein	73
Figure 27 Calibration curves of purified FPs for the discrimination of the calibration factor f_{AD} , shown on the example of Aquamarine and Citrine.....	74
Figure 28 FRET by FLIM confirms specific CC-terminal interaction between $p47^{\text{phox}}$ and $p67^{\text{phox}}$	76
Figure 29 FRET by FLIM: Influence of the label on the results of $p47^{\text{phox}}$ – $p67^{\text{phox}}$ interaction	77

Figure 30 Two lifetimes of the donor derived from the bi-exponential fit of cells co-expressing donor and acceptor:	78
Figure 31 WB anti-GFP	82
Figure 32 WB anti-p67 ^{phox}	84
Figure 33 WB anti-p47 ^{phox}	85
Figure 34 WB of p40 ^{phox} ± mCherry 0	87
Figure 35 TIRF: Time series of the subunits' arrival on the membrane and intensity profile plot	91
Figure 36 TIRF: Intensity-time series plot of the subunits' arrival on the cell membrane	93
Figure 37 Luminometry confirms the activatability of the complex	95
Figure 38 FCET reveals interaction between p67 ^{phox} and p47 ^{phox}	98
Figure 39 Interaction of p47 ^{phox} and p67 ^{phox} is mediated by the C-terminus of p47 ^{phox}	99
Figure 40 NC-terminal interaction of p67 ^{phox} and p47 ^{phox} show a low FRET efficiency	100
Figure 41: NN-terminal tagged p67 ^{phox} and p47 ^{phox} do not show any FRET	101
Figure 42: Interactions of p67 ^{phox} with p40 ^{phox} with different tag positions	103
Figure 43 Lifetime distribution of NN- and CC-terminal tagged p67 ^{phox} and p40 ^{phox}	104
Figure 44 CN-terminal tagged p47 ^{phox} and p40 ^{phox} show a specific interaction mediated via the C-terminus of p47 ^{phox}	105
Figure 45 p47 ^{phox} interacts with p40 ^{phox} via its PRR domain	106
Figure 46 p67 ^{phox} does not show any homo-dimerization	107
Figure 47 p47 ^{phox} does not reveal any dimerization	108
Figure 48 Overview homo-dimerization of the cytosolic subunits	109
Figure 49 FRET by Flow Cytometry shows very small amount of FRET positive cells for the p47 ^{phox} tandem	111
Figure 50 p47 ^{phox} tandem reveals a moderate FRET level	112
Figure 51 Lifetime distribution of the CN-terminal tagged subunits (tandems)	112
Figure 52 p67 ^{phox} tandem shows low FRET levels	113
Figure 53 Preliminary results for p40 ^{phox} tandem reveal FRET	114
Figure 54 Comparison of the results of the bound fraction obtained with FCCS with and without FLCS filters	116
Figure 55 In silico construct of full length p47 ^{phox} in resting state	136
Figure 56 Structure of the p40 ^{phox} tandem	138
Figure 57 Structure of the p67 ^{phox} tandem	140
Figure 58 Structure of the interaction between p67 ^{phox} and p47 ^{phox}	142
Figure 59 Localization of the p47 ^{phox} C-terminus in interaction with p67 ^{phox}	143
Figure 60 Crystal structure of the interacting PB1 domains of p67 ^{phox} and p40 ^{phox}	144
Figure 61 Interaction site of p67 ^{phox} and the PB1 domain of p40 ^{phox}	145

Figure 62 Aligement of the full-length crystal structure of p40 ^{phox} with the one of the interaction to p47 ^{phox}	146
Figure 63 Full-length p40 ^{phox} in interaction with full length p47 ^{phox}	147
Figure 64 Model of the complete cytosolic complex	148
Figure 65 New model of the cytosolic complex	150
Figure 66 Fluorescence lifetime filters for spectral cross talk correction of FCCS	159

11 Literature

- ABANKWA, D. & VOGEL, H. (2007) A FRET map of membrane anchors suggests distinct microdomains of heterotrimeric G proteins. *Journal of Cell Science*, 120, 2953-2962.
- ADAMS, E. R., DRATZ, E. A., GIZACHEW, D., DELEO, F. R., YU, L., VOLPP, B. D., VLASES, M., JESAITIS, A. J. & QUINN, M. T. (1997) Interaction of human neutrophil flavocytochrome b with cytosolic proteins: transferred-NOESY NMR studies of a gp91phox C-terminal peptide bound to p47phox. *Biochem J*, 325 (Pt 1), 249-57.
- AGO, T., KURIBAYASHI, F., HIROAKI, H., TAKEYA, R., ITO, T., KOHDA, D. & SUMIMOTO, H. (2003) Phosphorylation of p47phox directs phox homology domain from SH3 domain toward phosphoinositides, leading to phagocyte NADPH oxidase activation. *Proceedings of the National Academy of Sciences*, 100, 4474-4479.
- AGO, T., NUNOI, H., ITO, T. & SUMIMOTO, H. (1999) Mechanism for Phosphorylation-induced Activation of the Phagocyte NADPH Oxidase Protein p47 phox : TRIPLE REPLACEMENT OF SERINES 303, 304, AND 328 WITH ASPARTATES DISRUPTS THE SH3 DOMAIN-MEDIATED INTRAMOLECULAR INTERACTION IN p47 phox , THEREBY ACTIVATING THE OXIDASE. *Journal of Biological Chemistry*, 274, 33644-33653.
- ALTENHÖFER, S., RADERMACHER, K. A., KLEIKERS, P. W. M., WINGLER, K. & SCHMIDT, H. H. H. W. (2014) Evolution of NADPH Oxidase Inhibitors: Selectivity and Mechanisms for Target Engagement. *Antioxidants & Redox Signaling*.
- ALVAREZ, L. (2010) Imagerie moléculaire quantitative en cellule vivante. *Physical Chemistry*. Université Paris Sud, France.
- AOKI, K., KOMATSU, N., HIRATA, E., KAMIOKA, Y. & MATSUDA, M. (2012) Stable expression of FRET biosensors: A new light in cancer research. *Cancer Science*, 103, 614-619.
- AUTORE, F., PAGANO, B., FORNILI, A., RITTINGER, K. & FRATERNALI, F. (2010) In Silico Phosphorylation of the Autoinhibited Form of p47phox: Insights into the Mechanism of Activation. *Biophysical Journal*, 99, 3716-3725.
- BACIA, K., KIM, S. A. & SCHWILLE, P. (2006) Fluorescence cross-correlation spectroscopy in living cells. *Nat Meth*, 3, 83-89.
- BACIOU, L., ERARD, M., DAGHER, M.-C. & BIZOUARN, T. (2009) The cytosolic subunit p67phox of the NADPH-oxidase complex does not bind NADPH. *FEBS Letters*, 583, 3225-3229.
- BANERJEE, D. & PAL, S. K. (2007) Simultaneous Binding of Minor Groove Binder and Intercalator to Dodecamer DNA: Importance of Relative Orientation of Donor and Acceptor in FRET. *The Journal of Physical Chemistry B*, 111, 5047-5052.
- BANNING, C., VOTTELER, J., HOFFMANN, D., KOPPENSTEINER, H., WARMER, M., REIMER, R., KIRCHHOFF, F., SCHUBERT, U., HAUBER, J. & SCHINDLER, M. (2010) A Flow Cytometry-Based FRET Assay to Identify and Analyse Protein-Protein Interactions in Living Cells. *PLoS ONE*, 5, e9344.
- BASTIAENS, P. I., MAJOUL, I. V., VERVEER, P. J., SÖLING, H. D. & JOVIN, T. M. (1996) Imaging the intracellular trafficking and state of the AB5 quaternary structure of cholera toxin. *The EMBO Journal*, 15, 4246-4253.
- BECKER, W. (2012) Fluorescence lifetime imaging – techniques and applications. *Journal of Microscopy*, 247, 119-136.
- BEDARD, K. & KRAUSE, K.-H. (2007) The NOX Family of ROS-Generating NADPH Oxidases: Physiology and Pathophysiology. *Physiological Reviews*, 87, 245-313.

- BEEMILLER, P., HOPPE, A. D. & SWANSON, J. A. (2006) A Phosphatidylinositol-3-Kinase-Dependent Signal Transition Regulates ARF1 and ARF6 during Fc γ Receptor-Mediated Phagocytosis. *PLoS Biol*, 4, e162.
- BEEMILLER, P., ZHANG, Y., MOHAN, S., LEVINSOHN, E., GAETA, I., HOPPE, A. D. & SWANSON, J. A. (2010) A Cdc42 activation cycle coordinated by PI 3-kinase during Fc receptor-mediated phagocytosis. *Mol Biol Cell*, 21, 470-80.
- BENE, L., UNGVÁRI, T., FEDOR, R., SASI SZABÓ, L. & DAMJANOVICH, L. (2013) Intensity Correlation-Based Calibration of FRET. *Biophysical Journal*, 105, 2024-2035.
- BENNA, J. E., FAUST, L. R. P., JOHNSON, J. L. & BABIOR, B. M. (1996) Phosphorylation of the Respiratory Burst Oxidase Subunit p47 as Determined by Two-dimensional Phosphopeptide Mapping: PHOSPHORYLATION BY PROTEIN KINASE C, PROTEIN KINASE A, AND A MITOGEN-ACTIVATED PROTEIN KINASE. *Journal of Biological Chemistry*, 271, 6374-6378.
- BEREZIN, M. Y. & ACHILEFU, S. (2010) Fluorescence Lifetime Measurements and Biological Imaging. *Chemical Reviews*, 110, 2641-2684.
- BIBERSTINE-KINKADE, K. J., DELEO, F. R., EPSTEIN, R. I., LEROY, B. A., NAUSEEF, W. M. & DINAUER, M. C. (2001) Heme-ligating Histidines in Flavocytochrome b 558 : IDENTIFICATION OF SPECIFIC HISTIDINES IN gp91 phox. *Journal of Biological Chemistry*, 276, 31105-31112.
- BIBERSTINE-KINKADE, K. J., YU, L. & DINAUER, M. C. (1999) Mutagenesis of an Arginine- and Lysine-rich Domain in the gp91 phox Subunit of the Phagocyte NADPH-oxidase Flavocytochrome b 558. *Journal of Biological Chemistry*, 274, 10451-10457.
- BOURGEOIS, D., REGIS-FARO, A. & ADAM, V. (2012) Photoactivated structural dynamics of fluorescent proteins. *Biochemical Society Transactions*, 40, 531-538.
- BRAVO, J., KARATHANASSIS, D., PACOLD, C. M., PACOLD, M. E., ELLSON, C. D., ANDERSON, K. E., BUTLER, P. J., LAVENIR, I., PERISIC, O., HAWKINS, P. T., STEPHENS, L. & WILLIAMS, R. L. (2001) The crystal structure of the PX domain from p40(phox) bound to phosphatidylinositol 3-phosphate. *Mol Cell*, 8, 829-39.
- BROWN, D. I. & GRIENGLING, K. K. (2009) Nox proteins in signal transduction. *Free Radical Biology and Medicine*, 47, 1239-1253.
- CAMPION, Y., JESAITIS, A. J., NGUYEN, M. V. C., GRICHINE, A., HERENGER, Y., BAILLET, A., BERTHIER, S., MOREL, F. & PACLET, M. H. (2009) New p22-Phox Monoclonal Antibodies: Identification of a Conformational Probe for Cytochrome *b*₅₅₈. *Journal of Innate Immunity*, 1, 556-569.
- CARDARELLI, F., BIZZARRI, R., SERRESI, M., ALBERTAZZI, L. & BELTRAM, F. (2009) Probing Nuclear Localization Signal-Importin α Binding Equilibria in Living Cells. *Journal of Biological Chemistry*, 284, 36638-36646.
- CHESSA, T. A. M., ANDERSON, K. E., HU, Y., XU, Q., RAUSCH, O., STEPHENS, L. R. & HAWKINS, P. T. (2010) Phosphorylation of threonine 154 in p40phox is an important physiological signal for activation of the neutrophil NADPH oxidase. *Blood*, 116, 6027-6036.
- CHOI, W., FANG-YEN, C., BADIZADEGAN, K., OH, S., LUE, N., DASARI, R. R. & FELD, M. S. (2007) Tomographic phase microscopy. *Nat Meth*, 4, 717-719.
- CURL, C. L., BELLAIR, C. J., HARRIS, T., ALLMAN, B. E., HARRIS, P. J., STEWART, A. G., ROBERTS, A., NUGENT, K. A. & DELBRIDGE, L. M. D. (2005) Refractive index measurement in viable cells using quantitative phase-amplitude microscopy and confocal microscopy. *Cytometry Part A*, 65A, 88-92.
- DAHAN, I., ISSAEVA, I., GORZALCZANY, Y., SIGAL, N., HIRSHBERG, M. & PICK, E. (2002) Mapping of Functional Domains in the p22 phox Subunit of Flavocytochrome

- b 559 Participating in the Assembly of the NADPH Oxidase Complex by “Peptide Walking”. *Journal of Biological Chemistry*, 277, 8421-8432.
- DAY, R. N. (2014) Measuring protein interactions using Förster resonance energy transfer and fluorescence lifetime imaging microscopy. *Methods*, 66, 200-207.
- DECOURSEY, T. E. & LIGETI, E. (2005) Regulation and termination of NADPH oxidase activity. *Cellular and Molecular Life Sciences*, 62, 2173-2193.
- DELEO, F. R. & QUINN, M. T. (1996) Assembly of the phagocyte NADPH oxidase: molecular interaction of oxidase proteins. *Journal of Leukocyte Biology*, 60, 677-91.
- DELEO, F. R., YU, L., BURRITT, J. B., LOETTERLE, L. R., BOND, C. W., JESAITIS, A. J. & QUINN, M. T. (1995) Mapping sites of interaction of p47-phox and flavocytochrome b with random-sequence peptide phage display libraries. *Proceedings of the National Academy of Sciences*, 92, 7110-7114.
- DEMCHENKO, A. P. (2008) *Introduction to fluorescence sensing*, Springer Science & Business Media.
- DRUMMOND, G. R., SELEMIDIS, S., GRIENGLING, K. K. & SOBEY, C. G. (2011) Combating oxidative stress in vascular disease: NADPH oxidases as therapeutic targets. *Nat Rev Drug Discov*, 10, 453-471.
- DUAN, C., ADAM, V., BYRDIN, M., RIDARD, J., KIEFFER-JAQUINOD, S., MORLOT, C., ARCIZET, D., DEMACHY, I. & BOURGEOIS, D. (2013) Structural Evidence for a Two-Regime Photobleaching Mechanism in a Reversibly Switchable Fluorescent Protein. *Journal of the American Chemical Society*, 135, 15841-15850.
- DUPRÉ-CROCHET, S., ERARD, M. & NÜBE, O. (2013) ROS production in phagocytes: why, when, and where? *Journal of Leukocyte Biology*, 94, 657-670.
- DURAND, D., CANNELLA, D., DUBOSCLARD, V., PEBAY-PEYROULA, E., VACHETTE, P. & FIESCHI, F. (2006) Small-Angle X-ray Scattering Reveals an Extended Organization for the Autoinhibitory Resting State of the p47phox Modular Protein. *Biochemistry*, 45, 7185-7193.
- DURAND, D., VIVÈS, C., CANNELLA, D., PÉREZ, J., PEBAY-PEYROULA, E., VACHETTE, P. & FIESCHI, F. (2010) NADPH oxidase activator p67phox behaves in solution as a multidomain protein with semi-flexible linkers. *Journal of Structural Biology*, 169, 45-53.
- DWANE, S. & KIELY, P. A. (2011) Tools used to study how protein complexes are assembled in signaling cascades. *Bioengineered Bugs*, 2, 247-259.
- EL-BENNA, J., DANG, P.-C. & GOUGEROT-POCIDALO, M.-A. (2008) Priming of the neutrophil NADPH oxidase activation: role of p47phox phosphorylation and NOX2 mobilization to the plasma membrane. *Seminars in Immunopathology*, 30, 279-289.
- EL-BENNA, J., DANG, P. M., GOUGEROT-POCIDALO, M. A., MARIE, J. C. & BRAUT-BOUCHER, F. (2009) p47phox, the phagocyte NADPH oxidase/NOX2 organizer: structure, phosphorylation and implication in diseases. *Exp Mol Med*, 41, 217-25.
- EL BENNA, J., RUEDI, J. M. & BABIOR, B. M. (1994) Cytosolic guanine nucleotide-binding protein Rac2 operates in vivo as a component of the neutrophil respiratory burst oxidase. Transfer of Rac2 and the cytosolic oxidase components p47phox and p67phox to the submembranous actin cytoskeleton during oxidase activation. *Journal of Biological Chemistry*, 269, 6729-6734.
- ERARD, M., FREDJ, A., PASQUIER, H., BELTOLNGAR, D. B., BOUSMAH, Y., DERRIEN, V., VINCENT, P. & MEROLA, F. (2013) Minimum set of mutations needed to optimize cyan fluorescent proteins for live cell imaging. *Mol Biosyst*, 9, 258-67.
- FÁBIÁN, Á. I., RENTE, T., SZÖLLÖSI, J., MÁTYUS, L. & JENEI, A. (2010) Strength in Numbers: Effects of Acceptor Abundance on FRET Efficiency. *ChemPhysChem*, 11, 3713-3721.

- FAURE, M. C., SULPICE, J.-C., DELATTRE, M., LAVIELLE, M., PRIGENT, M., CUIF, M.-H., MELCHIOR, C., TSCHIRHART, E., NÜBE, O. & DUPRÉ-CROCHET, S. (2013) The recruitment of p47phox and Rac2G12V at the phagosome is transient and phosphatidylserine dependent. *Biology of the Cell*, 105, 501-518.
- FAUST, L. R., EL BENNA, J., BABIOR, B. M. & CHANOCK, S. J. (1996) The phosphorylation targets of p47phox, a subunit of the respiratory burst oxidase. Functions of the individual target serines as evaluated by site-directed mutagenesis. *The Journal of Clinical Investigation*, 96, 1499-1505.
- FINAN, P., SHIMIZU, Y., GOUT, I., HSUAN, J., TRUONG, O., BUTCHER, C., BENNETT, P., WATERFIELD, M. D. & KELLIE, S. (1994) An SH3 domain and proline-rich sequence mediate an interaction between two components of the phagocyte NADPH oxidase complex. *Journal of Biological Chemistry*, 269, 13752-13755.
- FINEGOLD, A. A., SHATWELL, K. P., SEGAL, A. W., KLAUSNER, R. D. & DANCIS, A. (1996) Intramembrane Bis-Heme Motif for Transmembrane Electron Transport Conserved in a Yeast Iron Reductase and the Human NADPH Oxidase. *Journal of Biological Chemistry*, 271, 31021-31024.
- FOO, YONG H., NAREDI-RAINER, N., LAMB, DON C., AHMED, S. & WOHLAND, T. (2012) Factors Affecting the Quantification of Biomolecular Interactions by Fluorescence Cross-Correlation Spectroscopy. *Biophysical Journal*, 102, 1174-1183.
- FREDJ, A., PASQUIER, H., DEMACHY, I., JONASSON, G., LEVY, B., DERRIEN, V., BOUSMAH, Y., MANOUSSARIS, G., WIEN, F., RIDARD, J., ERARD, M. & MEROLA, F. (2012) The Single T65S Mutation Generates Brighter Cyan Fluorescent Proteins with Increased Photostability and pH Insensitivity. *PLoS ONE*, 7, e49149.
- FREITAS, M., LIMA, J. L. F. C. & FERNANDES, E. (2009) Optical probes for detection and quantification of neutrophils' oxidative burst. A review. *Analytica Chimica Acta*, 649, 8-23.
- FUCHS, A., DAGHER, M.-C., FAURE, J. & VIGNAIS, P. V. (1996) Topological organization of the cytosolic activating complex of the superoxide-generating NADPH-oxidase. Pinpointing the sites of interaction between p47phox, p67phox and p40phox using the two-hybrid system. *Biochimica et Biophysica Acta (BBA) - Molecular Cell Research*, 1312, 39-47.
- FUCHS, A., DAGHER, M.-C. & VIGNAIS, P. V. (1995) Mapping the Domains of Interaction of p40 with Both p47 and p67 of the Neutrophil Oxidase Complex Using the Two-hybrid System. *Journal of Biological Chemistry*, 270, 5695-5697.
- GANESAN, A. & ZHANG, J. (2012) How cells process information: Quantification of spatiotemporal signaling dynamics. *Protein Science*, 21, 918-928.
- GLATTER, O. & KRATKY, O. (1982) *Small Angle X-ray Scattering*, London, Academic Press Inc. (London) Ltd.
- GOEDHART, J., VAN WEEREN, L., HINK, M. A., VISCHER, N. O. E., JALINK, K. & GADELLA, T. W. J. (2010) Bright cyan fluorescent protein variants identified by fluorescence lifetime screening. *Nat Meth*, 7, 137-139.
- GRAILHE, R., MEROLA, F., RIDARD, J., COUVIGNOU, S., LE POUPON, C., CHANGEUX, J.-P. & LAGUITTON-PASQUIER, H. (2006) Monitoring Protein Interactions in the Living Cell Through the Fluorescence Decays of the Cyan Fluorescent Protein. *ChemPhysChem*, 7, 1442-1454.
- GRIESBECK, O., BAIRD, G. S., CAMPBELL, R. E., ZACHARIAS, D. A. & TSIEN, R. Y. (2001) Reducing the environmental sensitivity of yellow fluorescent protein. Mechanism and applications. *J Biol Chem*, 276, 29188-94.

- GRIZOT, S., FIESCHI, F., DAGHER, M.-C. & PEBAY-PEYROULA, E. (2001a) The Active N-terminal Region of p67 phox : STRUCTURE AT 1.8 Å RESOLUTION AND BIOCHEMICAL CHARACTERIZATIONS OF THE A128V MUTANT IMPLICATED IN CHRONIC GRANULOMATOUS DISEASE. *Journal of Biological Chemistry*, 276, 21627-21631.
- GRIZOT, S., GRANDVAUX, N., FIESCHI, F., FAURÉ, J., MASSENET, C., ANDRIEU, J. P., FUCHS, A., VIGNAIS, P. V., TIMMINS, P. A., DAGHER, M. C. & PEBAY-PEYROULA, E. (2001b) Small Angle Neutron Scattering and Gel Filtration Analyses of Neutrophil NADPH Oxidase Cytosolic Factors Highlight the Role of the C-Terminal End of p47phox in the Association with p40phox †. *Biochemistry*, 40, 3127-3133.
- GROEMPING, Y., LAPOUGE, K., SMERDON, S. J. & RITTINGER, K. (2003) Molecular Basis of Phosphorylation-Induced Activation of the NADPH Oxidase. *Cell*, 113, 343-355.
- GROEMPING, Y. & RITTINGER, K. (2005) Activation and assembly of the NADPH oxidase: a structural perspective. *Biochemical Journal*, 386, 401-416.
- GROSS, L. A., BAIRD, G. S., HOFFMAN, R. C., BALDRIDGE, K. K. & TSIEN, R. Y. (2000) The structure of the chromophore within DsRed, a red fluorescent protein from coral. *Proceedings of the National Academy of Sciences*, 97, 11990-11995.
- HAN, C.-H., FREEMAN, J. L. R., LEE, T., MOTALEBI, S. A. & LAMBETH, J. D. (1998) Regulation of the Neutrophil Respiratory Burst Oxidase: IDENTIFICATION OF AN ACTIVATION DOMAIN IN p67 phox. *Journal of Biological Chemistry*, 273, 16663-16668.
- HEIKAL, A. A., HESS, S. T., BAIRD, G. S., TSIEN, R. Y. & WEBB, W. W. (2000) Molecular spectroscopy and dynamics of intrinsically fluorescent proteins: Coral red (dsRed) and yellow (Citrine). *Proceedings of the National Academy of Sciences of the United States of America*, 97, 11996-12001.
- HENDRIX, J., FLORS, C., DEDECKER, P., HOFKENS, J. & ENGELBORGH, Y. (2008) Dark States in Monomeric Red Fluorescent Proteins Studied by Fluorescence Correlation and Single Molecule Spectroscopy. *Biophysical Journal*, 94, 4103-4113.
- HILLESHEIM, L. N., CHEN, Y. & MÜLLER, J. D. (2006) Dual-Color Photon Counting Histogram Analysis of mRFP1 and EGFP in Living Cells. *Biophysical Journal*, 91, 4273-4284.
- HOFFMANN, B., ZIMMER, T., KLOCKER, N., KELBAUSKAS, L., KONIG, K., BENNDORF, K. & BISKUP, C. (2008) Prolonged irradiation of enhanced cyan fluorescent protein or Cerulean can invalidate Förster resonance energy transfer measurements. *J Biomed Opt*, 13, 031205.
- HOM, E. F. Y. & VERKMAN, A. S. (2002) Analysis of Coupled Bimolecular Reaction Kinetics and Diffusion by Two-Color Fluorescence Correlation Spectroscopy: Enhanced Resolution of Kinetics by Resonance Energy Transfer. *Biophysical Journal*, 83, 533-546.
- HONBOU, K., MINAKAMI, R., YUZAWA, S., TAKEYA, R., SUZUKI, N. N., KAMAKURA, S., SUMIMOTO, H. & INAGAKI, F. (2007) Full-length p40phox structure suggests a basis for regulation mechanism of its membrane binding. *EMBO J*, 26, 1176-1186.
- HONBOU, K., YUZAWA, S., SUZUKI, N. N., FUJIOKA, Y., SUMIMOTO, H. & INAGAKI, F. (2006) Crystallization and preliminary crystallographic analysis of p40(phox), a regulatory subunit of NADPH oxidase. *Acta Crystallographica Section F: Structural Biology and Crystallization Communications*, 62, 1018-1020.

- HOPPE, A., CHRISTENSEN, K. & SWANSON, J. A. (2002) Fluorescence Resonance Energy Transfer-Based Stoichiometry in Living Cells. *Biophysical Journal*, 83, 3652-3664.
- HOPPE, A. D. & SWANSON, J. A. (2004) Cdc42, Rac1, and Rac2 Display Distinct Patterns of Activation during Phagocytosis. *Molecular Biology of the Cell*, 15, 3509-3519.
- HUMPHREY, W., DALKE, A. & SCHULTEN, K. (1996) VMD - Visual Molecular Dynamics. *J. Molec. Graphics*, 14, 33-38.
- INAGAKI, F. & SUZUKI, N. N. (2005) Crystal structure of the N-terminal TPR domain (1-203) of p67phox. *1WM5*. PDB.
- ISHIKAWA-ANKERHOLD, H. C., ANKERHOLD, R. & DRUMMEN, G. P. C. (2012) Advanced Fluorescence Microscopy Techniques—FRAP, FLIP, FLAP, FRET and FLIM. *Molecules*, 17, 4047-4132.
- ITO, T., NAKAMURA, R., SUMIMOTO, H., TAKESHIGE, K. & SAKAKI, Y. (1996) An SH3 domain-mediated interaction between the phagocyte NADPH oxidase factors p40phox and p47phox. *FEBS Letters*, 385, 229-232.
- KAMI, K., TAKEYA, R., SUMIMOTO, H. & KOHDA, D. (2002) Diverse recognition of non-PxxP peptide ligands by the SH3 domains from p67phox, Grb2 and Pex13p.
- KAPUSTA, P., WAHL, M., BENDA, A., HOF, M. & ENDERLEIN, J. (2007) Fluorescence Lifetime Correlation Spectroscopy. *Journal of Fluorescence*, 17, 43-48.
- KARIMI, G. (2014) Etude de l'assemblage de la NADPH Oxydase du phagocyte. *470 Chimie, Laboratoire de Chimie physique UMR8000*. Université Paris Sud.
- KARIMI, G., HOUÉE LEVIN, C., DAGHER, M. C., BACIOU, L. & BIZOUARN, T. (2014) Assembly of phagocyte NADPH oxidase: A concerted binding process? *Biochimica et Biophysica Acta (BBA) - General Subjects*, 1840, 3277-3283.
- KATSUYAMA, M., MATSUNO, K. & YABE-NISHIMURA, C. (2012) Physiological roles of NOX/NADPH oxidase, the superoxide-generating enzyme. *Journal of Clinical Biochemistry and Nutrition*, 50, 9-22.
- KENWORTHY, A. K. & EDIDIN, M. (1998) Distribution of a Glycosylphosphatidylinositol-anchored Protein at the Apical Surface of MDCK Cells Examined at a Resolution of <100 Å Using Imaging Fluorescence Resonance Energy Transfer. *The Journal of Cell Biology*, 142, 69-84.
- KRAUSE, K. H. (2004) Tissue distribution and putative physiological function of NOX family NADPH oxidases. *Jpn J Infect Dis*, 57, S28-9.
- KUMAR, S., ALIBHAI, D., MARGINEANU, A., LAINE, R., KENNEDY, G., MCGINTY, J., WARREN, S., KELLY, D., ALEXANDROV, Y., MUNRO, I., TALBOT, C., STUCKEY, D. W., KIMBERLY, C., VIELLEROBE, B., LACOMBE, F., LAM, E. W. F., TAYLOR, H., DALLMAN, M. J., STAMP, G., MURRAY, E. J., STUHMEIER, F., SARDINI, A., KATAN, M., ELSON, D. S., NEIL, M. A. A., DUNSBY, C. & FRENCH, P. M. W. (2011) FLIM FRET Technology for Drug Discovery: Automated Multiwell-Plate High-Content Analysis, Multiplexed Readouts and Application in Situ. *ChemPhysChem*, 12, 609-626.
- LAKOWICZ, J. R. (2006) Principles of Fluorescence Spectroscopy. 3 ed., Springer US.
- LANG, P., YEOW, K., NICHOLS, A. & SCHEER, A. (2006) Cellular imaging in drug discovery. *Nat Rev Drug Discov*, 5, 343-356.
- LAPOUGE, K., SMITH, S. J., GROEMPING, Y. & RITTINGER, K. (2002) Architecture of the p40-p47-p67phox complex in the resting state of the NADPH oxidase. A central role for p67phox. *J Biol Chem*, 277, 10121-8.
- LAPOUGE, K., SMITH, S. J. M., WALKER, P. A., GAMBLIN, S. J., SMERDON, S. J. & RITTINGER, K. (2000) Structure of the TPR Domain of p67phox in Complex with Rac·GTP. *Molecular Cell*, 6, 899-907.

- LARRAINZAR, E., O'GARA, F. & MORRISSEY, J. P. (2005) APPLICATIONS OF AUTOFLUORESCENT PROTEINS FOR IN SITU STUDIES IN MICROBIAL ECOLOGY. *Annual Review of Microbiology*, 59, 257-277.
- LEUSEN, J., FLUITER, K., HILARIUS, P., ROOS, D., VERHOEVEN, A. & BOLSCHER, B. (1995) Interactions between the cytosolic components p47phox and p67phox of the human neutrophil NADPH oxidase that are not required for activation in the cell-free system. *Journal of Biological Chemistry*, 270, 11216-11221.
- LI, X. J., GRUNWALD, D., MATHIEU, J., MOREL, F. & STASIA, M.-J. (2005) Crucial Role of Two Potential Cytosolic Regions of Nox2, 191TSSTKTIRRS200 and 484DESQANHFVHHDEEKD500, on NADPH Oxidase Activation. *Journal of Biological Chemistry*, 280, 14962-14973.
- LI, X. J., TIAN, W., STULL, N. D., GRINSTEIN, S., ATKINSON, S. & DINAUER, M. C. (2009) A Fluorescently Tagged C-Terminal Fragment of p47phox Detects NADPH Oxidase Dynamics during Phagocytosis. *Molecular Biology of the Cell*, 20, 1520-1532.
- LOBANOV, M. Y., BOGATYREVA, N. S. & GALZITSKAYA, O. V. (2008) Radius of gyration as an indicator of protein structure compactness. *Molecular Biology*, 42, 623-628.
- LU, S. & WANG, Y. (2010) Fluorescence Resonance Energy Transfer Biosensors for Cancer Detection and Evaluation of Drug Efficacy. *Clinical Cancer Research*, 16, 3822-3824.
- MACHÁŇ, R., KAPUSTA, P. & HOF, M. (2014) Statistical filtering in fluorescence microscopy and fluorescence correlation spectroscopy. *Analytical and Bioanalytical Chemistry*, 406, 4797-4813.
- MACHÁŇ, R. & WOHLAND, T. (2014) Recent applications of fluorescence correlation spectroscopy in live systems. *FEBS Letters*, 588, 3571-3584.
- MAEHARA, Y., MIYANO, K. & SUMIMOTO, H. (2009) Role for the first SH3 domain of p67phox in activation of superoxide-producing NADPH oxidases. *Biochemical and Biophysical Research Communications*, 379, 589-593.
- MAEHARA, Y., MIYANO, K., YUZAWA, S., AKIMOTO, R., TAKEYA, R. & SUMIMOTO, H. (2010) A conserved region between the TPR and activation domains of p67phox participates in activation of the phagocyte NADPH oxidase. *J Biol Chem*, 285, 31435-45.
- MARCOUX, J., MAN, P., CASTELLAN, M., VIVÈS, C., FOREST, E. & FIESCHI, F. (2009) Conformational changes in p47phox upon activation highlighted by mass spectrometry coupled to hydrogen/deuterium exchange and limited proteolysis. *FEBS Letters*, 583, 835-840.
- MARCOUX, J., MAN, P., PETIT-HAERTLEIN, I., VIVES, C., FOREST, E. & FIESCHI, F. (2010) p47(phox) Molecular Activation for Assembly of the Neutrophil NADPH Oxidase Complex. *Journal of Biological Chemistry*, 285, 28980-28990.
- MASSENET, C., CHENAVAS, S., COHEN-ADDAD, C., DAGHER, M.-C., BRANDOLIN, G., PEBAY-PEYROULA, E. & FIESCHI, F. (2005) Effects of p47phox C Terminus Phosphorylations on Binding Interactions with p40phox and p67phox: STRUCTURAL AND FUNCTIONAL COMPARISON OF p40phox and p67phox SH3 DOMAINS. *Journal of Biological Chemistry*, 280, 13752-13761.
- MATUTE, J. D., ARIAS, A. A., WRIGHT, N. A. M., WROBEL, I., WATERHOUSE, C. C. M., LI, X. J., MARCHAL, C. C., STULL, N. D., LEWIS, D. B., STEELE, M., KELLNER, J. D., YU, W., MEROUEH, S. O., NAUSEEF, W. M. & DINAUER, M. C. (2009) A new genetic subgroup of chronic granulomatous disease with autosomal recessive mutations in p40phox and selective defects in neutrophil NADPH oxidase activity. *Blood*, 114, 3309-3315.

- MEIJLES, D. N., FAN, L. M., HOWLIN, B. J. & LI, J.-M. (2014) Molecular Insights of p47phox Phosphorylation Dynamics in the Regulation of NADPH Oxidase Activation and Superoxide Production. *Journal of Biological Chemistry*, 289, 22759-22770.
- MEIJLES, D. N., HOWLIN, B. J. & LI, J.-M. (2012) Consensus in silico computational modelling of the p22phox subunit of the NADPH oxidase. *Computational Biology and Chemistry*, 39, 6-13.
- MEROLA, F., FREDJ, A., BETOLNGAR, D. B., ZIEGLER, C., ERARD, M. & PASQUIER, H. (2013) Newly engineered cyan fluorescent proteins with enhanced performances for live cell FRET imaging. *Biotechnol J*.
- MEROLA, F., LEVY, B., DEMACHY, I. & PASQUIER, H. (2010) Photophysics and Spectroscopy of Fluorophores in the Green Fluorescent Protein Family. IN DEMCHENKO, A. P. (Ed.) *Advanced Fluorescence Reporters in Chemistry and Biology I*. Springer Berlin Heidelberg.
- MEYER, B. H., SEGURA, J. M., MARTINEZ, K. L., HOVIUS, R., GEORGE, N., JOHANSSON, K. & VOGEL, H. (2006) FRET imaging reveals that functional neurokinin-1 receptors are monomeric and reside in membrane microdomains of live cells. *Proc Natl Acad Sci U S A*, 103, 2138-43.
- MIYAWAKI, A. (2011) Development of Probes for Cellular Functions Using Fluorescent Proteins and Fluorescence Resonance Energy Transfer. *Annual Review of Biochemistry*, 80, 357-373.
- MÜLLER, B. K., ZAYCHIKOV, E., BRÄUCHLE, C. & LAMB, D. C. (2005) Pulsed Interleaved Excitation. *Biophysical Journal*, 89, 3508-3522.
- NAGY, P., BENE, L., HYUN, W. C., VEREB, G., BRAUN, M., ANTZ, C., PAYSAN, J., DAMJANOVICH, S., PARK, J. W. & SZÖLLSI, J. (2005) Novel calibration method for flow cytometric fluorescence resonance energy transfer measurements between visible fluorescent proteins. *Cytometry Part A*, 67A, 86-96.
- NAUSEEF, W. M. (2004) Assembly of the phagocyte NADPH oxidase. *Histochemistry and Cell Biology*, 122, 277-291.
- NAUSEEF, W. M. & BORREGAARD, N. (2014) Neutrophils at work. *Nat Immunol*, 15, 602-611.
- NISIMOTO, Y., MOTALEBI, S., HAN, C. H. & LAMBETH, J. D. (1999) The p67(phox) activation domain regulates electron flow from NADPH to flavin in flavocytochrome b(558). *J Biol Chem*, 274, 22999-3005.
- NOBUHISA, I., TAKEYA, R., OGURA, K., UENO, N., KOHDA, D., INAGAKI, F. & SUMIMOTO, H. (2006) Activation of the superoxide-producing phagocyte NADPH oxidase requires co-operation between the tandem SH3 domains of p47phox in recognition of a polyproline type II helix and an adjacent α -helix of p22phox. *Biochem J*, 396, 183-192.
- NORDENFELT, P. & TAPPER, H. (2011) Phagosome dynamics during phagocytosis by neutrophils. *J Leukoc Biol*, 90, 271-84.
- NUNES, P., DEMAUREX, N. & DINAUER, M. C. (2013) Regulation Of The NADPH Oxidase And Associated Ion Fluxes During Phagocytosis. *Traffic*, n/a-n/a.
- NÜSSE, O. (2011) Biochemistry of the Phagosome: The Challenge to Study a Transient Organelle. *TheScientificWorldJournal*, 11, 2364-2381.
- OGURA, K., NOBUHISA, I., YUZAWA, S., TAKEYA, R., TORIKAI, S., SAIKAWA, K., SUMIMOTO, H. & INAGAKI, F. (2006) NMR Solution Structure of the Tandem Src Homology 3 Domains of p47phox Complexed with a p22phox-derived Proline-rich Peptide. *Journal of Biological Chemistry*, 281, 3660-3668.
- PACLET, M.-H., COLEMAN, A. W., VERGNAUD, S. & MOREL, F. (2000) P67-phox-Mediated NADPH Oxidase Assembly: Imaging of Cytochrome b558 Liposomes by Atomic Force Microscopy†. *Biochemistry*, 39, 9302-9310.

- PADILLA-PARRA, S., AUDUGE, N., COPPEY-MOISAN, M. & TRAMIER, M. (2011a) Non fitting based FRET–FLIM analysis approaches applied to quantify protein–protein interactions in live cells. *Biophysical Reviews*, 3, 63-70.
- PADILLA-PARRA, S., AUDUGÉ, N., COPPEY-MOISAN, M. & TRAMIER, M. (2011b) Dual-color fluorescence lifetime correlation spectroscopy to quantify protein–protein interactions in live cell. *Microscopy Research and Technique*, 74, 788-793.
- PADILLA-PARRA, S. & TRAMIER, M. (2012) FRET microscopy in the living cell: Different approaches, strengths and weaknesses. *BioEssays*, 34, 369-376.
- PICCIOCCHI, A., DEBEURME, F., BEAUMEL, S., DAGHER, M.-C., GRUNWALD, D., JESAITIS, A. J. & STASIA, M.-J. (2011) Role of Putative Second Transmembrane Region of Nox2 Protein in the Structural Stability and Electron Transfer of the Phagocytic NADPH Oxidase. *Journal of Biological Chemistry*, 286, 28357-28369.
- PICK, E. (2014) Role of the Rho GTPase Rac in the activation of the phagocyte NADPH oxidase. *Small GTPases*, 5, e27952.
- PIEHLER, J. (2014) Spectroscopic techniques for monitoring protein interactions in living cells. *Current Opinion in Structural Biology*, 24, 54-62.
- PORTER, C., PARKAR, M., VERHOEVEN, A., LEVINSKY, R., COLLINS, M. & KINNON, C. (1994) p22-phox-deficient chronic granulomatous disease: reconstitution by retrovirus-mediated expression and identification of a biosynthetic intermediate of gp91-phox. *Blood*, 84, 2767-2775.
- PREUS, S. & WILHELMSSON, L. M. (2012) Advances in Quantitative FRET-Based Methods for Studying Nucleic Acids. *ChemBioChem*, 13, 1990-2001.
- PRICE, M. O., MCPHAIL, L. C., LAMBETH, J. D., HAN, C.-H., KNAUS, U. G. & DINAUER, M. C. (2002) Creation of a genetic system for analysis of the phagocyte respiratory burst: high-level reconstitution of the NADPH oxidase in a nonhematopoietic system. *Blood*, 99, 2653-2661.
- PRINZ, A., REITHER, G., DISKAR, M. & SCHULTZ, C. (2008) Fluorescence and bioluminescence procedures for functional proteomics. *PROTEOMICS*, 8, 1179-1196.
- QUINN, M. T. & GAUSS, K. A. (2004) Structure and regulation of the neutrophil respiratory burst oxidase: comparison with nonphagocyte oxidases. *Journal of Leukocyte Biology*, 76, 760-781.
- RAVEL, P. & LEDERER, F. (1993) Affinity-Labeling of an NADPH-Binding Site on the Heavy Subunit of Flavocytochrome b558 in Particulate NADPH Oxidase from Activated Human Neutrophils. *Biochemical and Biophysical Research Communications*, 196, 543-552.
- ROTROSEN, D., YEUNG, C., LETO, T., MALECH, H. & KWONG, C. (1992) Cytochrome b558: the flavin-binding component of the phagocyte NADPH oxidase. *Science*, 256, 1459-1462.
- SAHOO, H. & SCHWILLE, P. (2011) FRET and FCS—Friends or Foes? *ChemPhysChem*, 12, 532-541.
- SATHYAMOORTHY, M., DE MENDEZ, I., ADAMS, A. G. & LETO, T. L. (1997) p40phox Down-regulates NADPH Oxidase Activity through Interactions with Its SH3 Domain. *Journal of Biological Chemistry*, 272, 9141-9146.
- SCHILLER, C., DIAKOPOULOS, K. N., ROHWEDDER, I., KREMMER, E., VON TOERNE, C., UEFFING, M., WEIDLE, U. H., OHNO, H. & WEISS, E. H. (2013) LST1 promotes the assembly of a molecular machinery responsible for tunneling nanotube formation. *Journal of Cell Science*, 126, 767-777.
- SEGAL, A. W. (2005) How neutrophils kill microbes. *Annual Review of Immunology*.
- SEGAL, A. W., WEST, I., WIENTJES, F., NUGENT, J. H., CHAVAN, A. J., HALEY, B., GARCIA, R. C., ROSEN, H. & SCRACE, G. (1992) Cytochrome b-245 is a

- flavocytochrome containing FAD and the NADPH-binding site of the microbicidal oxidase of phagocytes. *Biochemical Journal*, 284, 781-788.
- SHANER, N. C., CAMPBELL, R. E., STEINBACH, P. A., GIEPMANS, B. N. G., PALMER, A. E. & TSIEN, R. Y. (2004) Improved monomeric red, orange and yellow fluorescent proteins derived from *Discosoma* sp. red fluorescent protein. *Nat Biotech*, 22, 1567-1572.
- SHANER, N. C., PATTERSON, G. H. & DAVIDSON, M. W. (2007) Advances in fluorescent protein technology. *Journal of Cell Science*, 120, 4247-4260.
- SHAPIRO, H. M. (2005) Practical Flow Cytometry. IN JOHN WILEY & SONS, I. (Ed.) 4 ed.
- SHIMOZONO, S., HOSOI, H., MIZUNO, H., FUKANO, T., TAHARA, T. & MIYAWAKI, A. (2006) Concatenation of Cyan and Yellow Fluorescent Proteins for Efficient Resonance Energy Transfer†. *Biochemistry*, 45, 6267-6271.
- SHIMOZONO, S. & MIYAWAKI, A. (2008) Engineering FRET Constructs Using CFP and YFP. *Methods in Cell Biology*. Academic Press.
- SINNECKER, D., VOIGT, P., HELLWIG, N. & SCHAEFER, M. (2005) Reversible Photobleaching of Enhanced Green Fluorescent Proteins†. *Biochemistry*, 44, 7085-7094.
- SMITH, K. C. (2009) BASIC PHOTOCHEMISTRY.
- SNAPP, E. (2005) Design and Use of Fluorescent Fusion Proteins in Cell Biology. *Current Protocols in Cell Biology*. John Wiley and Sons, Inc.
- STAMPOULIS, P., UEDA, T., MATSUMOTO, M., TERASAWA, H., MIYANO, K., SUMIMOTO, H. & SHIMADA, I. (2012) Atypical Membrane-embedded Phosphatidylinositol 3,4-Bisphosphate (PI(3,4)P2)-binding Site on p47phox Phox Homology (PX) Domain Revealed by NMR. *Journal of Biological Chemistry*, 287, 17848-17859.
- STASIA, M. & LI, X. (2008) Genetics and immunopathology of chronic granulomatous disease. *Seminars in Immunopathology*, 30, 209-235.
- STEINBERG, I. Z. (1968) Nonradiative Energy Transfer in Systems in which Rotatory Brownian Motion is Frozen. *The Journal of Chemical Physics*, 48, 2411-2413.
- SUH, C.-I., STULL, N. D., LI, X. J., TIAN, W., PRICE, M. O., GRINSTEIN, S., YAFFE, M. B., ATKINSON, S. & DINAUER, M. C. (2006) The phosphoinositide-binding protein p40phox activates the NADPH oxidase during FcγIIA receptor-induced phagocytosis. *The Journal of Experimental Medicine*, 203, 1915-1925.
- SUMIMOTO, H. (2008) Structure, regulation and evolution of Nox-family NADPH oxidases that produce reactive oxygen species. *FEBS J*, 275, 3249-77.
- SUN, Y., DAY, R. N. & PERIASAMY, A. (2011a) Investigating protein-protein interactions in living cells using fluorescence lifetime imaging microscopy. *Nat. Protocols*, 6, 1324-1340.
- SUN, Y., ROMBOLA, C., JYOTHIKUMAR, V. & PERIASAMY, A. (2013) Förster resonance energy transfer microscopy and spectroscopy for localizing protein-protein interactions in living cells. *Cytometry Part A*, 83, 780-793.
- SUN, Y., WALLRABE, H., SEO, S.-A. & PERIASAMY, A. (2011b) FRET Microscopy in 2010: The Legacy of Theodor Förster on the 100th Anniversary of his Birth. *Chemphyschem*, 12, 462-474.
- SZENTESI, G., HORVÁTH, G., BORI, I., VÁMOSI, G., SZÖLLŐSI, J., GÁSPÁR, R., DAMJANOVICH, S., JENEI, A. & MÁTYUS, L. (2004) Computer program for determining fluorescence resonance energy transfer efficiency from flow cytometric data on a cell-by-cell basis. *Computer Methods and Programs in Biomedicine*, 75, 201-211.

- TAMURA, M., SHIOZAKI, I., ONO, S., MIYANO, K., KUNIHIRO, S. & SASAKI, T. (2007) p40phox as an alternative organizer to p47phox in Nox2 activation: A new mechanism involving an interaction with p22phox. *FEBS Letters*, 581, 4533-4538.
- THEWS, E., GERKEN, M., ECKERT, R., ZÄPFEL, J., TIETZ, C. & WRACHTRUP, J. (2005) Cross Talk Free Fluorescence Cross Correlation Spectroscopy in Live Cells. *Biophysical Journal*, 89, 2069-2076.
- TIAN, W., LI, X. J., STULL, N. D., MING, W., SUH, C.-I., BISSONNETTE, S. A., YAFFE, M. B., GRINSTEIN, S., ATKINSON, S. J. & DINAUER, M. C. (2008) FcγR-stimulated activation of the NADPH oxidase: phosphoinositide-binding protein p40phox regulates NADPH oxidase activity after enzyme assembly on the phagosome. *Blood*, 112, 3867-3877.
- TLILI, A., ERARD, M., FAURE, M. C., BAUDIN, X., PIOLOT, T., DUPRE-CROCHET, S. & NUSSE, O. (2012) Stable accumulation of p67phox at the phagosomal membrane and ROS production within the phagosome. *J Leukoc Biol*, 91, 83-95.
- TOCHIO, N., CHIKAYAMA, E., KOSHIBA, S., INOUE, M., KIGAWA, T. & YOKOYAMA, S. (2006) Refined solution structure of the 1st SH3 domain from human Neutrophil cytosol factor 2 (NCF-2). *2DMO*. PDB.
- TRAMIER, M., ZAHID, M., MEVEL, J.-C., MASSE, M.-J. & COPPEY-MOISAN, M. (2006) Sensitivity of CFP/YFP and GFP/mCherry pairs to donor photobleaching on FRET determination by fluorescence lifetime imaging microscopy in living cells. *Microscopy Research and Technique*, 69, 933-939.
- TRÓN, L., SZÖLLÖSI, J., DAMJANOVICH, S., HELLIWELL, S. H., ARNDT-JOVIN, D. J. & JOVIN, T. M. (1984) Flow cytometric measurement of fluorescence resonance energy transfer on cell surfaces. Quantitative evaluation of the transfer efficiency on a cell-by-cell basis. *Biophysical Journal*, 45, 939-946.
- TSOURKAS, A., NEWTON, G., PEREZ, J. M., BASILION, J. P. & WEISSLEDER, R. (2005) Detection of Peroxidase/H₂O₂-mediated oxidation with enhanced yellow fluorescent protein. *Analytical Chemistry*, 77, 2862-2867.
- UEYAMA, T., NAKAKITA, J., NAKAMURA, T., KOBAYASHI, T., KOBAYASHI, T., SON, J., SAKUMA, M., SAKAGUCHI, H., LETO, T. L. & SAITO, N. (2011) Cooperation of p40phox with p47phox for Nox2-based NADPH Oxidase Activation during Fcγ Receptor (FcγR)-mediated Phagocytosis: MECHANISM FOR ACQUISITION OF p40phox PHOSPHATIDYLINOSITOL 3-PHOSPHATE (PI(3)P) BINDING. *Journal of Biological Chemistry*, 286, 40693-40705.
- UEYAMA, T., TATSUNO, T., KAWASAKI, T., TSUJIBE, S., SHIRAI, Y., SUMIMOTO, H., LETO, T. L. & SAITO, N. (2007) A Regulated Adaptor Function of p40phox: Distinct p67phox Membrane Targeting by p40phox and by p47phox. *Molecular Biology of the Cell*, 18, 441-454.
- VALEUR, B. (2006) *Molecular Fluorescence*.
- VAN MANEN, H.-J., VERKUIJLEN, P., WITTENDORP, P., SUBRAMANIAM, V., VAN DEN BERG, T. K., ROOS, D. & OTTO, C. (2008) Refractive Index Sensing of Green Fluorescent Proteins in Living Cells Using Fluorescence Lifetime Imaging Microscopy. *Biophysical Journal*, 94, L67-L69.
- VILLOING, A., RIDHOIR, M., CINQUIN, B., ERARD, M., ALVAREZ, L., VALLVERDU, G., PERNOT, P., GRAILHE, R., MÉROLA, F. & PASQUIER, H. (2008) Complex Fluorescence of the Cyan Fluorescent Protein: Comparisons with the H148D Variant and Consequences for Quantitative Cell Imaging†. *Biochemistry*, 47, 12483-12492.
- VON LÖHNEYSSEN, K., NOACK, D., WOOD, M. R., FRIEDMAN, J. S. & KNAUS, U. G. (2010) Structural Insights into Nox4 and Nox2: Motifs Involved in Function and Cellular Localization. *Molecular and Cellular Biology*, 30, 961-975.

- WAHL, M. (2009) Time-Correlated Single Photon Counting. 2.1 ed. Berlin, Germany, PicoQuant GmbH.
- WAHL, M., DELBRUECK, H., OSCHKINAT, H. & HEINEMANN, U. (2003) p47phox PX domain. *1KQ6*. PDB.
- WALTHER, K. A., PAPKE, B., SINN, M. B., MICHEL, K. & KINKHABWALA, A. (2011) Precise measurement of protein interacting fractions with fluorescence lifetime imaging microscopy. *Mol Biosyst*, 7, 322-36.
- WIJNTJES, F. B., PANAYOTOU, G., REEVES, E. & SEGAL, A. W. (1996) Interactions between cytosolic components of the NADPH oxidase: p40phox interacts with both p67phox and p47phox. *Biochem J*, 317 (Pt 3), 919-24.
- WILSON, M. I., GILL, D. J., PERISIC, O., QUINN, M. T. & WILLIAMS, R. L. (2003) PB1 Domain-Mediated Heterodimerization in NADPH Oxidase and Signaling Complexes of Atypical Protein Kinase C with Par6 and p62. *Molecular Cell*, 12, 39-50.
- WLODAWER, A., MINOR, W., DAUTER, Z. & JASKOLSKI, M. (2008) Protein crystallography for non-crystallographers, or how to get the best (but not more) from published macromolecular structures. *FEBS Journal*, 275, 1-21.
- YU, L., CROSS, A. R., ZHEN, L. & DINAUER, M. C. (1999) *Functional Analysis of NADPH Oxidase in Granulocytic Cells Expressing a Δ 488-497 gp91 phox Deletion Mutant*.
- YU, L., ZHEN, L. & DINAUER, M. C. (1997) Biosynthesis of the Phagocyte NADPH Oxidase Cytochrome b 558 : ROLE OF HEME INCORPORATION AND HETERODIMER FORMATION IN MATURATION AND STABILITY OF gp91 phox and p22 phox SUBUNITS. *Journal of Biological Chemistry*, 272, 27288-27294.
- YUZAWA, S., MIYANO, K., HONBOU, K., INAGAKI, F. & SUMIMOTO, H. (2009) The domain organization of p67 phox, a protein required for activation of the superoxide-producing NADPH oxidase in phagocytes. *J Innate Immun*, 1, 543-55.
- YUZAWA, S., OGURA, K., HORIUCHI, M., SUZUKI, N. N., FUJIOKA, Y., KATAOKA, M., SUMIMOTO, H. & INAGAKI, F. (2004) Solution Structure of the Tandem Src Homology 3 Domains of p47phox in an Autoinhibited Form. *Journal of Biological Chemistry*, 279, 29752-29760.
- ZACHARIAS, D. A., VIOLIN, J. D., NEWTON, A. C. & TSIEN, R. Y. (2002) Partitioning of Lipid-Modified Monomeric GFPs into Membrane Microdomains of Live Cells. *Science*, 296, 913-916.

Imagerie quantitative de l'assemblage de la NADPH oxydase des phagocytes en cellules vivantes par des approches FRET-FLIM

Mots clés : Imagerie Quantitative, FRET, FLIM, protéine fluorescente, NADPH oxydase

Résumé : La NADPH oxydase des phagocytes (NOX2) est responsable de la production d'anions superoxydes qui sont les précurseurs des autres formes réactives de l'oxygène. NOX2 est une enzyme majeure de la réponse immunitaire. Les dysfonctionnements de NOX2 sont associés à de nombreuses pathologies et donc il convient d'en comprendre les détails de la régulation. Cette oxydase est composée de cinq sous-unités : deux protéines membranaires, gp91phox et p22phox et 3 protéines cytosoliques p47phox, p67phox et p40phox. D'après les études *in vitro* avec des protéines purifiées, les protéines cytosoliques sont supposées former un complexe ternaire qui se déplace à la membrane avec une petite protéine G, Rac, au moment l'activation.

L'objectif de ce projet est de caractériser les interactions spécifiques entre les sous-unités cytosoliques de NOX2 en cellules vivantes en utilisant le phénomène de transfert résonant d'énergie de type Förster (FRET) entre deux fluorophores, un donneur et un accepteur. Ici les fluorophores seront des protéines fluorescentes de la famille de la GFP. Elles sont fusionnées à deux sous-unités. L'efficacité du FRET dépend de la distance entre les fluorophores et permet ainsi de caractériser les interactions entre les protéines d'intérêt. Une méthode rapide d'identification des situations où le FRET est positif a été mise au point par cytométrie en flux. Des études détaillées et quantitatives ont ensuite été réalisées en utilisant l'imagerie de durée de fluorescence (FLIM) du donneur. Le FLIM, combiné à l'utilisation de donneurs présentant une durée de vie mono-exponentielle, permet de déterminer directement des efficacités de FRET apparentes et moléculaires, qui contiennent, toutes les deux, des informations qualitatives et quantitatives sur l'interaction et la structure des protéines impliquées. De ces données, il est possible d'extraire la fraction des donneurs interagissant avec un accepteur.

Les informations obtenues à partir des données de FRET-FLIM permettent une meilleure compréhension de l'organisation et de la régulation de NOX2 tout en permettant une estimation des constantes de dissociation (Kd). Afin de confirmer ces résultats, des expériences de spectroscopie de corrélation de fluorescence à deux couleurs (FCCS) ont été réalisées. Cette méthode complètement indépendante n'est pas basée sur la distance entre fluorophores comme le FRET mais sur leur co-diffusion à travers un petit volume d'observation dans le cytoplasme cellulaire.

L'approche FRET-FLIM nous a tout d'abord permis d'observer les interactions entre hétéro-dimères formés de deux sous-unités différentes en cellules vivantes et d'exclure la formation d'homodimères entre deux sous-unités identiques. Etant donné la bonne précision des mesures de FLIM, nous avons pu comparer les informations structurales obtenues en cellules avec les données structurales issues d'études sur les protéines purifiées *in vitro* et nous avons constaté qu'elles sont en bon accord. Nous avons ensuite aligné les structures disponibles pour proposer un premier modèle 3D du complexe cytosolique de la NADPH oxydase au repos dans le cytosol cellulaire.

Les fractions de protéines en interaction sont pour tous les hétéro-dimères autour de 20% ce qui n'est pas en accord avec l'hypothèse courante qui propose que toutes les sous-unités cytosoliques soient sous forme de complexe. Toutefois nos premiers résultats de FCCS confirment ce résultat extrait des données de FRET-FLIM. Nous proposons donc que la complexation des sous-unités cytosolique pourrait être impliquée dans la régulation de la NADPH oxydase. Des études complémentaires seront nécessaires pour valider cette nouvelle hypothèse. Les constantes de dissociation Kd estimées à partir de nos résultats sont micromolaires et donc un ordre de grandeur plus élevé que les valeurs nanomolaires déterminées *in vitro*. Des mesures plus détaillées de FCCS pourront compléter et valider ces résultats.



Imaging the assembly of the phagocyte NADPH oxidase in live cells - a quantitative FRET-FLIM approach

Keywords : Quantitative Imaging, FRET, FLIM, fluorescent protein, NADPH oxidase

Abstract : The phagocyte NADPH oxidase (NOX2) is a key enzyme of the immune system generating superoxide anions, which are precursors for other reactive oxygen species. Any dysfunctions of NOX2 are associated with a plethora of diseases and thus detailed knowledge about its regulation is needed. This oxidase is composed of five subunits, the membrane-bound gp91phox and p22phox and the cytosolic p47phox, p67phox, and p40phox. The latter are assumed to be in a ternary complex that translocates together with the small GTPase Rac to the membranous subunits during activation.

Our aim was to discover and to characterize specific interactions of the cytosolic subunits of NOX2 in live cells using a Förster Resonance Energy Transfer (FRET) based approach: Since FRET depends on the distance between two fluorophores, it can be used to reveal protein-protein interactions non-invasively by studying fluorescent protein tagged subunits. To have a rapid method on hand to reveal specific interactions, a flow cytometer based FRET approach was developed. For more detailed studies, FRET was measured by fluorescence lifetime imaging microscopy (FLIM), because it allows a direct determination of the apparent and molecular FRET efficiency, which contains both qualitative and quantitative information about the interaction and the structure of the interacting proteins. Furthermore, the FRET-FLIM approach enables an estimation of the fraction of bound donor. This information itself is important for a better understanding of the organisation and regulation of the NOX2, but it is also necessary for the calculation of the dissociation constant K_d from the FRET-FLIM data. To confirm the findings obtained by FRET-FLIM fluorescence cross correlation spectroscopy (FCCS) experiments were performed. This completely independent method is not based on distances like FRET but on the observation of the co-diffusion of the fluorescently labelled samples when they move across a small observation volume inside the cells.

The FRET-FLIM approach allowed us in a first step to discover heterodimeric interactions between all cytosolic subunits in live cells. Due to the good precision of the results, we were able to extract structural information about the interactions and to compare them with available structural data obtained from in vitro studies. The information from FRET-FLIM was coherent with in vitro data. We then aligned the available structures leading to the first 3D-model of the cytosolic complex of the NADPH oxidase in the resting state in live cells.

Additionally, the bound fraction for all heterodimeric interactions derived by FRET-FLIM is around 20 %, which is in contrast to the general belief that all cytosolic subunits are bound in complex. The first FCCS results support our findings. Therefore, we believe that the complexation of the cytosolic subunits could be involved in the regulation of the NADPH oxidase and should be investigated further. The estimated K_d derived from the FRET-FLIM approach is in the low micromolar range, which is an order of a magnitude higher than the nanomolar range of in vitro studies.

In conclusion, we showed that our quantitative FRET-FLIM approach is not only able to distinguish between specific and unspecific protein-protein interactions, but gives also information about the structural organisation of the interacting proteins. The high precision of the FRET-FLIM data allow the determination of the bound fraction and an estimation of the K_d in live cells. FCCS is a complementary method, which can verify these quantitative findings. However, it cannot replace FRET-FLIM completely as it does not give any structural information.

With respect to the biological outcome of this project, we can propose for the first time a 3D-model of the cytosolic complex of the NADPH oxidase covering the in vitro as well as the live cell situation. Additionally, the small bound fraction found here may raise new ideas on the regulation of this vital enzyme.

